Realization and study of substrates with modular rigidity and integratable devices for cellular and tissue engineering

Bin Wang

To cite this version:

Bin Wang. Realization and study of substrates with modular rigidity and integratable devices for cellular and tissue engineering. Analytical chemistry. Université Paris sciences et lettres, 2017. English. NNT : 2017PSLEE043 . tel-01816037

HAL Id: tel-01816037
https://theses.hal.science/tel-01816037

Submitted on 14 Jun 2018

THÈSE DE DOCTORAT

de l'Université de recherche Paris Sciences et Lettres
PSL Research University

École Normale Supérieure de Paris

Realization and study of substrates with modular rigidity and integratable devices for cellular and tissue engineering

Réalisation et étude de substrates de rigidité modulable et de dispositifs intégrables pour l'ingénierie cellulaire et tissulaire

Ecole doctorale n°388

Chimie physique et chimie analytique de Paris Centre

Spécialité Chimie Physique et Chimie Analytique

COMPOSITION DU JURY :

M. Ladoux Benoit
Professeur Paris Diderot, Rapporteur

Mme. Peng Ling
Directrice de recherche CNRS, Rapporteur

M. Agbulut Onnik
Professeur UPMC, Examinateur

M. Tribet Christophe
Directeur de recherche CNRS, Examinateur

M. Chen Yong
Directeur de recherche CNRS, Directeur de thèse

Soutenue par Bin WANG
le 26 septembre 2017

Dirigée par **Yong CHEN**

Acknowledgement

Completing my PhD degree program is probably the most challenging activity of the first 28 years of my life. It has been a great privilege to spend three years in the Chemistry Department at the École normale supérieure (Paris), and its members will always remain dear to me.

Before anything, I would like to present my gratitude to Chinese Scholar Council (CSC) for supporting me to study abroad during the whole three years, to École normale supérieure for providing me the excellent research environment on my thesis, to doctoral school ED388 for accepting me as a doctor candidate.

Then, I would like to offer my sincerest gratitude to my advisor, Professor Yong Chen, for his motivation, enthusiasm and immense knowledge, and for brainstorming the most challenging ideas with me. His keen and vigorous academic observation enlightens me not only in this thesis but also in my future study. I have learnt from him a lot not only about the professional skills, but also the modes of thinking. And also, many thanks to him for leading me into this thesis topic at the interface of several scientific disciplines. There are so many fantastic learning materials which are far beyond my original imagination.

Besides my advisor, I would like to thank the rest of my thesis committee: Prof. Benoit Ladoux, Prof. Ling Peng, Prof. Onnik Agbulut and Prof. Christophe Tribet for their insightful comments, constructive feedback, and challenging questions.

Next, I am also grateful to the professors, colleagues and friends in France for their kindly help, support and encouragement. They are: Dr. Jian Shi, Dr. Dr. Li Wang, Dr. Yadong Tang, Dr. Jacques Fattaccioli, Jin Wei, Xiaolong Tu, Olivier Mesdjian, Alexandra Sasha Laniece, Dr. Sandrine Quignard, Dr. Diana Molino, Dr. Yohan Farouz, Dr. Kalthoum Ben M’barek, Dr. Maria Kitsara, Dr. Isabelle Aujard, Dr. Louise.Hespel, Xiaoqing Liu, Chenge Li, Lihui Hu, Ruikang Zhang, Na Pan, Ming Ding, Boxing Huang.

My gratitude also goes to Mr. Auguste Filippi, Mr. Stéphane Emery, Mme Anne Halloppe, Mr. Stéphane Paties-Gorizza, Mme Marie Chayla in ENS and Mme Soobrayen

Koonavadee in UPMC, who were always so kind to arrange everything for me in student affairs management.

Thanks to my closest family, I cannot faithfully express my feelings of love, admiration and gratitude with the limited vocabulary. Dad, thanks for your education, for teaching me the values of our roots; Mom, thanks for your unconditional and blind support regardless of my decisions, like my choice to pursue an academic career abroad. And thanks to my sister, nephew, niece and parents-in -law for their endless support.

To my beloved Meng, thanks for choosing to come abroad to accompany me; for having made my life as easy as possible for the sake of this PhD; for taking care of Simon along while I had to feed iPS cells even on the weekends; for cooking delicious food and dishes even you never did it before and have to find the "protocol" online; for encouraging me when I encountered fail experiments; for bringing me new perspectives on the word…

July 2017

Bin Wang

Table of Contents

Outline

Tissue engineering aims at biocompatible scaffolds or substitutes that can used to restore, maintain or improve tissue functions. On one hand, these scaffolds or substitutes have to offer mechanical and biological supports to guide the cell growth, migration and integration to form tissues, which leads to a major challenge in tissue engineering: designing and manufacturing reliable materials and devices to fulfill the functions and physiological conditions in vivo. Tissue consists mostly of cells and extracellular matrix (ECM) biopolymers. With the increasingly understanding of the intricate interactions between cells and the ECM, more attention is now focused on the preparation of scaffolds that can imitate the componential, structural and functional aspects of ECM to de-novo ECM milieu and neo tissue genesis. In vivo, a tissue can have different stiffness and different physiological conditions. It is therefore important to have scaffolds or substrates with controllable rigidity and to investigate the mechanical-driven cell behaviors such as migration. In addition, the scaffolds should also have the capability of providing a transitional three-dimensional (3D) support to facilitate cell recruiting, adhesion, migration, and proliferation. On the other hand, the use of stem cells is becoming a common practice for research purposes. Of particular interesting is the use of the so-call induced pluripotent stem cells (iPSCs), which can be derived from stromal cells of the body, due to their capability of self-renewal infinitively and differentiation to different adult cells. This means that iPSCs can be used as infinite and powerful resources for the development of new methods and new tools in tissue engineering, in addition to the mesenchymal stem cells and other adult stem cells. However, the iPSC capability is highly dependent on the culture condition. The conventional culture methods which rely on the daily use of hard substrates provided by such as plastic culture dish, flask and multiwell, are not appropriate for most of envisaged applications, though they also allow the pluripotency maintenance and the guided differentiation after biochemical surface medication of the substrates. This is because of the lack of mechanical compatibility since the stiffness values of the substrates are generally much higher than that of hiPSCs or the derived cells. To this regard, it is highly desirable to develop new substrates and new culture methods for iPSCs applications.

The purpose of this thesis work is to develop new substrates and new scaffolds with the assist of advanced micro- and nanofabrication techniques to recapitulate the structural and functional features of ECM. We are mainly interested in

i) Fabrication of elastomer micropillars as low stiffness substrates,

ii) Control of the substrate stiffness by varying pillar height,

iii) Generation of a stiffness gradient for cell migration (durotaxis) studies,

iv) Realization of nanofibrous scaffolds for 3D cell handing,

v) Creation of a patch form of cardiac tissues from iPSCs.

The thesis is organized in five chapters:

The first chapter is a general introduction to the work. We first introduce the basic concepts of cells, cytoskeleton, ECM and cell-ECM interaction. Then we discuss in more detail the cell-substrate interaction, including the mechanotransduction and the culture substrates. Afterward, we describe the technology of iPSCs. Finally, we present the scaffolds fabrication methods for tissue engineering, before defining the objectives of this work.

In the second chapter, we review different micro- and nanofabrication techniques that can be used to obtain micro-patterns and devices for cell analyses. After a brief introduction, UV photolithography, soft lithography and electrospinning techniques will be described in detail. More specific fabrication processes will be presented in the following chapters.

The third chapter is dedicated to the fabrication of dense elastomer pillar arrays using photolithography and soft-lithography techniques. In particular, we obtained with micropillars of different heights on the same substrate having the same top level. This has be achieved by backside UV exposure of a low-viscosity resist layer spin-coated on a substrate with pre-patterned stripes. Thus, we could be able to create a substrate with a stiffness gradient at high resolution. Cells on such a substrate showed remarkable effects of elongation and directed migration. Elastomer micropillars organized in more complex patterns such as ripple-like height gradient patterns showed similar cell behaviors, thereby enabling easy mechanotransduction of cell functions.

The fourth chapter reports a method of fabrication of a cell culture device made of narrowly spaced monolayers of gelatin nanofibers for 3D cell handling. These fibers were electrospun and crosslinked on the two side of a membrane of poly (ethylene glycol) diacrylate (PEGDA) hydrogel with through holes. When the NIH 3T3 cells were seeded, they could infiltrate into and proliferate in the free-space between the two fiber layers. Such a culture support is permeable in 3D and mechanically robust which should be useful for microfluidic device integration for drug screening.

In the fifth chapter, we demonstrate human iPSCs differentiation of the micropillar substrates with controlled stiffness. Our results showed that stiffer substrates favor the hiPSCs attachment and proliferation. With the help of a PDMS stencil with honeycomb pattern, we could be able to obtain uniform embryoid bodies (EBs) on micropillar arrays and demonstrate a stiffness-dependent EBs formation. More specifically, the dimensionality, morphology and pluripotency of the EBs on different micropillar substrates were investigated, showing that hiPSCs on stiff substrates prefer to spread and form flatter aggregation whereas the soft substrates promote cell-cell contraction and result in EBs-like formation. Finally, hiPSCs differentiation to cardiac tissue has been carried out the micropillar substrates, showing a clear stiffness dependence of the processes.

In appendix, we present a simple and flexible process for fabricating microwave-like patterns with precisely controlled features using photolithography. With this method, microwave shapes, rice leaf-like microstructures and convex microlens arrays (MLAs) could be generated. Afterwards, the hydrophobic property of rice leaf-like micropatterns and the imaging property of MLAs were demonstrated. This unique method could be a potential alternative to fabricate complex substrates to explore numerous applications in biotechnology, surface engineering and microfluidics.

Chapter 1

General Introduction

This chapter provides a general introduction to this thesis work. We first present the fundamental notions of cells, cytoskeleton, extracellular matrix (ECM) and cell-ECM interaction. We then discuss in more detail the cell-substrate interaction, including the mechanotransduction and the culture substrates effects. Afterward, we describe the technology of induced pluripotent stem cells (iPSCs). Finally, we present the scaffolds fabrication methods for tissue engineering, before defining the objectives of this work.

1.1 Cell and cellular microenvironment

Cells are the smallest components in living things. Their functions and behaviors are not only determined by their genes but also regulated by the cellular microenvironment. Therefore, recapitulating the cellular microenvironment and understanding the interaction of the cell and the cellular microenvironment is of great importance in cell biology. This is also important to define a development strategy of cell-based arrays and tissue engineering for a large variety of applications. Enormous efforts have been devoted to this general task [1, 2] but many unsolved issues remain to be addressed in order to meet the new challenges in disease modeling, drug discovery and regenerative medicine.

1.1.1 Cell and cell cytoskeleton

In human body, cells are the intermediate building blocks made of atoms and molecules and the sub-constituents of tissues, organs, and organ systems. Groups of one particular type of cell or of a few types make up a tissue, two or more tissue types make up an organ, and a group of organs make up an organ system. Therefore, almost all functions of human physiology and pathology have their original at cellular levels. For instance, cardiac muscle cells make up cardiac muscle tissue and the cardiac muscle tissues make up the heart, while heart is the main part of the circulatory system, as schematic shown in **Fig. 1.1**.

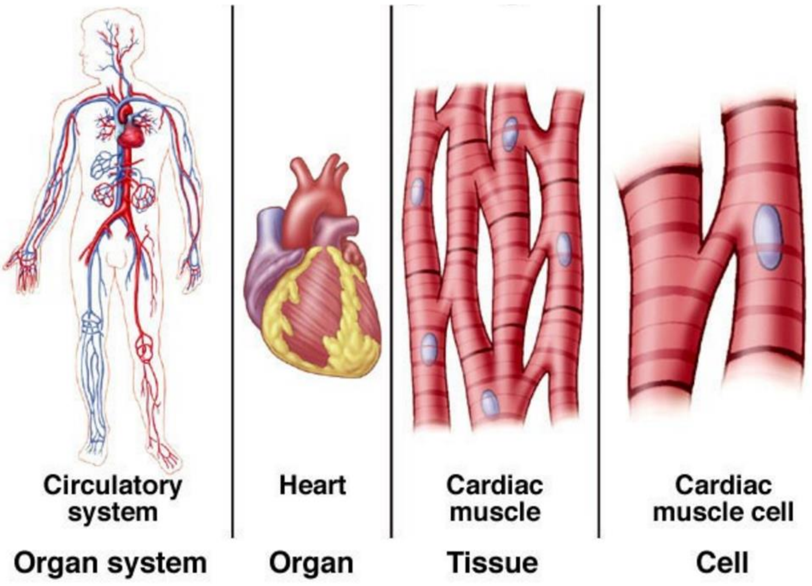

Figure 1.1 Schematic diagram of the hierarchy of cells, tissue and organs that comprise an organ system: the circulatory system [3].

Cells have complicated microstructures that evolve in response to its chemo-physical environment [4, 5]. **Fig. 1.2** shows a schematic presentation of a eukaryotic cell in which some main components of the cell can be identified:

a) Plasma membrane: The plasma membrane is a boundary between the cell and its surroundings, acting as a protective barrier for the cell and controlling what enters and exits the cell by selective permeability. This selectively permeable membrane also contains receptor proteins that allow cells to detect external signaling molecules.

b) Cytoplasm: Cytoplasm is the substance where all the other organelles are located, which is composed mostly of water and proteins that regulate the cells metabolism.

c) Nucleus: As cell's information center, cell nucleus is the most conspicuous organelle. It is separated from the cytoplasm by a double membrane called the nuclear envelope. The nucleus is the place where almost all deoxyribonucleic acid (DNA) replication and ribonucleic acid (RNA) synthesis (transcription) occur. DNA is transcribed, or copied into a special RNA, called messenger RNA (mRNA). This mRNA is then transported out of the nucleus, where it is translated into a specific protein molecule. A human cell has genetic material mainly contained in the cell nucleus. It is divided into 46 linear DNA molecules called chromosomes, including 22 homologous chromosome pairs and a pair of sex chromosomes

d) Cytoskeleton: Cytoskeleton is composed of protein fibers (microfilaments, intermediate filaments, and microtubules) that are located throughout the cytoplasm, providing support, shape, and motility to the cell.

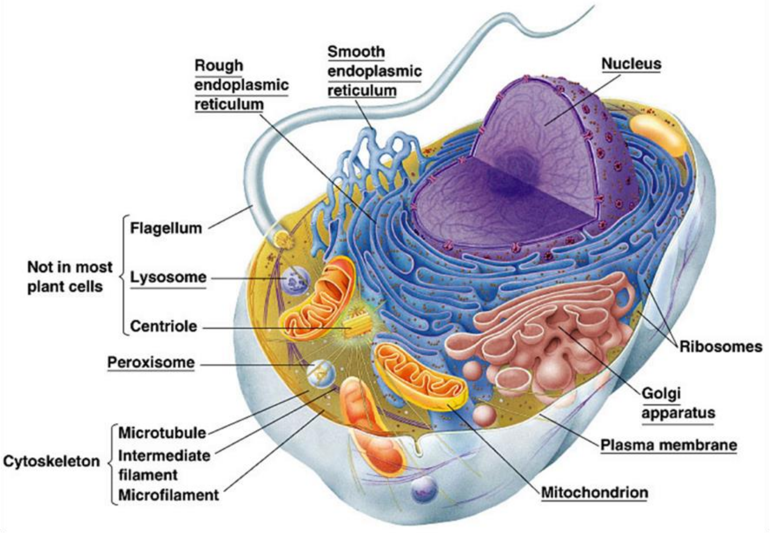

Figure 1.2 Schematic diagram of the intracellular structure of a typical animal cell [6].

The cytoskeleton is a network of different protein fibers that function to: maintain or change the shape of the cell; secure some organelles in specific positions; enable movement of cytoplasm and vesicles within the cell; and enable the cell to move in response to stimuli [7–9]. There are three types of fibers within the cytoskeleton: microfilaments, intermediate filaments, and microtubules (**Fig. 1.3**). The “backbone” of the cytoskeleton is the actin filaments which are composed of actin subunits. Actin is one of the most abundant protein in eukaryotic cells and comprises 20% of total cellular proteins by weight in muscle cells. Actin can be present as either a free monomer called G-actin (globular) or as part of a polymer microfilament called F-actin ('F' for filamentous). The actin filament itself has structural polarity, which refers to the fact that there are two distinct ends to the filament. These ends are called the "(-) end" and the "(+) end". At the "(+) end", actin subunits are adding onto the elongating filament and at the "(-) end", actin subunits are disassembling, or falling off of the filament. This process of assembly and disassembly is controlled by the ATP:ADP ratio in the cytoplasm. Filaments can be bundled or cross-linked to each other by several actin binding proteins to create a network [8, 10].

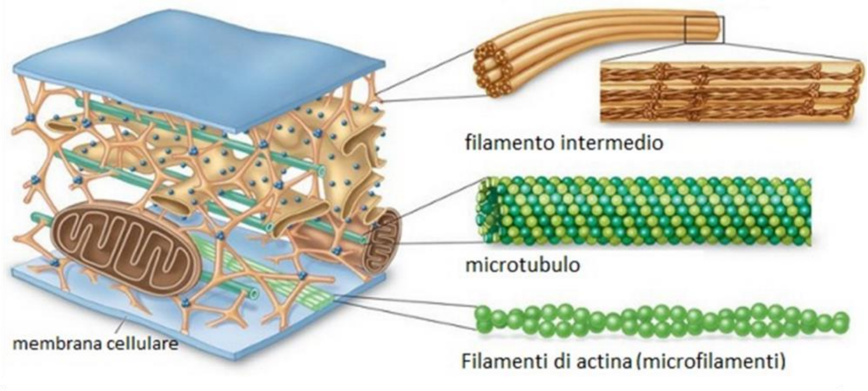

Figure 1.3 Scheme of the typical organization of cytoskeleton [10].

The actin network is of great importance in the regulation of the mechanical properties of living cells. The cell cytoskeleton, unlike synthetic polymer networks, is highly dynamic since the on-off kinetics of the cross-linking proteins and the assembly and disassembly process of the filaments. Moreover, motor proteins, as some of the cross-linkers, are capable of consuming chemical energy and thus generating forces between the filaments. The highly complex and active cell cytoskeleton also leads to the unique cell mechanical properties, for instance, the process of crawling, dividing and assembling to higher functional units. Besides, the crawling movement of cells is driven by the continuous reorganization and turnover of the actin cytoskeleton. At the cell front, actin filaments are all polarized in one direction, with their fast polymerizing ends forwards (for pushing); in the body of the cytoskeleton, actin filaments form bipolar assemblies with myosin to form contractile arrays (for retracting) [11].

1.1.2 Cellular microenvironment

1.1.2.1 Extracellular matrix

The Extracellular Matrix (ECM) provides mechanical supports and biochemical signaling to cells which regulate many cell functions such as cell division, motility, embryonic development, and wound healing [12, 13]. In addition, the ECM plays an important role in forming the mass of skin, bones, and tendons. The ECM also forms extracellular structures such as the cornea of the eye and filtering networks in the kidney. A simplified diagram of the composition of the ECM is illustrated in **Fig. 1.4**.

The ECM is composed of ECM biopolymers such as collagen, elastin, laminin perlecan and other proteins proteoglycans. Collagen is made of long fibrous glycoproteins with a triple helix structure, which leads to a high tensile strength and great elasticity. Proteoglycans are consisted of small proteins attached to long polysaccharides, regulating movement of molecules through the matrix and also the binding of cations and water. Among others, fibronectin, a high-molecular weight (~440 kDa) ECM glycoprotein, can bind efficiently to the membrane-spanning receptor proteins called integrins and to the ECM, which decide the overall communication of the ECM [14–16]. Thus, fibronectin is of great importance in cell attachment and in the wound healing processes. It is also widely used for substrate treatment before cell culture. Elastin is the component that allows the ECM to be more "rubbery" and form elastic structures. While laminin is found in between the cells and it forms webs that help hold them together [17].

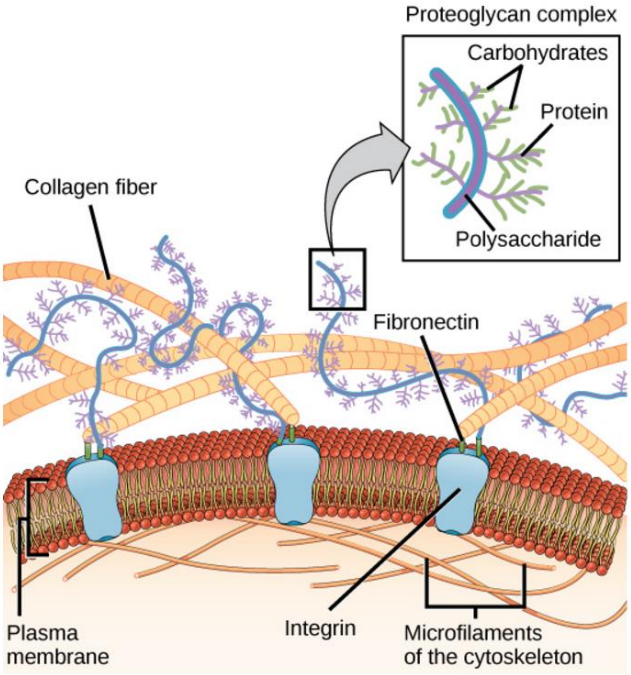

Figure 1.4 Schematic diagram of the compositions of the ECM [18].

1.1.2.2 Cell-ECM interaction

The effects of the ECM to cells are primarily mediated through receptor-mediated signaling. Integrins (**Fig. 1.4**), a family of cell surface receptors, whose structure consists of the heterodimeric non-covalent association of α and β subunits. While β subunits seem to have a non-specific role in ligand binding activity, α subunits on the contrary confer high specificity of signal transduction. In their inactive state, integrins are freely diffusive within the cell membrane until they encounter an available binding domain in the ECM. Integrins change conformational once ligand binding, which leads to the recruitment cytoplasmic proteins [19, 20].

A premature adhesive junction between intercellular and extracellular molecules, formed by localized integrins cluster and structure proteins, activates the intracellular signaling events. As soon as ECM molecules bind to their specific integrin or non-integrin receptors, a change in cytoplasmic domain of the receptor occurs, which associates with the cytoskeleton at focal adhesion sites. Consequently, an assembly of the focal contact proteins occurs with other intercellular components, such as phosphorylated proteins. These changes can promote cytoskeleton rearrangement, which may determine differential interactions of chromatin and nuclear matrix at the nuclear level. The dynamic association of integrin receptors with the actin cytoskeleton may also induce changes in cell shape, which in turn alters the ability of cells to proliferate or differentiate [21].

1.1.2.3 Cell-cell interaction

Cell-cell interactions allow cells to communicate with each other in response to changes in their microenvironment, which is of great importance in the development and maintenance of multicellular organisms. Interactions between cells can be stable through cell junctions which have the ability of sending and receiving signals. Stable cell-cell interactions are essential for the communication and organization within tissues, otherwise the loss of communication between cells can result in uncontrollable cell growth and cancer spread.

Intercellular junctions normally have three main types, i.e., tight junctions, desmosomes and gap junctions (shown as **Fig. 1.5**), classified by the strength of the cell-cell interaction, which depends on the mixture, concentration, distribution and also cytoskeletal linkages of adhesion molecules on the cell surface. The main tight junction forms a seal between the two membranes. This seal consists of the transmembrane proteins and provides transcellular and paracellular transport of molecules, but prevents passive flow between cells. Desmosomes, adherent or anchoring junctions, build an encircling structure, with the main function of strengthening and stabilizing the circular occluding bands. Another important function is the linking cytoskeletons of adjacent cells.

This is made possible by the transmembrane glycoprotein cadherin, which functions in presence of Ca^{2+}. The major function of gap junctions, consisted of proteins named connexin, is the direct transfer and exchange of nutrients and signal molecules between the cells [23, 24]. The complex of connexin has a hydrophilic pore with the diameter of 1.5 nm, which permit the exchange of larger molecules.

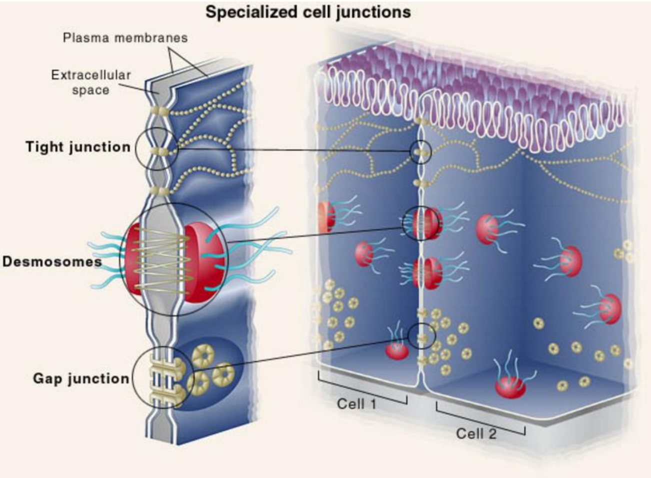

Figure 1.5 Schematic diagram of the three major types of intercellular junctions [22].

1.2 Cell-substrate interaction from mechanotransduction aspect

Cells in the human body have different tissues in the body have specific cell types and characteristic microenvironments that work together to achieve their function. Since cells exploit mechanical forces to explore their environments and recognize material properties, the physical characteristics of their microenvironment profoundly impact cell behavior and fate [25]. Traditionally, researchers have tried to understand disease through altered cell phenotype, while paying comparatively little attention to the cell environment. Recently, considerable evidence has emerged that many diseases are associated with transformations of the tissue-specific cellular microenvironments. This is a classical “chicken and egg” problem: which comes first? Do unhealthy cells remodel their microenvironment, or do diseased microenvironments drive changes in cell behavior? It is never fully possible to disentangle this complex feedback. The popular approach is to manipulate key elements inside (i.e., cytoskeletal or nuclear elements) or outside the cell (i.e., ECM stiffness, strain, or phosphorylation state) and then analyze the resulting signaling in both directions. Insights into mechanobiology will help us to better understand both normal physiology and disease states [26–28].

1.2.1 Mechanotransduction

Fig. 1.9 shows the schematic diagram of cell mechanical stimulation with substrate. Mechanical forces stimulate cells through the activation of mechanosensors, including the receptors that respond to ligand [29]. Cells are exposed to different types of forces: extracellular forces such as shear forces through fluid flow over the cell surface, tensile/traction forces through the ECM, intercellular forces through contact with neighboring cells, and intracellular cytoskeleton generated contractile forces (actomyosin contraction, microtubule polymerization and depolymerization, osmotic forces) [30]. In particular, the forces generated through cell–substrate interactions are important to initiate a cellular response to any adherent substrate. For cell–substrate interactions, integrin binding to an ECM protein, commonly fibronectin, laminin, or collagen or peptides derived from them, is a primary contributor to cell recognition. Binding of the cell to the substrate is the first stage to transmitting force across the cell membrane, and through this binding, integrins interact with the extracellular environment. Next, adaptor proteins bind to actin in the cytoskeleton, linking it to the cell membrane. Then, forces are transmitted from the actin filaments through the myosin head. Overall, integrins and adaptor proteins, such as those that form focal adhesions, initiate signaling pathways for various cell functions, such as survival, proliferation and differentiation.

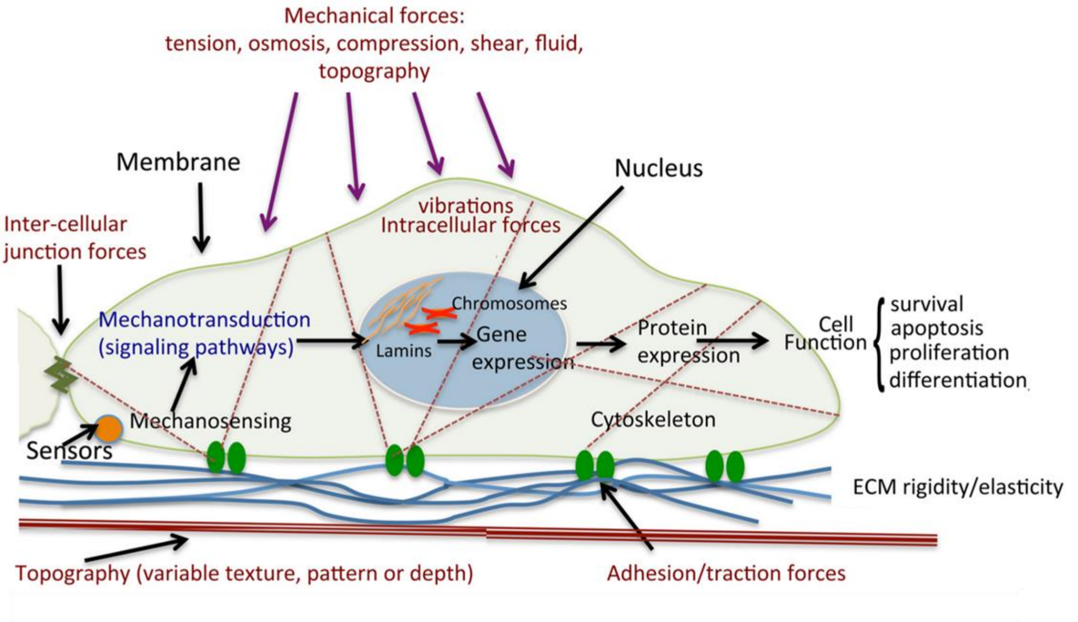

Figure 1.9 Proposed mechano-transduction mechanisms [30].

In the study of these various cellular responses, the focal adhesions, an important component of substrate-mediated mechano-transduction, formed through integrin clustering is considered as regulator of the Rho signaling pathway (**Fig. 1.10)** [29], which controls myosin II phosphorylation and affects the cytoskeleton tension in adherent cells [31–35]. Other mechanotransduction pathways involve Src family kinases (SFKs), which respond to integrin clustering to activate the Rho GTPases family, Rac, Cdc42, and Rho, and also control cytoskeleton organization by regulating actin at focal adhesions and ERK1/2, which is activated by focal adhesion kinase (FAK) to participate in actin filament formation. FAK, activated by intrgrin binding, is one of the first mechanosensitive proteins and has recently been demonstrates as a link between mechanotransduction and differentiation, where increased FAK phosphorylation correlated with increased MAP2 expression, a mature neuronal marker [36, 37].

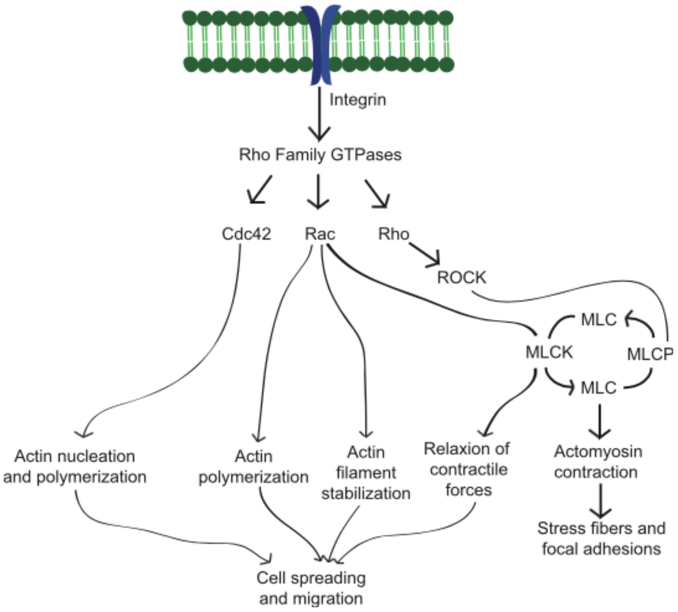

Figure 1.10 Rho family GTPase pathway. The Rho family GTPases, Cdc42, Rac, and Rho, control the cell shape, focal adhesions, and migration through signaling mechanisms to regulate actin filaments and the cytoskeleton [29].

1.2.2 Substrate stiffness

The ability of cells to sense the rigidity of the ECM affects the regulation of cellular activities in development, wound healing and even malignant transformation [31, 38, 39]. Integrins are transmembrane adhesion receptors that anchor cells to the ECM and transduce ‘outside-in’ or ‘inside-out’ biochemical signals [40]. For outside-in signaling, integrins transmit information about a cell’s adhesive state through a cascade of biochemical reactions that in turn regulates subsequent cellular responses such as motility and differentiation. In contrast, inside-out signaling involves intracellular reactions that result in changes in the integrin affinity for its extracellular ligand [41]. Interestingly, recent evidence suggests that integrins can undergo changes in affinity that depend on the stiffness of the culture substrate [42]. Because of their mechanotransductive properties, integrins have thus long been thought to be responsible for sensing (and responding to) the rigidity of the cell’s microenvironment.

Cells sense matrix rigidity through integrin binding dynamics. At low rigidities (soft substrates), the matrix deforms as the cell pulls on it, causing the rate of force loading of the integrin–fibronectin bond to be so low that the bonds detach stochastically because of their intrinsic unbinding rate (k_{off}). In this case, the unbinding of the integrin-fibronectin bond is controlled by k_{off} (schematic demonstrated in **Fig. 1.11**). On substrates with intermediate rigidities, the matrix effectively resists the cell-generated force, resulting in increased bond loading and force-enhanced dissociation. In this regime, $k_{off} > k_{on}$, and thus bonds break before new bonds are formed, which results in decreased adhesive forces. On high-rigidity substrates, the high force-loading rate exceeds the threshold value for integrin recruitment, where integrins cluster at the site of force application [43]. This reinforcement mechanism compensates for the increased unbinding, hence providing enhanced traction force. Therefore, cellular-traction forces reach a local minimum at intermediate substrate rigidities.

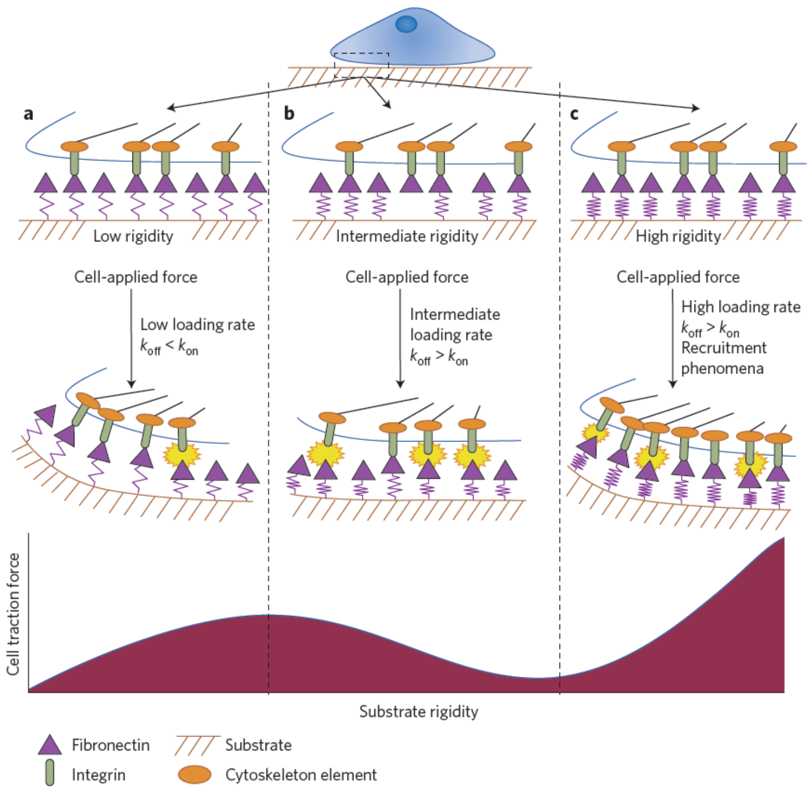

Figure 1.11 Schematic diagram of cells sensing matrix rigidity through integrin binding dynamics [43].

1.2.3 Substrate topography

The pervious researches show that mimicking in vivo microscale and nanoscale topography in implantable biomaterials is critical to guide cellular behaviors [44–46]. Recently, advances in micro- and nanofabrication methods are enabling researchers to develop sophisticated substrates with micro/nanotopography [47, 48]. Techniques such as photolithography [49], electron beam lithography [50], electrospinning [51] and 3D printing [52] have been utilized to recreate certain ECM topographical features at specific length scales or exactly replicated complex and hierarchical topography in vitro. The primary example of cells response to the substrate topography is the adhesion formation, which resides predominantly on the ridge structures [53]. The constraint of focal adhesions to the ridges of gratings could be due to the cell membrane stiffness which prevents a radical bending and hence favoring the plasma membrane to bridge the grooves rather than entering them. While larger grooves may allow enough bending of the membrane, lead to cell penetration into the grooves to form adhesions, which results in cell alignment as schematically shown in **Fig. 1.13a**. Moreover, recent studies reveal the intriguing observation that topographical cues may drive the differentiation of stem cells [54–56]. For instance, hMSCs cultured on electrospun aligned fibers show upregulation of myogenic markers Pax-3, Pax-7 and myogenin to indicate myogenic lineage commitment, whereas cells cultured on flat film composed of the same polymer do not [57].

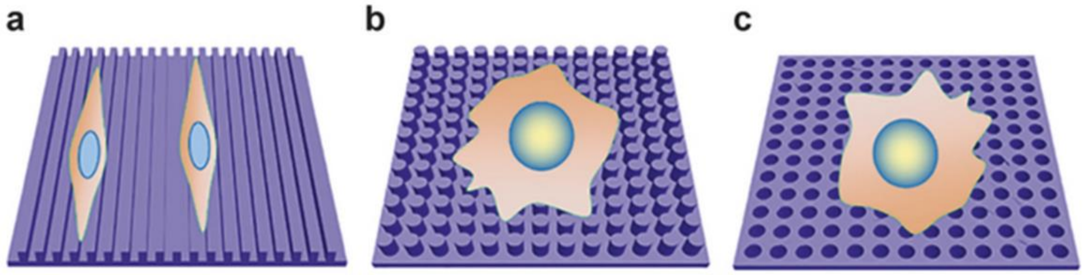

Figure 1.13 Schematic depictions of representative topography geometries. Three basic nanotopography geometries include (a) grooves, (b) post array, and (c) pit array [58].

1.2.4 2D versus 3D culture

Currently, the understanding of majority of biological processes is based largely on studies of cells cultured on two-dimensional flat substrates, i.e., glass slide or plastic petri dish. Nevertheless, cells, in vivo, primarily exist within a complex and information-rich environment, interacting with multiple ECM components and medley factors. The striking disparity between traditional monolayer culture and the in vivo scenario lead to the different cell function, such as cell adhesion, migration and mechanical forces, etc [59–63].

Cells assume two-dimensional (2D) or three-dimensional (3D) geometries largely on the basis of whether integrin-mediated adhesions to the ECM form on one face of the cell or all around the cell surface. Different cellular responses in 2D versus 3D culture could arise from these variations in the spatial distribution of adhesions [64, 65]. One of the most striking differences observed when comparing cells in 2D and 3D is the dissimilarity in morphology [66–68] (**Fig. 1.12**). Cells grown in a monolayer are flat, and can adhere and spread freely in the horizontal plane but have no support for spreading in the vertical dimension. One consequence of this is that cells cultured on 2D surfaces have a forced apical-basal polarity [69]. This polarity is arguably relevant for some cell types, such as epithelial cells, but is unnatural for most mesenchymal cells, which-when embedded in a 3D ECM-assume a stellate morphology and only polarize from front to rear during migration [70]. These changes in cell geometry and organization can directly impact cell function.

Mechanical stresses generated or experienced by cells as they adhere to the ECM and to their neighbors represent a central component of how cells transduce adhesion-mediated signaling and process [71]. Traditional 2D culture on glass or plastic substrates places cells in a static mechanical environment that is supra-physiological in terms of stiffness. Recognizing the disparity between these artificial conditions and the markedly more-compliant microenvironment of most tissues, recent work using soft 2D gels has confirmed that ECM stiffness can influence adhesions, morphogenesis, and stem cell differentiation and maintenance [72–74]. Low stiffness is not necessarily an intrinsic property of 3D environments; however, it is a feature common to most 3D systems and a factor that should be taken into consideration when differences are noticed between cell behavior in 2D and 3D.

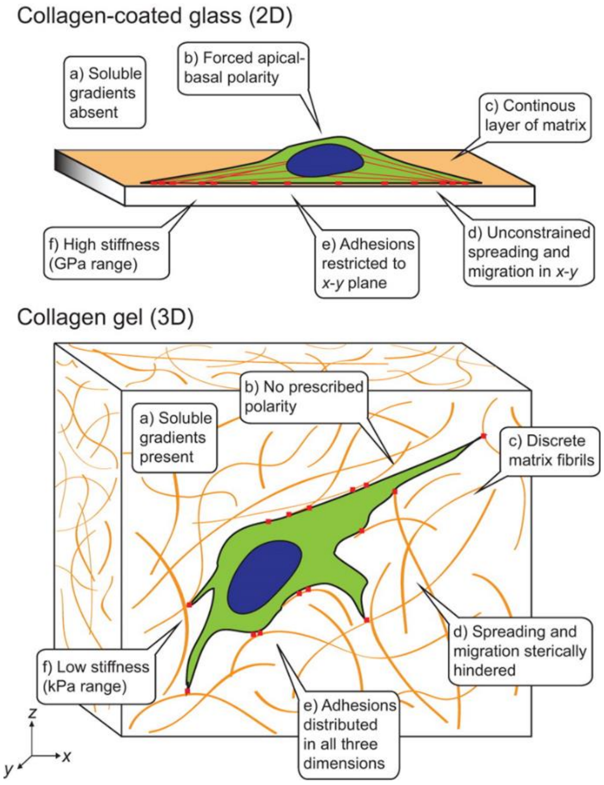

Figure 1.12 Schematic diagram of the adhesive, topographical, mechanical, and soluble cues in 2D and 3D [26].

1.3 Technology of induced pluripotent stem cells

1.3.1 The induced pluripotent stem cells

Induced pluripotent stem cells (iPSCs) are embryonic stem cells like obtained by reprogramming somatic cells. Typically, the reprogramming procedure involves ectopic expression of four transcription factors: Oct3/4, Sox2, c-Myc and Klf4, which are all crucial for the maintenance of pluripotency in embryonic stem cells [75]. The resulting iPS cells show close resemblance to the embryonic stem cells regarding to their morphology, i.e., high nucleus to cytoplasm ratio, generating flat compact colonies in culture with defined edges, their gene expression, i.e., SSEA3/4, Tra-1-60/80, Oct4, Sox2, Nanog, and their ability of differentiation into different types of somatic cells.

The iPSC reprogramming procedure was firstly introduced by Yamanaka and Takahashi in 2006, they managed to transform mouse embryonic and adult fibroblasts into a pluripotent state when introduced with viral vectors. A year after the generation of murine iPS cells, they showed that human somatic cells could be converted with the same set of factors, generating the first human iPS (hiPSCs) cells. At the same time, a different set of reprogramming factors, such as Oct4, Sox2, Nanog and Lin28, also revealed by the Thomson group. At present, the general knowledge is that Oct4 is an essential factor, while Sox2 and Klf4 can be omitted only if the genes endogenous expression is high in the somatic cells. Nanog, c-Myc and Lin28 are dispensable, but they do act to enhance conversion rate. Gurdon and Yamanaka received the Nobel Prize in medicine in 2012 for their historic contribution in iPS-technology, which inspired an astonishing flurry of follow-up studies, including successfully reprogramming of a wide variety of other cell types to pluripotency, differentiation to specific linages and also disease modeling [76–78].

Human iPS cells are strikingly similar to human embryonic stem cells (hESCs). They replicate via mitotic division whilst maintaining an undifferentiated state, and they have the potential to differentiate into all somatic cell types when provided with the necessary stimuli. Furthermore, the arrival of iPS cell technology marked the start of an exciting new dimension of stem cell research, avoiding the ethical and immunological issues that typically hamper ES cell research, which expand the potential of regenerative cell medicine [79]. iPS-technology has produced great hope for an unlimited source of patient specific stem cells for tissue regenerative applications, the possibility to study disease specific cells and developmental processes without ethical concerns compared with the use of hESCs (**Fig. 1.6**).

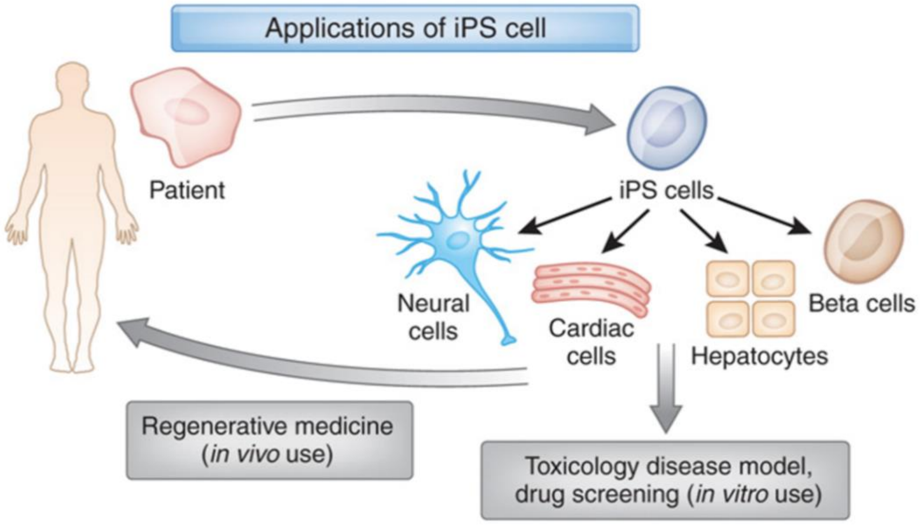

Figure 1.6 Human iPSCs derivation, differentiation and applications [80].

1.3.2 Differentiation of induced pluripotent stem cells

The iPSC technology can be applied to cell replacement therapy, disease modelling and drug discovery if they can be robustly and efficiently differentiated to relevant cell types [81, 82]. In practice the in-vitro differentiation of hiPSCs has only been developed for a small subset of cell types, such as some subtypes of neurons, hematopoietic progenitors, cardiomyocytes or keratinocytes [83, 84].

1.3.3.1 Differentiation via EB formation

Embryoid bodies (EBs), the three-dimensional aggregates of the pluripotent stem cells, are an amalgam of the three developmental germ layers [85]. The iPSCs are placed in suspension with this approach, which promotes differentiation into different cell lineages. The formation of EBs is a common approach used in the differentiation of hiPSCs, providing the ability to demonstrate tri-lineage differentiation and analysis in a more controlled, reproducible manner [86, 87]. Numerous approaches have been developed to generate EBs for a variety of purpose, from the generation of specific tissue types to illustrate potency of candidate pluripotent stem cell line [86, 88, 89]. For specific tissue lineages, EBs have been shown to be beneficial in the initiation of differentiation and to enhance the differentiation towards certain lineages [90] such as hematopoietic [88, 91], neural [92, 93], and cardiac tissues [94–97]. Methods for developing EBs differ in their ability to form aggregates of uniform size, which has also been studied as an important parameter in differentiation, and the maintenance of their long-term viability. Particularly, controlling the uniform size of EBs is crucial for the reproducible differentiation of specific cell types. Moreover, control of EB size has been demonstrated to influence viability, proliferation, and differentiation potential to cardiomyocytes [96], endothelial tissue [97], as well as instruct hematopoiesis [91]. For instance, by controlling EB size, differentiation could be specifically promoted toward endothelial lineages with smaller diameter (150 μm) EBs and toward cardiomyocyte lineages with larger diameter (450 μm) EBs, though this study was performed on mouse ES cells and it remains to be shown whether similar results would be observed using iPSCs [98].

Liquid suspension culture (LSC) [88] is a common method for creating EBs, which depends on the ability to grow cellular aggregates without attachment to the tissue culture vessel. Though these surface treatments prevent the cell attachment to the tissue culture vessel resulting in aggregation, initial seeding densities need to be optimized in order to facilitate the cell-cell interactions required to form appropriately sized EBs. However, most EB formation protocols form this LSC method contain undefined components [99, 100], such as Fetal Bovine Serum (FBS), Knock-Out Serum Replacement (KOSR) or albumin product. These animal-sourced components significantly limit the application of EB formation to generate potentially clinically relevant cell products. Meanwhile, unlike their mouse counterparts, human iPSCs usually cannot survive in suspension unless in aggregates or under ROCK inhibitor treatment. As an alternative, more controlled EB formation methods for increased reproducibility and size control to facilitate the differentiation towards specific tissue types [101, 102]. For example, a patterned agarose microwell was prepared for stem cell aggregation and EB formation with precise scalable control [103]. Previous work in our group also developed a patch method by electrospinning and crosslinking of monolayer gelatin nanofibers on a honeycomb frame made of poly (ethylene glycol) diacrylate (PEGDA), where the hiPSCs could form uniform EBs with controllable size depend on the treat time of rock inhibitor (**Fig. 1.7**). Most importantly, the subsequent differentiation could benefit from the high permeability of the device [104, 105].

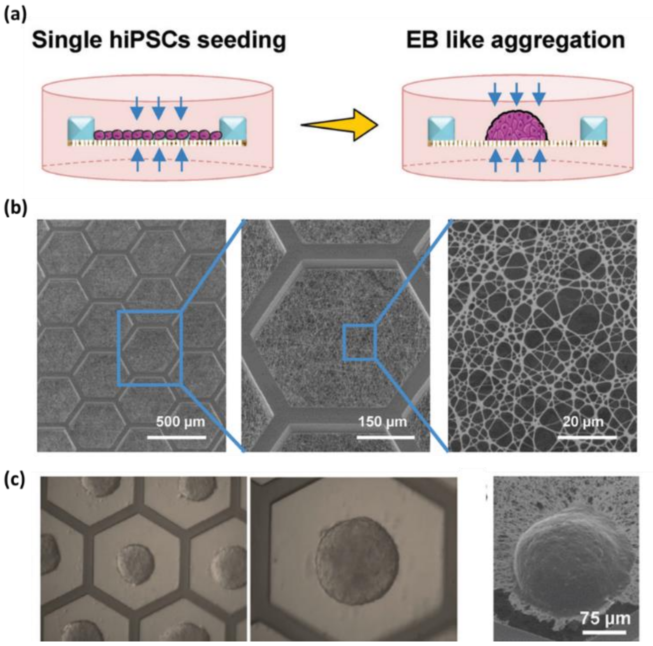

Figure 1.7 (a) Schematic of off-ground patch method. (b) Scanning electron microscope (SEM) images of the patch. (c) Phase contrast images and SEM image of generated EBs [104].

1.3.3.2 Substrate for stem cell differentiation

It is critically important for stem cell fate regulation which influenced largely by the cellular microenvironment [106–109]. Previously, a variety of iPSCs culture and differentiation protocols has been demonstrated but most of them used glass or petri dish as substrates which cannot mimic the in vivo organization of ECM and the in vivo hydrodynamic of nutrient and cellular factors. In addition, the stem cells have to be induced to the targeting cell line at high purity, high efficiency and yield. Since these targeting cells are tissue specific, they have to be differentiated on different types of substrates and under different physiological conditions. It is therefore a real challenge to develop a general culture perform for culture and differentiation of iPSCs.

So far, the research on substrate or scaffold development for iPSCs is rare which mainly focus on the effects of substrate stiffness on stem cell culture and differentiation [110–113]. It is now clear, for example, that substrate stiffness can regulate both the behavior of mature cells and the differentiation pathway of stem cells. For instance, when mesenchymal stem cells (MSCs) were grown on soft gels that mimic the elasticity of muscle, differentiation down a myogenic lineage was observed, whereas when MSCs were grown on rigid gels that mimic pre-calcified bone the cells differentiated down an osteogenic pathway [114]. Similarly, with neural stem cells, neuron differentiation is favored on soft scaffolds that mimic normal brain tissue (**Fig. 1.8**) [115, 116]. In addition, cardiomyocytes have been shown to beat best on a substrate with heart-like elasticity, whereas on harder substrates, that mechanically mimic a post-infarct fibrotic scar, cells overstrain themselves and stop beating [117]. Therefore, increasing research is now being directed at utilizing the mechanosensitive capacity of cells to develop scaffolds and biomaterials with specific mechanical properties that can be used to direct the behavior and differentiation pathway of stem cells.

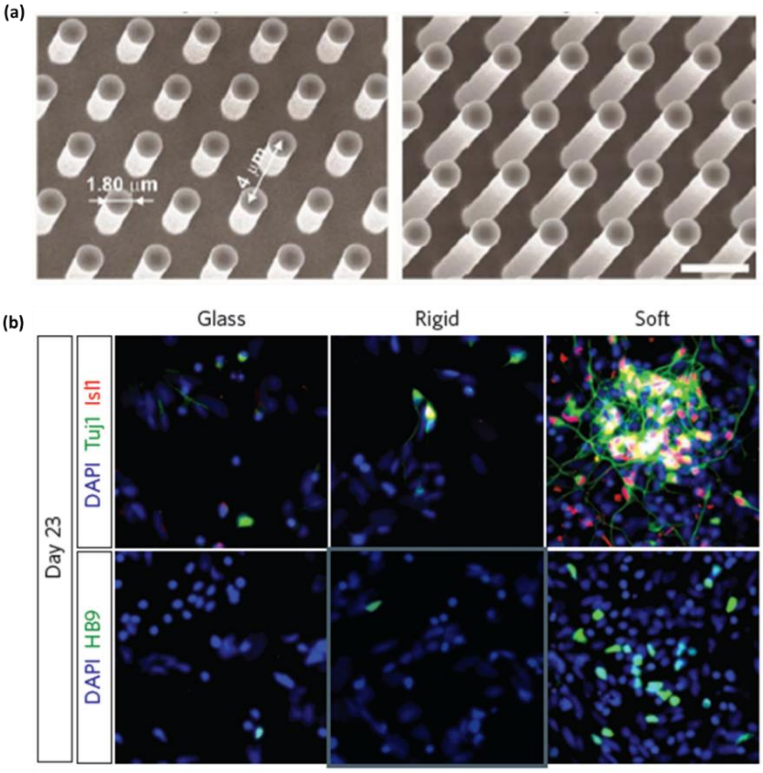

Figure 1.8 (a) SEM images showing arrays of microposts with different heights. (b) Representative immunofluorescence images showing motor neuron differentiation at Day 23 as a function of substrate rigidity [115].

1.4 Scaffold engineering

Conventional cell culture is based on the use of stiff and flat material substrates and the development of physiologically compromised cells. Lack of de-novo ECM milieu, which plays a crucial role in generating physical and chemical signals besides providing structural support, is attributed to be the major hurdle in normal cell growth in vitro [118]. Scaffold should also play an important role in regulating the morphology, development, migration and metabolic functions of the cells besides providing anchorage and mechanical scaffolding for tissue renewal [119].

So far, the most of studies on biology, especially iPSCs research, have been based on the use of conventional culture techniques, which poses a problem of quality control and the risk of genetic instability, tumorigenicity, etc. Hence, to comprehend the outcome of cell biology research in clinical context, it is important that the cell culture based models should incorporate both the in vivo microenvironment organization and multi cellular complexity of an organ, allowing experimental interventions in a desirable manner. More specifically, several requirements have been identified as crucial for the production of tissue engineering scaffolds:

a) Biocompatibility

The very first criterion of any scaffold is that it must be biocompatible, permitting cell adhere, function normally and proliferation.

b) Mechanical properties

The scaffold should have mechanical properties consistent with the anatomical site into which it is to be implanted and, from a practical perspective, it must be strong enough to allow surgical handling during implantation.

c) Surface chemistry

It should have the excellent surface chemistry to allow attachment, migration, proliferation, and differentiation of the cells [120].

d) Permeability

Scaffolds should have an interconnected pore structure and high porosity, to ensure cellular penetration and adequate diffusion of nutrients to cells within the construct and to the ECM [121].

e) Manufacturing technology

It should be cost effective and it should be possible to scale-up from making one at a time in a research laboratory to small batch production

Regarding the above criteria and requirements, a wide variety of bio-scaffolds have been fabricated by different techniques and biomaterials for the applications in tissue engineering.

1.4.1 Biomaterials

The primary criterion for scaffolds in tissue engineering is the choice of biomaterial from which the scaffold should be fabricated. Typically, three individual groups of biomaterials, ceramics, synthetic polymers and natural polymers, are used in the fabrication of scaffolds for tissue engineering.

a) Ceramic

Ceramic scaffolds, not generally used for soft tissue engineering, has been widespread used for bone regeneration applications, such as hydroxyapatite (HA) and tri-calcium phosphate (TCP) which have high mechanical stiffness, extremely low elasticity, and a hard-brittle surface [122, 123]. From a bone perspective, they exhibit excellent biocompatibility due to their chemical and structural similarity to the mineral phase of native bone. The interactions of osteogenic cells with ceramics are of great benefit for bone regeneration as ceramics are known to enhance osteoblast differentiation and proliferation. Moreover, various ceramics have been used in dental and orthopedic surgery to fill bone defects and to coat metallic implant surfaces to improve implant integration with the host bone [124]. However, due to the properties of brittleness, difficulty of shaping and uncontrollable degradation rate, they have limited clinical application for soft tissue engineering. In addition, the renewal bone formed in a porous HA network cannot sustain the mechanical loading needed for remodeling.

b) Synthetic polymers

In past decades, a variety of synthetic polymers have been developed and used to produce improved scaffolds including polystyrene, poly-l-lactic acid (PLLA), polyglycolic acid (PGA) and poly (lactic-co-glycolic acid) (PLGA), as they can be fabricated with a tailored architecture, and their degradation characteristics can be controlled by varying the polymer itself or the composition of the individual polymer [125–127]. While they also have drawbacks like the risk of rejection from host because of the reduced bioactivity. In addition, the degradation of PLLA and PGA caused by hydrolysis can produce carbon dioxide and therefore lowering the local pH, which will lead to cell and tissue necrosis [128].

c) Natural polymers

The common used approach is the use of natural polymers as scaffold biomaterials, such as collagen, chitosan, alginate, agarose and various proteoglycans, which have all been demonstrated in the production of scaffold for tissue engineering [129–131]. Unlike synthetic polymer-based scaffolds, natural polymers are biologically active, which promote the cellular attachment, proliferation and avoid risk of rejection of implantation. Nevertheless, it is challenging to fabricate scaffold from biological materials with homogeneous and reproducible structures due to the poor mechanical strength, which limits their use in, for instance, load-bearing orthopedic applications [132].

Among them, collagen, as one of the key structural proteins existed in ECM, has been demonstrated to be a suitable biomaterial for biomedical research, such as collagen nanofibrous patch for iPS cells differentiation and cardiac repairing [133]. However, the potential antigenic and immunogenic response with in vivo application restrain the usage of collagen. While gelatin, as a product obtained from thermal denaturation or disintegration of collagen, has gained great interest since the lower immunogenicity in vivo and been widely utilized in the area of tissue engineering [104]. Gelatin has also been chosen as one of the materials used in this work in Chapter 4.

1.4.2 Fabrication techniques

According to the criterions of the desired scaffold and the available materials, a variety of fabrication methods have been developed to generate scaffolds with improved function and architecture.

a) Solvent casting

The method of solvent casting for the scaffolds fabrication, which is totally based upon the evaporation of solvent, is quite simple and inexpensive [134]. One strategy is to dip the mold into polymeric solution and allow sufficient time to draw off the solution, resulting in a layer of polymeric membrane; other strategy is to add the polymeric solution into a mold and allow sufficient time to evaporate the solvent that generate the polymeric membrane or porous structure on the mold.

b) Particulate-leaching

Particulate leaching, as a common method to create the pores and channels, has been widely used to fabricate porous scaffold for the application of tissue engineering [135]. Firstly, porogen such as salt, wax or sugars is grounded into small particles which have controllable size and added into polymer solution, then the mixture is shaped into its final geometry by casting into a mold. After the evaporation of the solvent, the salt crystals are leached away using water, resulting in the formation of the pores of the scaffold [136]. With this method, the porosity or pore size can be easily regulated by control the particles size or the particles to polymer ratio.

c) Phase separation

Phase separation technique for scaffolds designing requires temperature change, leading to thermodynamically unstable polymeric solution, that separates the polymeric solution in two phases, one having low polymer concentration (polymer lean phase) and other having the high polymer concentration (polymer rich phase). Polymer is dissolved in phenol or naphthalene, followed by dispersion of biologically active molecule in these solutions. By lowering the temperature, the subsequent liquid-liquid extraction, evaporation and sublimation give porous scaffolds with bioactive molecules integrated into that structure [137]. The structures formed by such technique are often not uniformly distributed, and typically has pores with diameter on the order of a few to tens microns, which limited its application in tissue engineering.

d) Self-assembly

Self-assembly is a technique of spontaneous organization of individual components into ordered and stable structure with preprogrammed non-covalent bonds [138]. For instance, the peptide amphiphile, a chemical compound possessing both hydrophobic and hydrophilic properties, is commonly investigated for self-assembled nanofibrous matrix generation [139]. The generated 3D scaffolds can have a fiber diameter around 10 nm which is much smaller compared to fibers obtained from electrospinning technique. Additionally, this method can also produce scaffold with microscale architectures, for instance, **Fig. 1.14** shows the poly (N-vinylcaprolactam) scaffold with high porous and ordered structure obtained by self-assembly.

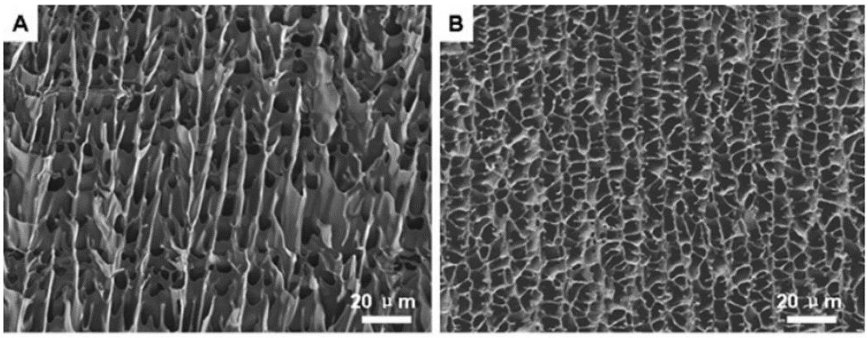

Figure 1.14 SEM images of porous poly (N-vinylcaprolactam) scaffold fabricated by self-assembly [140].

e) Electrospinning

Electrospinning is a drawing process based on the electrostatic force to obtain polymeric fibers with both solid and hollow interiors that are uniform in diameter ranging from nanoscale to microscale mainly depending on the materials solution [141]. This process is control by high intensity electric field between two electrodes having electric charges of opposite polarity. With the force generated by the electric field, the droplets of polymer solution can overcome the surface tension and then ejected, which produces the fibers.

Compared with other techniques for scaffold designing, fibrous substrates from electrospinning have several advantages. At first, the obtained 3D structures hold similarity to the ECM microenvironment. What’s more, numerous materials including natural polymers can be used to electrospinning. Lastly, the electrospining setup is simple only consisted of a syringe pump, a high voltage source as well as a collector.

f) 3D printing

Three-dimensional printing technology was emerged recently as a promising method to generate scaffold with high precision and biomimetic 3D structures. This technique can produce scaffold with size ranging from millimeter to nanometer, and also produce complex shapes with capable of homogenous cell distribution [142]. However, the availability of biomaterials is restricted since the demand of stability and properties of materials used 3d printing. In addition, the production time that it takes to form scaffold dramatically increases with more precise and intricate design. **Fig. 1.15** shows the 3D printer in our lab and the resulted Eiffel tower and porous scaffold.

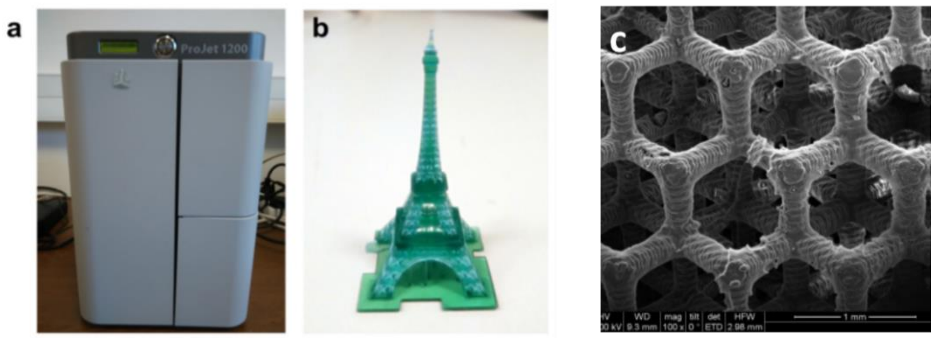

Figure 1.15 (a) 3D printer (ProJet® 1200, 3D Systems) in ENS. (b) Photo of the 3D-printed Eiffel tower. (c) SEM image of the 3D-printed PEGDA scaffold [143].

g) Freeze drying

Freeze drying technique is widely used for the fabrication of porous scaffold, which based upon the principle of sublimation [144, 145]. The solution with desired concentration is firstly frozen and then the solvent is removed by lyophilization under the high vacuum, resulting in scaffold with high porosity and inter connectivity [146], which can be controlled by the freezing rate and pH.

1.4.3 State of the art and future directions

So far, the most of the previous studies were based on 2D patterning or chemical organization of nature or synthetic polymers. A major challenge is the consistent design of 3D scaffolds that mimic the structure and biological functions of ECM [59, 65]. In order to facilitate maximal cell seeding efficiency and subsequent cell expansion, the scaffold should have high and interconnected porosity and a high surface area per volume. It should be mechanically robust and ideally incorporate signals to guide cellular migration and activity [118]. Numerous attempts have been made to obtain 3D network scaffold. Taken electrospinning as an example, a common approach for producing electrospun mats with large pores is by the selective removal of sacrificial materials (**Fig. 1.16**) [147]. For instance, scaffolds of high porosity and pore sizes in the range of 900–5000 μm^2 were fabricated by a cryogenic electrospinning process that uses ice crystals as templates, whereas scaffolds comprising large fiber-free regions were produced by combining electrospinning and salt leaching [148]. High-porosity scaffolds have also been synthesized by co-electrospinning PCL functional material and water-soluble polyethylene oxide (PEO) and, finally, removing the PEO fibers by water rinsing. Although the scaffolds of these studies show increased cell infiltration compared to those processed by conventional electrospinning, they are also characterized by mechanical instabilities, including distortion, shrinkage and delamination or pore collapse, because the increase of the pore size and porosity is detrimental to the mechanical properties [149].

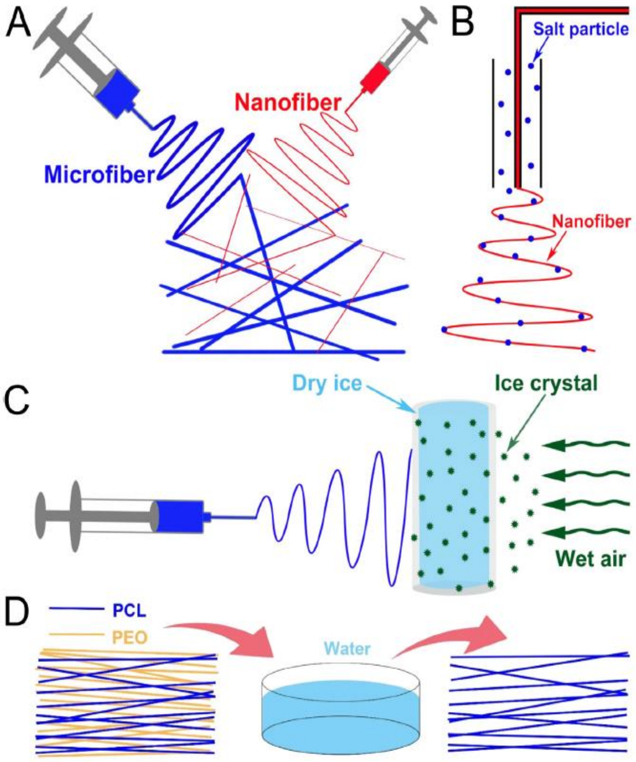

Figure 1.16 (A) Preparation of a micro- and nano-fiber hybrid scaffold by two-jet electrospinning [150]. (B) Introduction of salt particles into electrospun mesh in the surrounding sheath [151]. (C) Schematic setup for cryogenic electrospinning. A cylindrical aluminum drum containing dry ice is exposed in saturated atmosphere to simultaneously create ice crystals and collect the electrospun nanofibers [148]. (D) PEO nanofibers are used as a sacrificial component and leached out in a water bath to obtain electrospun PCL nanofibrous scaffolds with improved porosity [149].

Another challenge in scaffold assisted tissue engineering is the lack of engineered tissue constructs. For example, the lack of vascularity formed in engineered scaffolds, one strategy to improve vascularization might to be engineer microvasculature by cells in the scaffolds prior to implantation [152, 153], which is a complex method, involved with initially harvesting cells from a donor and then engineering a nascent microvasculature. From a clinical perspective, the efficiency of this in vitro tissue engineering strategy has been questioned since the need for at least two procedures and the delay in treatment. From a commercial perspective, this strategy is also difficult to achieve as the prolonged regulatory process required before such a tissue engineered construct can be approved for clinical use. While in tissues like cartilage that is not able to regenerate and repair themselves when damages, the in vitro tissue engineering may be the only way to prevent the requirement of an eventual joint arthroplasty [154].

In addition, providing a dynamic heterogeneous constellation of microstructural, compositional and mechanical cues within scaffold is critical for recapitulating the cellular microenvironment and better understanding the interaction of the cell and the cellular microenvironment. In particular, re-performing of mechanosensitive capacity of cells in vitro holds immerse potential in tissue engineering. Key roles in machanotransduction signaling pathways are played by cell adhesion complexes and the cellular cytoskeleton, whose contractile forces are affected by the stiffness of substrates, therefore the mechanical properties of substrate or scaffold underlying cells are crucial to regulate cellular machanotransduction and subsequent cellular behavior. Plenty of works reported, for example, that the behavior of mature cells and the differentiation pathway of stem cells can be regulated by the substrate stiffness. For instance, differentiation down to a myogenic lineage from MSCs was observed when cultured on gels with mimetic elasticity of muscle, while the cells differentiation down an osteogenic pathway when drown on rigid gels [114]. Similarly, neuron differentiation is favored on soft substrate (less than 1KPa), whereas the differentiation of glial cells, neuron supporting cells, is promoted on rigid matrices [115, 116]. Therefore, utilizing the mechanosensitive capacity of cells to develop scaffolds is of great importance to direct the behavior of cells.

Regarding prospective in tissue engineering, the use of scaffolds as delivery systems for growth factors, adhesion peptides and cytokines is receiving considerable attention in the field. With this purpose, the incorporation of drugs into scaffolds has been proposed as an approach to avoid or reduce the risk of infection after surgery [155, 156]. Meanwhile, the strategy of using scaffolds as delivery systems for gene therapy is undergoing, which utilize DNA encoding for therapeutic genes potentially provide a more stable and effective approach to allow sustained and controlled release of therapeutic factors [157]. Gene therapy can thus be a valuable tool to avoid the limitations of the local delivery of growth factors, including the short half-life, large dose requirement, high cost, need for repeated applications, and poor distribution [158].

1.5 Research objectives of this work

The fundamental knowledge of cell-substrate interactions is of great importance for tissue engineering. In particular, the control of cell-substrate interaction in regulating cell behavior such as cell migration, proliferation and differentiation reserves a huge potential for regenerative medicine and pharmaceutical industries. In such a context, the ultimate purpose of this work is to develop cell devices and methods for advanced biological and biomedical studies. More specifically, we were interested in cell-substrate interaction which rely critically on the progress of the microdevice engineering.

As we know, the cells are sensitive to the stiffness of the underlying substrates, and display different morphology and phenotype. Meantime, cell migration can be also regulated by the rigidity of the substrate. To better understand mechanically driven cell migration, we wish to developed a novel method to fabricate dense elastomer pillar arrays with height gradient and thus creating a stiffness gradient. Unlike the conventional substrates with stiffness gradient which created mainly with hydrogel, the micropillar arrays in polydimethylsiloxane (PDMS) were chosen as the substrate in this work because the stiffness can be controlled easily just by changing the parameter of the design and also due to the permeability contributed by the space between pillars. We also wish to investigate the effect of complex stiffness gradient strength on motility of cells, as well as the resulted cell morphology and self-patterning.

For cell culture scaffold, although great effort has been devoted to developing fibrous scaffold by using electrospinning, most of them obtained tightly packed layers of nanofibers with only a superficially porous network, which restricted cell performance, particularly cell migration. Therefore, we wish to generate a real 3D scaffold permitted cell infiltration, resulting in a 3D cell sheet. The migration behavior in z direction can be also studied within this scaffold. In addition, regarding the poor mechanical property of normal fiber scaffold, we also would like to improve that and make the scaffold mechanically robust for easy handling.

The capability of hiPSCs to self-renew and guided differentiation to multiple lineages makes them a promising strategy for cell-based therapies such as tissue engineering, disease modelling and drug screening. However, the possibility of tumorigenesis or teratoma formation within the body restrict the use of use of hiPSCs. Therefore, guided differentiating hiPSCs to specific lineage before transplantation is supposed to the solution of minimizing the risk of uncontrolled self-renewal or differentiation in vivo. Normally, the existed differentiation protocols require the formation of embryoid bodies (EBs). Nevertheless, methodologies of generating EBs need multiple steps, normally from detach cells to form cell aggregates by low attach treatment or suspension, and finally seeded onto scaffolds to induce differentiation, which need complex processes and have low repeatability. In this work, we would like to use micropillar arrays with controlled stiffness as substrates to induce hiPSCs differentiation and investigate the effect of substrate stiffness on the dimensionality and morphology of the EBs. In order to formate hiPSCs EBs with uniform and controlled size, we wish to use a PDMS stencil as a regular of cell aggregation. Moreover, the effect of substrate stiffness on the dimensionality and morphology of the EBs is of great interest to study. Finally, the induced cardiomyocytes differentiation from hiPSCs EBs was investigated, showing a clear stiffness dependence of the substrates.

References

[1] T.A. Desai, Y. Xia, G. Whitesides, D. Branch, A. Prokop, D. Hunkeler, R. Green, K. Shahrokhi, A. Powers, F. Ligler, Micro- and nanoscale structures for tissue engineering constructs., Med. Eng. Phys. 22 (2000).

[2] A. Khademhosseini, R. Langer, J. Borenstein, J.P. Vacanti, Microscale technologies for tissue engineering and biology., Proc. Natl. Acad. Sci. U. S. A. 103 (2006) 2480–7.

[3] https://online.science.psu.edu/biol011_sandbox_7239/node/7312.

[4] http://www.etymonline.com/index.php term=cell.

[5] https://opentextbc.ca/anatomyandphysiology/chapter/1-2-structural-organization-of-the-human-body-2/.

[6] http://sscell.weebly.com/cell-structures-and-functions.html.

[7] P. Liang, T.H. MacRae, Molecular chaperones and the cytoskeleton, J. Cell Sci. 110 (1997).

[8] D.A. Fletcher, R.D. Mullins, Cell mechanics and the cytoskeleton, Nature. 463 (2010) 485–492.

[9] D. Stanley, A Review of the Muscle Cell Cytoskeleton and Its Possible Relation to Meat Texture and Sarcolemma Emptying, Food Struct. 2 (1983).

[10] http://tundra.cnx.rice.edu:8888/contents/609c7858-a692-4fb1-9c49-69462e3c739f@1/07-5-the-cytoskeleton-ms.

[11] http://cellix.imba.oeaw.ac.at/cytoskeleton/actin.

[12] http://wiki.pingry.org/u/ap-biology/index.php/Extracellular_matrix.

[13] G.E. Davis, K.J. Bayless, M.J. Davis, G.A. Meininger, S. Fowler, M. Klagsbrun, R. Langer, D. Cheresh, M. Sy, A. Schor, G. Yancopoulos, Regulation of tissue injury responses by the exposure of matricryptic sites within extracellular matrix molecules., Am. J. Pathol. 156 (2000) 1489–98.

[14] C.S. Barros, S.J. Franco, U. Muller, Extracellular Matrix: Functions in the Nervous System, Cold Spring Harb. Perspect. Biol. 3 (2011) a005108–a005108.

[15] A. Teti, Regulation of cellular functions by extracellular matrix., J. Am. Soc. Nephrol. 2 (1992) S83-7.

[16] S. BADYLAK, D. FREYTES, T. GILBERT, Extracellular matrix as a biological scaffold material: Structure and function, Acta Biomater. 5 (2009) 1–13.

[17] C. Frantz, K.M. Stewart, V.M. Weaver, The extracellular matrix at a glance, J. Cell Sci. 123 (2010).

[18] https://www.boundless.com/biology/textbooks/boundless-biology-textbook/cell-structure-4/connections-between-cells-and-cellular-activities-63/extracellular-matrix-of-animal-cells-324-11461/.

[19] F.M. Watt, H. Fujiwara, Cell-extracellular matrix interactions in normal and diseased skin., Cold Spring Harb. Perspect. Biol. 3 (2011).

[20] S.S. Chen, W. Fitzgerald, J. Zimmerberg, H.K. Kleinman, L. Margolis, Cell-Cell and Cell-Extracellular Matrix Interactions Regulate Embryonic Stem Cell Differentiation, Stem Cells. 25 (2007) 553–561.

[21] F. Rosso, A. Giordano, M. Barbarisi, A. Barbarisi, From Cell-ECM interactions to tissue engineering, J. Cell. Physiol. 199 (2004) 174–180.

[22] https://prezi.com/zyhfo4lljre-/cell-junctions/.

[23] http://www.mhhe.com/biosci/genbio/raven6b/graphics/raven06b/other/raven06b_07.pdf.

[24] https://www.boundless.com/physiology/textbooks/boundless-anatomy-and-physiology-textbook/organization-at-the-cellular-level-3/external-cellular-components-47/intercellular-junctions-351-11462/.

[25] C.S. Chen, M. Mrksich, S. Huang, G.M. Whitesides, D.E. Ingber, Geometric Control of Cell Life and Death, Science (80). 276 (1997).

[26] B.M. Baker, C.S. Chen, Deconstructing the third dimension – how 3D culture microenvironments alter cellular cues, J. Cell Sci. 125 (2012) 3015–24.

[27] P.M. Gilbert, K.L. Havenstrite, K.E.G. Magnusson, A. Sacco, N.A. Leonardi, P. Kraft, N.K. Nguyen, S. Thrun, M.P. Lutolf, H.M. Blau, Substrate Elasticity Regulates Skeletal Muscle Stem Cell Self-Renewal in Culture, Science (80-.). 329 (2010).

[28] F. Brandl, F. Sommer, A. Goepferich, Rational design of hydrogels for tissue engineering: Impact of physical factors on cell behavior, Biomaterials. 28 (2007) 134–146.

[29] J.M. Stukel, R.K. Willits, Mechanotransduction of Neural Cells Through Cell?Substrate Interactions, Tissue Eng. Part B Rev. 22 (2016) 173–182.

[30] P. Tsimbouri, P. M., Adult Stem Cell Responses to Nanostimuli, J. Funct. Biomater. 6 (2015) 598–622.

[31] M.A. Schwartz, Integrins and extracellular matrix in mechanotransduction., Cold Spring Harb. Perspect. Biol. 2 (2010) a005066.

[32] G.F. Weber, M.A. Bjerke, D.W. DeSimone, Integrins and cadherins join forces to form adhesive networks., J. Cell Sci. 124 (2011) 1183–93.

[33] Z. Sun, S.S. Guo, R. Fässler, Integrin-mediated mechanotransduction, J. Cell Biol. (2016).

[34] Q. Wei, T.L.M. Pohl, A. Seckinger, J.P. Spatz, E.A. Cavalcanti-Adam, Regulation of integrin and growth factor signaling in biomaterials for osteodifferentiation, Beilstein J. Org. Chem. 11 (2015) 773–783.

[35] M.W. Renshaw, D. Toksoz, M.A. Schwartz, Involvement of the small GTPase rho in integrin-mediated activation of mitogen-activated protein kinase., J. Biol. Chem. 271 (1996) 21691–4.

[36] J.D. Humphrey, E.R. Dufresne, M.A. Schwartz, Mechanotransduction and extracellular matrix homeostasis, Nat. Rev. Mol. Cell Biol. 15 (2014) 802–812.

[37] S. Huveneers, E.H.J. Danen, Adhesion signaling - crosstalk between integrins, Src and Rho, J. Cell Sci. 122 (2009) 1059–1069.

[38] D. Choquet, D.P. Felsenfeld, M.P. Sheetz, Extracellular Matrix Rigidity Causes Strengthening of Integrin?Cytoskeleton Linkages, Cell. 88 (1997) 39–48.

[39] B. Geiger, A. Bershadsky, R. Pankov, K.M. Yamada, Transmembrane crosstalk between the extracellular matrix and the cytoskeleton, Nat. Rev. Mol. Cell Biol. 2 (2001) 793–805.

[40] R.O. Hynes, Integrins: bidirectional, allosteric signaling machines., Cell. 110 (2002) 673–87.

[41] Y. Lad, D.S. Harburger, D.A. Calderwood, Integrin Cytoskeletal Interactions, in: Methods Enzymol., 2007: pp. 69–84.

[42] J. Du, X. Chen, X. Liang, G. Zhang, J. Xu, L. He, Q. Zhan, X.-Q. Feng, S. Chien, C. Yang, Integrin activation and internalization on soft ECM as a mechanism of

induction of stem cell differentiation by ECM elasticity., Proc. Natl. Acad. Sci. U. S. A. 108 (2011) 9466–71.

[43] J.R. Garc?a, A.J. Garc?a, Cellular mechanotransduction: Sensing rigidity, Nat. Mater. 13 (2014) 539–540.

[44] C.J. Bettinger, R. Langer, J.T. Borenstein, Engineering Substrate Topography at the Micro- and Nanoscale to Control Cell Function, Angew. Chemie Int. Ed. 48 (2009) 5406–5415.

[45] A. Curtis, C. Wilkinson, Topographical control of cells, Biomaterials. 18 (1997) 1573–1583.

[46] A.M. Ross, Z. Jiang, M. Bastmeyer, J. Lahann, Physical Aspects of Cell Culture Substrates: Topography, Roughness, and Elasticity, Small. 8 (2012) 336–355.

[47] M. Nikkhah, F. Edalat, S. Manoucheri, A. Khademhosseini, Engineering microscale topographies to control the cell?substrate interface, Biomaterials. 33 (2012) 5230–5246.

[48] J.J. Norman, T.A. Desai, Methods for Fabrication of Nanoscale Topography for Tissue Engineering Scaffolds, Ann. Biomed. Eng. 34 (2006) 89–101.

[49] M. HAHN, L. TAITE, J. MOON, M. ROWLAND, K. RUFFINO, J. WEST, Photolithographic patterning of polyethylene glycol hydrogels, Biomaterials. 27 (2006) 2519–2524.

[50] N.Q. Balaban, U.S. Schwarz, D. Riveline, P. Goichberg, G. Tzur, I. Sabanay, D. Mahalu, S. Safran, A. Bershadsky, L. Addadi, B. Geiger, Force and focal adhesion assembly: a close relationship studied using elastic micropatterned substrates, Nat. Cell Biol. 3 (2001) 466–472.

[51] A.S. Badami, M.R. Kreke, M.S. Thompson, J.S. Riffle, A.S. Goldstein, Effect of fiber diameter on spreading, proliferation, and differentiation of osteoblastic cells on electrospun poly(lactic acid) substrates, Biomaterials. 27 (2006) 596–606.

[52] C.X.. Lam, X.. Mo, S.. Teoh, D.. Hutmacher, Scaffold development using 3D printing with a starch-based polymer, Mater. Sci. Eng. C. 20 (2002) 49–56.

[53] K. Kulangara, K.W. Leong, X.S. Jiang, K.W. Leong, H.Q. Mao, H.Q. Mao, H.Q. Mao, N. Winograd, H.J. Donahue, Substrate topography shapes cell function, Soft Matter. 5 (2009) 4072.

[54] G. Abagnale, M. Steger, V.H. Nguyen, N. Hersch, A. Sechi, S. Joussen, B. Denecke, R. Merkel, B. Hoffmann, A. Dreser, U. Schnakenberg, A. Gillner, W. Wagner, Surface topography enhances differentiation of mesenchymal stem cells towards osteogenic and adipogenic lineages, Biomaterials. 61 (2015) 316–326.

[55] K. Metavarayuth, P. Sitasuwan, X. Zhao, Y. Lin, Q. Wang, Influence of Surface Topographical Cues on the Differentiation of Mesenchymal Stem Cells in Vitro, ACS Biomater. Sci. Eng. 2 (2016) 142–151.

[56] L. Qi, N. Li, R. Huang, Q. Song, L. Wang, Q. Zhang, R. Su, T. Kong, M. Tang, G. Cheng, The Effects of Topographical Patterns and Sizes on Neural Stem Cell Behavior, PLoS One. 8 (2013) e59022.

[57] J.M. Dang, K.W. Leong, Myogenic Induction of Aligned Mesenchymal Stem Cell Sheets by Culture on Thermally Responsive Electrospun Nanofibers., Adv. Mater. 19 (2007) 2775–2779.

[58] T. Gong, J. Xie, J. Liao, T. Zhang, S. Lin, Y. Lin, Nanomaterials and bone regeneration, Bone Res. 3 (2015) 15029.

[59] A.I. Khoruzhenko, 2D- and 3D-cell culture, Biopolym. Cell. 27 (2011) 17–24.

[60] M. Pickl, C.H. Ries, Comparison of 3D and 2D tumor models reveals enhanced HER2 activation in 3D associated with an increased response to trastuzumab, Oncogene. 28 (2009) 461–468.

[61] J. Lee, G.D. Lilly, R.C. Doty, P. Podsiadlo, N.A. Kotov, In vitro Toxicity Testing of Nanoparticles in 3D Cell Culture, Small. 5 (2009) NA-NA.

[62] B.A. Justice, N.A. Badr, R.A. Felder, 3D cell culture opens new dimensions in cell-based assays, Drug Discov. Today. 14 (2009) 102–107.

[63] M. Ghibaudo, L. Trichet, J. Le Digabel, A. Richert, P. Hersen, B. Ladoux, Substrate Topography Induces a Crossover from 2D to 3D Behavior in Fibroblast Migration, Biophys. J. 97 (2009) 357–368.

[64] T. Sun, D. Norton, R.J. McKean, J.W. Haycock, A.J. Ryan, S. MacNeil, Development of a 3D cell culture system for investigating cell interactions with electrospun fibers, Biotechnol. Bioeng. 97 (2007) 1318–1328.

[65] S. Zhang, F. Gelain, X. Zhao, Designer self-assembling peptide nanofiber scaffolds for 3D tissue cell cultures, Semin. Cancer Biol. 15 (2005) 413–420.

[66] P. Tayalia, C.R. Mendonca, T. Baldacchini, D.J. Mooney, E. Mazur, 3D Cell-Migration Studies using Two-Photon Engineered Polymer Scaffolds, Adv. Mater. 20 (2008) 4494–4498.

[67] H. Baharvand, S.M. Hashemi, S. Kazemi Ashtiani, A. Farrokhi, Differentiation of human embryonic stem cells into hepatocytes in 2D and 3D culture systems in vitro., Int. J. Dev. Biol. 50 (2006) 645–52.

[68] M.W. Tibbitt, K.S. Anseth, Hydrogels as extracellular matrix mimics for 3D cell culture, Biotechnol. Bioeng. 103 (2009) 655–663.

[69] M. Akhmanova, E. Osidak, S. Domogatsky, S. Rodin, A. Domogatskaya, Physical, Spatial, and Molecular Aspects of Extracellular Matrix of In Vivo Niches and Artificial Scaffolds Relevant to Stem Cells Research., Stem Cells Int. 2015 (2015) 167025.

[70] T. Mseka, J.R. Bamburg, L.P. Cramer, ADF/cofilin family proteins control formation of oriented actin-filament bundles in the cell body to trigger fibroblast polarization, J. Cell Sci. 120 (2007).

[71] A.W. Orr, B.P. Helmke, B.R. Blackman, M.A. Schwartz, Mechanisms of Mechanotransduction, Dev. Cell. 10 (2006) 11–20.

[72] M.J. Paszek, N. Zahir, K.R. Johnson, J.N. Lakins, G.I. Rozenberg, A. Gefen, C.A. Reinhart-King, S.S. Margulies, M. Dembo, D. Boettiger, D.A. Hammer, V.M. Weaver, Tensional homeostasis and the malignant phenotype, Cancer Cell. 8 (2005) 241–254

[73] A.L. Lark, C.A. Livasy, L. Dressler, D.T. Moore, R.C. Millikan, J. Geradts, M. Iacocca, D. Cowan, D. Little, R.J. Craven, W. Cance, High focal adhesion kinase expression in invasive breast carcinomas is associated with an aggressive phenotype, Mod. Pathol. 18 (2005) 1289–1294.

[74] P. Gilbert, K. McEwan, C. Irons, R. Bhundia, R. Christie, C. Broomhead, H. Rockliff, Self-harm in a mixed clinical population: The roles of self-criticism, shame, and social rank, Br. J. Clin. Psychol. 49 (2010) 563–576.

[75] K. Takahashi, S. Yamanaka, Induction of pluripotent stem cells from mouse embryonic and adult fibroblast cultures by defined factors., Cell. 126 (2006) 663–76.

[76] X.-L. Guo, J.-S. Chen, Research on induced pluripotent stem cells and the application in ocular tissues., Int. J. Ophthalmol. 8 (2015) 818–25.

[77] J. Yu, M.A. Vodyanik, K. Smuga-Otto, J. Antosiewicz-Bourget, J.L. Frane, S. Tian, J. Nie, G.A. Jonsdottir, V. Ruotti, R. Stewart, I.I. Slukvin, J.A. Thomson, Induced Pluripotent Stem Cell Lines Derived from Human Somatic Cells, Science (80-.). 318 (2007) 1917–1920.

[78] M.H. Chin, M.J. Mason, W. Xie, S. Volinia, M. Singer, C. Peterson, G. Ambartsumyan, O. Aimiuwu, L. Richter, J. Zhang, I. Khvorostov, V. Ott, M. Grunstein, N. Lavon, N. Benvenisty, C.M. Croce, A.T. Clark, T. Baxter, A.D. Pyle, M.A. Teitell, M. Pelegrini, K. Plath, W.E. Lowry, Induced Pluripotent Stem Cells and Embryonic Stem Cells Are Distinguished by Gene Expression Signatures, Cell Stem Cell. 5 (2009) 111–123.

[79] K. Takahashi, K. Tanabe, M. Ohnuki, M. Narita, T. Ichisaka, K. Tomoda, S. Yamanaka, Induction of Pluripotent Stem Cells from Adult Human Fibroblasts by Defined Factors, Cell. 131 (2007) 861–872.

[80] http://www.nuwacell.com/main/service/2/2.

[81] https://www.rndsystems.com/cn/resources/articles/differentiation-potential-induced-pluripotent-stem-cells.

[82] S.M. Chambers, C.A. Fasano, E.P. Papapetrou, M. Tomishima, M. Sadelain, L. Studer, Highly efficient neural conversion of human ES and iPS cells by dual inhibition of SMAD signaling, Nat. Biotechnol. 27 (2009) 275–280.

[83] B.-Y. Hu, J.P. Weick, J. Yu, L.-X. Ma, X.-Q. Zhang, J.A. Thomson, S.-C. Zhang, Neural differentiation of human induced pluripotent stem cells follows developmental principles but with variable potency., Proc. Natl. Acad. Sci. U. S. A. 107 (2010) 4335–40.

[84] E.P. Papapetrou, M.J. Tomishima, S.M. Chambers, Y. Mica, E. Reed, J. Menon, V. Tabar, Q. Mo, L. Studer, M. Sadelain, Stoichiometric and temporal requirements of Oct4, Sox2, Klf4, and c-Myc expression for efficient human iPSC induction and differentiation., Proc. Natl. Acad. Sci. U. S. A. 106 (2009) 12759–64.

[85] R. Jaenisch, R. Young, Stem Cells, the Molecular Circuitry of Pluripotency and Nuclear Reprogramming, Cell. 132 (2008) 567–582.

[86] S. Rungarunlert, M. Techakumphu, M.K. Pirity, A. Dinnyes, Embryoid body formation from embryonic and induced pluripotent stem cells: Benefits of bioreactors., World J. Stem Cells. 1 (2009) 11–21.

[87] M. Koike, H. Kurosawa, Y. Amano, A Round-bottom 96-well Polystyrene Plate Coated with 2-methacryloyloxyethyl Phosphorylcholine as an Effective Tool for Embryoid Body Formation, Cytotechnology. 47 (2005) 3–10.

[88] S.M. Dang, M. Kyba, R. Perlingeiro, G.Q. Daley, P.W. Zandstra, Efficiency of embryoid body formation and hematopoietic development from embryonic stem cells in different culture systems, Biotechnol. Bioeng. 78 (2002) 442–453.

[89] J. Itskovitz-Eldor, M. Schuldiner, D. Karsenti, A. Eden, O. Yanuka, M. Amit, H. Soreq, N. Benvenisty, Differentiation of human embryonic stem cells into embryoid bodies compromising the three embryonic germ layers., Mol. Med. 6 (2000) 88–95.

[90] G.M. Keller, In vitro differentiation of embryonic stem cells, Curr. Opin. Cell Biol. 7 (1995) 862–869.

[91] E.S. Ng, R.P. Davis, L. Azzola, E.G. Stanley, A.G. Elefanty, Forced aggregation of defined numbers of human embryonic stem cells into embryoid bodies fosters robust, reproducible hematopoietic differentiation, Blood. 106 (2005).

[92] P.G. Wilson, S.S. Stice, A. Trounson, A. Ellisdon, S. Bottomley, Y. Verlinsky, D. Cram, Development and differentiation of neural rosettes derived from human embryonic stem cells, Stem Cell Rev. 2 (2006) 67–77.

[93] M. Kumar, B. Bagchi, S.K. Gupta, A.S. Meena, P. Gressens, S. Mani, Neurospheres Derived from Human Embryoid Bodies Treated with Retinoic Acid Show an Increase in Nestin and Ngn2 Expression That Correlates with the Proportion of Tyrosine Hydroxylase-Positive Cells, Stem Cells Dev. 16 (2007) 667–682.

[94] J.C. Mohr, J. Zhang, S.M. Azarin, A.G. Soerens, J.J. de Pablo, J.A. Thomson, G.E. Lyons, S.P. Palecek, T.J. Kamp, The microwell control of embryoid body size in order to regulate cardiac differentiation of human embryonic stem cells., Biomaterials. 31 (2010) 1885–93.

[95] S.D. Sheridan, V. Surampudi, R.R. Rao, Analysis of Embryoid Bodies Derived from Human Induced Pluripotent Stem Cells as a Means to Assess Pluripotency, Stem Cells Int. 2012 (2012) 1–9.

[96] S. Takei, H. Ichikawa, K. Johkura, A. Mogi, H. No, S. Yoshie, D. Tomotsune, K. Sasaki, Bone morphogenetic protein-4 promotes induction of cardiomyocytes from human embryonic stem cells in serum-based embryoid body development, AJP Hear. Circ. Physiol. 296 (2009) H1793–H1803.

[97] P.W. Burridge, D. Anderson, H. Priddle, M.D. Barbadillo Muñoz, S. Chamberlain, C. Allegrucci, L.E. Young, C. Denning, Improved Human Embryonic Stem Cell Embryoid Body Homogeneity and Cardiomyocyte Differentiation from a Novel V-96 Plate Aggregation System Highlights Interline Variability, Stem Cells. 25 (2007) 929–938.

[98] L. Schukur, P. Zorlutuna, J.M. Cha, H. Bae, A. Khademhosseini, Directed differentiation of size-controlled embryoid bodies towards endothelial and cardiac lineages in RGD-modified poly (ethylene glycol) hydrogels., Adv. Healthc. Mater. 2 (2013) 195–205.

[99] Y. Lin, G. Chen, Embryoid body formation from human pluripotent stem cells in chemically defined E8 media, Harvard Stem Cell Institute, 2008.

[100] K.A. Purpura, Controlling the Emergence of Hematopoietic Progenitor Cells from Pluripotent Stem Cells, (2012).

[101] M. Maldonado, G. Ico, K. Low, R.J. Luu, J. Nam, Enhanced Lineage-Specific Differentiation Efficiency of Human Induced Pluripotent Stem Cells by Engineering Colony Dimensionality Using Electrospun Scaffolds, Adv. Healthc. Mater. 5 (2016) 1408–1412.

[102] M. Maldonado, L.Y. Wong, C. Echeverria, G. Ico, K. Low, T. Fujimoto, J.K. Johnson, J. Nam, The effects of electrospun substrate-mediated cell colony morphology on the self-renewal of human induced pluripotent stem cells, Biomaterials. 50 (2015) 10–19.

[103] J. Dahlmann, G. Kensah, H. Kempf, D. Skvorc, A. Gawol, D.A. Elliott, G. Dräger, R. Zweigerdt, U. Martin, I. Gruh, The use of agarose microwells for scalable embryoid body formation and cardiac differentiation of human and murine pluripotent stem cells, Biomaterials. 34 (2013) 2463–2471.

[104] Y. Tang, L. Liu, J. Li, L. Yu, L. Wang, J. Shi, Y. Chen, J. Nam, A. Baessler, M. Fischer, R. Passier, L. Tertoolen, I. Gruh, A. Haverich, U. Martin, R. Zweigerdt, Induction and differentiation of human induced pluripotent stem cells into functional cardiomyocytes on a compartmented monolayer of gelatin nanofibers, Nanoscale. 8 (2016) 14530–14540.

[105] Y. Tang, L. Liu, J. Li, L. Yu, F.P.U. Severino, L. Wang, J. Shi, X. Tu, V. Torre, Y. Chen, Y. Chen, C. Zhang, B.J. Wainger, M. Peitz, D.M. Kovacs, C.J. Woolf, S.L. Wagner, R.E. Tanzi, D.Y. Kim, Effective motor neuron differentiation of hiPSCs on a patch made of crosslinked monolayer gelatin nanofibers, J. Mater. Chem. B. 4 (2016) 3305–3312.

[106] F. Guilak, D.M. Cohen, B.T. Estes, J.M. Gimble, W. Liedtke, C.S. Chen, Control of Stem Cell Fate by Physical Interactions with the Extracellular Matrix, Cell Stem Cell. 5 (2009) 17–26.

[107] Chen, Mechanical control of stem cell differentiation, StemBook. (2008).

[108] A.W. Lund, B. Yener, J.P. Stegemann, G.E. Plopper, The Natural and Engineered 3D Microenvironment as a Regulatory Cue During Stem Cell Fate Determination, Tissue Eng. Part B Rev. 15 (2009) 371–380.

[109] C.J. Flaim, D. Teng, S. Chien, S.N. Bhatia, Combinatorial Signaling Microenvironments for Studying Stem Cell Fate, Stem Cells Dev. 17 (2008) 29–40.

[110] A.J. Engler, S. Sen, H.L. Sweeney, D.E. Discher, Matrix Elasticity Directs Stem Cell Lineage Specification, Cell. 126 (2006) 677–689.

[111] D.E. Discher, P. Janmey, Y.-L. Wang, Tissue Cells Feel and Respond to the Stiffness of Their Substrate, Science (80-.). 310 (2005) 1139–43.

[112] N.D. Leipzig, M.S. Shoichet, The effect of substrate stiffness on adult neural stem cell behavior, Biomaterials. 30 (2009) 6867–6878.

[113] J.R. Tse, A.J. Engler, M. Radmacher, Y. Wang, M. Sheetz, Stiffness Gradients Mimicking In Vivo Tissue Variation Regulate Mesenchymal Stem Cell Fate, PLoS One. 6 (2011) e15978.

[114] L. MacQueen, Y. Sun, C.A. Simmons, Mesenchymal stem cell mechanobiology and emerging experimental platforms., J. R. Soc. Interface. 10 (2013) 20130179.

[115] Y. Sun, K.M.A. Yong, L.G. Villa-Diaz, X. Zhang, W. Chen, R. Philson, S. Weng, H. Xu, P.H. Krebsbach, J. Fu, Hippo/YAP-mediated rigidity-dependent motor neuron differentiation of human pluripotent stem cells, Nat. Mater. 13 (2014) 599–604.

[116] S. Musah, P.J. Wrighton, Y. Zaltsman, X. Zhong, S. Zorn, M.B. Parlato, C. Hsiao, S.P. Palecek, Q. Chang, W.L. Murphy, L.L. Kiessling, Substratum-induced differentiation of human pluripotent stem cells reveals the coactivator YAP is a potent regulator of neuronal specification., Proc. Natl. Acad. Sci. U. S. A. 111 (2014) 13805–10.

[117] A.J. Engler, C. Carag-Krieger, C.P. Johnson, M. Raab, H.-Y. Tang, D.W. Speicher, J.W. Sanger, J.M. Sanger, D.E. Discher, Embryonic cardiomyocytes beat best on a matrix with heart-like elasticity: scar-like rigidity inhibits beating, J. Cell Sci. 121 (2008) 3794–3802.

[118] S. Bose, M. Roy, A. Bandyopadhyay, Recent advances in bone tissue engineering scaffolds., Trends Biotechnol. 30 (2012) 546–54.

[119] R.C. Dutta, A.K. Dutta, Cell-interactive 3D-scaffold; advances and applications, Biotechnol. Adv. 27 (2009) 334–339.

[120] K.M. Woo, V.J. Chen, P.X. Ma, Nano-fibrous scaffolding architecture selectively enhances protein adsorption contributing to cell attachment, J. Biomed. Mater. Res. 67A (2003) 531–537.

[121] S. Li, J.R. de Wijn, J. Li, P. Layrolle, K. de Groot, Macroporous Biphasic Calcium Phosphate Scaffold with High Permeability/Porosity Ratio, Tissue Eng. 9 (2003) 535–548.

[122] R. Sultana, J. Yang, X. Hu, Deposition of Micro-Porous Hydroxyapatite/Tri-Calcium Phosphate Coating on Zirconia-Based Substrate, J. Am. Ceram. Soc. 95 (2012) 1212–1215.

[123] J. Wiltfang, H.A. Merten, K.A. Schlegel, S. Schultze-Mosgau, F.R. Kloss, S. Rupprecht, P. Kessler, Degradation characteristics of tri-calcium-phosphate (TCP) in minipigs, J. Biomed. Mater. Res. 63 (2002) 115–121.

[124] T.J. Webster, Nanophase ceramics: The future orthopedic and dental implant material, in: 2001: pp. 125–166.

[125] G. Chen, T. Ushida, T. Tateishi, Development of biodegradable porous scaffolds for tissue engineering, Mater. Sci. Eng. C. 17 (2001) 63–69.

[126] X. Biomedical Engineering Society., P.X. American Institute of Physics., Annals of biomedical engineering., Academic Press, 2004.

[127] X. Liu, P.X. Ma, Polymeric scaffolds for bone tissue engineering., Ann. Biomed. Eng. 32 (2004) 477–86.

[128] H.-Y. Cheung, K.-T. Lau, T.-P. Lu, D. Hui, A critical review on polymer-based bio-engineered materials for scaffold development, Compos. Part B Eng. 38 (2007) 291–300.

[129] Z. Li, M. Zhang, Chitosan-alginate as scaffolding material for cartilage tissue engineering, J. Biomed. Mater. Res. Part A. 75A (2005) 485–493.

[130] H.A. Awad, M. Quinn Wickham, H.A. Leddy, J.M. Gimble, F. Guilak, Chondrogenic differentiation of adipose-derived adult stem cells in agarose, alginate, and gelatin scaffolds, Biomaterials. 25 (2004) 3211–3222.

[131] J.L. van Susante, J. Pieper, P. Buma, T.H. van Kuppevelt, H. van Beuningen, P.M. van der Kraan, J.H. Veerkamp, W.B. van den Berg, R.P. Veth, Linkage of chondroitin-sulfate to type I collagen scaffolds stimulates the bioactivity of seeded chondrocytes in vitro, Biomaterials. 22 (2001) 2359–2369.

[132] H.M. Powell, S.T. Boyce, Engineered Human Skin Fabricated Using Electrospun Collagen?PCL Blends: Morphogenesis and Mechanical Properties, Tissue Eng. Part A. 15 (2009) 2177–2187.

[133] P. Joanne, M. Kitsara, S.-E. Boitard, H. Naemetalla, V. Vanneaux, M. Pernot, J. Larghero, P. Forest, Y. Chen, P. Menasché, O. Agbulut, Nanofibrous clinical-grade collagen scaffolds seeded with human cardiomyocytes induces cardiac remodeling in dilated cardiomyopathy, Biomaterials. 80 (2016) 157–168.

[134] D. Sin, X. Miao, G. Liu, F. Wei, G. Chadwick, C. Yan, T. Friis, Polyurethane (PU) scaffolds prepared by solvent casting/particulate leaching (SCPL) combined with centrifugation, Mater. Sci. Eng. C. 30 (2010) 78–85.

[135] C.-J. Liao, C.-F. Chen, J.-H. Chen, S.-F. Chiang, Y.-J. Lin, K.-Y. Chang, Fabrication of porous biodegradable polymer scaffolds using a solvent merging/particulate leaching method, J. Biomed. Mater. Res. 59 (2002) 676–681.

[136] J. Reignier, M.A. Huneault, Preparation of interconnected poly(ε-caprolactone) porous scaffolds by a combination of polymer and salt particulate leaching, Polymer (Guildf). 47 (2006) 4703–4717.

[137] E. Sachlos, J.T. Czernuszka, Making tissue engineering scaffolds work. Review: the application of solid freeform fabrication technology to the production of tissue engineering scaffolds., Eur. Cell. Mater. 5 (2003) 29-39-40.

[138] W.A. Lopes, H.M. Jaeger, Hierarchical self-assembly of metal nanostructures on diblock copolymer scaffolds, Nature. 414 (2001) 735–738.

[139] J.D. Hartgerink, E. Beniash, S.I. Stupp, Self-Assembly and Mineralization of Peptide-Amphiphile Nanofibers, Science (80-.). 294 (2001).

[140] X. Yao, H. Yao, Y. Li, C. Berkland, A.I. Cooper, F. Rojo, M.L. Ferrer, F. del Monte, Hierarchically aligned porous scaffold by ice-segregation-induced self-assembly and thermally triggered electrostatic self-assembly of oppositely charged thermosensitive microgels, J. Mater. Chem. 19 (2009) 6516.

[141] J. Lannutti, D. Reneker, T. Ma, D. Tomasko, D. Farson, Electrospinning for tissue engineering scaffolds, Mater. Sci. Eng. C. 27 (2007) 504–509.

[142] F. Asa'ad, G. Pagni, S.P. Pilipchuk, A.B. Giannì, W. V Giannobile, G. Rasperini, 3D-Printed Scaffolds and Biomaterials: Review of Alveolar Bone Augmentation and Periodontal Regeneration Applications., Int. J. Dent. 2016 (2016) 1239842.

[143] X. Tu, L. Wang, J. Wei, B. Wang, Y. Tang, J. Shi, Z. Zhang, Y. Chen, 3D printed PEGDA microstructures for gelatin scaffold integration and neuron differentiation, Microelectron. Eng. 158 (2016) 30–34.

[144] K. Whang, C.H. Thomas, K.E. Healy, G. Nuber, A novel method to fabricate bioabsorbable scaffolds, Polymer (Guildf). 36 (1995) 837–842.

[145] H. Schoof, J. Apel, I. Heschel, G. Rau, Control of pore structure and size in freeze-dried collagen sponges, J. Biomed. Mater. Res. 58 (2001) 352–357.

[146] B.B. Mandal, S.C. Kundu, Cell proliferation and migration in silk fibroin 3D scaffolds, Biomaterials. 30 (2009) 2956–2965.

[147] J. Wu, Y. Hong, Enhancing cell infiltration of electrospun fibrous scaffolds in tissue regeneration, Bioact. Mater. 1 (2016) 56–64.

[148] M. Simonet, O.D. Schneider, P. Neuenschwander, W.J. Stark, Ultraporous 3D polymer meshes by low-temperature electrospinning: Use of ice crystals as a removable void template, Polym. Eng. Sci. 47 (2007) 2020–2026.

[149] B.M. Baker, A.O. Gee, R.B. Metter, A.S. Nathan, R.A. Marklein, J.A. Burdick, R.L. Mauck, The potential to improve cell infiltration in composite fiber-aligned electrospun scaffolds by the selective removal of sacrificial fibers, Biomaterials. 29 (2008) 2348–2358.

[150] Quynh P. Pham, and Upma Sharma, A.G. Mikos, Electrospun Poly(ε-caprolactone) Microfiber and Multilayer Nanofiber/Microfiber Scaffolds: Characterization of Scaffolds and Measurement of Cellular Infiltration, (2006).

[151] J. Nam, Y. Huang, S. Agarwal, J. Lannutti, Improved Cellular Infiltration in Electrospun Fiber via Engineered Porosity, Tissue Eng. 13 (2007) 2249–2257.

[152] T. Kushibiki, A. Saito, S. Hayashi, K. Ishii, Y. Sawa, K. Awazu, Quantitative Estimates of Vascularity in a Collagen-Based Cell Scaffold Containing Basic Fibroblast Growth Factor by Noninvasive Near-Infrared Spectroscopy for Regenerative Medicine, Photomed. Laser Surg. 26 (2008) 247–250.

[153] J.E. Valentin, N.J. Turner, T.W. Gilbert, S.F. Badylak, Functional skeletal muscle formation with a biologic scaffold, Biomaterials. 31 (2010) 7475–7484.

[154] C.-H. CHANG, F.-H. LIN, T.-F. KUO, H.-C. LIU, CARTILAGE TISSUE ENGINEERING, Biomed. Eng. Appl. Basis Commun. 17 (2005) 61–71.

[155] K. Lee, E.A. Silva, D.J. Mooney, Growth factor delivery-based tissue engineering: general approaches and a review of recent developments, J. R. Soc. Interface. 8 (2010).

[156] M.J. Whitaker, R.A. Quirk, S.M. Howdle, K.M. Shakesheff, Growth factor release from tissue engineering scaffolds, J. Pharm. Pharmacol. 53 (2001) 1427–1437.

[157] E. Jabbarzadeh, T. Starnes, Y.M. Khan, T. Jiang, A.J. Wirtel, M. Deng, Q. Lv, L.S. Nair, S.B. Doty, C.T. Laurencin, Induction of angiogenesis in tissue-engineered scaffolds designed for bone repair: a combined gene therapy-cell transplantation approach., Proc. Natl. Acad. Sci. U. S. A. 105 (2008) 11099–104.

[158] R.M. Schek, E.N. Wilke, S.J. Hollister, P.H. Krebsbach, Combined use of designed scaffolds and adenoviral gene therapy for skeletal tissue engineering, Biomaterials. 27 (2006) 1160–1166.

Chapter 2

Micro- and Nano-fabrication Techniques

In this chapter, we present the development of the fabrication technologies to pattern the culture substrates. After a brief introduction, UV photolithography, soft lithography and electrospinning techniques will be described in detail. The application of these techniques will be found in each of the following chapters.

2.1 Introduction

The topographic pattern has proven to be an important factor that affects the cell morphology and the cell functions [1]. The organization of the extracellular matrix protein in-vivo shows typically nanoscale features, which indicates the importance of the nanostructure fabrication for in-vitro studies. In fact, the substrates with patterned micro and nanostructures have been frequently used to study the cytoskeleton organization, the cell adhesion, polarization, migration, proliferation etc. [2-4]. However, the most of the existing micro and nanofabrication techniques have been developed by semiconductor industries which can only be used to pattern conventional substrates such as silicon and glass [5]. More recent techniques such as nanoimprint and soft lithography techniques can be used to fabricate micro and nanostructures in polymers or elastomers but they are not flexible to work with natural biopolymers. In contrast, non-lithography techniques such as electrospinning allow working with different types of natural and synthetic polymers. Combining both lithography and non-lithography techniques, we should be able to fabricate sophisticated structures with high-resolution and in vivo ECM like features for cell biology studies.

Among others, photolithography is the most popular approach and is often used to generate regular surface features, such as grooves, posts, and pits. Photolithography and other micro- and nanofabrication techniques are typically fine-tuned for silicon, silicon oxide, polycrystalline silicon, and other inorganic systems such as titanium. Therefore, either these inorganic materials, such as silicon or titanium, or organic polymers replicas of inorganic master molds have been utilized as cell culture substrates to study the effect of topography on cell behavior [6]. Enhanced patterning techniques will continue to lead cell substrate fabrication towards sophisticated, user-defined configurations of topographic and chemical patterns, providing a new platform to establish mechanisms of cellular response to cell-material interfaces [7].

2.2 UV photolithography

2.2.1 General principles

The process of photolithography normally consists of mask design and fabrication, substrate cleaning, photoresist spin-coating, soft baking, mask alignment, exposure and development [8]. The schematic diagram of the UV photolithography methods using positive and negative resists is shown in **Fig. 2.1**. Firstly, a liquid photoresist is spin-coated on a clean substrate (e.g., Si wafer), the thickness of the photoresist is controlled by rotate speed and resist type. After the coating, soft bake of the substrate is proceeded to remove the solvent in the resist and to improve the adhesion between the resist and substrate. Then, the substrate is exposed to ultraviolet (UV) light through an absorber mask positioned on the surface. The more tensely contact between the mask and resist, the higher of the pattern resolution. Some optical chemical reactions occur in the resist film during the selective irradiation by the UV light under the transparent mask. Exposure to UV light alters the chemistry of the photoresist and changes its solubility relative to unexposed resist. There are two types of resist, “positive” and “negative” [9]. For the positive resist, when the resist is exposed to UV light, the energetic photons of the light break certain bonds in the long-chain polymers of the resist. It will cause the resist to become shorter and thus more soluble. For the negative resist, when the resist is exposed to UV light, it will cause the cross-linking between the resist polymers making the exposed areas less soluble [10]. The developer removes the unexposed resist, leaving behind a negative image of the mask. The negative resist should be post baked after the UV expose to further activate cross-linking process and improve the mechanical stability of the pattern. Finally, the resist pattern will be left on the substrate by development, in which step the exposed resist (positive resist) or unexposed resist (negative resist) are removed by the developer. **Fig. 2.2** shows scanning electron microscope (SEM) images of microstructure obtained with positive resist and negative resist. For all the process of photolithography, the following steps are critical: mask design, photoresist, baking and development.

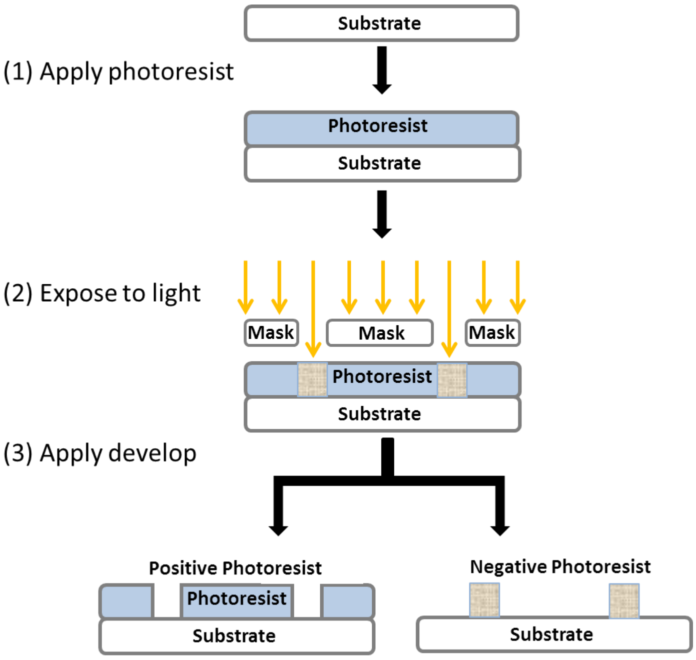

Figure 2.1 Schematic diagram of photolithography process (positive and negative photoresist).

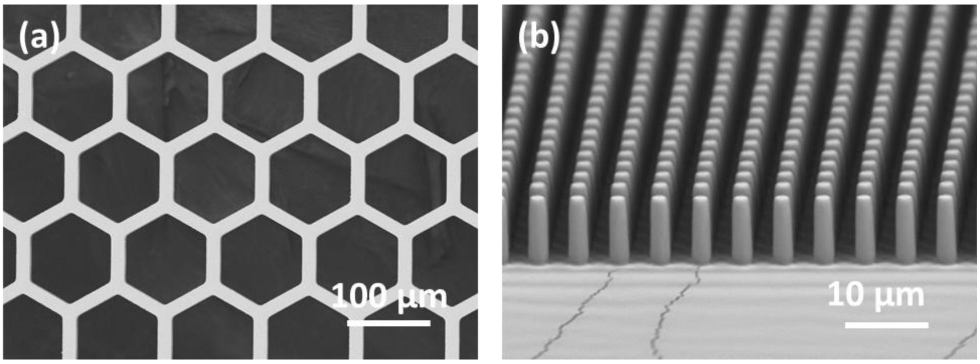

Figure 2.2 SEM images of micro-pattern fabricated by photolithography using (a) positive resist and (b) negative resist.

2.2.2 Mask design and exposure

The mask used in photolithography process normally is a printed transparency or a glass or quartz plate with absorber features that allow light to shine through in the defined pattern, as shown in **Fig. 2.3a**. In our lab, we use the photolithographic mask design program L-Edit 11.1 from Tanner research. A mask can be fabricated in several ways, mainly depending on the targeted resolution.

Transparencies for overhead projectors are often used for simple and crude structures, which are cheap and simple solutions to fabricate mask. The system can be used to give line width of 20 μm. When fabricated mask with line width below 1 μm, electron beam writer can be used. In ENS microfluidic group, μPG 101 manufactured by Heidelberg Instruments was used to generate the micro-patterns (**Fig. 2.3b**). Commercial blank optical masks, i.e., glass plates coated with 1000 Å thick chrome and 1 μm thick AZ 1518 positive photoresist (Nanofilm, CIPEC Company) were used as received. Firstly, the patterns for the mask was designed by the software L-edit, and the resulted file was transferred into the computer, which could be read by the μPG 101 software. Then the substrate with AZ 1518 was fixed to central of the sample stage. The expose of the resist was carried out by the writing of the UV laser. Using the μPG 101 system, the standard 5-inch mask plates can be fabricated with a minimum feature size down to 1 μm with an accuracy of 0.1 μm. After UV exposure, the optical mask was developed in MIF-726 positive developer (Microchemicals Company) and rinsed with DI water. In this step, the patterns of the resist could be monitored with the optical microscopy. Afterwards, the chrome metal layer exposed to the air could be removed by the commercially available chrome etches (Honeywell, chrome-Etch 3144), which mainly consists of nitric acid. Finally, the resist on the mask could be removed by acetone under sonication. And the photo mask with desired patterns could be obtained. Although this method is flexible and low cost, it is limited the pattern generation throughput.

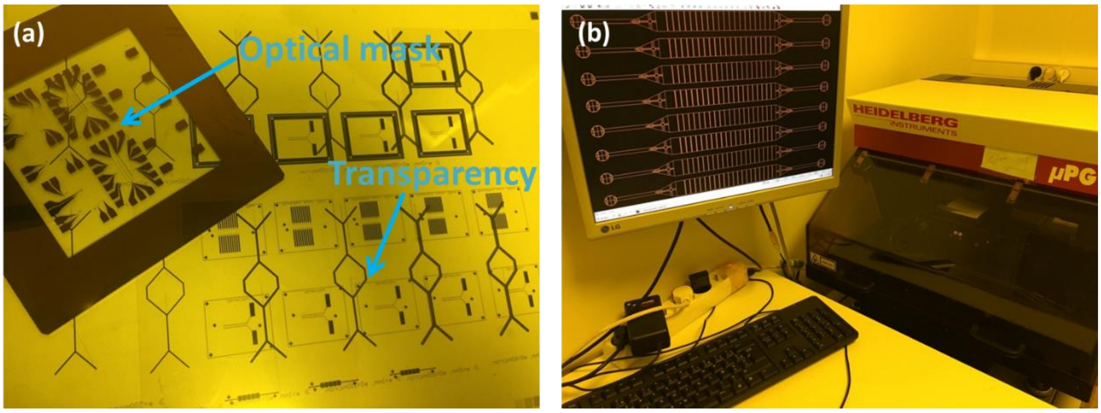

Figure 2.3 (a) Illustrations of the transparency mask and optical mask. (b) Photo of the μPG 101 direct laser writer (Heidelberg Instruments) installed in the ENS laboratory.

2.2.3 Photoresist

A photoresist is a light-sensitive material used in several processes, such as photolithography and photoengraving, to form a patterned coating on a surface, which is crucial in the whole electronic industry. There are several types of photoresists and different photoresists exhibit different sensitivities to different wavelengths. In general, photoresist is composed of basic material (e.g., epoxy resin), photoactive compound and solvent [11]. Among these, resin act as a binder that provides mechanical properties (adhesion, chemical resistance) and the solvent is used to dissolve the resin, allowing the resin to be applied in a liquid state. Photoactive compound (PAC) act to inhibit or promote the dissolution of the resin in the developer. PAC inhibits dissolution in positive resists before light exposure. After exposure, the PAC promotes dissolution of the resin. Negative (SU-8) and positive (AZ40XT and AZ5214E) resists are commonly photoresists used in our lab. **Table 2.1** introduces the major differences between positive and negative resist.

Characteristic	**Positive**	**Negative**
Adhesion to Silicon	Fair	Excellent
Relative Cost	More expensive	Less expensive
Developer Base	Aqueous	Organic
Solubility in the developer	Exposed region is soluble	Exposed region is insoluble
Minimum Feature	0.5 μm	2 μm
Step Coverage	Better	Lower
Wet Chemical Resistance	Fair	Excellent

Table 2.1 Differences between positive and negative resist. Note: This table is based on generalizations which are generally accepted in the microelectromechanical systems fabrication industry [12].

Fig. 2.4 shows the typical SEM photos of microstructures result from two kinds of resists. The standard fabrication protocols for these two resists are as follows:

SU8 3050, negative, ~50 μm

- Substrate pre-treatment: piranha (H_2SO_4: H_2O_2=3:1) for 30 min, followed by DI water rinse, and bake at 200 °C for at least 1 minutes on a hotplate;
- Spinning coat: 500 rpm for 10 s and 3000 rpm for 30s;
- Soft bake: 65 °C on hotplate for 3 min and 95 °C on hotplate for 15 min;
- Exposure: 20 s using UV light (365 nm) with power of 12.7 mJ/cm2;
- Post exposure bake: 65 °C for 3 min and 95 °C for 5 min (on hotplate);
- Development: about 30 s in SU8 developer, and rinse with isopropanol.

SU8 3050, negative, ~50 µm

- Substrate pre-treatment: piranha (H_2SO_4: H_2O_2=3:1) for 30 min, followed by DI water rinse, and bake at 200 °C for at least 1 minutes on a hotplate;
- Spinning coat: 500 rpm for 10 s and 3000 rpm for 30s;
- Soft bake: 65 °C on hotplate for 3 min and 95 °C on hotplate for 15 min;
- Exposure: 20 s using UV light (365 nm) with power of 12.7 mJ/cm2;
- Post exposure bake: 65 °C for 3 min and 95 °C for 5 min (on hotplate);
- Development: about 30 s in SU8 developer, and rinse with isopropanol.

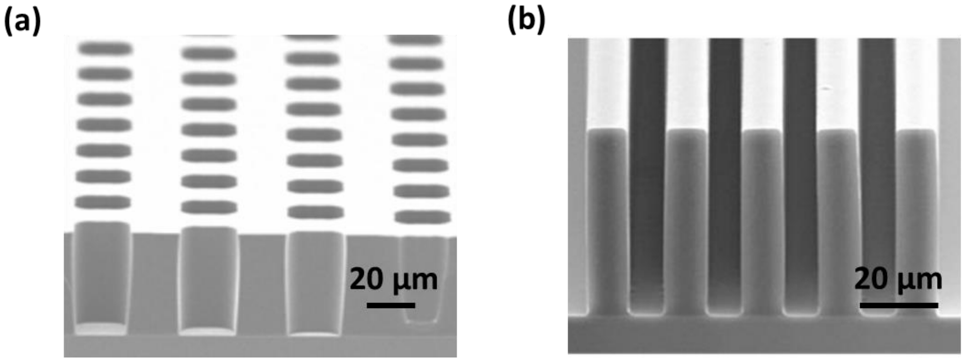

Figure 2.4 Microstructures generated by photoresists. SEM images of (a) 20 µm features in AZ40XT with thickness 40 µm. (b) 10 µm features in SU-8 3050 with thickness 50 µm [13].

When the negative resists exposed under the UV light, crosslink reaction occurs and results in the resist less soluble in the developer. Use SU-8 as an example, the triarylsulfonium hexafluoroantimonate salt (**Fig. 2.5a**) act as the photoacid generator and decomposes to form hexafluoroantimonic acid under UV light, which protonates the epoxides on the bisphenol a novolak epoxy oligomer (**Fig. 2.5b**) [12]. After bake of heat, the protonated oxonium ions react with neutral epoxides in a series of crosslinking reactions, resulting in the regeneration of the acid catalyst which will amplify the sensitivity of the resist.

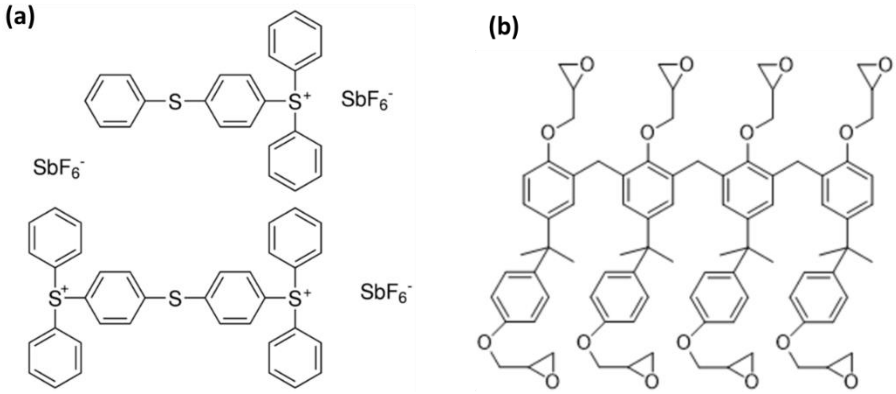

Figure 2.5 The structures of the photoactive compounds in SU-8 (a) and basic resin materials (b).

On the contrary, positive resist materials exhibit enhanced solubility in the developer after exposure to radiation. Mostly, the resistive polymers involve either chain scission or a polarity change. Novolak resins (**Fig. 2.6a**), as the favorite positive resist, are soluble in common organic solvents (including ethyl cellosolve acetate and diglyme) and aqueous base solutions. The positive photoresist sensitizers are substituted diazonaphthoquinones which are formed by a reaction of diazonaphthoquinone sulfonyl chloride with an alcohol to form sulfonate ester; the sensitizers are then incorporated into the resist via a carrier or bonded to the resin [14].

The photochemical reaction of quinonediazide is illustrated in **Fig. 2.6b**. Upon absorption of a photon, the quinonediazide decomposes through Wolff rearrangement, specifically a Sus reaction, and produces gaseous nitrogen as a by-product. In the presence of water, the decomposition product forms an indene carboxylic acid, which is base-soluble [15]. However, the formation of acid may not be the reason for increased solubility; the release of nitrogen gas produces a porous structure through which the developer may readily diffuse, resulting in increased solubility.

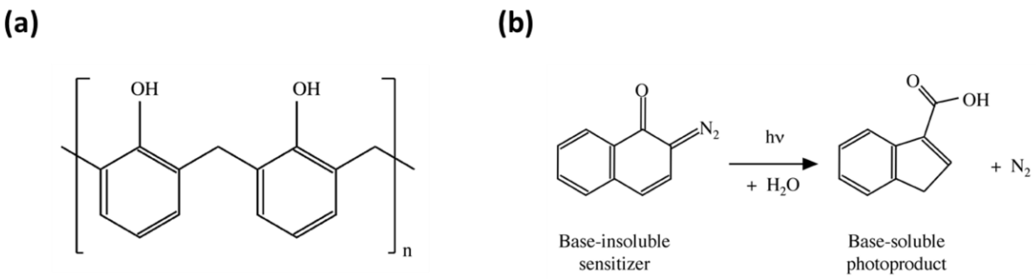

Figure 2.6 (a) Structure of a novolak resin. (b) The photochemical reaction equation of quinonediazide [15].

2.2.4 UV expose and development

As discussed before, the post-bake is important step during the photolithography. For the chemically amplified resists, post-exposure bake promotes the thermally activated diffusion of carboxylic acid formed during exposure from the photo active compound and catalytically completes the photo reaction initiated during exposure. AZ positive resist does not need post bake due to it is not belong to the chemically amplified resist. The effect of the post to the image reversal resist has been summarized before. The developer for the SU-8 and AZ resist are PM-Acetate and TMAH, respectively. To avoid the excess development, we can check the patterns under the microscopy and developing repeatedly until getting the good patterns.

2.3 Soft photolithography

Soft lithography represents a non-photolithographic strategy based on self-assembly and replica molding for carrying out micro- and nanofabrication. It provides a convenient, effective, and low-cost method for the formation and manufacturing of micro- and nanostructures [16, 17]. In soft lithography, an elastomeric stamp with patterned relief structures on its surface is used to generate patterns.

2.3.1 Mechanism and fabrication process

An elastomeric block with patterned relief structures on its surface is the key to soft lithography. The most common material used in soft lithography is polydimethylsiloxane (PDMS), which is inexpensive, nontoxic, and optically transparent. It is also chemically stable in a wide range of environments with desirable physical properties and the low surface energy (21.6×10-3 J m^{-2}) allows easy release from templates and surfaces [18].

Fig. 2.7 introduces the regular soft lithography process. Briefly, the PDMS stamp is replicated from a patterned master obtained by photolithography, focused ion beam or electron beam lithography method. For preparing the PDMS stamp, a solution of A and B at different ratios is mixed evenly and then casted on the mold. After that, the system is transferred to a vacuum chamber to remove the bubbles.

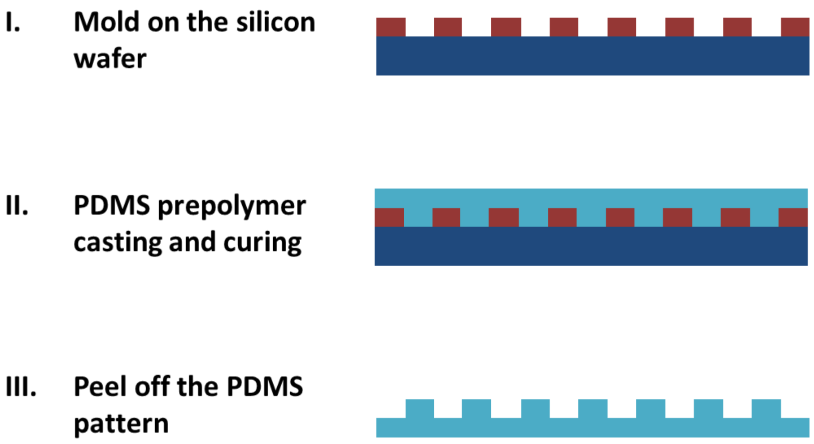

Figure 2.7 Illustration of soft lithography process

Then the PDMS prepolymer are transferred to an 80 °C oven to crosslink (Fig. 2.8). The volume ratio of B and the bake time will decide the stiffness of the PDMS stamp [19]. Increasing the volume ratio of B and the bake time will lead to higher rigidity. The master can be used repeatedly to make many replicas. There are size limitations of the features that can be produced, but patterns from nm to mm are routinely obtained.

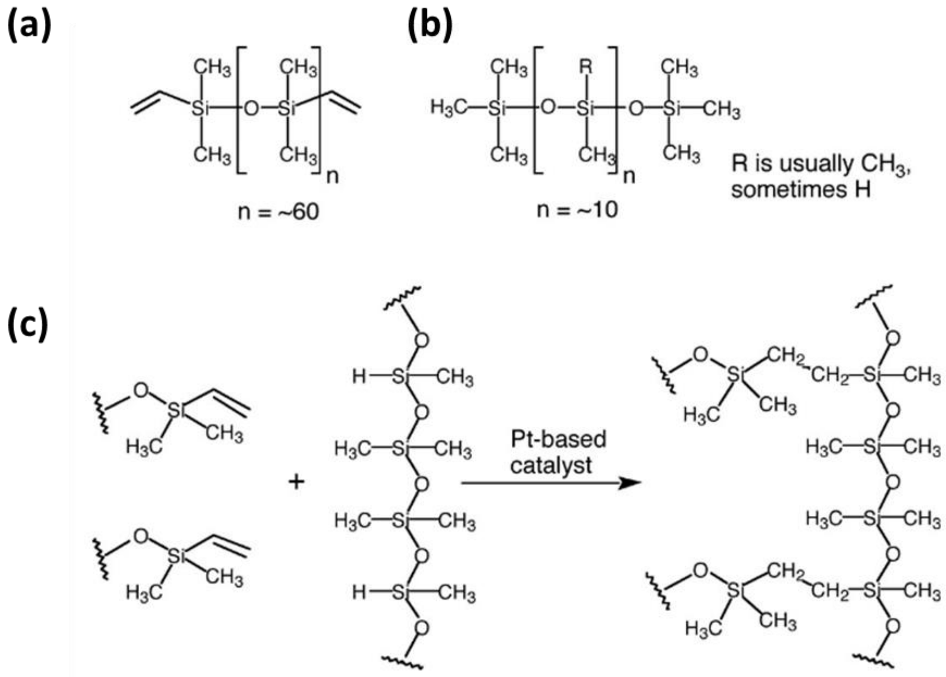

Figure 2.8 Chemical Structure of (a) siloxane oligomers and (b) siloxane cross-linkers. (c) Schematic of PDMS crosslink [20].

Nevertheless, before doing molding, the surface of the mold has to be treated with a release agent in order to prevent sticking between the polymer and the master, especially during the replication of small feature size patterns. Ideally, the adhesion force between the substrate and the mold should be much larger than that between the polymer layer and the mold. More generally, the adhesion force between the mold patterning surface and the imaging polymer layer should be significantly smaller than the adhesion forces between two adjacent layers in multilayer molds or resist systems.

In our experiment, two surface treatment methods are used according to structure feature size and aspect ratio. For replicate large feature size patterns (above 5 µm), the molds are generally treated with evaporated trichloromethylesilane (TMCS) [21]. The silanization mechanism is described in **Fig. 2.9**. Briefly, the mold treated with O_2 plasma to generate hydroxyl group as hydrophobic surface, then the mold and several drops of TMCS are put in a chamber, which then is sealed for a few minutes [22].

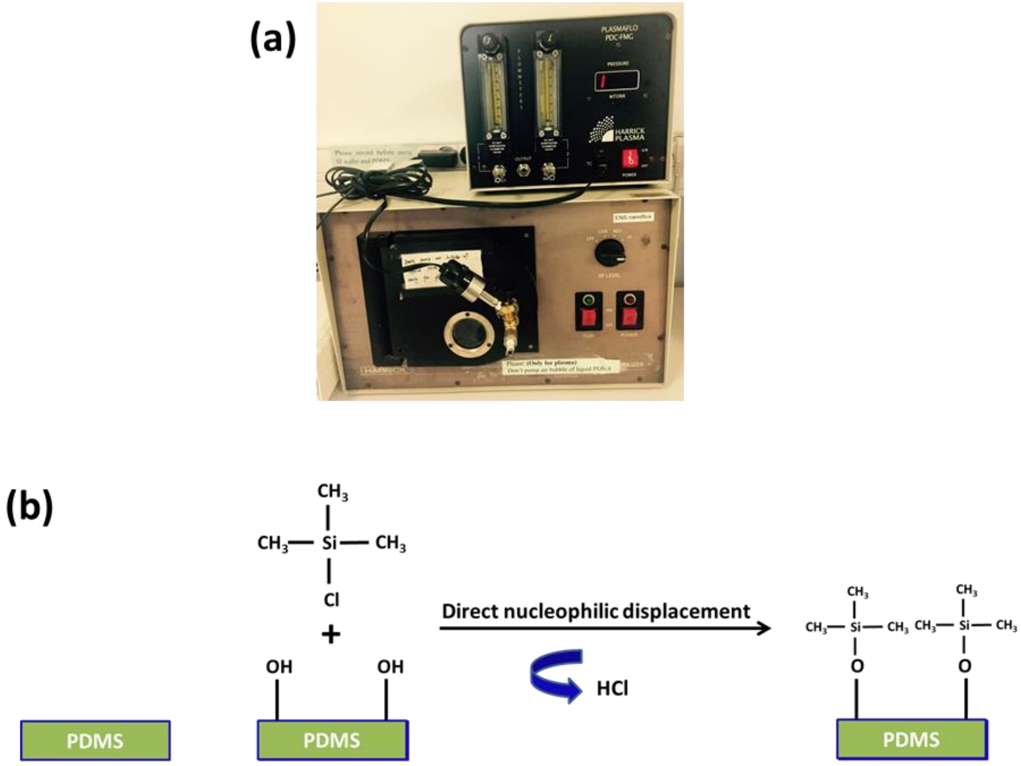

Figure 2.9 (a) Photo of plasma and (b) mechanism diagram of surface treatment using TMCS as an anti-sticking agent.

For micropillar arrays with high aspect ratio (above 1:5) used in this thesis, paralyne deposition method is introduced. Parylene is a family of chemically vapor deposited polymer with material properties that are attractive for biomedicine and nanobiotechnology (the machine installed in ENS lab shown in **Fig. 2.10**) [23]. Chemically inert parylene “peel-off” stencils have been demonstrated for micropatterning biomolecular arrays with high uniformity, precise spatial control down to nanoscale resolution [24]. Such micropatterned surfaces are beneficial in engineering biosensors and biological microenvironments. A variety of substituted precursors enables direct coating of functionalized parylenes onto biomedical implants and microfluidics, providing a convenient method for designing biocompatible and bioactive surfaces [25].

Figure 2.10 Photo of parylene deposition system (SCS Instruments) installed in the ENS laboratory

Due to the low surface free energy of untreated parylene-C surface (19.6 mN/m), corresponding to a hydrophobic surface [26], here parylene act as an inertial surface coating, which can be deposited more efficiently and easily via a chemical vapor deposition (CVD) process [27], as illustrated in **Fig. 2.11**. In this CVD process, the dimer precursor paracyclophane (or di-para-xylylene) is first vaporized and then undergoes vacuum pyrolysis at temperatures above 550 °C to yield the reactive monomer. The monomer adsorbs to the substrate surface and spontaneously polymerises at room temperature to form linear, high molecular weight parylene films. **Fig. 2.11** shows the typical CVD process parameters for depositing parylene-C using commercial systems and the chemical reactions underlying the CVD process and the chemical structures of para-cyclophane and parylene. The process enables control of the deposition parameters and full conversion of the precursor into parylene. It is appealing that the substrates are kept at room temperature during deposition, enabling parylene to be coated onto a variety of heat-sensitive substrates without thermal damage. Moreover, its hydrophobic property prevents sticking between the polymer and the master.

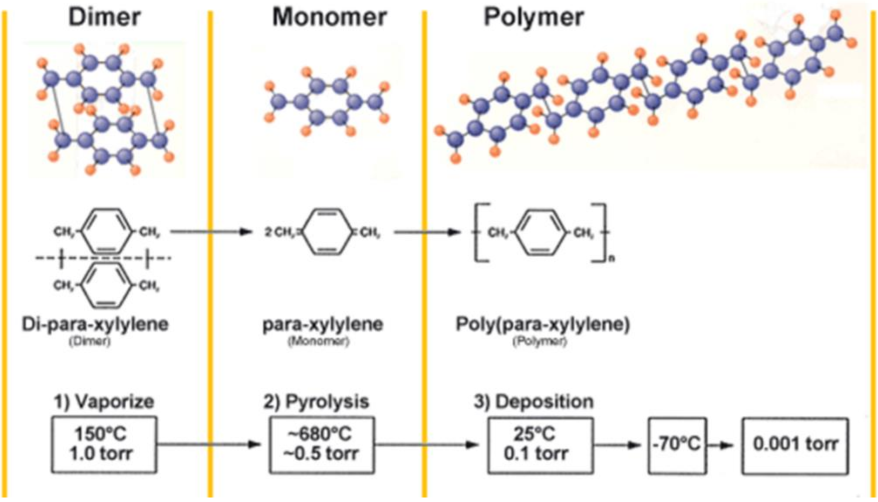

Figure 2.11 Precursor paracyclophane and its polymerization equation into parylene [27].

2.3.2 Micro-contact printing (μCP)

Microcontact printing is considered one of the most useful techniques for large area (> cm^2) patterning of functional organic surfaces. The process is very similar to using a common stamp to transfer ink from an ink pad to a piece of paper. The PDMS mold is "inked" with the material solution to be transferred to the substrate and contact is made between the substrate and the protruding features of the mold [28]. This allows the material to be transferred from the mold to the substrate for patterning the substrate as desired (**Fig. 2.12**). Depending on the type of the substrate, the inked molecule can be physically or chemically adsorbed on the substrate. In general, the resolution of microcontact printing is limited by the stamp feature size and the diffusion of the ink molecules around the contact areas [29]. In practice, the PDMS stamps provide a minimum feature size of ~200 nm but smaller features can be obtained by using stamps of a higher stiffness and/or less diffused molecules.

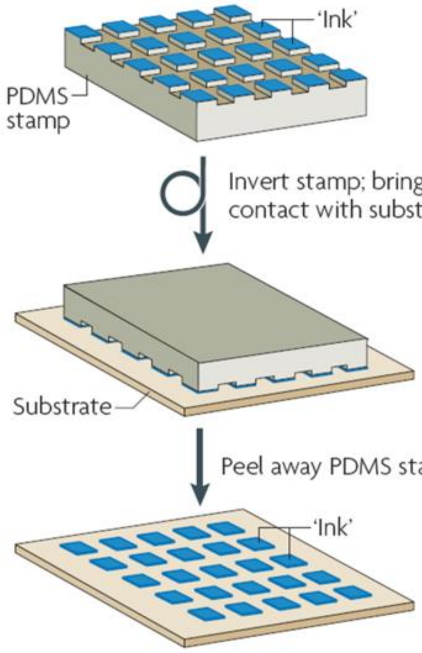

Fig. 2.12 Illustration of microcontact printing [30].

2.3.3 Replica molding

Replica molding can be defined a process that transfers a pattern from a rigid or elastomeric mold into another material by way of a liquid solidifying when in contact with the mold. Replica molding can further be sorted into subfields microtransfer molding and micromolding in capillaries (**Fig. 2.13**).

(a) In microtransfer molding, the patterned surface of a PDMS layer is filled with a liquid polymer. When the excess polymer has been removed, the PDMS layer is inverted and brought into contact with a substrate. After the curing of polymer, the PDMS layer is cautiously peeled away, leaving a solid structure with a feature size down to 1µm on the surface of the substrate. Similar to replica molding, the same PDMS layer can be refilled many times [31].

(b) Capillary molding is a second technique where a patterned PDMS is used as a mold. The patterns of the PDMS layer must first be brought into contact with a substrate (e.g., a glass slide). Capillary molding is then intended to fill the patterns of the PDMS mold with a liquid polymer (thermally or photo curable). As the name of the technique implies, capillarity is exploited to progressively fill the patterns. As an alternative, suction can be used. After having cured the polymer, the PDMS can be gently removed, leaving solid microstructures at the surface of the substrate [32].

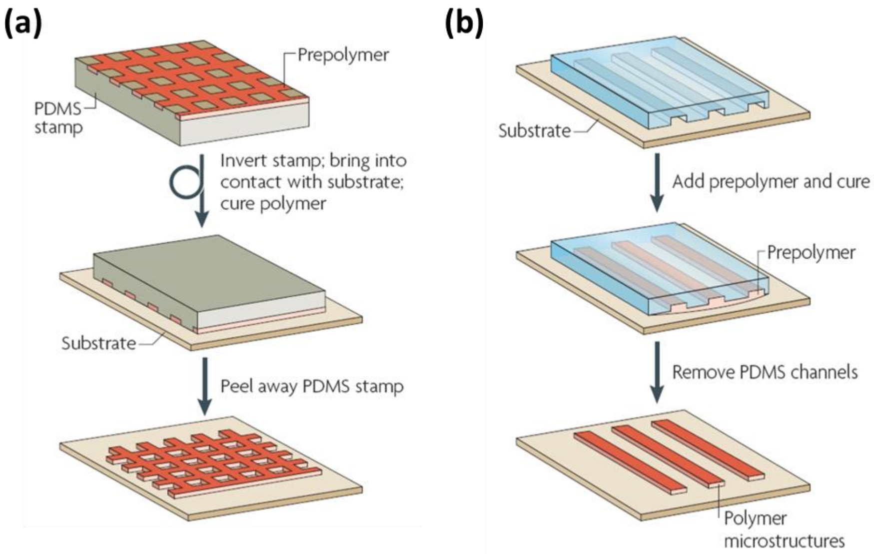

Figure 2.13 Schematic illustration of steps for (a) microtransfer molding and (b) micromolding in capillaries [30].

2.4 Electrospinning

Electrospinning is a widely used technique for the formation of electrostatic fibers with diameters ranging from 2 nm to several micrometers by using electrical forces on polymer solutions of natural and synthetic polymers, which has evinced tremendous interest and attention in both research and commerce over the past [33–35]. With the purpose of producing novel natural micro- or nano-fibers with controllable properties and function, researchers all over the world have been re-examining the electrospinning process since the beginning of this century. Due to its versatility in spinning a wide variety of natural and polymeric fibers with submicron range consistently that is otherwise difficult to achieve by using standard mechanical fiber-spinning technologies and in mimicking extracellular matrix components much closely as compared to the conventional techniques, this process of electrospinning has gained much attention in the last decade [36, 37]. With the properties of extremely high surface-to-volume ratio, tunable porosity, malleability to conform to a wide variety of sizes and shapes and the ability to control the nanofiber composition, the sub-micron range spun fibers produced by this process have been successfully applied in various fields, such as, nanocatalysis, tissue engineering scaffolds, protective clothing, filtration, biomedical, pharmaceutical, optical electronics, healthcare, biotechnology, defense and security, and environmental engineering (**Fig. 2.14**), and also gained great attention from academic research (**Table 2.2**) [34, 37, 38]. Overall, this is a relatively robust and simple technique to produce nanofibers from a wide variety of polymers.

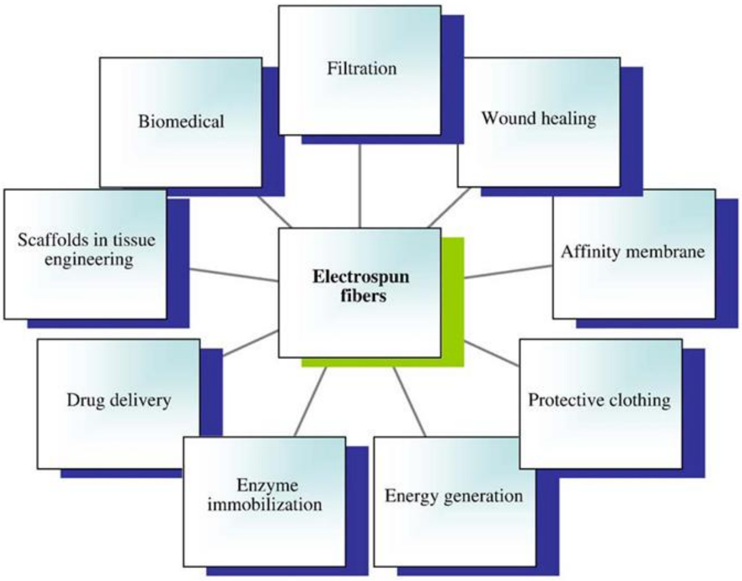

Figure 2.14 Applications of electrospun fibers in different sectors [35].

Field: Publication Years	Record Count	% of 17606	Bar Chart
2016	2577	14.637 %	▬
2015	2458	13.961 %	▬
2014	2373	13.478 %	▬
2013	2007	11.400 %	▬
2012	1811	10.286 %	▬
2011	1584	8.997 %	▬
2010	1231	6.992 %	▬
2009	1002	5.691 %	▬
2008	860	4.885 %	▬
2007	578	3.283 %	▬

Table 2.2 Number of articles about electrosinning by web of science [39].

2.4.1 Principles

Generally, the basic setup for electrospinning is composed of three parts: the high-voltage power supply, a conductive collector and a syringe (**Fig. 2.15a**). The polymer solution is fed by syringe, which is generally driven by a pump to control the constant flow rate. A nozzle is mounted on the tip of the syringe, connecting with the positive electrode to form the Taylor cone. A variety of conductive structures are employed such as silicon wafer and aluminum foil as collector to connect to negative electrode. When a sufficiently high voltage is applied to the two electrodes, there are two forces coexisting in the Taylor cone [35]. One is the surface tension that shrinks the drop as a sphere. On the other hand, the body of the liquid becomes charged, resulting in the electrical repulsion force. At a critical point, a stream of liquid erupts from the surface. If the molecular cohesion of the liquid is sufficiently high, stream breakup does not occur (if it does, droplets are electrosprayed) and a charged liquid jet is formed. As the jet dries in flight, the mode of current flow changes from ohmic to convective as the charge migrates to the surface of the fiber [33]. The jet is then elongated by a whipping process caused by electrostatic repulsion initiated at small bends in the fiber, until it is finally deposited on the grounded collector. The elongation and thinning of the fiber resulting from this bending instability leads to the formation of uniform fibers with nanometer- scale diameters, as illustrated in **Fig. 2.15b**. **Fig. 2.16** shows the electrospinning setup used in our laboratory and the fiber sample deposition on aluminum foil.

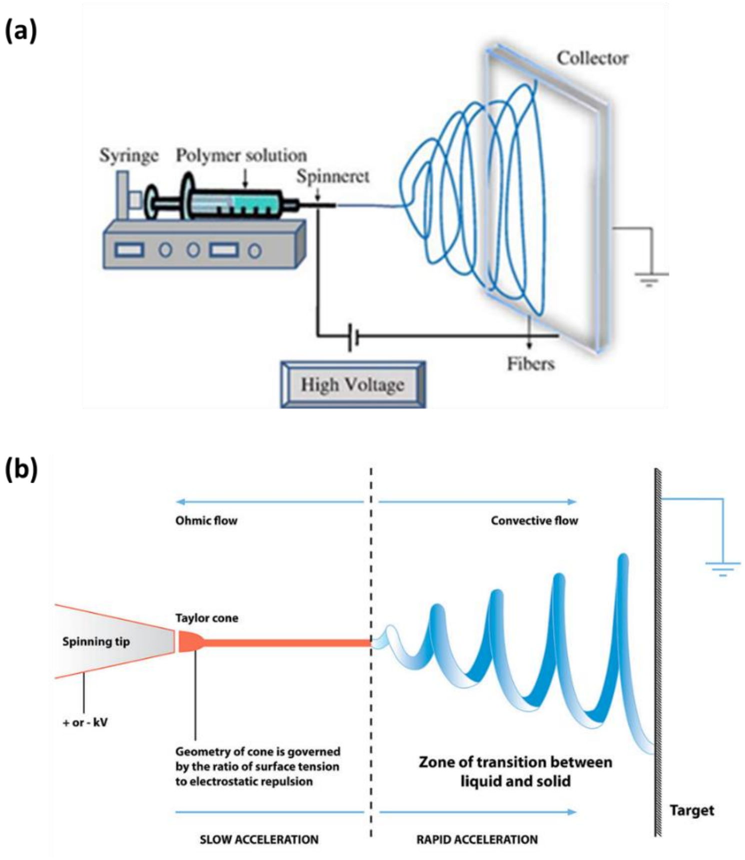

Figure 2.15 (a) Schematic diagram of set up of electrospinning apparatus. (b) Diagram showing fiber formation by electrospinning [40, 41].

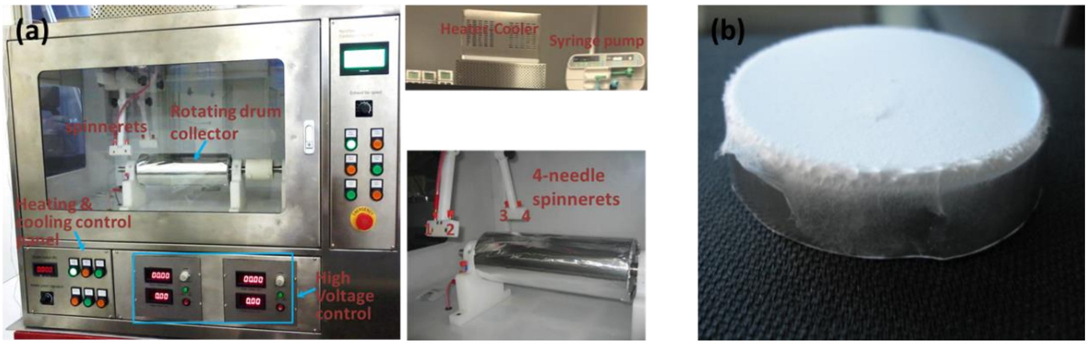

Figure 2.16 Photos of (a) electrospinning set up installed in the ENS laboratory (b) fiber sample deposition.

2.4.2 Effects of various parameters on electrospinning

The electrospinning process is solely governed by process parameters, classified broadly into applied voltage, flow rate, tip to collector distance and the structure of the collectors [33].

2.4.2.1 Applied voltage

The applied voltage is a crucial element in the electrospinning process. Fiber formation occurs only after attainment of the threshold voltage, which induces the necessary charges on the solution along with electric field and initiates the electrospinning process. When higher voltages are applied, there is more polymer ejection which facilitates the formation of a larger diameter fiber. With the voltage increased, the electrostatic repulsive force on the fluid jet also strengthened which ultimately favors the narrowing of fiber diameter [42, 43]. Generally, a higher voltage leads to greater stretching of the solution because of the greater columbic forces as well as a stronger electric field, which reduce the diameter of the fiber and accelerate the evaporation of the solvent. Researchers have showed that doubling the applied electric field would decrease the fiber diameter by roughly half. There is also greater probability of the beads formation under a higher voltage [44].

2.4.2.2 Flow rate and tip to collector distance

The flow rate of the solution influences the jet velocity and the material transfer rate. Normally, a lower feed rate is more desirable as the solvent evaporate relatively completed. It has been proved that with the increase of the polymer flow rate, the fiber diameter and the pore diameter increases and the morphological structure also can be slightly changed. Moreover, high flow rates result in beaded fibers due to unavailability of proper drying time prior to reaching the collector [44]. The distance between the tip and the collector has been examined as another approach to control the fiber diameters and morphology. A minimum distance is required to give the fibers sufficient time to dry before reaching the collector, otherwise with distances that are either too close or too far, beads have been observed. It has been reported that increasing the distance results in rounder fibers with the spinning of silk-like polymer, but with closer distances can produce flatter fibers [33, 43]. One important physical aspect of the electrospinning nanofibers is their dryness from the solvent used to dissolve the polymer. Thus, there should be optimum distance between the tip and collector which favors the evaporation of solvent from the nanofibers.

2.4.2.3 Alignment, collector-pattern and 3D structure

Electrospun nanofibers are normally collected with random orientation, whereas most native ECM found in tissues or organs, such as heart and blood vessel, have anisotropic architecture, which is crucial for tissue function [45, 46]. Therefore, a well-defined architecture is believed to be necessary in order to precisely imitate native ECM for guiding cell growth or tissue regeneration. To this end, electrospun fibrous scaffolds with alignment architecture have shown superior capacity in shaping cell morphology, guiding cell migration, and affecting cell differentiation [47].

A variety of strategies have been demonstrated to obtain alignment fibers. Overall, these methods can be classified into two major categories, i.e., collector configuration and controlling syringe moving. A number of collector have been tested to generate highly align fibers. Among them, the parallel rods and rotating cylinder are the most used collectors [47], as shown in **Fig. 2.17a** and **b**. Another approach is to control the moving of syringe, by which the deposition of fibers can be well controlled if the moving speed of syringe is fast enough. Moreover, nanofibers with various orientation integrated in one sample can be achieved (**Fig. 2.17c** and **d**) [48].

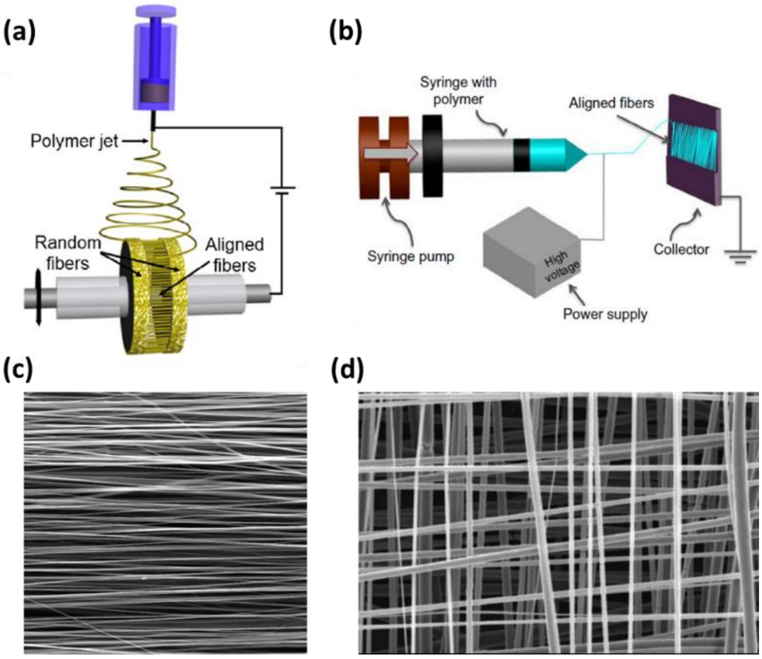

Figure 2.17 (a, b) Typical electrospinning setup model for fiber alignment [47]. (c) Highly aligned polymer fibers and (d) fibers deposited in 90 degree turns [48].

Recent studies have begun to identify new collector plate designs to generate electrospun scaffolds with ordered 3D fibrous structures (**Fig. 2.18**) [48]. For instance, additive manufacturing approach has been used to design novel collector geometries that when placed on the collector plate and electrospun onto, produced hybrid scaffolds consisting of both random fibers and a defined 3D micro-topography at the surface [49]. Besides, 3D structured composites made of nanofibers and microparticules obtained due to controlled electrostatic interactions during alternate electrospinning and electrospraying on micro patterned collectors. The typical structures of electrospun membranes and the specific electrospinning strategies used to produce these structures hold great potential in applications of tissue engineering and drug delivery [50].

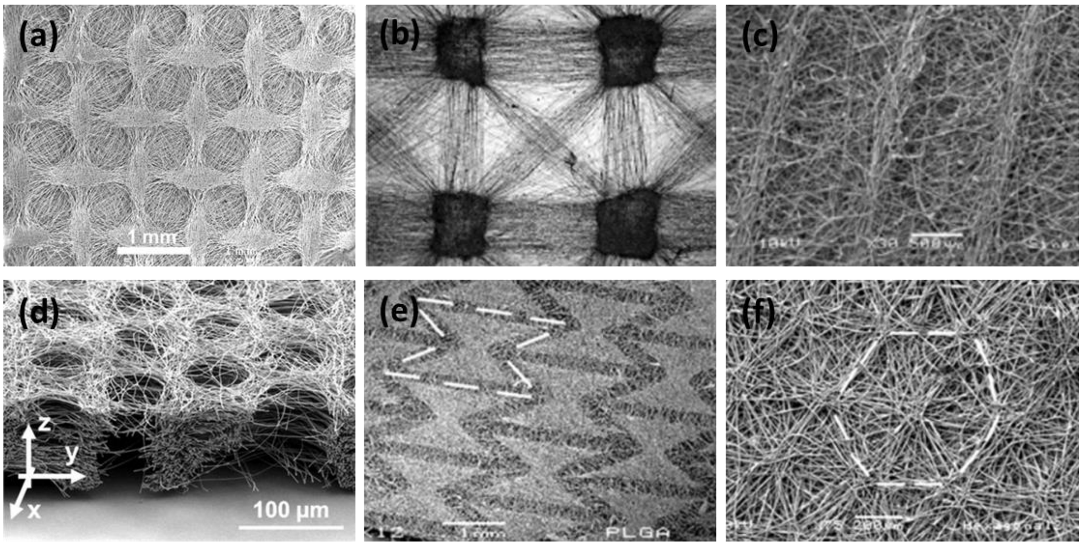

Figure 2.18 SEM images of (a, d) 3D fibrous structure generated from electrospinning [51] and (b, c, d, e) patterned fibers mat [49].

2.5 Conclusion

UV photolithography, soft lithography and electrospinning are now widely used for micro- and nanofabrication purposes, because of their low cost, high resolution and high throughput. These techniques can be easily combined to obtain more complex pattern structures, providing a highly efficient treatment of the surface of cell culture substrates of different materials. More systematic design and integration of material and pattern types are expected for high throughput screening which should be useful for different purposes in cell biology and biomedical device manufacturing.

Reference

[1] K. Kulangara, K.W. Leong, X.S. Jiang, K.W. Leong, H.Q. Mao, H.Q. Mao, H.Q. Mao, N. Winograd, H.J. Donahue, Substrate topography shapes cell function, Soft Matter. 5 (2009) 4072.

[2] D.-H. Kim, P.P. Provenzano, C.L. Smith, A. Levchenko, Matrix nanotopography as a regulator of cell function, J. Cell Biol. 197 (2012).

[3] M.J.P. Biggs, R.G. Richards, M.J. Dalby, Nanotopographical modification: a regulator of cellular function through focal adhesions, Nanomedicine Nanotechnology, Biol. Med. 6 (2010) 619–633.

[4] C. Bettinger, R. Langer, J. Borenstein, Engineering Substrate Topography at the Micro- and Nanoscale to Control Cell Function, Angew. Chemie Int. Ed. 48 (2009) 5406–5415.

[5] C.A. Mirkin, J.A. Rogers, Emerging Methods for Micro- and Nanofabrication, MRS Bull. 26 (2001) 506–509.

[6] D.B. Weibel, W.R. DiLuzio, G.M. Whitesides, Microfabrication meets microbiology, Nat. Rev. Microbiol. 5 (2007) 209–218.

[7] R. Ayala, C. Zhang, D. Yang, Y. Hwang, A. Aung, S.S. Shroff, F.T. Arce, R. Lal, G. Arya, S. Varghese, Engineering the cell-material interface for controlling stem cell adhesion, migration, and differentiation, Biomaterials. 32 (2011) 3700–3711.

[8] http://www.lithoguru.com/scientist/lithobasics.html.

[9] http://www.microchem.com/Prod-LithographyOverviewPosNeg.htm.

[10] https://www.microsi.com/the-difference-between-positive-and-negative photoresist/.

[11] http://www.lithoguru.com/scientist/litho_tutor/TUTOR05 (Winter 94).pdf .

[12] https://www.wikiwand.com/en/Photoresist.

[13] http://www.microchem.com/Prod-SU8_KMPR.htm.

[14] https://www.wikiwand.com/en/Phenol_formaldehyde_resin.

[15] http://cnx.org/contents/KZdIG-zX@2/Composition-and-Photochemical-.

[16] D. Qin, Y. Xia, G.M. Whitesides, Soft lithography for micro- and nanoscale patterning, Nat. Protoc. 5 (2010) 491–502.

[17] Y. Xia, G.M. Whitesides, SOFT LITHOGRAPHY, Annu. Rev. Mater. Sci. 28

(1998) 153–184.

[18] G.M. Whitesides, E. Ostuni, S. Takayama, X. Jiang, D.E. Ingber, Soft Lithography in Biology and Biochemistry, Annu. Rev. Biomed. Eng. 3 (2001) 335–373.

[19] R.N. Palchesko, L. Zhang, Y. Sun, A.W. Feinberg, Y. Joyce, Development of Polydimethylsiloxane Substrates with Tunable Elastic Modulus to Study Cell Mechanobiology in Muscle and Nerve, PLoS One. 7 (2012) e51499.

[20] http://education.mrsec.wisc.edu/background/PDMS/.

[21] F. Carvalho, P. Paradiso, B. Saramago, A.M. Ferraria, A.M.B. do Rego, P. Fernandes, An integrated approach for the detailed characterization of an immobilized enzyme, J. Mol. Catal. B Enzym. 125 (2016) 64–74.

[22] P. Zucca, E. Sanjust, Inorganic Materials as Supports for Covalent Enzyme Immobilization: Methods and Mechanisms, Molecules. 19 (2014) 14139–14194.

[23] https://www.wikiwand.com/en/Parylene.

[24] C.P. Tan, B. Ri Seo, D.J. Brooks, E.M. Chandler, H.G. Craighead, C. Fischbach, Parylene peel-off arrays to probe the role of cell?cell interactions in tumour angiogenesis, Integr. Biol. 1 (2009) 587.

[25] https://vsiparylene.com/industries/medical/.

[26] C.P. Tan, H.G. Craighead, Surface Engineering and Patterning Using Parylene for Biological Applications, Materials (Basel). 3 (2010) 1803–1832.

[27] http://microencapsulation.net/parylene.html.

[28] https://www.wikiwand.com/en/Microcontact_printing.

[29] H.A. Biebuyck, N.B. Larsen, E. Delamarche, B. Michel, Lithography beyond light: Microcontact printing with monolayer resists, IBM J. Res. Dev. 41 (1997) 159–170.

[30] http://www.elveflow.com/microfluidic-tutorials/soft-lithography-reviews-and-tutorials/introduction-in-soft-lithography/introduction-about-soft-lithography-and-polymer-molding-for-microfluidic/.

[31] C.K.Y. Wong, O.C.T. Cheung, Bing Xu, M.M.F. Yuen, Using PDMS microtransfer molding (/apl mu/TM) for polymer flip chip, in: 53rd Electron. Components Technol. Conf. 2003. Proceedings., IEEE, pp. 652–657.

[32] E. Kim, Y. Xia, G.M. Whitesides, Polymer microstructures formed by moulding in capillaries, Nature. 376 (1995) 581–584.

[33] M.K. Leach, Z.-Q. Feng, S.J. Tuck, J.M. Corey, Electrospinning fundamentals: optimizing solution and apparatus parameters., J. Vis. Exp. (2011).

[34] Z.-M. Huang, Y.-Z. Zhang, M. Kotaki, S. Ramakrishna, A review on polymer nanofibers by electrospinning and their applications in nanocomposites, Compos. Sci. Technol. 63 (2003) 2223–2253.

[35] N. Bhardwaj, S.C. Kundu, Electrospinning: A fascinating fiber fabrication technique, Biotechnol. Adv. 28 (2010) 325–347.

[36] R. Vasita, D.S. Katti, Nanofibers and their applications in tissue engineering., Int. J. Nanomedicine. 1 (2006) 15–30.

[37] T.J. Sill, H.A. von Recum, Electrospinning: Applications in drug delivery and tissue engineering, Biomaterials. 29 (2008) 1989–2006.

[38] L. Jin, T. Wang, M.-L. Zhu, M.K. Leach, Y.I. Naim, J.M. Corey, Z.-Q. Feng, Q. Jiang, Electrospun fibers and tissue engineering., J. Biomed. Nanotechnol. 8 (2012) 1–9.

[39] X. Shi, W. Zhou, D. Ma, Q. Ma, D. Bridges, Y. Ma, A. Hu, Electrospinning of Nanofibers and Their Applications for Energy Devices, J. Nanomater. 2015 (2015) 1–20.

[40] G. Taylor, Disintegration of Water Drops in an Electric Field, Proc. R. Soc. A Math. Phys. Eng. Sci. 280 (1964) 383–397.

[41] http://zach-tronstad-srp.weebly.com/blog/electrospinning-an-overview.

[42] K.H. Lee, H.Y. Kim, H.J. Bang, Y.H. Jung, S.G. Lee, The change of bead morphology formed on electrospun polystyrene fibers, Polymer (Guildf). 44 (2003) 4029–4034.

[43] S.-H. Tan, R. Inai, M. Kotaki, S. Ramakrishna, Systematic parameter study for ultra-fine fiber fabrication via electrospinning process, Polymer (Guildf). 46 (2005) 6128–6134.

[44] J.. Deitzel, J. Kleinmeyer, D. Harris, N. Beck Tan, The effect of processing variables on the morphology of electrospun nanofibers and textiles, Polymer (Guildf). 42 (2001) 261–272.

[45] D. Kai, M.P. Prabhakaran, G. Jin, S. Ramakrishna, Guided orientation of cardiomyocytes on electrospun aligned nanofibers for cardiac tissue engineering, J. Biomed. Mater. Res. Part B Appl. Biomater. 98B (2011) 379–386.

[46] C. Xu, Aligned biodegradable nanofibrous structure: a potential scaffold for blood vessel engineering, Biomaterials. 25 (2004) 877–886.

[47] F. Yang, R. Murugan, S. Wang, S. Ramakrishna, Electrospinning of nano/micro scale poly (l-lactic acid) aligned fibers and their potential in neural tissue engineering, Biomaterials. 26 (2005) 2603–2610.

[48] Y. Yang, M. Kamudzandu, P. Roach, R. Fricker, Nanofibrous scaffolds supporting optimal central nervous system regeneration: an evidence-based review, J. Neurorestoratology. 3 (2015) 123.

[49] C.M. Rogers, G.E. Morris, T.W.A. Gould, R. Bail, S. Toumpaniari, H. Harrington, J.E. Dixon, K.M. Shakesheff, J. Segal, F.R.A.J. Rose, A novel technique for the production of electrospun scaffolds with tailored three-dimensional micro-patterns employing additive manufacturing, Biofabrication. 6 (2014) 35003.

[50] N.M. Neves, R. Campos, A. Pedro, J. Cunha, F. Macedo, R.L. Reis, Patterning of polymer nanofiber meshes by electrospinning for biomedical applications., Int. J. Nanomedicine. 2 (2007) 433–48.

[51] C.R. Wittmer, A. H?braud, S. Nedjari, G. Schlatter, Well-organized 3D nanofibrous composite constructs using cooperative effects between electrospinning and electrospraying, Polymer (Guildf). 55 (2014) 5781–5787.

Chapter 3

Elongation and Cell Migration on Dense Elastomer Pillars with Stiffness Gradient

In this chapter, we study cell culture behaviors on dense micropillar arrays with height gradients. We firstly develop a method to fabricate elastomer pillar arrays with uniform top surface but different pillar heights by photolithography and soft-lithography techniques. Due to the height variation, the fabricated pillars could be used as a new type of substrate with modulated surface stiffness. We then investigate the cell culture behaviors on the pillar arrays and show remarkable cell elongation and directed cell migration, both depending on the gradient strength. The micropillar array could also be organized to have ripple-like height gradient, showing similar cell culture behaviors. Thus, this approach enables regulation of mechanical properties of substrates with designed stiffness gradient for cell culture studies.

3.1 Introduction and motivation

In their native environment, adhesion cells are surrounded by extracellular matrix (ECM), which interacts with cells to transmit complex biochemical and biophysical signals [1–3]. One of the important parameters of the cellular environment is the elastic modulus of the ECM, which determines, for example, the focal adhesion development, the cytoskeletal reorganization, the differentiation characteristics and the apoptosis [4–6]. The mechanosensitive receptors of the cellular membrane, such as integrin and cadherin, sense the external mechanical stimuli that transmitted to the cell nucleus together with biochemical signals through mechanotransduction in the form of tension, and influence biologic process such as cell cycle and differentiation [7, 8]. Previously, hydrogel and PDMS substrates with varying stiffness have been developed to approach the native ECM stiffness of tissues in order to investigate mechanically coupled cellular functions [9–11]. These investigations were mostly based on substrates with uniform stiffness. It is known that not only the stiffness of cell microenvironment has high variation between different tissues, ranging from very soft, such as brain tissue (260–490 Pa) to stiffer tissue like kidney (2.5 kPa) and even higher for bone tissue (around 15 MPa) [12, 13] but also the local stiffness can vary strongly, giving rise to complex stiffness gradients that can span several orders of magnitude, such as those noted at interfacial tissues [14]. Such stiffness gradient may play important role, for example, to tune directional cell migration [15, 16].

Stiffness gradients can be generated in hydrogels, such as polyacrylamide (PAA), by changing the crosslink density in flowing sols or by differentially exposing a photo-curable gel to UV radiation using a photomask [17–19]. In such cases, altered cross-linker amount impacts not only bulk mechanics but also molecular-scale material properties including porosity, surface chemistry, and backbone flexibility and binding properties of immobilized adhesive ligands [20]. These substrates were, furthermore, often limited by inaccurate tuning of the stiffness value and incapability of creating high stiffness gradients.

More recently, advances in micro- and nanofabrication methods are enabling researchers to develop sophisticated substrates and scaffolds. Micropillar arrays with uniform height fabricated by lithography techniques have been used to study the cell traction force, the cell focal adhesion development, the cell morphology and the cell migration in response to the substrate rigidity and [21–23]. However, the most of these studies have been based on micropillar substrates with uniform height, as illustrate in **Fig. 3.1a**. Micropillar arrays with stiffness gradient have also been proposed by changing the pillar sizes or creating a stepped change of pillar height [24, 25]. These approaches are also limited by either aspect ratio of the pillars or small area that cells can sense.

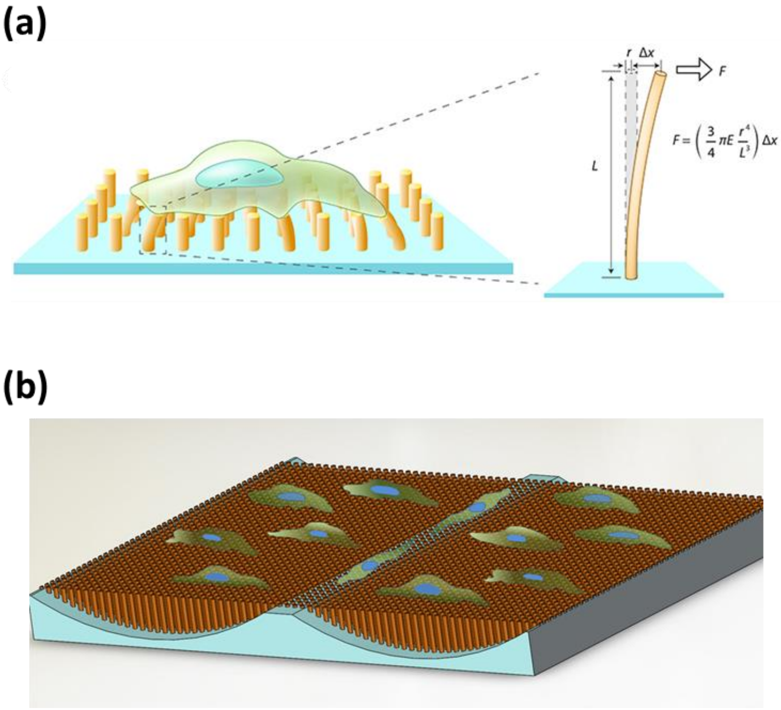

Figure 3.1 Schematic diagrams of (a) micropillar substrate with uniform height and (b) micropillar substrate with periodic height gradient for rigidity dependent cell distribution.

Herein, we present a simple yet straightforward method to fabricate dense pillar arrays with stiffness gradient by continuously varying the pillar height. We show that such pillar arrays are reliable to control cell migration (schematically shown in **Fig. 3.1b**). Variable gradient strengths could also be obtained by modulating the wavy period. Interestingly, different cells localization, elongation and orientation behaviors were observed on such pillar substrates.

3.2 Materials and methods

3.2.1 Materials

A polydimethylsiloxane (PDMS) kit (GE RTV 615) was purchased from Eleco (France). SU8 photoresists (SU8-3005 & SU8-3010) and SU8 developer were obtained from CTS (France). DMEM, fetal bovine serum (FBS), penicillin, streptomycin, L-glutamine and fungizone were purchased from Gibco (France). NIH 3T3 cells, fibronection from bovine plasma, trimethylsilanechloride (TMCS) and all other chemicals without mention were purchased from Sigma-Aldrich (France).

3.2.2 Fabrication of the substrate

PDMS micropillar arrays with height gradient were prepared by incorporating geometry-guided spin coating, photolithography and soft lithography, as schematically illustrated in **Fig. 3.2** [26]. Briefly, hole arrays with designed parameters were firstly patterned on a blank Cr mask pre-coated with AZ 1518 photoresist (Nanofilm, Wetlake Village, California) by means of direct laser writing (DLW) using a μPG101 system (Heidelberg Instruments, Germany). After development and chrome-etch, the mask was spin coated with first layer SU-8 resist (Microchem, USA). This resist layer was then exposed with another mask consisted of stripes, letters, cycles or other designed patterns. After development, the sample was spin-coated with the second SU-8 resist layer and UV exposed without mask. Note that the thickness of the second SU-8 layer should be thinner compared to that of the first SU-8 resist layer, which resulted in a wavy pattern due to the relative small thickness. Next, the sample was coated with a third SU-8 resist layer and UV exposed from back side, resulted in SU-8 micropillar arrays with height gradients and uniform top surfaces. The fabricated SU-8 micropillar arrays were then used as mold (master) for PDMS casting after exposed to TMCS vapor for 30 min. A pre-polymer solution of PDMS was prepared at a ratio of base polymer to cross-liker 10:1 (GE RTV 615 kit). After casting, the sample was placed in a vacuum chamber to remove air bubbles and then cured in an oven of 80 °C for 2 h. After peeling-off, the negative-tone replica of the master in PDMS was treated by parylene coating as introduce in chapter 2 before second PDMS casting. Finally, PDMS micropillar arrays with height gradients and uniform top surfaces were obtained.

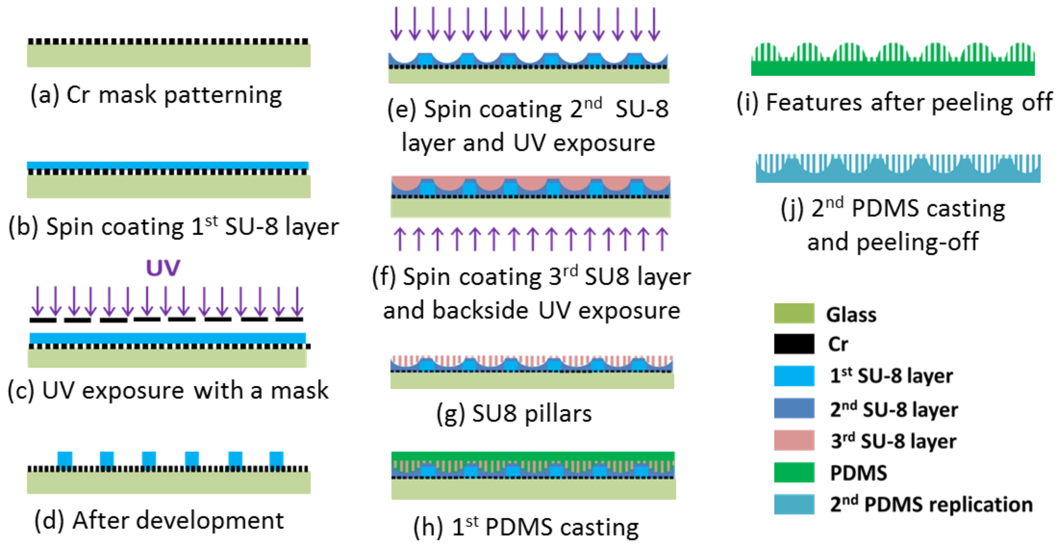

Figure 3.2 Schematic diagram of the fabrication process of PDMS pillar arrays with height gradient. Stripes were patterned on a pre-patterned Cr mask with dense anti-dot arrays. Then, a thin layer of photoresist was spin-coated, resulting in periodic wavy structures. Afterward, a new resist layer was spin-coated and backside UV exposed. The resulted micropillar arrays with height gradient were finally used as mold for replication. Positive-tone features of the mold could be obtained in PDMS by casting the replica of the mold.

3.2.3 Microfluidic device integration

The micropillars with height gradient were integrated into a microfluidic channel to demonstrate the stiffness gradient of pillars. Briefly, a thin layer of PDMS patterned with micropillar arrays was bonded to a glass slide after treated with plasma for 2 min. The top PDMS layer containing a channel with width 6 mm and height 20 μm was produced by soft lithography. First, a chromium mask with designed parameter was produced and then replicated into a photoresist layer (SU8-3010). After the development and evaporation of

TMCS, PDMS was poured on the SU8 mold and cured at 80 °C for 2 h. After peeling off, holes of the inlet and outlet were punched. The surfaces of upper and bottom PDMS layers were treated by plasma for 2 min, following by a thermal bonding at 80 °C for 10 min.

To demonstrate height-dependent stiffness of pillars, a method based on gas-liquid interfacial tension was introduced, as illustrated in **Fig. 3.6a**. Briefly, deionized water was firstly loaded into the device, and then the gas (air) was introduced into the channel, the flow was controlled using a multichannel pressure generator (Fluidic controller FC-PVL-Ⅱ, Mesobiosys). The binary interface was controlled at the first row of micropillar arrays by adapting the applied pressure. The displacements of micropillars in one gradient period were recorded.

3.2.4 Cell culture

Before culture, PDMS samples were sterilized with a UV light overnight and the uniform top surfaces of the pillars were functionalized by micro-contact printing. Firstly, a flat PDMS layer was immersed in a solution of 50 μg ml^{-1} fibronectin (Sigma-Aldrich, France) in distilled water for 1 h. After washing three times in distilled water and blowing with dry under nitrogen, the PDMS layer was placed in conformal contact with the PDMS micropillar substrate for 15 min. Before that, the sample was treated by oxygen plasma for 7 min to facilitate fibronectin to transfer from the flat PDMS layer to the top surface of the PDMS micropillar substrate. After microcontact printing, protein adsorption to all PDMS surfaces not coated with fibronectin was prevented by incubating in 0.2% Pluronics F127 in distilled water for 30 min at room temperature.

NIH 3T3 and Hela cells were cultured with DMEM (Gibco) supplemented with 10% fetal bovine serum and 1% penicillin and streptomycin, 1% L-glutamine and 1/10,000 fungizone (Sigma-Aldrich, France) separately. Cells were dissociated with 0.05% Trypsin EDTA solution at 37°C for 3 min. After centrifugation, cells were re-suspended in the medium. The fabricated PDMS pillar substrates were placed in 6-well plate and 4 ml cell suspension was dropped in each well, yielding a final concentration of about 20,000 cells ml^{-1}. Immediately after seeding, the entire system was moved to an incubator (37°C, 5% CO_2) for cell culture. Finally, medium was changed every other day.

3.2.5 Immunocytochemistry

The cells were fixed with 4% formaldehyde in PBS for 30 min and the sample was washed with PBS three times after the formaldehyde solution was completely removed. The cells were then permeabilized with PBS containing 0.5% Triton-X-100 (TX) for 10 min and washed again with PBS three times. The blocking proceeded in Antibody diluting solution containing 0.1% TX and 3% BSA for 30 min. After washed with PBS three times, skeleton and nuclear of the cells were stained with Phalloidin-FITC and DAPI (Sigma, Deisenhofen, Germany) respectively at the same time for 20 min. After washed with PBS three times, the cells could be observed under the fluorescence microscope.

3.2.6 Imaging and statistical analysis

Fluorescent microscopy was performed with an Axio Observe D1 inverted microscope (Zeiss), equipped with a high sensitive EM-CCD camera (PhotoMax 512B, Princeton Scientific). Time-lapse imaging was performed using confocal microscope (Zeiss LSM 710) maintained at 37 °C and CO_2 concentration 5%. The Image J software (open source image analysis software, Version 1.41) was introduced to analyze the fluorescence images of cells. To evaluate alignment, the cell nucleus was fitted with an ellipse. From the ellipses, the major and minor axes, and angle between the major axis and the reference direction (micropillars height gradient direction) were then computed. The alignment angles and anisotropy (ratio of the major axis to minor axes) were calculated accordingly. Three sets of experiments were conducted, the final data were calculated from the mean value of three sets.

3.3 Results and discussion

3.3.1 Fabrication of the micropillar substrate

This novel fabrication method is based on geometry-guided resist non-uniformly distribution. The critical step is to create the microwavy structures, as shown in **Fig. 3.3**, which is a challenge to obtain with standard planar photolithography techniques. Normally, in order to fabricate this kind of curve micro-structure, grey-scale lithography or 3D laser techniques are used. With our processes, we take advantage of the resist viscous property and geometry assistant to obtain this 3D pattern.

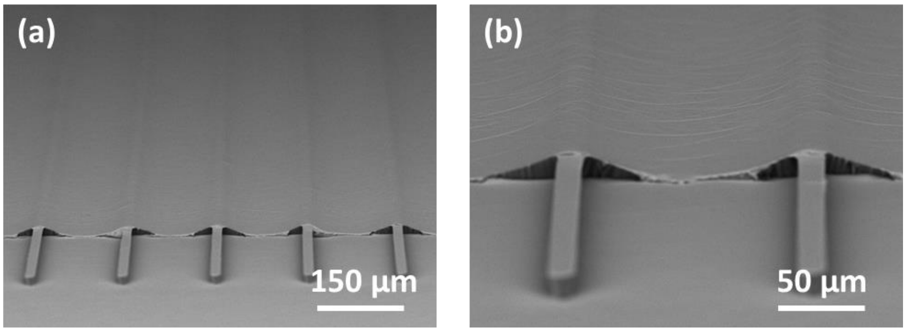

Figure 3.3 SEM images of the fabricated wavy resist pattern of 160 µm period.

Based on the wavy structures, a third layer of SU-8 resist was spin coated on in order to obtain pillar arrays with height gradient and uniform top surface. By adapting the designed mask, a variety of micropillar arrays with different parameters could be fabricated. Note that the parameters of the designed hole mask and the thickness of the three resist layers were crucial for organize the height range. **Fig. 3.4** shows PDMS pillars arrays with height gradient, uniform top surface but different feature size or organization. **Fig. 3.4a** illustrates the capability to form high aspect ratio (~ 6) PDMS pillar arrays with the three resist layers' thickness being 20 µm, 7 µm and 15 µm, respectively, resulting in height range from around 2.8 µm to 17.0 µm. **Fig. 3.4b** shows small spacing (3 µm) PDMS pillars with the three resist layers' thickness being 20 µm, 10 µm and 10 µm, respectively. In this case, we obtained the micropillar arrays with height ranging from 3.8 µm to 15.3 µm. As can be seen, the range of the PDMS pillar height variation could also be modulated by changing the curvature of the underneath wavy features. By changing the first resist pattern, we illustrated the capability to create height gradient of variable organizations, as shown in **Fig. 3.4c** and **d**.

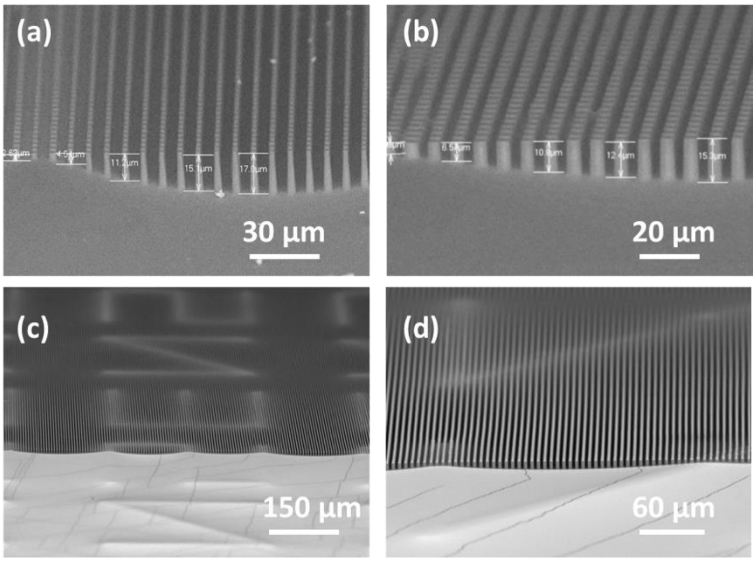

Figure 3.4 SEM images of PDMS pillar arrays of different diameters and variable heights but uniform top surface. (a) High aspect ratio PDMS pillar arrays (3 µm average diameter and 17 µm height). (b) Large diameter and small spacing PDMS pillar arrays (5 µm average diameter and 3 µm spacing). (c, d) PDMS pillars of variable heights form letters with uniform top surface.

In order to decouple the stiffness range of the cells microenvironment, micropillar arrays with diameter 2 µm and height range from around 3.5 µm to 10.5 µm were used. The substrates were designed as follows: the holes mask with diameter 2 µm and period 5.5 µm were firstly developed. Then the mask was spin coated with 15 µm thick SU-8 3010 resist at a speed of 2000 rpm for 30 s. This resist layer was then exposed with another mask consisted of 10 µm linewidth and 160 µm or 310 µm pitch-size absorber stripes. After development, the sample was spin-coated with 7 µm thick SU-8 3005 at a speed of 2000 rpm and UV exposed without mask. Next, the sample was coated with 7 µm thick SU-8 3005 at 2000 rpm for 30 s and UV exposed from back side, resulting in SU-8 micropillar arrays which then were used as mold for soft lithography to obtain PDMS pillars.

Fig. 3.5a, **b** and **c**, **d** show scanning electron microscopy (SEM) images of micropillar arrays with gradient period of 310 µm (P310) and 160 µm (P160), respectively, with the underneath periodic wavy structures also been observed. The SU-8 3005 resist spin-coated on the substrate with pre-patterned stripes was aside each of the stripes, resulting in a concave wave pattern due to spinning and relatively low viscosity of SU-8 3005 resist. For the same reason, a flat surface can be obtained after spinning coating another SU-8 3005 resist on such a non-plan substrate. After backside UV exposure and development, micropillars with periodic height gradient could be worked out. **Fig. 3.5e** displays the variation of the pillar height as a function of position of a sample P160 (P310), ranging from 3.79 ± 0.13 (3.52 ± 0.11) µm to 10.13 ± 0.12 (10.25 ± 0.05) µm, suggesting that there is no significant difference in the range of the pillar height variation for different periods.

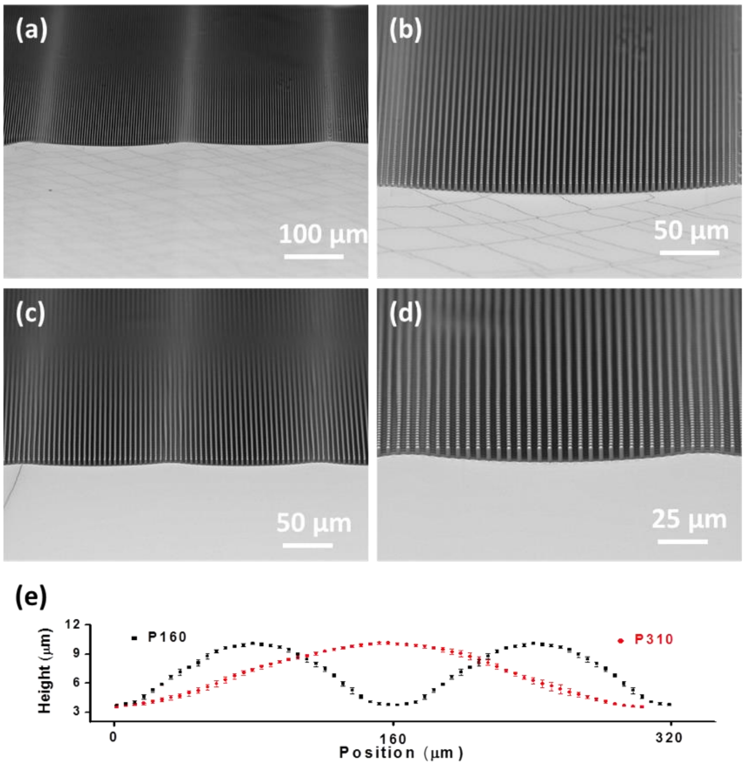

Figure 3.5 (a,b) and (c,d) SEM images of PDMS micropillars of height gradient with period 310 µm (P3100) and 160 µm (P160), respectively. (e) Variation of the pillar height as a function of pillar position for samples P160 and P310.

3.3.2 Rigidity of the micropillar substrates

To demonstrate the stiffness variety of the micropillars, a method based on gas-liquid interface tension in microfluidic channel was illustrated, as schemed in **Fig. 3.6a**. **Fig. 3.6b** and **c** shows images of micropillars before and after displacement in one period (160 µm), it could be seen that the interface was arcuate because of the different displacements of the pillars. It could qualitatively prove that the micropillar arrays with gradient height resulted in rigidity variation, assuming that the surface tension force was uniform. **Fig. 3.6 d** and **e** were corresponding to the situation of micropillar substrates with period 310 µm. From the statistic of the displacements (**Fig. 3.7 a** and **b** for period 160 µm and 310 µm, respectively), it could be seen that the displacements in substrates with period 160 µm 310 µm were almost in the same range, from 0.03 µm to 1.73 µm, but the variation trends were different.

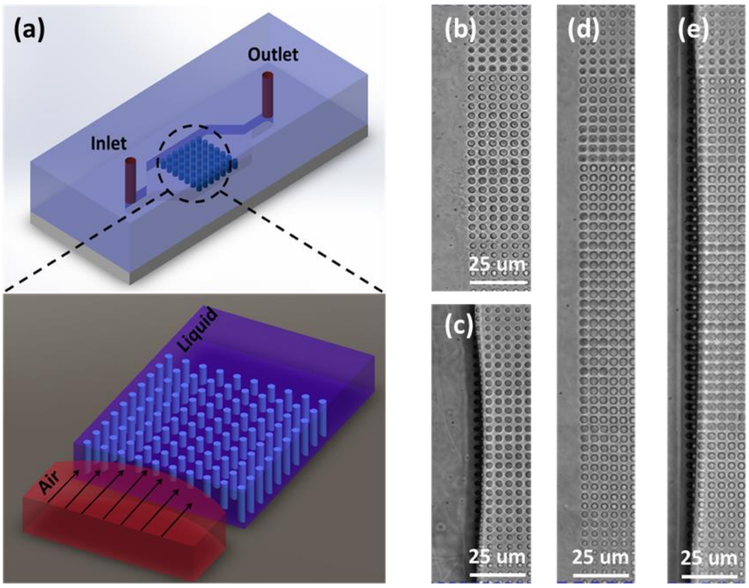

Figure 3.6 (a) Illustration of microfluidic device for micopillars stiffness measurement. Gas-liquid interface was introduced at the first row of pillar arrays. (b, d) and (c, e) phase contrast images of one period (160 µm, 310 µm) of gradient pillars in channel before and after deformation.

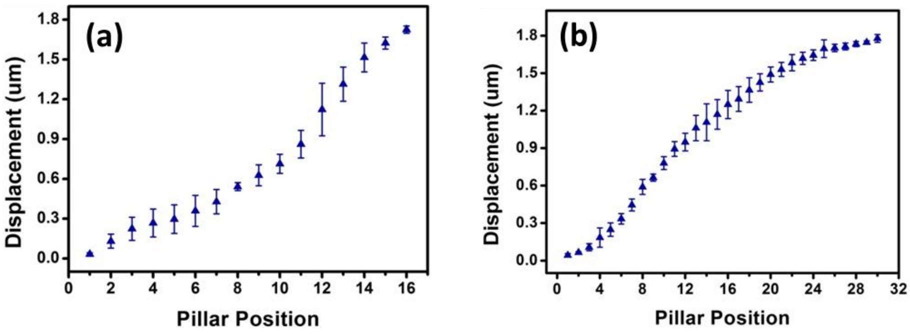

Figure 3.7 The displacement of pillars with period (a) 160 µm and (b) 310 µm in microfluidic channel.

To assess the effective stiffness gradient quantitatively, the spring constant were firstly calculated using the Euler-Bernoulli beam theory [27],

$$k = \frac{3}{4}\pi E \frac{r^4}{H^3} \tag{1}$$

Where *E* is the Young's modulus of the bulk PDMS, *r* and *H* are the radius and height of the pillar, respectively. Assuming a pillar diameter of 2 μm and a Young's module of bulk PDMS of 2 MPa, we obtained a sprint constant of 77.87 ± 7.86 and 4.07 ± 0.11 nN/μm for a PDMS pillar with height of 3.80 ± 0.12 and 10.13 ± 0.14 μm, respectively (**Fig. 3.8**).

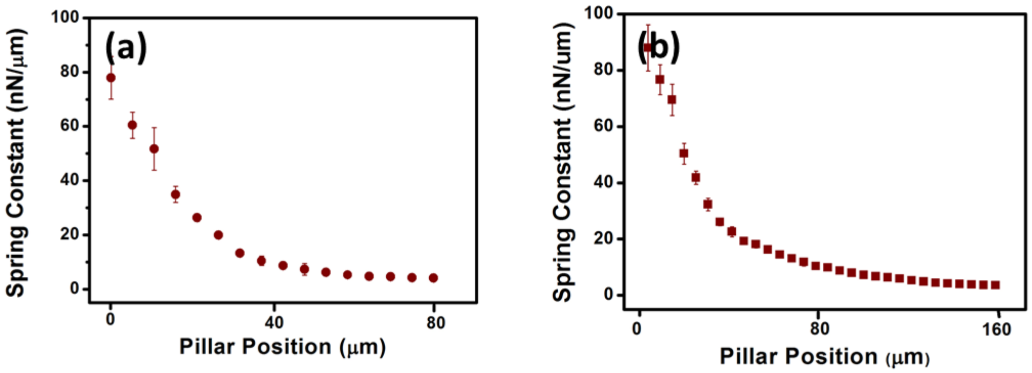

Figure 3.8 The deduced spring constant of micropillars in sample (a) P160 and (b) P310 from half period.

In the limit of small deflection, considering our dense pillar arrays as continuous elastic substrates, the effective Young's modulus of the pillar for cellular response is given by [28]

$$Ee = \frac{9k}{4\pi a} \tag{2}$$

Where *a* is the characteristic length representing the pillar radius or the mean size of focal adhesion for a continuous substrate. Accordingly, we obtained variation of the effective Young's modulus of PDMS pillar samples P160 and P310 (**Fig. 3.9a and b**), suggesting a stiffness change of almost 30 times from the softer (2.4 KPa) to the harder

(60.0 KPa) areas due simply to the pillar height changes in half period. Note that the ranging wide was almost kept constant with these two types of substrates, whereas resulting in different gradient strengths.

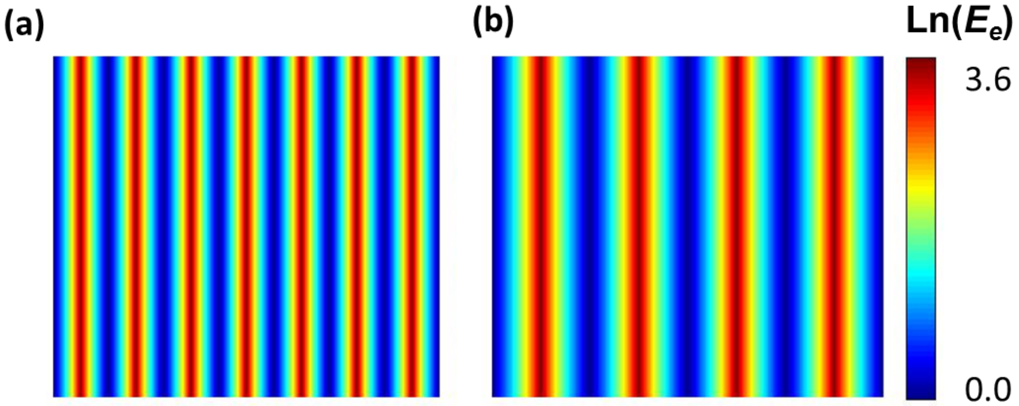

Figure 3.9 Calculated effective Young's modules of samples (a) P160 and (b) P310.

3.3.3 Cell motility and cell migration

NIH 3T3 cells are commonly used to study interaction of fibroblasts with culture substrates [15, 29]. They have been chosen also because of their comparable Young's modulus of our PDMS pillar substrates [30]. Indeed, NIH 3T3 cells have different behaviors on different samples and in different area of the samples. **Fig. 3.10** shows snapshots of time-lapse image series of the cells on pillars of sample P160. After attachment, the cells began to spread and sense the surrounding environment. For those firstly attached on the soft area, the cells trended to migrate to the stiff area. For those already located on the stiff area, they maintained in the same area. Afterward, they spread, showing different migration behavior and different morphology in different area of the pillar arrays. After 18 h culture, the majority of the cells migrated to short pillar area and elongated along the stiff direction.

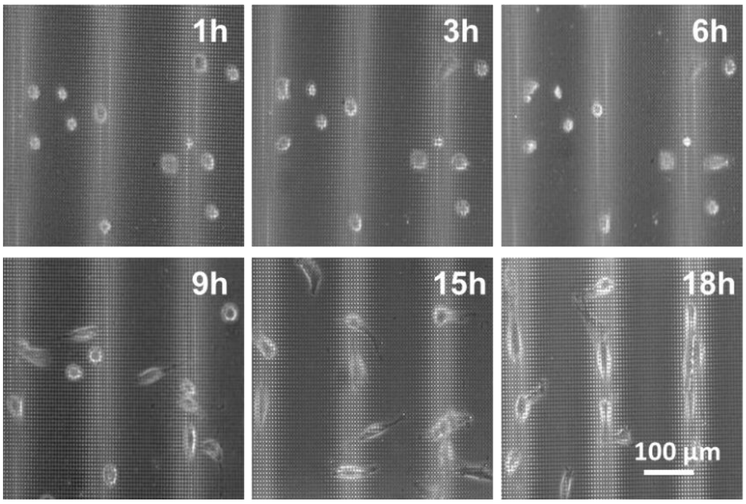

Figure 3.10 Snapshots of time-lapse images of NIH 3T3 cells showing migratory behaviors on PDMS pillar arrays with height gradient of sample P160.

Fig. 3.11a and **b** compare the distribution and the morphology of the cells on P160 and P310 samples after incubation for 24 h. Clearly, both are significantly different. On sample P160, most of the cells were found in the stiff area, whereas on sample P310, cells were more homogenously distributed but highly elongated along the direction of stiffness gradient. Hela cells were also tested on sample P160, showing neither elongation nor migration caused by stiffness gradient of PDMS pillars (**Fig. 3.11c**), illustrating that fibroblast cells are preferable to migrate with the mechanical stimulation, which is consistent with other group's reports [15].

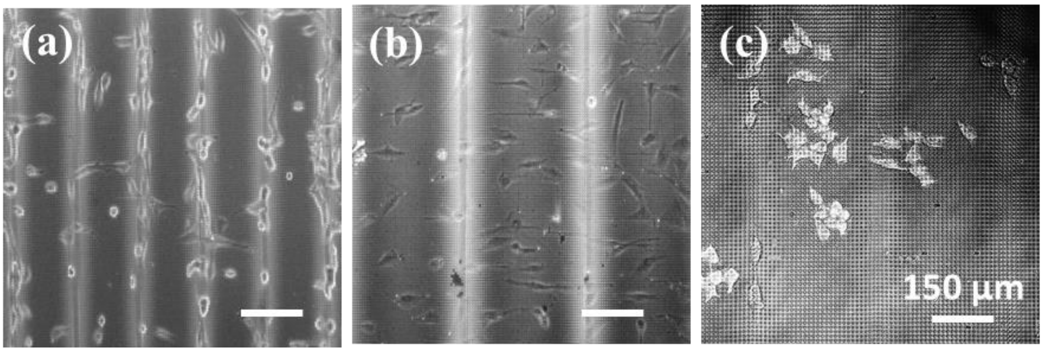

Figure 3.11 (a, b) Phase contrast images showing cell elongation and localization on PDMS pillar arrays of samples P160 and P310 after 24 h incubation. (c) Phase contrast image of Hela cells after 1 day incubation on sample P160, showing neither elongation nor migration caused by stiffness gradient of PDMS pillars.

The travelling distance of the cells on two types of substrates were plotted in **Fig. 3.12a** and **b**, showing an average travelling length of 59.33 ± 2.30 µm (21.45 ± 1.53 µm) along the stiffness gradient and 10.29 ± 3.74 µm (11.34 ± 3.21) in the perpendicular direction on sample P160 (P310), respectively. Accordingly, we obtained an average traveling speed of 3.23 ± 0.26 µm h^{-1} (1.38 ± 0.19 µm h^{-1}) along the stiffness gradient for sample P160 (P310), while no significant difference in travelling speed was observed in the perpendicular direction (**Fig. 3.12c**). These results suggest that not only the stiffness but also the stiffness gradient affect the behavior of NIH 3T3 cells. Apparently, a high stiff gradient causes a fast cell migration but a low stiffness gradient enables more effectively cell migration.

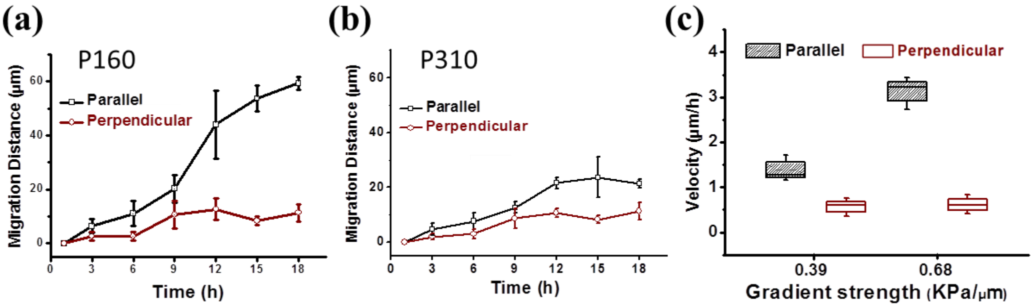

Figure 3.12 (a, b) NIH 3T3 cells migration distance parallel and perpendicular to the stiffness gradient of samples P160 and P310. n=34. (c) Cells migration velocity on PDMS pillar arrays with different gradient strengths.

3.3.4 Cell morphology and cell proliferation

Note also that the NIT 3T3 cells on stiff areas had relatively large spreading area comparing to that on soft area which had in general a rounded phenotype with prominent microvilli (**Fig. 3.13**), in agreement with previous studies [31, 32].

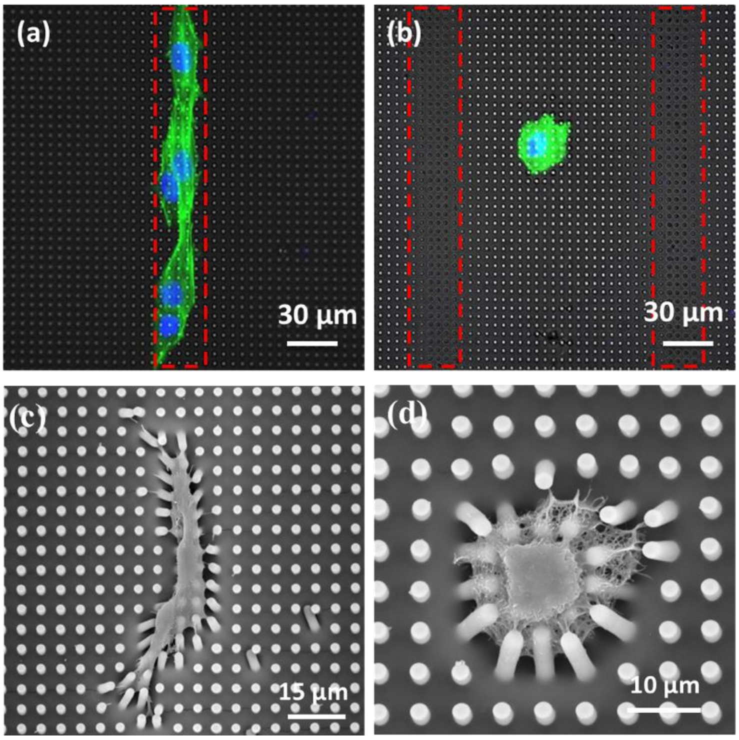

Figure 3.13 (a, b) Immunofluorescence images of NIH 3T3 cells after 3 h incubation on stiff area and soft area. Red dashed box: areas of greater stiffness or pillars with smaller heights. Cell nuclei were stained by DAPI (blue). Actin cytoskeletal networks are in green (Alexa Fluor 488 phalloidin). (c, d) SEM images of single NIH 3T3 cell after 3 h incubation on hard and soft areas of sample P160, showing different behaviors of cell-pillar interaction.

Fig. 3.14 shows immunofluorescence images of NIH 3T3 cells on flat PDMS, P160 and P310 PDMS pillar samples after incubation for 1 and 4 days. Clearly, cells were randomly distributed on the flat PDMS sample without defined orientation. On sample P160, most of the cells were elongated perpendicular to the stiffness gradient and preferentially located in the stiff area at day 1 but more cells were elongated parallel to the direction of the stiffness gradient after incubation for 4 days. On sample P310, cells were elongated parallel to the stiffness gradient at both day 1 and day 4, indicating that the proliferation did not affect the direction 0of cells elongation on P310.

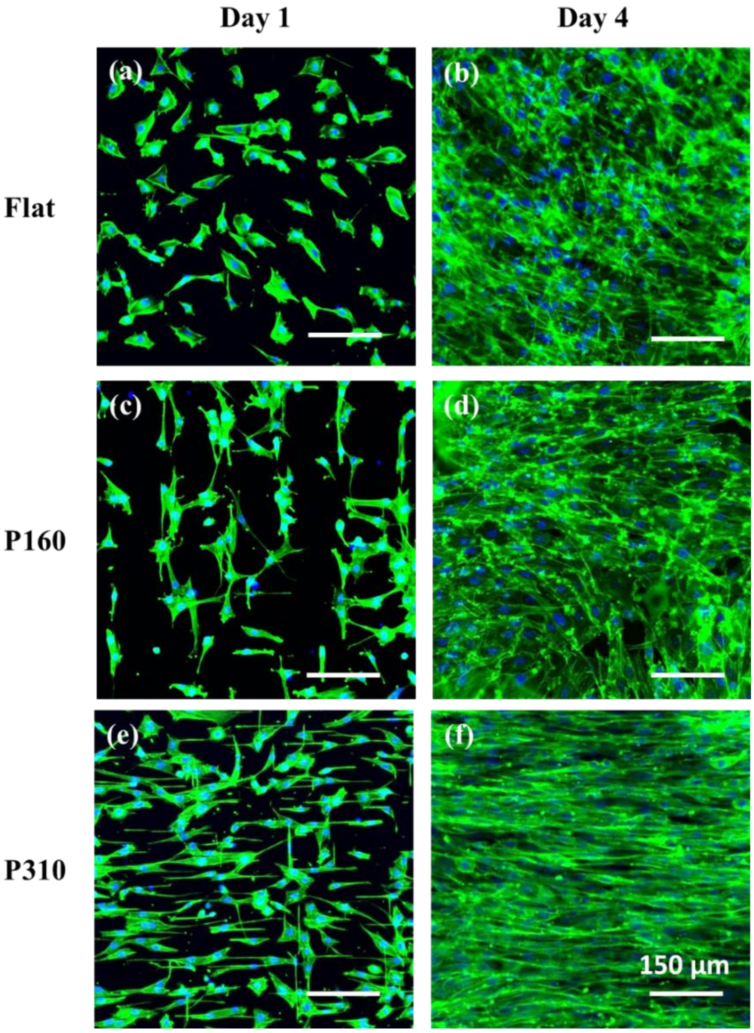

Figure 3.14 Immunofluorescence images of cells after 1 day (a, c, e) and 4 days (b, d, f) incubation on flat, P160 and P310 PDMS samples. Cell nuclei were stained by DAPI (blue) and actin cytoskeletal networks in green (Alexa Fluor 488 phalloidin).

Fig. 3.15 shows the measured aligned angles of cells cultured on P160 and P310 substrates at day 1 and day 4, which more clearly demonstrated the effect of the gradient strength on cell morphology and self-patterning. Apparently, cells showed no specific orientation on flat PDMS at day 1 or day 4 with the frequency evenly dispersed. However, cells on P160 substrate showed highly orientation at day 1, with almost 35% cells aligned (alignment angle 0°-10°) on the direction of perpendicular to the stiffness gradient. At day 4, the cell alignment behavior was not that clear, more cells elongated along the stiffness gradient, which may due to the mechanical induce for the proliferation cells. On

P310 substrate, around 50% cells elongated and orientated at an average angle of 0°-20° with respect to stiffness gradient direction no matter at day 1 or 4.

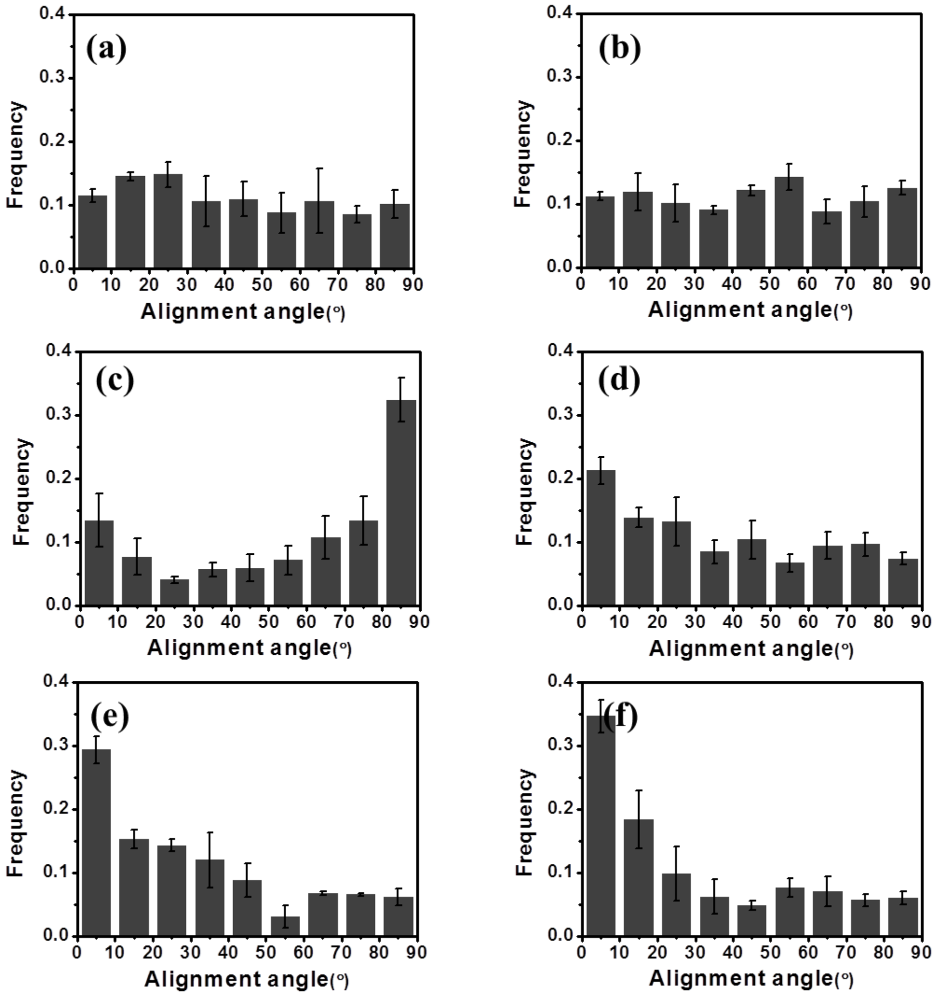

Figure 3.15 Distribution of alignment of NIH 3T3 cells after 1 day (a, c, e) and 4 days (b, d, f) incubation on flat (a, b), P160 (c, d) and P310 (e, f) samples.

The statistical data of the analyses are reported in **Fig. 3.16**. Here, the shape anisotropy is defined as the ratio of the length to the width of the cells and their nuclei, and only images of the cells after 1 day incubation were used for size and anisotropy analyses because of easy image processing. Interestingly, cells cultured on flat PDMS have large spreading and nucleus areas because of large stiffness (~2 MPa) comparing to the PDMS pillar substrates. The shape anisotropy of the cells on sample P310 is significantly larger than that on sample P160 but the nucleus shape anisotropy on both samples is larger than that on plat PDMS.

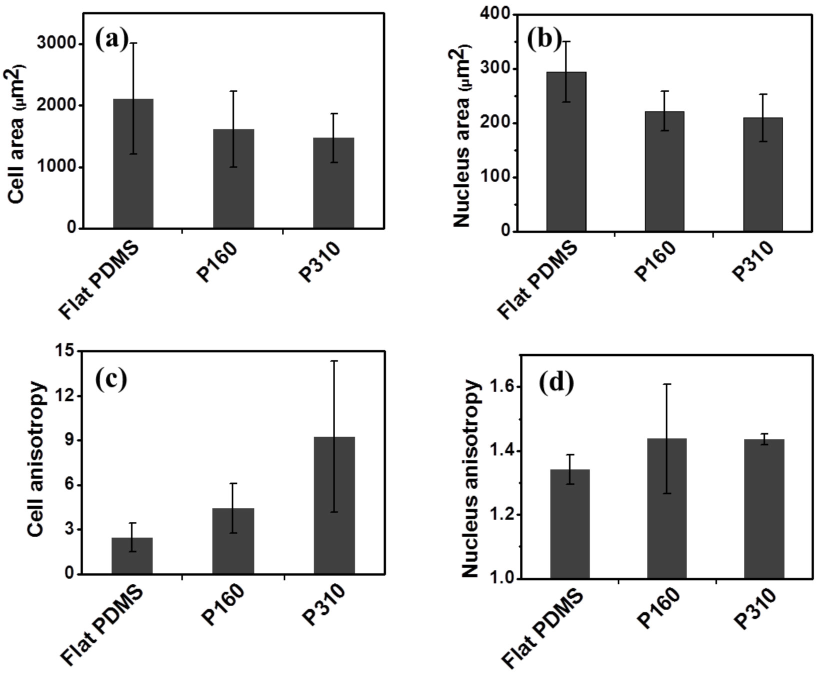

Figure 3.16 (a, b) Cell and nucleus area on the three types of substrates after 1 day incubation. (c, d) Substrate stiffness gradient induced shape anisotropy of cytoskeleton and nucleus (ratio of the length to the width for cells and their nuclei).

Fig. 3.17 clearly shows cells extended their cytoplasm along the parallel direction of stiffness gradient and displayed extensive elongation with a needle-like morphology on sample P310 (b) after incubated 1 day compared to that on sample P160 (a). These results indicated that the presented micropillar platforms provided an innovative platform to induce cell and nucleus shape anisotropy.

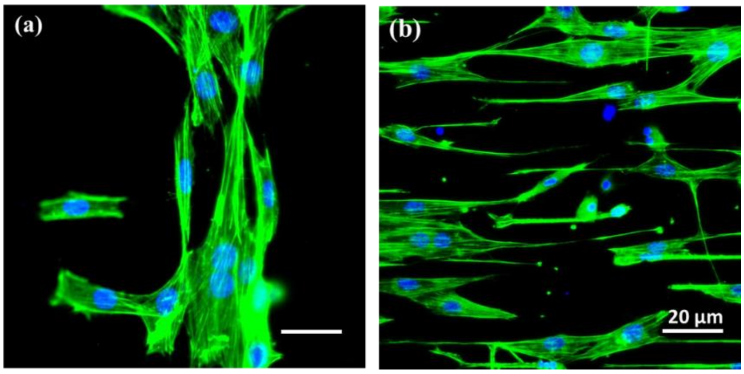

Figure 3.17 Immunofluorescence images of high magnitude of NIH 3T3 cells after 1 day incubation on samples P160 (a) and sample P310 (b).

In general, cells stress fibers sense mechanical tension through integrin complexes and leads to earliest focal adhesions formation, which then undergo stiffness dependent conformational changes to bind F-actin and require RhoA-mediated contractile force generation [33, 34]. Normally, the cytoplasmic could keep coherence when the traction forces located on both sides of cells meet symmetrically balanced. With the variation of the underlying matrix stiffness, the traction forces misbalance induces a polarization of the actin fibers that orient along the direction of stiffer part [35, 36]. Indeed, studies of cells on stepped micropillar arrays have already demonstrated that traction forces polarized during mechanosensing, and thus cells migrated across the soft-stiff boundary [22]. Our results with pillar samples suggest that the mechano-tranduction of the cells depends on the stiffness gradient of the substrate. On sample P160 with a large stiffness gradient (0.68 KPa/μm), the difference in contracile force between two extremes of the cell in the direction parellel to the stiffness gradient could be large enough to guide cell migration. Once entering in the stiff area, cells explore rigid part of the pillar arrays, giving rise to elongation perpendicular to the stiffness gradient. On sample P310 with a small stiffness gradient (0.39 KPa/μm), cells explore longer distance along in the direction parallel to the stiffness gradient but the difference in contracile force between two extremes of the cell might not be sufficient to stimulate the migration so that the motility of the cells is less remarkable, and the cell morphology remained mostly elongated.

3.3.5 Complex stiffness map

Other types of wavy structures could also be fabricated so that different stiffness gradients of pillar substrates can be obtained. **Fig. 3.18** shows a ripple-like design of PDMS pillar substrate using the same pillar parameters and 160 μm wavy-period (**Fig. 3.18a**, **b**), the calculated effective Young's module (**Fig. 3.18c**). It demonstrates that ability of this novel method to create complex stiffness map using the elastomer micropillar arrays, which provide a versatile tool to study the mechanotransduction in cells-substrate interaction.

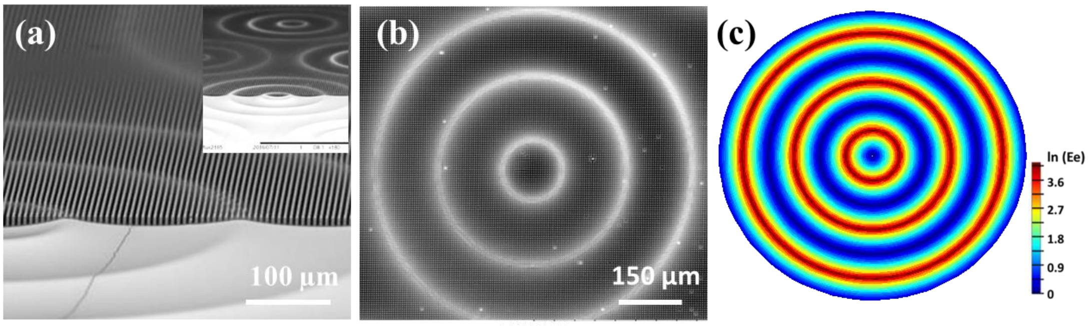

Figure 3.18 (a, b) SEM images of PDMS pillar arrays with ripple-like stiffness gradient (sample R160); (c) Calculated effective Young's modules of PDMS pillar arrays with ripple-like stiffness gradient

Fig. 3.19 shows immunofluorescence images of NIH 3T3 cells cultured on the pillar substrate after incubation for 1 day (d), 3 days (e) and 4 days (f). As expected, cells were mainly localized in the stiffer areas and they also elongated along the stiffness defined geometry during first 3 days culture (**Fig. 3.19a** and **b**). With cells proliferation, the cells orientation was guided with the micropillars (**Fig. 3.19c**). These results proved again the effect of stiffness gradient on cell migration.

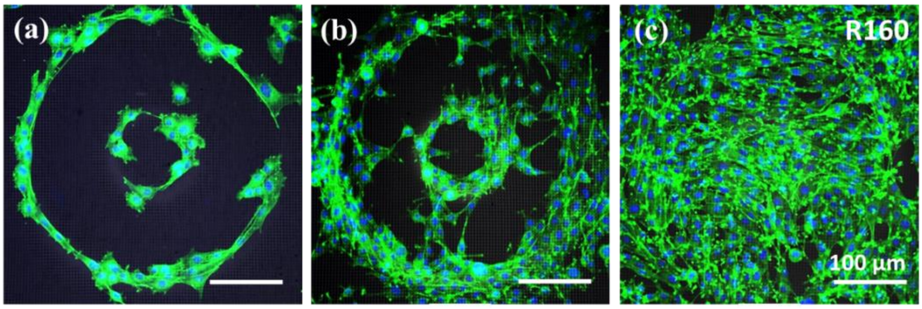

Figure 3.19 (a-c) Immunofluorescence images of NIH 3T3 cells after 1 day, 3 days and 4 days incubation on sample R160. Cell nuclei were stained by DAPI (blue) and actin cytoskeletal networks in green (Alexa Fluor 488 phalloidin).

3.4 Conclusion

We have proposed a simple method to fabricate elastomer pillar arrays of 2 µm diameter, 5.5 µm pitch size and variable height with uniform top surface. Such patterned surfaces could be used as a new type of substrates for stiffness gradient dependent cell culture studies. NIH 3T3 cells were used to demonstrate elongation and directed migration along the stiffness gradient. Interestingly, cells displayed different behaviors on the pillar substrates of different organization of the stiffness gradient. Therefore, this developed fabrication method enables to generate micropillar substrate with complex stiffness map regarding the applications, thereby providing a way to mechanically control the cell behaviors on a patterned substrate.

References

[1] E.D. Hay, Extracellular matrix., J. Cell Biol. 91 (1981) 205s–223s.

[2] R.O. Hynes, The extracellular matrix: not just pretty fibrils., Science. 326 (2009) 1216–9.

[3] Y. Sun, C.S. Chen, J. Fu, Forcing stem cells to behave: a biophysical perspective of the cellular microenvironment., Annu. Rev. Biophys. 41 (2012) 519–42.

[4] M.A. Wozniak, C.S. Chen, Mechanotransduction in development: a growing role for contractility, Nat. Rev. Mol. Cell Biol. 10 (2009) 34–43.

[5] A.J. Engler, S. Sen, H.L. Sweeney, D.E. Discher, Matrix Elasticity Directs Stem Cell Lineage Specification, Cell. 126 (2006) 677–689.

[6] Y. Bao, Y. Huang, M.L. Lam, T. Xu, N. Zhu, Z. Guo, X. Cui, R.H.W. Lam, T.-H. Chen, Substrate Stiffness Regulates the Development of Left?Right Asymmetry in Cell Orientation, ACS Appl. Mater. Interfaces. 8 (2016) 17976–17986.

[7] D.E. Ingber, TENSEGRITY: THE ARCHITECTURAL BASIS OF CELLULAR MECHANOTRANSDUCTION, Annu. Rev. Physiol. 59 (1997) 575–599.

[8] A.B. Castillo, C.R. Jacobs, Mesenchymal Stem Cell Mechanobiology, Curr. Osteoporos. Rep. 8 (2010) 98–104.

[9] B. Trappmann, J.E. Gautrot, J.T. Connelly, D.G.T. Strange, Y. Li, M.L. Oyen, M.A. Cohen Stuart, H. Boehm, B. Li, V. Vogel, J.P. Spatz, F.M. Watt, W.T.S. Huck, Extracellular-matrix tethering regulates stem-cell fate, Nat. Mater. 11 (2012) 642–649.

[10] A. Banerjee, M. Arha, S. Choudhary, R.S. Ashton, S.R. Bhatia, D. V. Schaffer, R.S. Kane, The influence of hydrogel modulus on the proliferation and differentiation of encapsulated neural stem cells, Biomaterials. 30 (2009) 4695–4699.

[11] T. Tzvetkova-Chevolleau, A. Stéphanou, D. Fuard, J. Ohayon, P. Schiavone, P. Tracqui, The motility of normal and cancer cells in response to the combined influence of the substrate rigidity and anisotropic microstructure., Biomaterials. 29 (2008) 1541–51.

[12] N.D. Leipzig, M.S. Shoichet, The effect of substrate stiffness on adult neural stem cell behavior, Biomaterials. 30 (2009) 6867–6878.

[13] I. Levental, P.C. Georges, P.A. Janmey, P.A. Janmey, V.M. Laurent, B. Louis, D. Isabey, E. Planus, B. Senger, C. Picart, Soft biological materials and their impact on cell function, Soft Matter. 3 (2007) 299–306.

[14] A. Seidi, M. Ramalingam, I. Elloumi-Hannachi, S. Ostrovidov, A. Khademhosseini, Gradient biomaterials for soft-to-hard interface tissue engineering, Acta Biomater. 7 (2011) 1441–1451.

[15] B.C. Isenberg, P.A. DiMilla, M. Walker, S. Kim, J.Y. Wong, Vascular Smooth Muscle Cell Durotaxis Depends on Substrate Stiffness Gradient Strength, Biophys. J. 97 (2009) 1313–1322.

[16] J.S. Martinez, A.M. Lehaf, J.B. Schlenoff, T.C.S. Keller, III, Cell durotaxis on polyelectrolyte multilayers with photogenerated gradients of modulus, Biomacromolecules. 14 (2013) 1311–20.

[17] H.-D. Kim, S.R. Peyton, Bio-inspired materials for parsing matrix physicochemical control of cell migration: a review, Integr. Biol. (Camb). 4 (2012) 37–52.

[18] C.M. Lo, H.B. Wang, M. Dembo, Y.L. Wang, Cell movement is guided by the rigidity of the substrate, Biophys. J. 79 (2000) 144–52..

[19] Y.K. Cheung, E.U. Azeloglu, D.A. Shiovitz, K.D. Costa, D. Seliktar, S.K. Sia, Microscale Control of Stiffness in a Cell-Adhesive Substrate Using Microfluidics-Based Lithography, 48 (2009) 7188-92.

[20] B.G. Keselowsky, D.M. Collard, A.J. García, Integrin binding specificity regulates biomaterial surface chemistry effects on cell differentiation., Proc. Natl. Acad. Sci. U. S. A. 102 (2005) 5953–7.

[21] J. Li, F. Zhang, L. Yu, N. Fujimoto, M. Yoshioka, X. Li, J. Shi, H. Kotera, L. Liu, Y. Chen, J. Inzunza, A.-S. Nilsson, D. Baker, R. Kuiper, Y. Sun, E. Blennow, M. Nordenskjöld, K.-H. Grinnemo, J. Kere, C. Betsholtz, O. Hovatta, K. Tryggvason, Culture substrates made of elastomeric micro-tripod arrays for long-term expansion of human pluripotent stem cells, J. Mater. Chem. B. 5 (2017) 236–244.

[22] L. Trichet, J. Le Digabel, R.J. Hawkins, S.R.K. Vedula, M. Gupta, C. Ribrault, P. Hersen, R. Voituriez, B. Ladoux, Evidence of a large-scale mechanosensing mechanism for cellular adaptation to substrate stiffness., Proc. Natl. Acad. Sci. U. S. A. 109 (2012) 6933–8.

[23] J. Wei, J. Shi, B. Wang, Y. Tang, X. Tu, E. Roy, B. Ladoux, Y. Chen, Fabrication of adjacent micropillar arrays with different heights for cell studies, Microelectron. Eng. 158 (2016) 22–25.

[24] R.D. Sochol, A.T. Higa, R.R.R. Janairo, S. Li, L. Lin, A. Levchenko, C.S. Chen, Unidirectional mechanical cellular stimuli via micropost array gradients, Soft Matter. 7 (2011) 4606.

[25] S. Lee, J. Hong, J. Lee, Cell motility regulation on a stepped micro pillar array device (SMPAD) with a discrete stiffness gradient, Soft Matter. 12 (2016) 2325–2333.

[26] B. Wang, J. Shi, J. Wei, L. Wang, X. Tu, Y. Tang, Y. Chen, Fabrication of elastomer pillar arrays with height gradient for cell culture studies, Microelectron. Eng. 175 (2017) 50–55.

[27] A. Saez, A. Buguin, P. Silberzan, B. Ladoux, Is the mechanical activity of epithelial cells controlled by deformations or forces?, Biophys. J. 89 (2005) L52-4.

[28] A. Saez, E. Anon, M. Ghibaudo, O. du Roure, J.-M. Di Meglio, P. Hersen, P. Silberzan, A. Buguin, B. Ladoux, Traction forces exerted by epithelial cell sheets, J. Phys. Condens. Matter. 22 (2010) 194119.

[29] P. Roca-Cusachs, R. Sunyer, X. Trepat, Mechanical guidance of cell migration: lessons from chemotaxis, Curr. Opin. Cell Biol. 25 (2013) 543–549.

[30] C. Rotsch, K. Jacobson, M. Radmacher, Dimensional and mechanical dynamics of active and stable edges in motile fibroblasts investigated by using atomic force microscopy., Proc. Natl. Acad. Sci. U. S. A. 96 (1999) 921–6.

[31] M. Gupta, B.R. Sarangi, J. Deschamps, Y. Nematbakhsh, A. Callan-Jones, F. Margadant, R.-M. Mège, C.T. Lim, R. Voituriez, B. Ladoux, Adaptive rheology and ordering of cell cytoskeleton govern matrix rigidity sensing, Nat. Commun. 6 (2015) 7525.

[32] L. Yang, Y. Yangben, M. Chiang, Cell Morphology Linked to Substrate Stiffness - A Possible Solution to Determine the Cell Modulus, Biophys. J. 100 (2011) 157a.

[33] B. Geiger, J.P. Spatz, A.D. Bershadsky, Environmental sensing through focal adhesions, Nat. Rev. Mol. Cell Biol. 10 (2009) 21–33.

[34] M. Chrzanowska-Wodnicka, K. Burridge, Rho-stimulated contractility drives the formation of stress fibers and focal adhesions., J. Cell Biol. 133 (1996).

[35] Y. Cai, O. Rossier, N.C. Gauthier, N. Biais, M.-A. Fardin, X. Zhang, L.W. Miller, B. Ladoux, V.W. Cornish, M.P. Sheetz, Cytoskeletal coherence requires myosin-IIA contractility, J. Cell Sci. 123 (2010).

[36] H. Delanoë-Ayari, R. Al Kurdi, M. Vallade, D. Gulino-Debrac, D. Riveline, Membrane and acto-myosin tension promote clustering of adhesion proteins., Proc. Natl. Acad. Sci. U. S. A. 101 (2004) 2229–34.

Chapter 4

Narrowly Spaced Monolayer Nanofibers for Three-dimensional Cell Handling

In this chapter, we present the development of narrowly spaced monolayer nanofibers for three-dimensional cell handling. Through holes were firstly fabricated on a thin layer of hydrogel. Then, monolayer nanofibers were electrospun on both sides of the thin layer-patterned layer. The fabricated device was used as scaffolds to culture fibroblasts, showing cell adhesion and infiltration into the free space between the two monolayer nanofibers. Such a culture device is mechanically robust and structurally compatible to a variety of cell based assay devices.

4.1 Introduction and motivation

Culturing cells in vitro while maintain in vivo characteristics holds great potential not only for cell function but also in tissue engineering and regenerative medicine [1, 2]. Conventional cell culture provides unnatural conditions, such as two-dimensional (2D) space, poor nutrient supporting, which leads to the development of physiologically compromised cells. While in vivo cells grow in three-dimensional environment surrounded by ECM and other cells bathed in tissue fluid. Lack of de-novo ECM milieu, which is crucial for generate physical and chemical signals except providing structural support, is the major hurdle in normal cell growth in vitro [3, 4]. This calls for the development of ECM-mimicking 3D scaffold, which can be integrated with relevant ECM cues to offer cell interactive versatility for different medical and non-medical applications [5–7]. Moreover, in order to facilitate maximal cell seeding efficiency and subsequent cell expansion, the scaffold should have high and interconnected porosity and a high surface area per volume [8–10]. It should be mechanically robust and ideally incorporate signals to guide cellular migration and activity [11].

Although considered as a 3D scaffold for cell culture and tissue engineering, electrospun fibers usually assembly tightly in packed layers or sheet-like formations with a superficially porous network, resulted in limited infiltration and confinement of cells [12–14]. Thus, it is imperative to develop an innovative strategy capable of fabricating an electrospun scaffold with a stable three-dimensional structure, while exhibiting nanofibrous morphologies and deep, interconnected pores [15]. Among various electrospinning methods for fabricating scaffolds with high porosity and large-diameter pores, a common approach for producing electrospun mats with large pores is by the selective removal of sacrificial materials [16–19]. Although the scaffolds of these studies show increased cell infiltration compared to those processed by conventional electrospinning, they are also characterized by mechanical instabilities, including distortion, shrinkage and delamination or pore collapse, because the increase of the pore size and porosity is detrimental to the mechanical properties. Thus, fabrication of scaffolds with large pores, high porosity and adequate mechanical strength is a challenging task of high importance in tissue engineering and regeneration [20].

Our approach to tackle these issues is to combine approaches that allow fabricating consistently a new type of three-dimensional cell culture supports with biocompatible hydrogel and gelatin fibers. In this method, a hydrogel thin layer with honeycomb through holes was firstly fabricated by photolithography methods, which acts as collector and mechanical support for the nanofibers deposition [21]. Moreover, with the hydrogel layer, the fabricated fibrous scaffold is easy handling [22]. Then, gelatin nanofibers were electrospun on both sides of the micro-patterned layer, resulting in spaced nanofiber layers suitable for 3D cell handling and migration. Gelatin, derived from collagen which is an important protein for cell proliferation and is found in the ECM, is one kind of rich matrix in arginine-glycine-aspartate (RGD) peptide sequences that are required for integrin-mediated cell adhesion and growth via activation of cellular signaling pathways [23–25]. With the three-dimensional fibrous structure and the natural biomaterial, the scaffold could better recapitulate the function of microenvironment in vivo. Such a culture support is mechanically robust and porous for cell infiltration allowing down-regulation of cell-matrix tractions, promoting 3D permeability and cells proliferation.

4.2 Materials and methods

4.2.1 Materials

Gelatin (from porcine skin), poly (ethylene glycol) diacrylate (PEGDA, Mw=250), acetic acid, ethyl acetate and photo-initiator Irgacure 2959 (Sigma, France) were purchased from Sigma-Aldrich (France). Polydimethylsiloxane (PDMS) was purchased from Eleco-EFD Co. (France). DMEM, fetal bovine serum (FBS), penicillin, streptomycin, L-glutamine and fungizone were purchased from Gibco.

4.2.2 Fabrication of tri-layer scaffold

The culture substrate is composed of double monolayer nets of nanofibers deposited on a hydrogel frame (**Fig. 4.1**) which is honeycomb patterned and highly porous membrane mounted on a ring of the same material for easy handling and mechanical support. The monolayers of nanofibers were fabricated by electrospinning while the patterned hydrogel frame was fabricated by lithography technique. The detail processes are composed of three steps as follows:

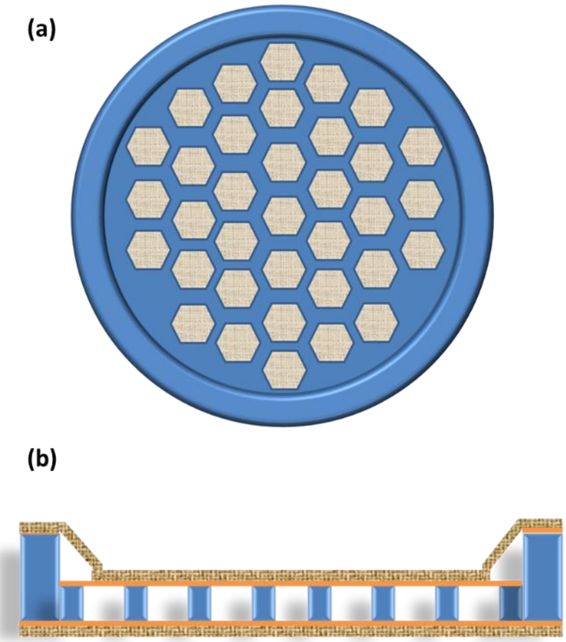

Figure 4.1 The top view (a) and side view (b) of the designed tri-layer patch composed of double layers of nanofibers and a porous hydrogel membrane.

4.2.2.1 PDMS mold fabrication

The hydrogel frame made of PEGDA was fabricated by UV assisted molding using a PDMS mold obtained by photolithography and soft lithography, as schemed in **Fig. 4.2a-d**. Firstly, a chromium mask of the honeycomb network with designed parameters was produced using a micro-pattern generator (µPG 101, Heidelberg Instruments, Germany). After expose, the chromium mask was developed in AZ726 MIF for 1 min to remove the exposed positive photoresist AZ1518, followed by washing with DI water, then chrome-etching for another 1 min and washing again with DI water. Finally, after ultrasonic treatment in acetone to remove the residual resist, a chromium mask with honeycomb patterns was obtained.

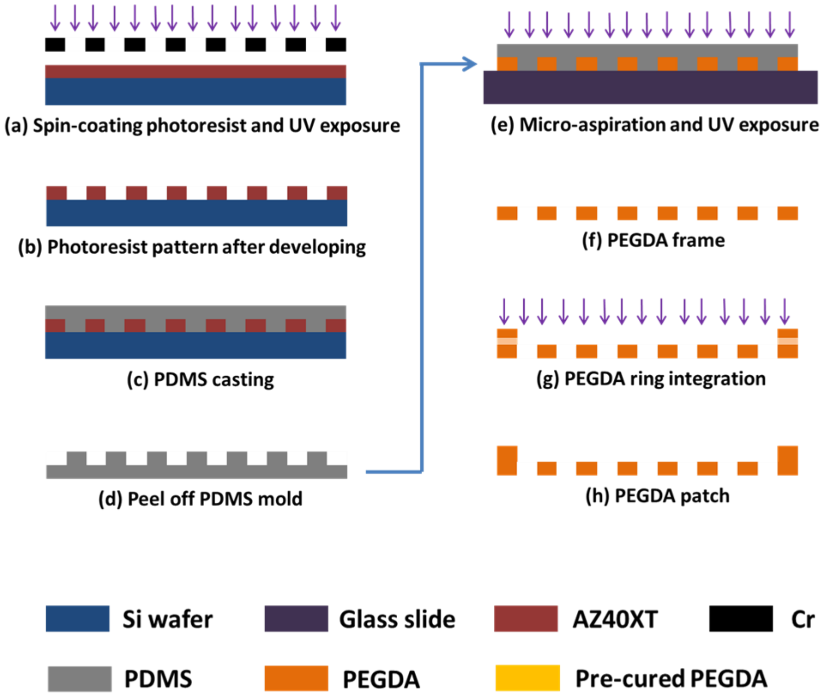

Figure 4.2 Fabrication sequence of PEGDA honeycomb frame. (a-d) Fabrication of PDMS mold by backside UV lithography of a resist layer spin-coated on a patterned Chromium mask and PDMS casting. (e, f) Fabrication of PEGDA honeycomb microframe by aspiration-assisted molding. (g, h) Binding of the PEGDA ring on the honeycomb frame.

For fabricate PEGDA frame with thickness 50 μm, positive resist AZ40XT was used to generate the master mold by UV lithography. The processes are as follows:

a) Spin-coating resist on the mask at 500 rpm for 10 s and then 1500 rpm for 20 s
b) Prebake: 1 min at 65°C, 1 min at 95°C and 10 min at 126°C.
c) Cool down to room temperature.
d) Expose to UV light at 12.7 mW cm^{-2} for 90 s.
e) Post-bake: 30 s at 65°C, 30 s at 95°C and 2 min at 105°C.
f) Develop in AZ 726 MIF for 3 min.
g) After washing with DI water, the mask with patterned resist was dried with nitrogen gun, resulting in AZ40XT master mold.

In order to obtain PEGDA frame with thickness 100 μm, negative resist SU-8 3050 was used because of the thickness demand. The corresponding process parameters are as follows:

a) Spin-coating resist on the mask at 500 rpm for 10 s and then 1000 rpm for 30 s
b) Prebake: 1 min at 65°C, 45 min at 95°C.
c) Cool down to room temperature.
d) Expose to UV light at 12.7 mW cm^{-2} for 30 s.
e) Post-bake: 1 min at 65°C and 5 min at 95°C.
f) Develop in SU-8 developer for 15 min.
g) After washing with isopropanol, the mask with patterned resist was dried with nitrogen gun, resulting in SU-8 master mold.

Next, these two kinds of resist master were exposed to a vapor of trimethylchlorosilane 3 min for anti-sticking treatment. A mixture of the PDMS pre-polymer and the cross-linker was prepared at a ratio of 10:1 and poured on the resist layer. After curing at 80 °C for 2 h, the PDMS layer was peeled off. For SU-8 master mold, it need to 2 times of PDMS soft replication to obtain the positive-tone replica (shown as **Fig. 4.3**).

Figure 4.3 Photo of PDMS mold.

4.2.2.2 Aspiration-assisted PEGDA frame production and ring mounting

The PEGDA honeycomb membrane was produced with PDMS aspiration-assisted molding technique (**Fig. 4.2e** and **f**). Briefly, the PDMS mold was firstly placed on a glass slide. The PDMS-glass assembly was then placed in a desiccator for degassing for 15 min. A PEGDA (average Mn = 250, Sigma, France) solution mixed with 1 v/v% Irgacure 2959 (Sigma, France) as a photo-initiator was prepared and dropped on glass at the edge of the PDMS mold to fill the cavity of the PDMS-glass assembly due to micro-aspiration. Then, a cured honeycomb frame of PEGDA was formed after UV exposure at 12.7 mW cm^{-2} for 30 s and peeling-off the PDMS mold, as shown in **Fig. 4.4**.

Figure 4.4 photo of the produced PEGDA frames.

For easier handling, a 100 µm thick PEGDA ring of 13 mm outer diameter and 9 mm inner diameter was prepared in a similar manner and then mounted on the honeycomb frame using pre-cured PEGDA solution as a binder with UV curing (**Fig. 4.2g** and **h**). Finally, the PEGDA honeycomb frame was gently taken off with the ring using a scalpel. Prior to electrospinning, both sides of the frame were deposited with 10 nm thick Au by sputter coater (K675X, EMITECH, Germany) at 25mA for 1 min to enhance the attachment of nanofibers.

4.2.2.3 Electrospinning nanofibers

Nanofibers of gelatin were electrospun on both sides of the PEGDA layer, 10wt% gelatin powder is dissolved in the mixed solution of acetic acid, ethyl acetate and DI water at a volume ratio of 21:14:10. To collect the electrospun nanofibers more evenly, the backside of the supporting PEGDA network was sputtered with 10 nm thick Au on both sides of frame to enhance the attachment of gelatin nanofibers on the PEGDA network. Then, a silicon wafer was grounded on which a PEGDA layer was taped for the nanofiber connection. After loading into a syringe, the gelatin solution was ejected to the collector at a distance of 10 cm, using a syringe pump (KD Scientific) at 0.2 mL h^{-1} pumping speed through a stainless steel 23-gauge needle. The spinneret was connected to the anode of high potential power supply (TechDempaz, Japan) with a bias voltage of 11 kV and the collector was connected to the cathode of the power supply. After both sides deposition, the samples were dried in a vacuum overnight to eliminate the remaining solvent.

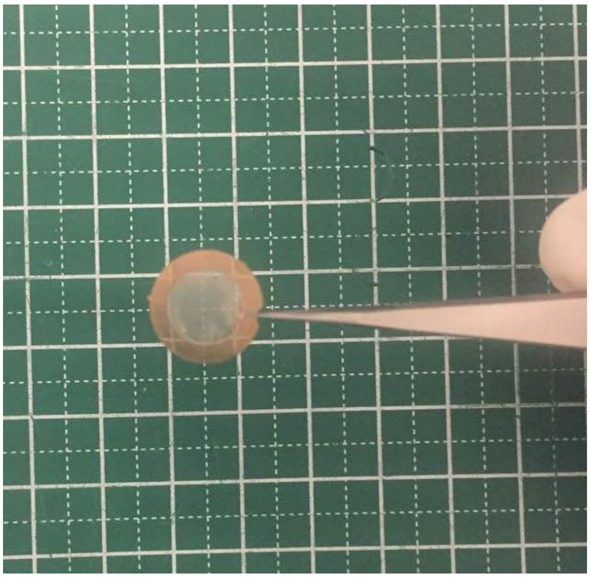

Figure 4.5 Photo of the PEGDA frame supported double layer of nanofiber net with a tweezer holding.

The crosslinking of electrospun gelatin nanofibers was obtained by soaking the sample in ethanol with 0.2 M 1-ethyl- 3-(3-dimethylaminopropyl) carbodiimide hydrochloride (EDC, Sigma, France) and 0.2 M N-hydroxysuccinimide (NHS, Sigma, France) for 4 h. Then, the samples were rinsed with ethanol three times and dried in a vacuum overnight to remove the remaining ethanol, resulting in crosslinked monolayer nanofibers on the PEGDA honeycomb frame, as shown in **Fig. 4.5**. The fiber diameter and pore size distribution were analyzed by software imageJ, no less than three areas of three samples were measured. The morphology of the scaffold was observed with scanning electron microscope (TM-3030, Hitachi, Japan).

4.2.3 Cell culture

Prior to cell seeding, the scaffolds were sterilized by immersing into 70% ethanol and meantime ultraviolet light for 30mins for each side. Then, the scaffolds were washed with DPBS 3times and stored in a culture medium before cell seeding. NIH-3T3 cells were prepared in endothelial growth media (DMEM with 10% fetal bovine serum and 1% penicillin and streptomycin, 1% L-glutamine and 1/10,000 fungizone) prior to seeding in the upper surface of the devices. They were then dissociated and re-suspended in the medium at the density of 4×10^5/mL and 50μL cell suspension was put onto the upper surface. Immediately after seeding, the entire system was kept in an incubator (37°C, 5% CO_2) for cell culture.

4.2.4 Immunocytochemistry

After cell culture, cells were first washed with phosphate-buffered saline (PBS) and fixed in PBS containing 4% formaldehyde for 30 min. Next the formaldehyde solution was removed completely and cells were washed with PBS three times. After that, cells were permeabilized with PBS containing 0.5% Triton- X-100 (TX) for 10 min and washed again with PBS three times. Then cells were blocked in PBS containing 0.1% TX, 3% BSA and 0.1% sodium azide at room temperature for 30 min. After removing blocking solution, cells were washed with PBS three times. Later, F-actin and nuclear of the cells were stained with Phalloidin-FITC and DAPI respectively for 20 min. Finally cells were washed with PBS three times and were observed under a LSM Zeiss 710 confocal microscope.

4.2.5 SEM observation

The patch with cells was fixed with 4% formaldehyde solution for 15 min and washed in PBS three times. The samples were then soaked in 30% ethanol solution (in DI water) for 30 min, and dehydrated by subsequent immersion in ethanol solutions containing 50%, 70%, 80%, 90%, 95%, and 100% ethanol in DI water, each for 10 min and dried with nitrogen gas. Afterward, an Au layer of 2 nm thickness was deposited by sputtering. Finally the samples were observed by using a scanning electron microscope (SEM, Hitachi S-800, 10 kV).

4.2.6 Live/dead assay

NIH 3T3 cells were seeded on the tri-layer scaffold at a density of 20,000 cells/ml. After culturing for 1 day, the cells were rinsed with warm DPBS twice and incubated for an additional 30 min in DPBS containing 2 μM calcein acetoxymethyl ester (calcein AM) and 1 μg/mL propidium iodide under 37°C. After rinse with DPBS, the fluorescence images were taken with an epifluorescence microscopy (Zeiss Axiovert 200) fitted with appropriate exciter and emitter filters to detect live (green fluorescent) and dead (red fluorescent) cells.

4.2.7 Cell proliferation

For proliferation study, 2×10^4 NIH 3T3 cells were seeded on the scaffolds with tissue culture plates (TCPs) as control. After 1, 2, 3, 4 and 5 days post seeding, culture medium was removed and unattached cells were washed out with PBS solution for three times. Subsequently, the proliferation of the cells on each specimen was determined by the standard MTT assay [26]. Briefly, the specimens were incubated with 1 mL FBS-free DMEM culture medium and 100 μL 5 mg/mL 3-[4,5-dimethyl-2-thiazolyl]-2,5-diphenyl-2H-tetrazolium bromide (MTT) for 4 h. Thereafter, the culture media were extracted and 200 μL dimethyl-sulfoxide (DMSO) was added, subsequently the plate was incubated in incubator at 37°C for 30 min. When the crystal was sufficiently dissolved, 100 μL of the solution was pipet-ted into the well of a 96-well plate and tested by a microplate reader, at an absorbance of 490 nm.

4.3 Results

4.3.1 Tri-layer scaffold formation

4.3.1.1 Frame pattern and size

In order to obtain fibrous scaffold with spaced nanofiber layers, PEGDA frame with different patterns and parameters were tested. We firstly fabricated frame with square pattern (length 300 μm), as shown in **Fig. 4.6a** and **b**. As we can see, the two layers of gelatin nanofibers were attached together in the area of holes, resulting in a single fiber layer. It may because of the relative large holes the fibers were sunken and easily attracted to another fiber layer during crosslinking. Then in order to obtain the 3D structure and realize maximum efficiency, we designed frame with honeycomb patterns and decreased the size of holes. **Fig. 4.6c** and **d** shows SEM results of the tri-layer scaffold after double side elestrospinning on honeycomb pattern with period 150 μm and line width 15 μm. with the decreased size, the homogenous gelatin nanofibers formed micron pores at the region of holes after crosslinking, and the fibers on both sides were separated by the middle-supported hydrogel layer, forming a three-layer scaffold. The scaffold remained real three dimensional, unlike some fiber scaffolds which were more likely to from a ultrathin film with increasing the fiber density.

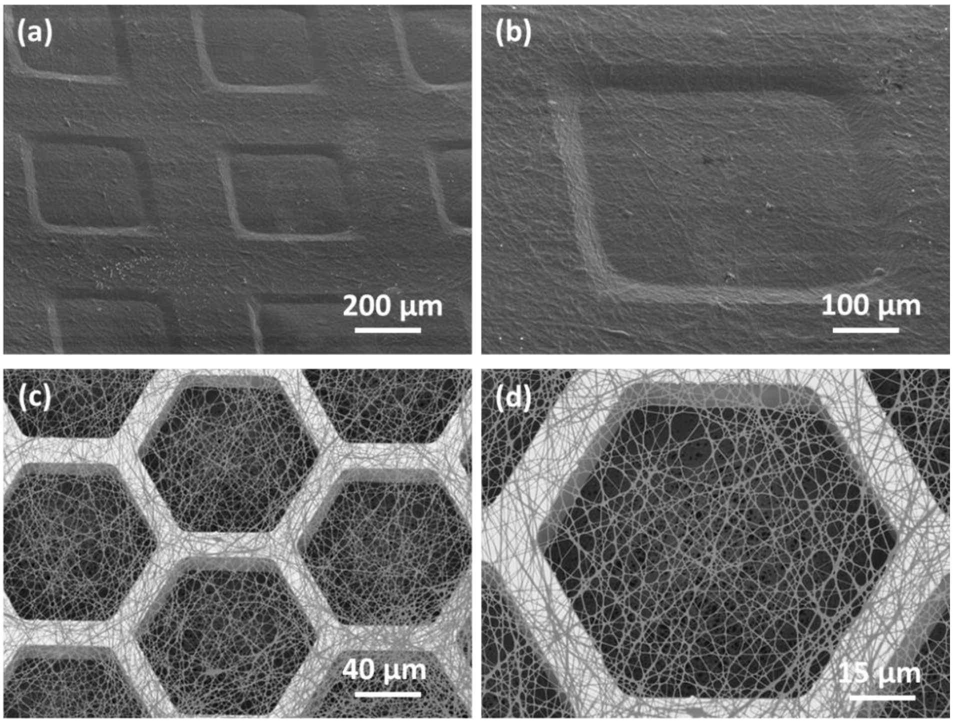

Figure 4.6 SEM images of nanofibers deposited on PEGDA frame with different pattern.

4.3.1.2 Frame thickness

With the aspiration-assisted fabrication method, thick frame can also obtain by changing the thickness of the spin-coated resist, as introduced in **4.2.2.1**, which could form more space benefit cell growth and migration. **Fig. 4.7** shows the SEM photos of fabricated PEGDA frame. It can be seen that the hydrogel frame was obtained with the PDMS mould fabricated by standard lithography. By changing the resist thickness during spin coating, frame with different thickness 50 μm and 100 μm can be obtained, but with the same the honeycomb network (period 150 μm and line width 15 μm).

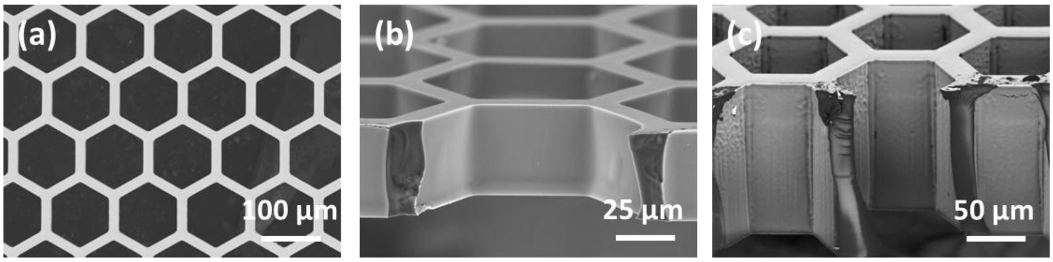

Figure 4.7 SEM images of (a) PEGDA frame from top view, (b) side view of frame with thickness 50 μm and (c) 100 μm.

4.3.1.3 Materials for electrospinning

Different materials were tested for electrospinning except gelatin, as shown in **Fig. 4.8**. Here we chosed polymethylglutarimide (PMGI) synthetic polymer as a nanofiber material because of its biocompatibility and cost effectiveness, **Fig. 4.8a** and **b** show the SEM images of PMGI fibers on frame, the fiber layers were separated clearly, but the fibers formed large pore size because of the high viscosity, which will weaken the advantage of fiber scaffold. And during electrospinning there were some drops formed because of its low electrospun processability. Polycaprolactone (PCL), as biodegradable polyester, was also tested, as shown in **Fig. 4.8c** and **d**. From the SEM observation, the fibers were in micro and nano hybrid status, but it is hard to tell the fiber layers on the frame. While with gelatin fibers, which is known as a natural glue with low toxicity, and biodegradability in the bodies of animals, the three-dimensional fibrous structure was clearly demonstrated (**Fig. 4.6a** and **b**). After crosslinking of the gelatin fibers, the nanofibers were formed spaced monolayer net which is beneficial to observation and cell migration.

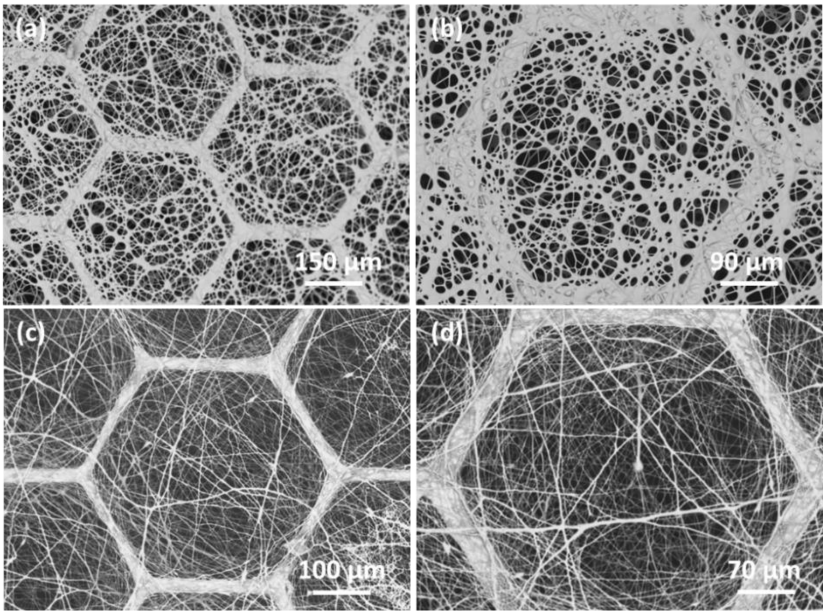

Figure 4.8 SEM photos of (a, b) PMGI nanofibers and (c, d) PCL nanofibers deposited on PEGDA frame.

4.3.1.4 Nanofiber density

In order to improve cell attachment, the 2D porosity or the open space ratio of the net-like structure should control, which depends essentially on the electrospinning time. The morphology of the fibers observed by SEM was shown as **Fig. 4.9**. When the electrospinning time is less than 20 min, monolayer nanofibers could be obtained after crosslinking. Otherwise, no hole could be found through the layer of the crosslinked nanofibers. On the other hand, if the electrospinning time is too short, this will lead few fibers deposited and relatively large pores formed, which is bad for cell attach on the top layer. From ImageJ analyses of the SEM images, the pores for 10 min spinning were mainly less than 4 µm after crosslinking, which was suitable for cell infiltration but could prevent fibroblast cells from falling into the holes when seeding as the size of fibroblasts was around 10µm. while the sample with 5 min electrospinning had pores with diameter up to around 20 µm (larger than that of the cells), which should be too large for cell attachment. Both of them are transparent enough for medium permeability, but for 20 min of electrospinning, the porosity was quite low since the multi-layer and the too small pores. Therefore, considering both high transparency and enough support for cells, the electrospinning time of 10 min was chosen as the optimum parameter for the next studies.

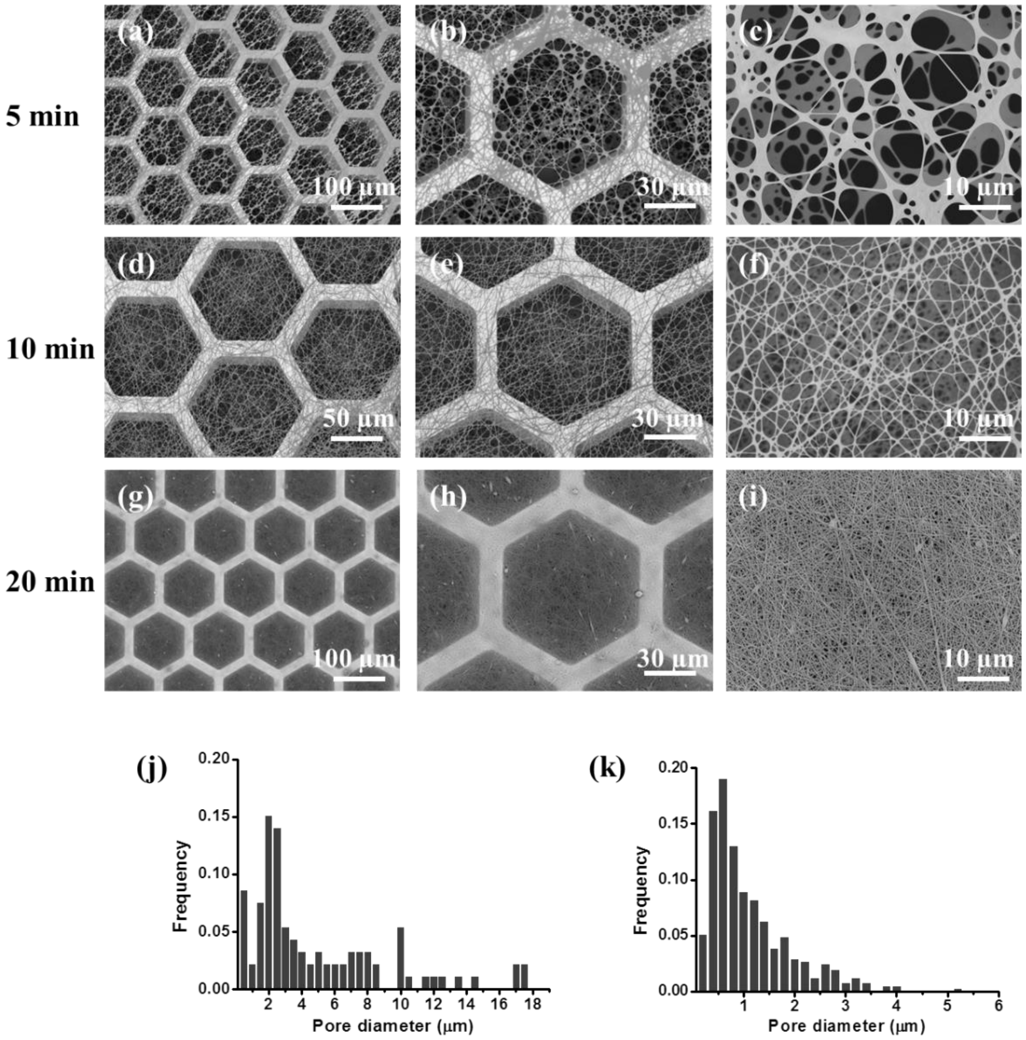

Figure 4.9 Electrospinning time dependent patch structure. (a) SEM images of crosslinked gelatin nanofibers obtained by 5 (a-c), 10 (d-f) and 20 min (g-i) electrospinning. (j, k) Pore size distribution of 5 and 10 min electrospun samples.

4.3.2 Cell attachment and spreading

To study the cell adhesion on tri-layer scaffold, cell morphology of fibroblast was observed via SEM just after seeding 1 h and 3 h, as shown in **Fig. 4.10**. The cells could well attach on the fiber net because of the biocompatible of gelatin and PEGDA, and also due to the fibrous structure could promote cell adhesion. The cells spread like star shape just after 3 h culture, this observation could be confirmed in **Fig. 4.12**.

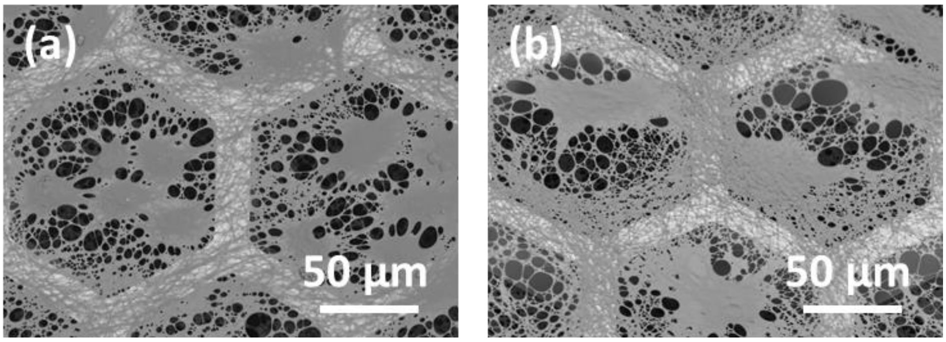

Figure 4.10 SEM images of cells on tri-layer scaffold after seeding (a) 1 h and (b) 3 h.

4.3.3 Cell viability

After 24 h of in vitro cell culture, a fluorescent cell viability assay was carried out and the results are shown in **Fig. 4.11**. As we can see, almost all the cells were alive and only few dead cells were found on the patch even after 4 days culture and proliferation. The results demonstrated that the cells on tri-layer scaffold maintained viability due to the biocompatibility of the composed materials, namely gelatin and PEGDA.

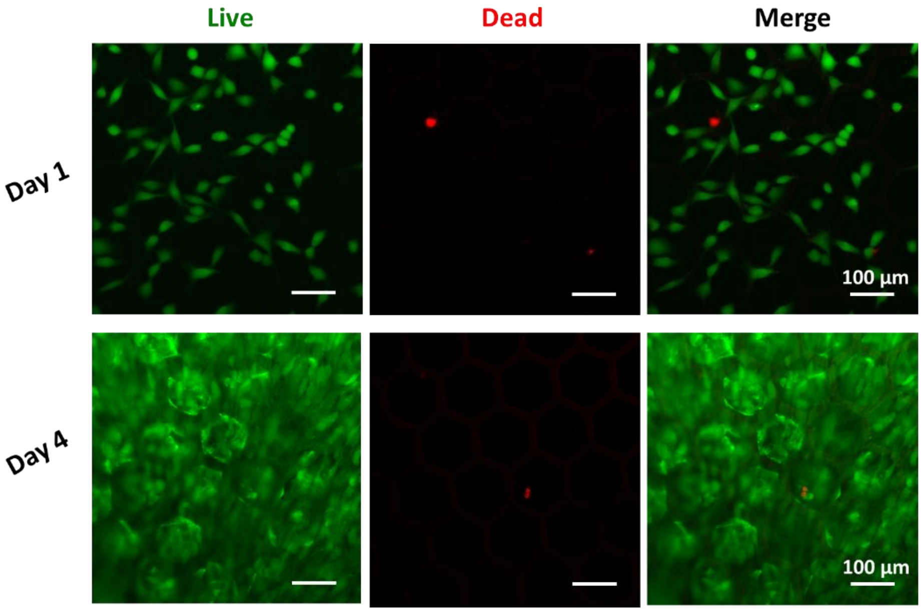

Figure 4.11 Live/dead cell assay showing NIH 3T3 cells viability on gelatin-PEGDA tri-layer scaffold after culture 1 and 4 days. Live cells produced green fluorescence and dead cells showed red fluorescence.

4.3.4 Cell morphology and 3D cell culture

Fig. 4.12 shows immunofluorescence images of NIH 3T3 cells cultured on the tri-layer scaffold (thickness 50 μm) from just attached to day 3, and also the 3D view of cell infiltration within the scaffold as a function of time. As can be seen, the cells attached on the top fiber layer and spread on the fibers just after seeding 3h. From the confocal z-stack 3D image, we can see there was no cells fall into the bottom side because of the controlled pore size (less than 5μm). With culture time, the cells began to proliferate. After 1 day, the cells covered the top surface with few cells infiltrated. From day 2, there were layered cells and more cells penetrated into the free space formed by separated nanofiber network. Finally at day 3, part of cells reached to the bottom surface and formed a 3D cell patch.

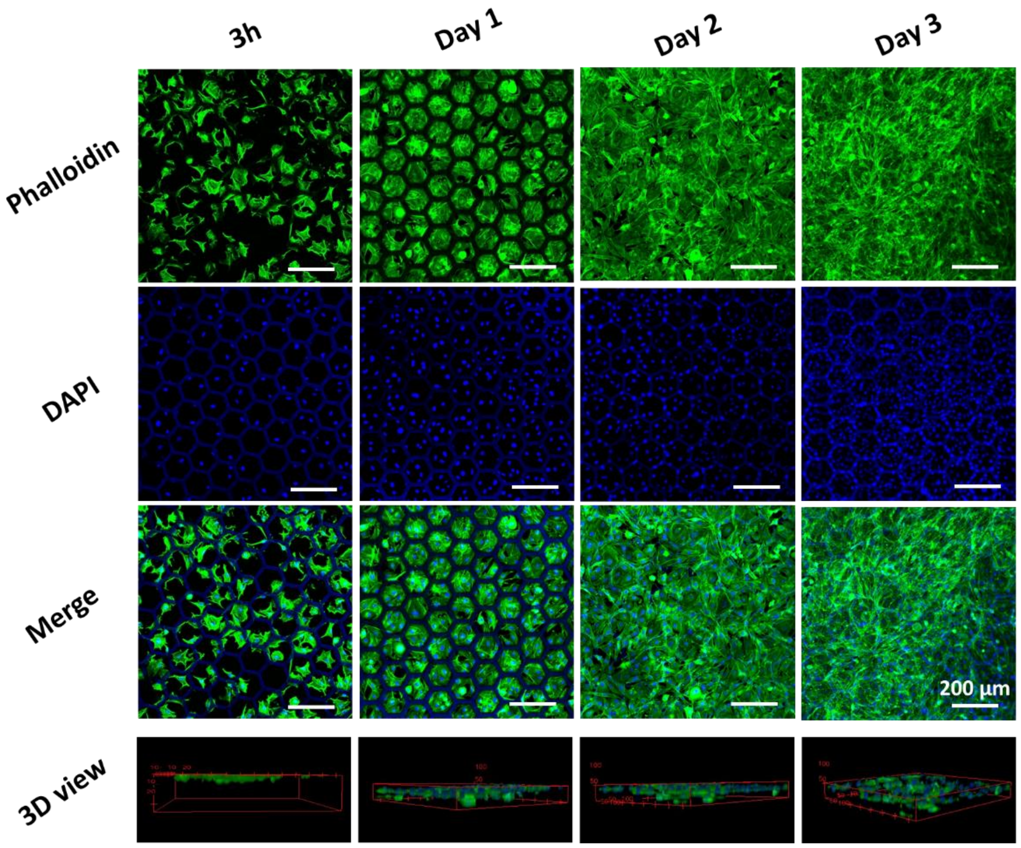

Figure 4.12 Immunofluorescence images and 3D view of NIH 3T3 cells on the tri-layer scaffold with thickness 50 μm. Cells were stained with FITC-phalloidin (green) for F-actin cytoskeleton and DAPI for nucleus (blue).

4.3.5 Cell migration

To investigate the cells migration behavior on this 3D fibrous scaffold, the infiltration of the cells from top or bottom side were investigated. Besides, two kinds of scaffold with different hydrogel layer thickness (50 µm and 100 µm) were tested to study the migration as a function of culture time.

4.3.5.1 Top to bottom migration

The cells were seeded on the top nanofibers layer to study the cells infiltration from top to bottom. Confocal z-stack microscopy allowed us to section the samples in the z-direction to observe the penetration of cells into the interiors of scaffolds and 3D growth inside the tri-layer scaffold by optical slicing. As shown in the confocal z-stack images of different planes stacked from top to bottom with 5 µm plane thickness in **Fig. 4.13**. It was obvious that all cells just attached on top layer fibers and rare cells detected on bottom side, indicating that the pore size distribution could prevent cells falling down when seeding. The cells were well attached to the gelatin nanofibrous net and their actin cytoskeletons were well developed just after seeding 3 h (**Fig. 4.13a**). After culture 24 h, the cells covered the top surface of the fibers due to proliferation, and we can see some of the cells began to migrate with a few cells reached depth 20-25 µm. Cells infiltrated well into the scaffold with culture time. At 3 days of cell culture, cells were able to penetrate to the bottom side of scaffold, and the number of cells in each plane was much more compared with day 2, indicating that cells proliferated in the hollow space.

In order to more clearly demonstrate cells localization with the culture time, the number of cell in each plane was counted base on the stained nuclei, as illustrate in **Fig. 4.14**. From the statistical data, we can directly see that there were no cells fall into the scaffold from pores. After culture 24h, around 80% cells still stayed within depth 10 µm with less than 5% cells penetrated to depth 25 µm. At day 2 of culture, even the nuclei were mostly found in the surface of nanofiber layer, an increasing number of cells infiltrated to the middle space formed by honeycomb holes and nanofibers. At day 3, almost 10% cells went through the space and finally spread at the bottom layer.

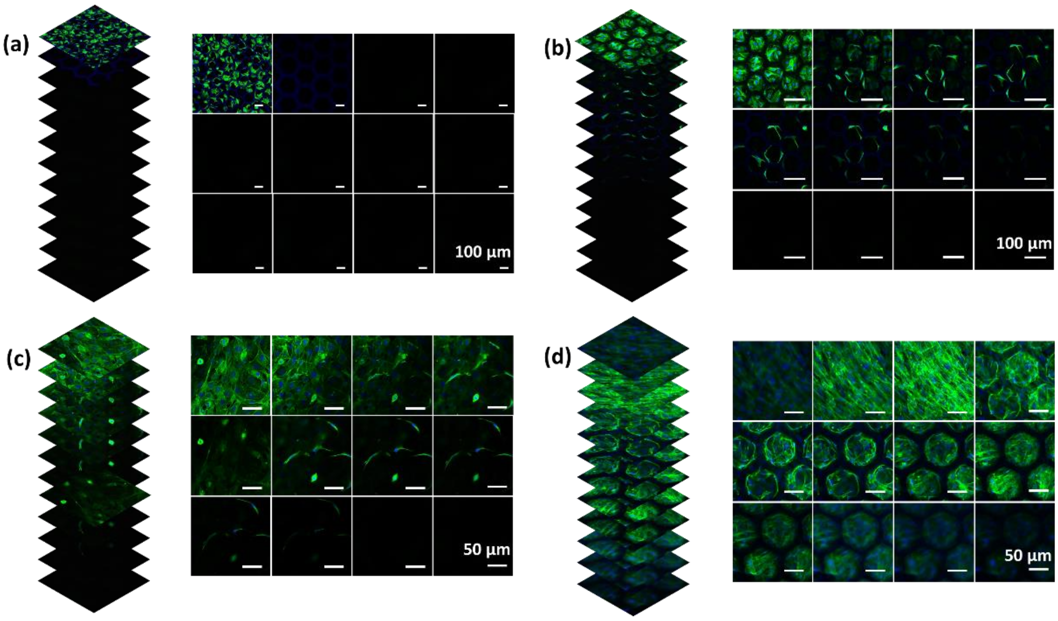

Figure 4.13 Confocal microscope z-stack images of NIH 3T3 cells seeded onto the tri-layer nanofibrous scaffolds with thickness 50 µm after (a) 3 h, (b) 24 h, (c) 2 days and (d) 3 days growth. In each group, a stacked and unstacked z-stack images of different planes showing from surface to bottom with 2 µm plane thickness are shown. Cells were stained with FITC-phalloidin (green) for F-actin cytoskeleton and DAPI for nucleus (blue).

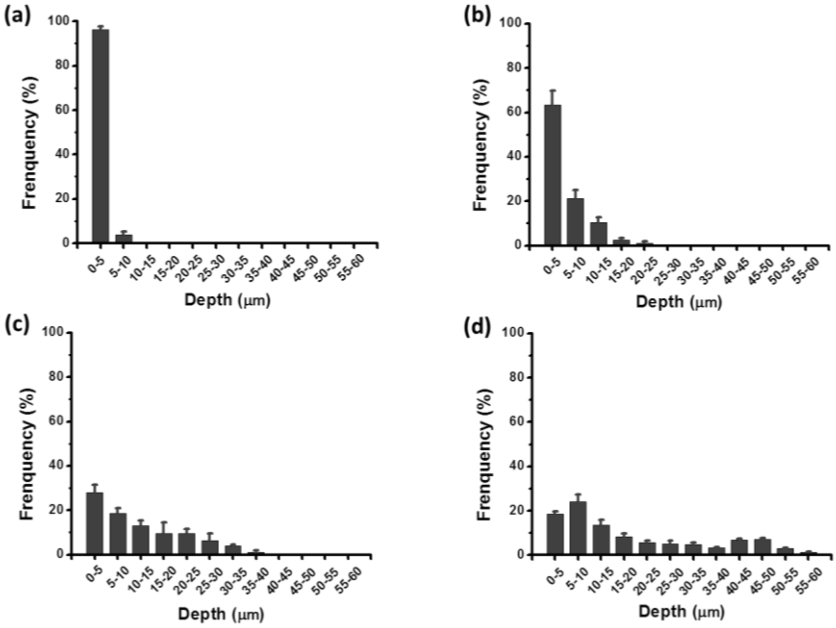

Figure 4.14 Nucleus localization in depth after culture (a-d) 3 h, 24 h, 2 days and 3 days.

In order to observe more details of cell distribution and migration behavior inside the tri-layer scaffold, cell colonized scaffolds were examined by confocal imaging. **Fig. 4.15** shows confocal z-stack images of cells cytoskeleton stretch and elongation into the hole-area after culture 3 days. As can be more clearly seen, some of the cells infiltrated the scaffold up to depths from the through holes. In **Fig. 4.15**, at the top surface of the scaffold cells formed sheet because of the proliferation. Immediately below this layer, cytoskeleton spread along the walls and stretched in the hollow space can be clearly seen (**Fig. 4.15d**). with further decrease of the focusing plane, the cell skeleton and nuclei can be both clearly seen, indicating that the cell penetrated into the paced area formed by two nanofiber layers (**Fig. 4.15e** to **g**). Note that the cells in the spaced area either attached on the wall of honeycomb holes or partly suspended in the free space. Thus, part of cells was more likely localized in the free space between the two fiber layers because of a favorable 3D microenvironment. When the focusing plane is close to the bottom fiber layer, we observed again a part a cytoskeleton but without the nucleus (**Fig. 4.15h** to **k**). Finally, when focusing on the bottom, a cell layer also can be found, indicating that part of cells migrated to the bottom and proliferated on the fibrous net (**Fig. 4.15l**).

Indeed, the most of the cytoskeleton is stretched alongside the fiber in the region of holes. Knowing that the separation distance between the two fiber layers is about 50 μm, it is possible that some of the cells are attached to both top and bottom fiber layers. Obviously, such a cellular infiltration should depend on the porosity of the nanofiber layer. Under optimal conditions, the infiltrated cells enjoy their quasi-3D scaffold and microenvironment provided by the spaced nanofibers due to enhanced permeability and ECM like structures.

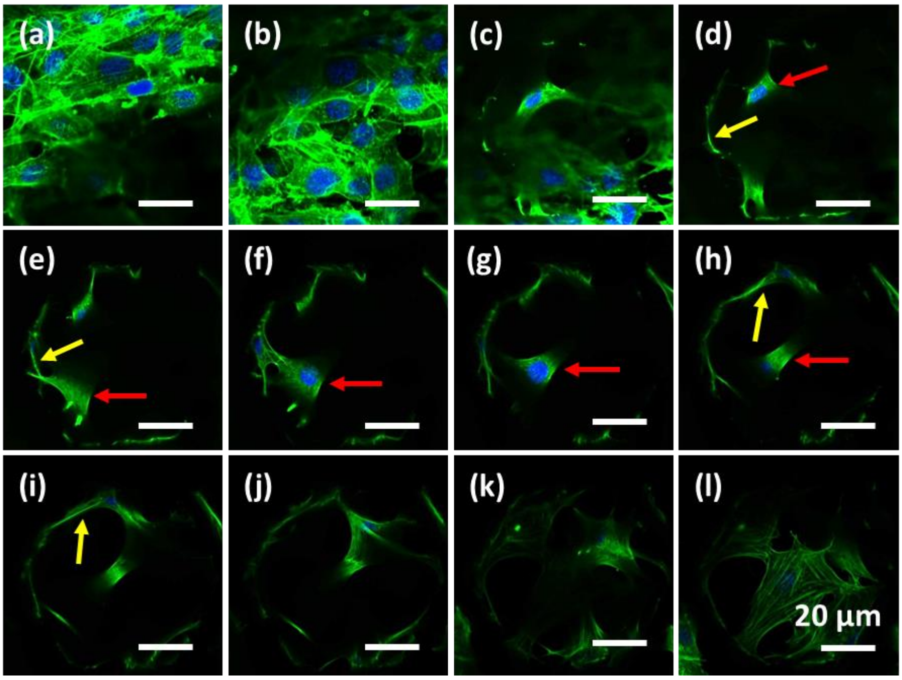

Figure 4.15 Confocal z-stack images of cells cytoskeleton stretch and elongation in the honeycomb space after culture 3 days. (a-l) Corresponding section at different focal planes with 5 µm plane thickness from the top to the bottom surfaces of the device. Arrows in red indicate cells in the hollow space, while arrows in yellow indicate cells migrate along the wall of honeycomb pattern.

4.3.5.2 Bottom to top migration

Our results proved that the cells could penetrate throughout the space in the scaffold after 3 days culture if they were seeded on the top surface. To investigate the driving force of cell migration on the tri-layer scaffold, we tested the situation of cells were firstly seeded on the bottom side, the confocal z stack images of cells in the scaffold after culture 3 days were shown in **Figure 4.16**. As we can see, around 70% cells remained on the bottom side with less than 5% cells migrated up to depth 30 µm. Compared to the situation of cells seeded on the top surface in which the cells spread throughout the free space and formed cell layer on the bottom, here just had few cells migrated, indicating that the natural gravity is one of the induce for migration, and also probably due to the enhanced permeability of the substrate and the effect of anisotropic force provided by gelatin fibers.

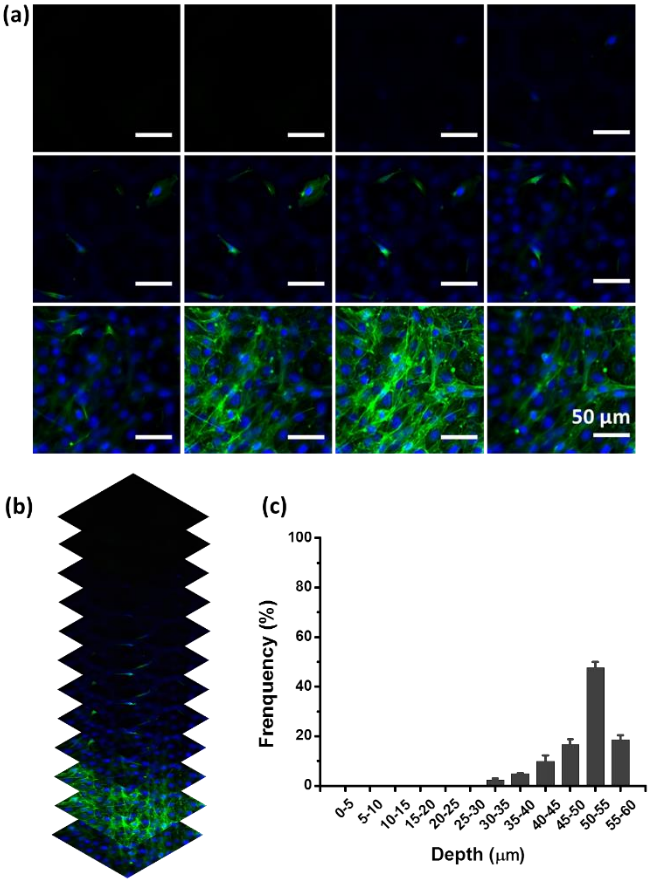

Figure 4.16 (a) unstacked and (b) stacked z-stack images of different planes showing from surface to bottom with 5 µm plane thickness are shown. (c) cell nuclei distribution on different planes.

4.3.5.3 Migration on thick scaffold

As shown in our previous results, we can obtain a 3D cell sheet in scaffold with thickness 50 µm after 3 days culture, in order to investigate the migration speed in thicker scaffold, we fabricated PEGDA hydrogel layer with 100 µm thickness, thus obtained a tri-layer fibrous scaffold with thickness 100 µm (S100). The cells localization images and nuclei distribution after cultured 3 days and 5 days are shown in **Fig. 4.17**. At 3 days of cell culture, less than 5% cells penetrated to depth 25 µm. Compared to that situation in scaffold with thickness 50 µm (S50) in which around 10% cells found in the bottom, it is perhaps because the bottom side nanofibrous net could provide attach spots and exert tractive forces on the cells, which wound promote cell migration. After 5 days culture, around 4% cells finally penetrated to the bottom, forming a thick cell sheet.

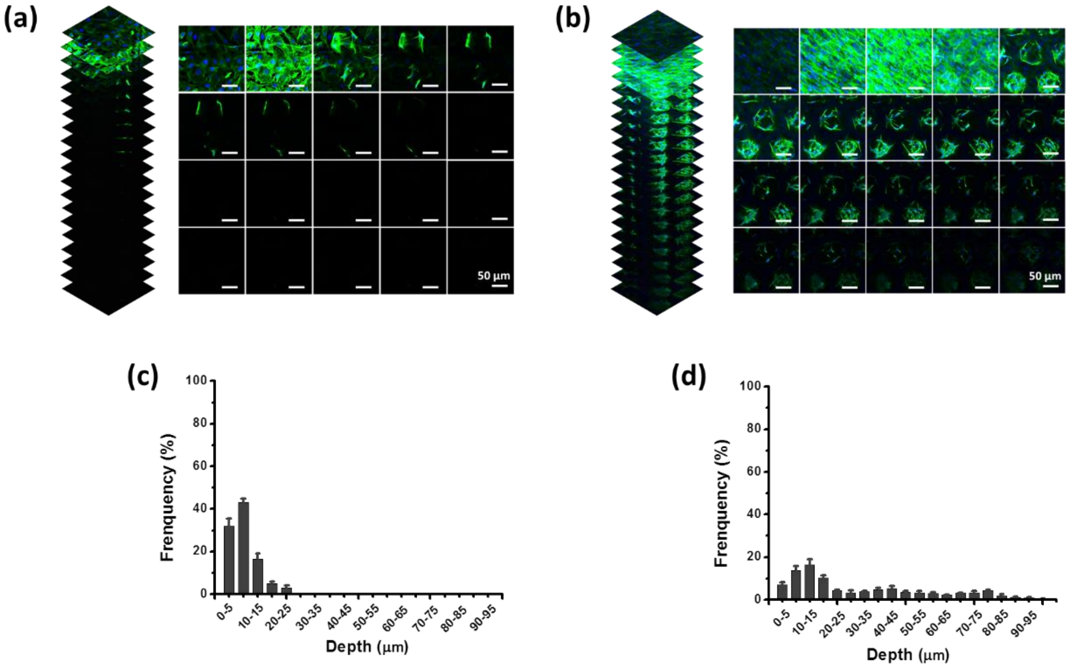

Figure 4.17 Confocal z stack images of cells after (a) 3 days and (b) 5 days culture. (c, d) Nuclei distribution after 3 days and 5 days culture.

4.3.6 Cell proliferation

To investigate cell proliferation on tri-layer scaffolds, MTT assay was carried out after 1, 2, 3, 4 and 5 days of culture to evaluate cell viability. **Fig. 4.18** indicates that viable cells on S50 scaffold had the highest proliferation rate before 4 days culture. Oppositely, on S100 scaffold, numbers of cells increased slightly during the first three days. A possible reason is that cells were more easily penetrated to bottom fiber layer during the first three days culture on S50 compared to S100 (**Fig. 4.13d** and **Fig. 4.17a**), which promote the proliferation. Whereas, at day 5, more viable cells on S100 scaffold may be contributed by the larger free space. Besides, compared to the cells on plates, cells on the fibrous scaffolds showed significant increase over time. The spreading of cells on tri-layer scaffolds showed a multilayered distribution, as shown in **Fig. 4.16d** and **Fig. 4.20b**. While cells on petri dish only spread on the surface, which restricted the cell proliferation.

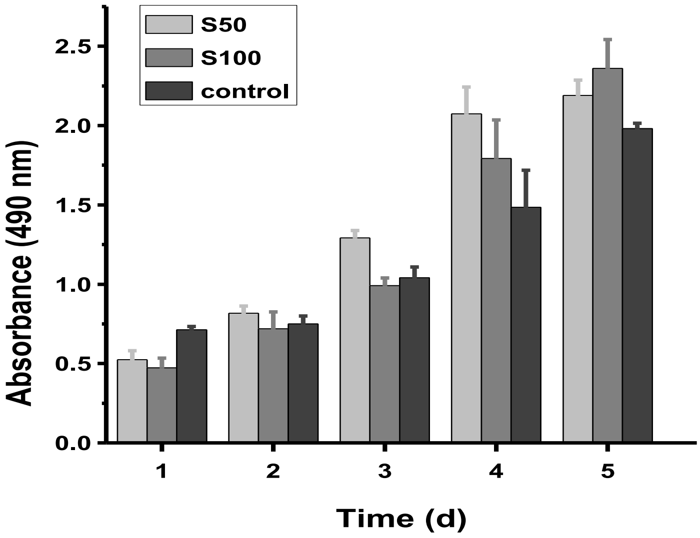

Figure 4.18 MTT assay of cell proliferation on scaffold with thickness 50 µm (S50) and 100 µm (S100). Cells seeded on tissue culture plates (TCPs) performed as control.

4.4 Conclusion

We have demonstrated the fabrication of a tri-layer scaffold with anisotropic properties similar to the structure and mechanics of the extracellular matrix by photolithography and electrospinning techniques. The results showed that these 3D scaffolds can sustain the adhesion of NIH 3T3 cells, and this real 3D structure promoted the cell penetration and proliferation. The cell handing device should also be useful for in-vivo assays or integration into microfluidic devices, thereby holding high potential for further investigations.

References

[1] A. Birgersdotter, R. Sandberg, I. Ernberg, Gene expression perturbation in vitro-A growing case for three-dimensional (3D) culture systems, Semin. Cancer Biol. 15 (2005) 405–412.

[2] R.C. Dutta, A.K. Dutta, Cell-interactive 3D-scaffold; advances and applications, Biotechnol. Adv. 27 (2009) 334–339.

[3] L.G. Griffith, M.A. Swartz, Capturing complex 3D tissue physiology in vitro, Nat. Rev. Mol. Cell Biol. 7 (2006) 211–224.

[4] K.R. Koehler, A.M. Mikosz, A.I. Molosh, D. Patel, E. Hashino, Generation of inner ear sensory epithelia from pluripotent stem cells in 3D culture, Nature. 500 (2013) 217–221.

[5] A. Martins, S. Chung, A.J. Pedro, R.A. Sousa, A.P. Marques, R.L. Reis, N.M. Neves, Hierarchical starch-based fibrous scaffold for bone tissue engineering applications, J. Tissue Eng. Regen. Med. 3 (2009) 37–42.

[6] S.C. Owen, M.S. Shoichet, Design of three-dimensional biomimetic scaffolds, J. Biomed. Mater. Res. Part A. 94A (2010).

[7] P. Viswanathan, M.G. Ondeck, S. Chirasatitsin, K. Ngamkham, G.C. Reilly, A.J. Engler, G. Battaglia, 3D surface topology guides stem cell adhesion and differentiation, Biomaterials. 52 (2015) 140–147.

[8] E. Volkmer, I. Drosse, S. Otto, A. Stangelmayer, M. Stengele, B.C. Kallukalam, W. Mutschler, M. Schieker, Hypoxia in Static and Dynamic 3D Culture Systems for Tissue Engineering of Bone, Tissue Eng. Part A. 14 (2008) 1331–1340.

[9] K.M. Woo, V.J. Chen, P.X. Ma, Nano-fibrous scaffolding architecture selectively enhances protein adsorption contributing to cell attachment, J. Biomed. Mater. Res. 67A (2003) 531–537.

[10] Y. Zhang, H. Ouyang, C.T. Lim, S. Ramakrishna, Z.-M. Huang, Electrospinning of gelatin fibers and gelatin/PCL composite fibrous scaffolds, J. Biomed. Mater. Res. 72B (2005) 156–165.

[11] K. Tonsomboon, M.L. Oyen, Composite electrospun gelatin fiber-alginate gel scaffolds for mechanically robust tissue engineered cornea, J. Mech. Behav. Biomed. Mater. 21 (2013) 185–194.

[12] W.-J. Li, J.A. Cooper, R.L. Mauck, R.S. Tuan, Fabrication and characterization of six electrospun poly (alpha-hydroxy ester)-based fibrous scaffolds for tissue engineering applications, Acta Biomater. 2 (2006) 377–385.

[13] W.-J. Li, C.T. Laurencin, E.J. Caterson, R.S. Tuan, F.K. Ko, Electrospun nanofibrous structure: A novel scaffold for tissue engineering, J. Biomed. Mater. Res. 60 (2002) 613–621.

[14] K. Kim, Y.K. Luu, C. Chang, D. Fang, B.S. Hsiao, B. Chu, M. Hadjiargyrou, Incorporation and controlled release of a hydrophilic antibiotic using poly(lactide-co-glycolide)-based electrospun nanofibrous scaffolds, J. Control. Release. 98 (2004) 47–56.

[15] X. Zhu, W. Cui, X. Li, Y. Jin, Electrospun Fibrous Mats with High Porosity as Potential Scaffolds for Skin Tissue Engineering, Biomacromolecules. 9 (2008) 1795–1801.

[16] B.M. Baker, A.O. Gee, R.B. Metter, A.S. Nathan, R.A. Marklein, J.A. Burdick, R.L. Mauck, The potential to improve cell infiltration in composite fiber-aligned electrospun scaffolds by the selective removal of sacrificial fibers, Biomaterials. 29 (2008) 2348–2358.

[17] J. Rnjak-Kovacina, A.S. Weiss, Increasing the Pore Size of Electrospun Scaffolds, Tissue Eng. Part B Rev. 17 (2011) 365–372.

[18] F.A. Sheikh, H.W. Ju, J.M. Lee, B.M. Moon, H.J. Park, O.J. Lee, J.-H. Kim, D.-K. Kim, C.H. Park, 3D electrospun silk fibroin nanofibers for fabrication of artificial skin, Nanomedicine Nanotechnology, Biol. Med. 11 (2015) 681–691.

[19] S. Zhong, Y. Zhang, C.T. Lim, Fabrication of Large Pores in Electrospun Nanofibrous Scaffolds for Cellular Infiltration: A Review, Tissue Eng. Part B Rev. 18 (2012) 77–87.

[20] G. Kim, W. Kim, Highly porous 3D nanofiber scaffold using an electrospinning technique, J. Biomed. Mater. Res. Part B Appl. Biomater. 81B (2007) 104–110.

[21] Y. Tang, L. Liu, J. Li, L. Yu, L. Wang, J. Shi, Y. Chen, Induction and differentiation of human induced pluripotent stem cells into functional cardiomyocytes on a compartmented monolayer of gelatin nanofibers, Nanoscale. 8 (2016) 14530–14540.

[22] Y. Tang, L. Liu, J. Li, L. Yu, F.P.U. Severino, L. Wang, J. Shi, X. Tu, V. Torre, Y. Chen, Effective motor neuron differentiation of hiPSCs on a patch made of crosslinked monolayer gelatin nanofibers, J. Mater. Chem. B. 4 (2016) 3305–3312.

[23] S.-M. Lien, L.-Y. Ko, T.-J. Huang, Effect of pore size on ECM secretion and cell growth in gelatin scaffold for articular cartilage tissue engineering, Acta Biomater. 5 (2009) 670–679.

[24] S. Gautam, C.-F. Chou, A.K. Dinda, P.D. Potdar, N.C. Mishra, Surface modification of nanofibrous polycaprolactone/gelatin composite scaffold by collagen type I grafting for skin tissue engineering, Mater. Sci. Eng. C. 34 (2014) 402–409.

[25] Y. Nakano, T. Tobe, N.-H. Choi-Miura, T. Mazda, M. Tomita, Isolation and Characterization of GBP28, a Novel Gelatin-Binding Protein Purified from Human Plasma, J. Biochem. 120 (1996) 803–812.

[26] J. van Meerloo, G.J.L. Kaspers, J. Cloos, Cell Sensitivity Assays: The MTT Assay, in: 2011: pp. 237–245.

Chapter 5

Differentiation of Human Induced Pluripotent Stem Cells on Micropillar Arrays

In this chapter, we report the results of cardiac differentiation of human pluripotent stem cells (hiPSCs) on micropillar arrays. PDMS micropillars of different height were obtained as previously described. To initiate homogenous aggregation of hiPSCs, we placed a PDMS stencil with a honeycomb pattern on the surface of the pillar samples. After cell seeding and attachment or embryoid body (EB) like aggregation formation in each of honeycomb apartment, an induced differentiation was performed. Our results showed a stiffness-dependent EBs formation and subsequent differentiation into functional cardiomyocytes.

5.1 Introduction

Human induced pluripotent stem cells (hiPSCs) hold high potential for industrial and clinical applications such as tissue engineering, disease modelling and drug screening due to their capability of infinity self-renewing and guided differentiation to multiple lineages [1–3]. However, important challenges have to be overcome to avoid risks of tumorigenesis or teratoma formation for clinical uses of hiPSCs derived products [4–8].

In general, the differentiation of hiPSCs starts by the formation three-dimensional spheroid aggregates called embryoid bodies (EBs), in which cells are subjected to complex cell-cell interactions and paracrine signaling, to approach the native processes and avoid single cell culture related apoptosis [9–11]. Then, cells within EBs undergo differentiation and specification along the three germ lineages – endoderm, ectoderm, and mesoderm, before being more precisely directed to a final type of somatic cells or micro-tissue [12–14]. Such micro-tissues are promising for both in vitro and in vivo cell-based arrays as well as regenerative medicine applications. A variety of methods have been used to promotes hiPSC EB formation, including liquid suspension culture [15], culture in methylcellulose semisolid media [16], culture in hanging drops [17], culture in round-bottomed multiwell plate or micro-engineered conical holes [18], hydrogel embedded culture [19], etc. Each of these methods has its own peculiarity but most of them suffered process complexity and low controllability of EB size and homogeneity. Indeed, the formation and maturation of EBs rely on non-adhesive culture or geometric confinement to avoid disassociation into single cells, whereas the differentiated cell or tissues is based on adhesion culture [20, 21]. Therefore, a new development strategy has to be worked out to stimulate uniform 3D aggregation of hiPSCs on a adhesion controllable 2D surface.

Our group previously demonstrated a culture patch method by electrospinning and crosslinking monolayer gelatin nanofibers on a honeycomb frame made of poly (ethylene glycol) diacrylate (PEGDA) [22, 23]. Such a patch method can be easily used as a general platform for cell culture, differentiation and assays. When used for hiPSC differentiation, cells are seeded, homogenously distributed in each of the honeycomb compartments, supported by the monolayer of gelatin nanofibers, leading to uniform formation of EBs in each of the honeycomb compartments. In addition, this device assures minimal exogenous contact of the cell and maximal efficiency of cell–medium exchange. Moreover, by using such a device the EBs formation can be controlled using small molecule Y-27632, an inhibitor of the rho associated kinase (ROCK) pathway. Finally, all steps, including EB formation, induction and differentiation can be formed using a single device with cell digestion or replating.

In this work, we study the influence of the substrate stiffness on the differentiation efficiency. Previously, Engler et al. have shown the importance of the substrate stiffness in differentiation of mesenchymal stem cells. Substrate stiffness should also be an importance factor for self-renewal and induced differentiation of hPSCs [24]. Musah et al. demonstrated that stiffer hydrogels (10 KPa) enable long-term self-renewal of hiPSCs [25]. Alternatively, Sun et al. used micropillar arrays to culture hPSCs and found an optimal effective stiffness of 1.2 MPa for pluripotency maintenance of human embryonic stem cells [26]. It was also reported that soft microenvironments promote the early neurogenic differentiation but not self-renewal of hPSCs [27]. These studies illustrate not only large discrepancies in substrate stiffness but also the complexity of cell–matrix interactions on different types of substrates.

As demonstrated in the previous chapters, elastomeric micropillar arrays can be easily produced and used as stiffness adjustable substrate for cell culture. The advantage of using this type of substrate for hiPSCs differentiation compared to the other types of substrates such as hydrogel relies on the precise stiffness control and localized adhesion when cells or EBs are attached on the top of the pillar area. Moreover, the free space underneath the cells or EBs facilitates the diffusion of nutrients, metabolites, and soluble cell factors. To obtain uniform EBs on micropillar substrates, a PDMS stencil with honeycomb patterns was placed on the substrate surface of the pillars when seeding and the removed after cell attachment, resulting uniform cell aggregation on the surface of a homogeneous pillar arrays. Then, the stiffness-dependent EBs formation and cardiomyocytes differentiation will be studied. In such a way, we demonstrate a facile method to modulate cell–cell and cell–matrix interaction for hiPSCs culture and subsequent cardiac differentiation in an efficient and reproducible manner. The effect of the substrate stiffness on EBs dimensionality and the maturation of differentiated cardiomyocytes will be discussed.

5.2 Materials and methods

5.2.1 Materials

Photoresist (SU-8) and resist developers were purchased from MicroChem (France). Chrome plates (Nanofilm) were purchased from CIPEC (France). PDMS kit (GE RTV 615) was purchased from Eleco (France). Fetal bovine serum (FBS), L-glutamine, penicillin/ streptomycin (P/S), 4',6-diamidino-2-phenylindole (DAPI) and phosphate-buffered saline (PBS) tablets were purchased from Invitrogen. Trypsin-EDTA, paraformaldehyde (PFA), ethanol, Triton-X-100, normal goat serum (NGS) and bovine serum albumin (BSA) were purchased from Sigma. E8 medium and vitronectin was purchased from Life Technologies.

5.2.2 Fabrication of elastomer micropillars

Fig. 5.1 shows schematic illustration of the fabrication process of PDMS micropillar substrate. First, commercial blank masks (AZ1518 with a resist thickness 530 nm, CIPEC, France) were used for absorbent (Cr) pattern generation by using a Micro Pattern generator (μPG 101Germany) with a UV laser beam, as introduced in Chapter 2. The UV lithography by backside exposure to fabricate resist template has been done in the following manner. Firstly, negative photoresist SU-8 (2002, 3005 and 3010) was coated on the surface of the mask (**Fig. 5.1b**). The resist was then soft baked on a hot plate at 65 °C for 1 min and 95 °C for 2 min. The backside exposure was done for 10 s with a UV lamp (365 nm wavelength and 12.9 mJ/cm^2 power density), as shown in **Fig. 5.1c**, which minimize the light diffraction effect caused by poor contact and light reflection from the substrate compared to the usual front-side exposure. The post-exposure bake on hot plate was done on a hot plate at 65 °C for 1 min and 95 °C for 3 min. Finally, the resist was developed in SU-8 developer for 2 min with mild agitation, followed by rinsing with isopropanol and baking on a hot plate at 125 °C for 15 min, resulting in resist pillar arrays, which can be used as master mold for sub-sequential replications, as shown in **Fig. 5.1d**.

In order to obtain elastomer micropillar substrates, PDMS was used to replicate the master mold. **Fig. 5.1e-h** shows the replication process of PDMS mold from SU-8 master. Firstly, trichloromethylsilane (TMCS) was evaporated as release agent on the master by chemical vapor deposition. Then, a mixture of PDMS A/B components was poured onto the master pattern, and degassed during 20 min in vacuum in order to remove air bubbles formed during the mixing process. Afterward, PDMS was cured at in an oven at 80 °C for 2 hours. After solidification, the negative-tone replica of the master in PDMS was gently detached from the SU8 master (**Fig. 5.1f**). To obtain PDMS micropillars, a second PDMS casting had to proceed, before which the mold was treated with TMCS in order to facilitate detachment. Finally, micropillar arrays in PDMS obtained (**Fig. 5.1h**).

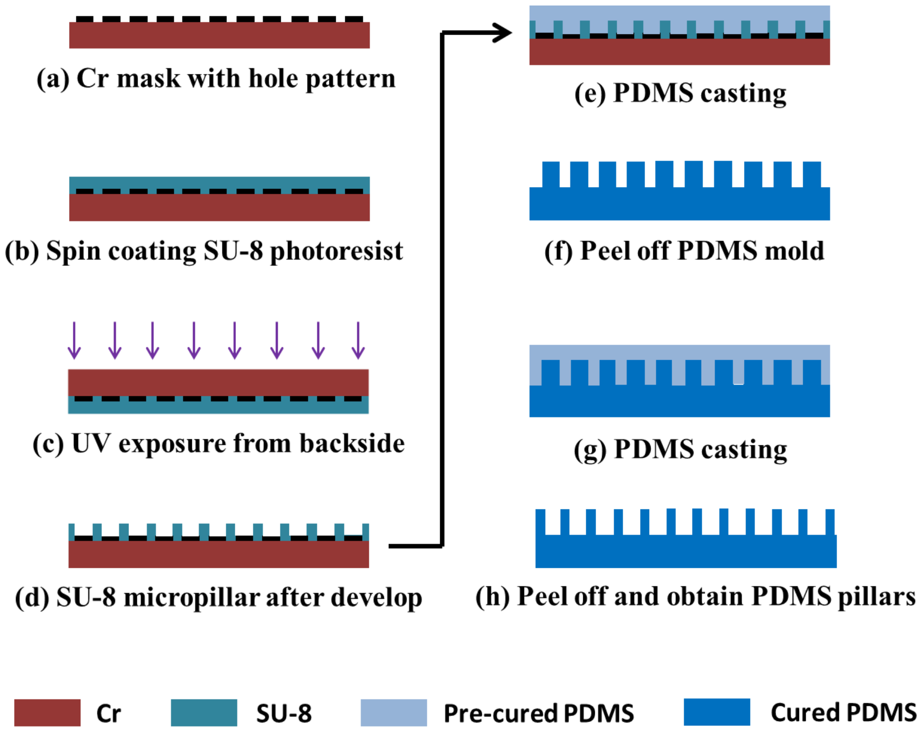

Figure 5.1 Schematic illustration of the fabrication process of micropillar substrates by photolithography and soft lithography.

5.2.3 Fabrication of the PDMS stencil

The processes of fabrication PDMS stencil is shown in **Fig. 5.2**. Firstly, the resist master mold was generated by using standard photolithographic techniques (**Fig. 5.2a** and

b). A SU-8 resist layer with thickness 50 µm spin coated on the Si wafer, followed by soft bake at 65 °C for 3 min and 95 °C for 15 min. After cooled down to room temperature, the wafer was exposed with a mask of the honeycomb network of a 500 µm period and a 100 µm line width and a UV light (365 nm) of 12.7 mJ/cm^2 for 20 s, following a post-bake process (3 min at 65°C and 5 min at 95°C). The mask was then developed in SU-8 developer for 5 min with mild agitation. After rinsing with isopropanol, the mask with patterned resist was dried with nitrogen gun, resulting in SU-8 master mold (**Fig. 5.2b**).

Then the PDMS stencil was fabricated base on weight compressing against the master, as illustrated in **Fig. 5.2c**. Before that, the resist master was treated with oxygen plasma and then parylene coating (introduced in Chapter 2). Then pre-cured PDMS (10:1) was spin coated on a silanized PDMS stamp (15:1) which was attached to a glass slide, at 500 rpm for 20s and then 2000 rpm for 20s. When spin-coating was complete, allow the sample to rest for 3 min before transferring it to a work bench. Then inverted the silanized PDMS slab and brought the PDMS-coated surface in contact with the silicon wafer containing an array of microfabricated honeycomb pillars. After that, place a 1 KG weight over the entire surface of the coverslip to allow microfabricated pillars to penetrate the uncured PDMS layer on the silanized PDMS slab at room temperature for 2 h, followed by curing at 100°C for 1 h. Next, place the entire assembly in a 60 °C oven for overnight to complete PDMS curing. Then a PDMS ring with inner and outer diameter 9 mm and 13 mm was mounting to the membrane after oxygen plasma treatment, with which the PDMS stencil could be easily peeled off (**Fig. 5.2d**).

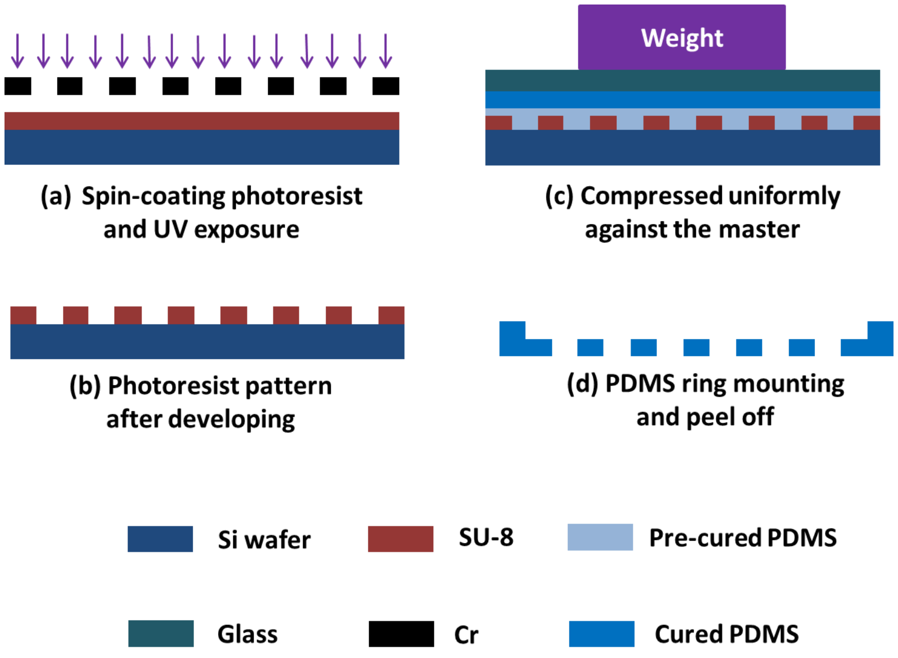

Figure 5.2 Schematic illustration of fabrication of PDMS stencil.

5.2.4 hiPSCs culture

hiPSCs of the 253G1 cell line were cultured with complete E8 medium in a culture dish coated with 1 : 100 diluted vitronectin at 37 °C in 5% CO_2. The medium was renewed every day until the cells reached about 80% confluence. Cells were then collected by dissociation using a 0.5 µM EDTA DPBS solution.

Before cell seeding, the micropillar substrates integrated with PDMS stencil were treated with oxygen plasma for 7 min to make them hydrophilic and avoid collapse. Then the samples were immediately immersed into 70% ethanol and meantime UV expose (30 min) for sterilization, followed by washing with DPBS twice. Afterwards, to obtain monolayer and hemisphere hiPSC aggregations, the micropillar substrates were treated in a DPBS solution with 1 : 100 and 1 : 500 diluted vitronectin for 1 h at 37 °C, respectively. Then, the substrates were placed in 12-well plate for cell seeding. hiPSCs at a cell density of 1.5×10^5 in 50 µL of E8 medium containing a 10 µM ROCK inhibitor (Y-27632) were plated on the surface of the substrates and the plate was transferred into an incubator for cell attachment for 1 h. Afterward, 2 mL of fresh E8 medium containing 10 µM ROCK inhibitor were added to the culture dish and the PDMS stencil was gently peeled off from the micropillar arrays. Then, the culture medium was replaced by E8 medium without the ROCK inhibitor after 24 h of incubation for monolayer or hemisphere hiPSC aggregation.

5.2.5 Scanning electron microscopy imaging

Cells cultured on different types of substrates were fixed with 4% v/v PFA in PBS for 30 min and then washed three times with PBS. Next, the samples were immersed in 30% ethanol for 30 min and successively in 50%, 70%, 80%, 90%, and 100% ethanol for 10 min each for dehydration, followed by nitrogen gas drying. The samples were sputter-coated with 5 nm platinum by sputtering. SEM images were obtained using a scanning electron microscope (SEM, Hitachi S3030) operated at 15 kV.

5.2.6 Immunocytochemistry

For immunostaining, samples were rinsed with PBS to remove unattached cells and the remaining cells were fixed with 4% PFA diluted in PBS for 15 min, followed by washing with PBS for three times. Then, cells were treated for permeabilization with 0.5% Triton X-100 15 min in PBS at room temperature to antigens outside nuclei. Next, cells were incubated in a blocking solution containing 10% v/v normal goat serum, 3% v/v bovine serum albumin, and 0.1% v/v Triton X-100 in D-PBS overnight at 4 °C to block out non-specific bindings. Afterward, cells were incubated with primary antibodies, i.e., anti-OCT4 (1 : 100 diluted, Life Technologies), anti-SSEA4 (1 : 100 diluted, Life Technologies), anti-α-actinin (Sarcomeric) antibody (1 : 100 diluted, Sigma), anti-Troponin T-C (1 : 200 diluted, Abcam), anti-connexin 43 (1 : 200 diluted, v) and anti-MYH6 (1 : 50 diluted, Santa Cruz), anti-Pax6 (1:100 diluted, Abcam), anti-Nestin (1:200 diluted, Sigma), anti-Olig2 (1 : 100 diluted, Abcam), anti-b tubulin III (1 : 400 diluted, Sigma) in blocking buffer overnight at 4 °C. After incubation with the primary antibody overnight at 4 °C, the samples were washed with PBS three times with each 5 min. Then cells were incubated with the appropriate secondary antibody in blocking buffer at room temperature for 1 h. For nuclei staining, cells were incubated with 300 ng/mL of DAPI for 30 min, and finally washed three times with PBS. The stained cells were observed under a LSM Zeiss 710 confocal microscope.

5.2.7 MTT assay

For proliferation study, 1×10^5 hiPSCs were seeded on the micropillar substrates with flat PDMS block as control. After 1, 2 and 3days post seeding, culture medium was removed and unattached cells were washed out with DPBS for three times. Subsequently, the proliferation of the cells on each specimen was determined by the standard MTT assay. Briefly, the specimens were incubated with 1 mL E8 culture medium and 100 µL 5 mg/mL 3-[4,5-dimethyl-2-thiazolyl]-2,5-diphenyl-2H-tetrazolium bromide (MTT) for 4 h. Thereafter, the culture media were extracted and 200 µL dimethyl-sulfoxide (DMSO) was added, subsequently the plate was incubated in incubator at 37°C for 30 min. When the crystal was sufficiently dissolved, 100 µL of the solution was pipet-ted into the well of a 96-well plate and tested by a microplate reader, at an absorbance of 490 nm.

5.2.8 Intracellular Ca^{2+} transient assays

To visualize the rhythmic activities, cells differentiated and cultured on micropillar substrates and flat PDMS were incubated in a mixture of 4 µL Fluo-4 AM (1mM), 500 µL Tyrode’s solution and 10 µL 10% pluronic F127 for 30 min and then renewed with a fresh Tyrode’s solution. Afterwards, optical images were recorded using a confocal microscope at 488 nm wavelength.

5.2.9 External electrical stimulation

The response of the differentiated cardiomyocytes cultured on micropillar substrates to the external electrical stimulation were investigated. Briefly, 2 platinum electrodes were assembled with a culture dish by silicone adhesive and connected to an electrochemical workstation (CH Instruments, Inc.) which generated pulsatile electrical signals. All connections were sealed using silicone adhesive and the assembled dish was sterilized before use by placing under UV light for 1 h. Electrical pulses at different frequencies (1 and 2 Hz) were considered for the experiment. The voltage remained at -1 V.

5.3 Results

5.3.1 Sample characterization

5.3.1.1 SEM imaging

We fabricated three types of micropillar arrays with the same diameter (2 µm) and pitch size (5.5 µm), but with different heights (2.7 µm, 7.2µm and 10.3µm). For clarity, the samples were labeled according to the pillar height (H), for example, H2.7 means a pillar array of height 2.7 µm. **Fig. 5.3** shows SEM images of the PDMS pillars of the three samples, illustrating the high quality of the fabrication. **Fig. 5.3** also shows the SEM pictures of PDMS honeycomb stencil with 500 μm period, 100 μm line width and 50 μm thickness, confirming the formation of transparent honeycomb holes.

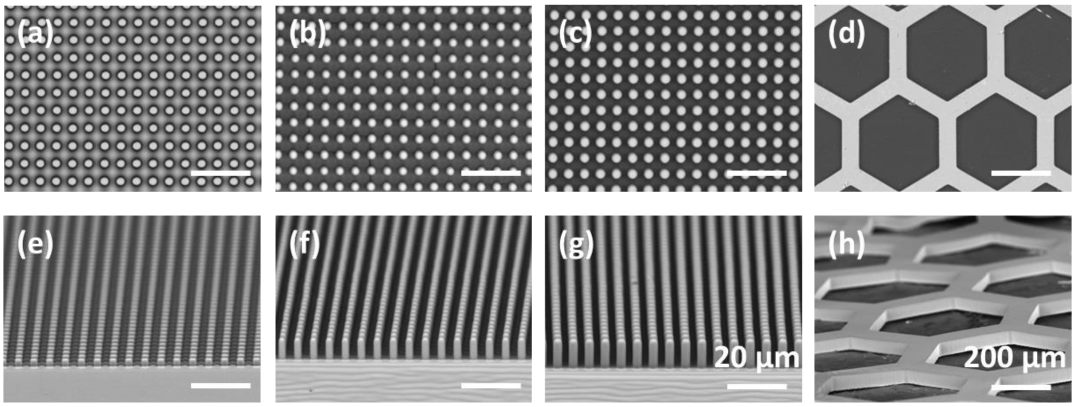

Figure 5.3 SEM images of fabricated micropillar arrays with different height. (a-c) Top view of micropillars with height 2.7 μm, 7.2μm and 10.3μm, respectively. (e-g) Side view of each substrate. (d, h) SEM images of PDMS stencil.

5.3.1.2 Effective stiffness of the elastomer pillars

To assess the effective stiffness of PDMS pillar substrates, the micropillars were considered as independent springs. The linear theory of elasticity was used to calculate the effective stiffness of the substrate as described in Chapter 3 and shown in **Fig. 5.4**, indicating a value of 168 KPa, 9 KPa and 3 KPa for the PDMS pillar arrays of heights 2.7 μm, 7.2μm and 10.3μm, respectively (2 μm diameter and 5.5 pitch size).

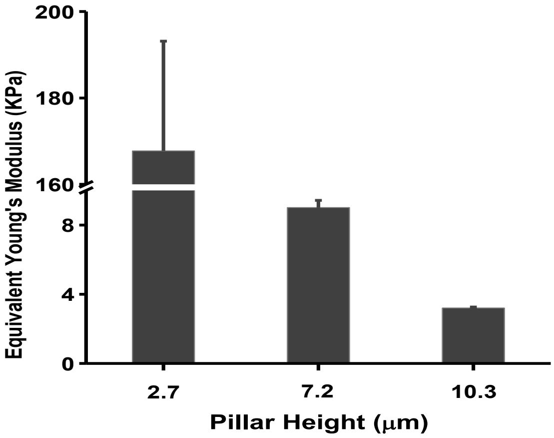

Figure 5.4 The equivalent Yong's modulus of the micropillar substrates.

5.3.2 hiPSC attachment and proliferation

The pillared PDMS substrate with height gradient was firstly used to evaluate the effect of the substrate stiffness on the hiPSCs attachment. Firstly, 1×10^5 cells in 50 μL of E8 medium containing different concentration of rock inhibitor (10 μM, 1 μM and 0.1 μM) were seeded on the pillar substrates coated with vitronectin at different dilution ratio in PBS (1:100, 1:500 and 1:1000). After 24h treatment with rock inhibitor, the culture medium was changed to E8 medium without rock inhibitor. After 24 h incubation, different aggregation morphology and attachment of hiPSCs on the micropillar substrates were formed, as shown in **Fig. 5.5**.

As can be seen, the concentration of rock inhibitor and vitronectin is critical for hiPSCs attachment. With 1:100 diluted vitronectin coating, the cells were well attached and spread after treatment with 10 μM rock inhibitor. With 1 μM rock inhibitor, the cells could merely attach on the short pillars area. With 0.1 μM rock inhibitor, much less cell attachment was found. Note that the hiPSCs formed stripe patterns due to the different attach ability of hiPSCs on the substrate area with different rigidity, indicating that the stiffness of the substrate affects the attachment of the hiPSCs. When the vitronectin dilution factor was 1:500, the cells were aggregated even with 10 μM rock inhibitor treatments and most of cells could not attach on the pillars and dies as single cells for treatment with low concentrations of rock inhibitor (1 μM and 0.1 μM). When coated with 1:1000 diluted vitronectin, the cells were aggregated as hemisphere after treat with 10 μM rock inhibitor, which detached after changing the medium. Thus, cells could hardly attach and survive on the pillars when a low concentration of vitronectin was applied for the surface coating and a low concentration of rock inhibitor was used for the EB aggregations on the pillar arrays.

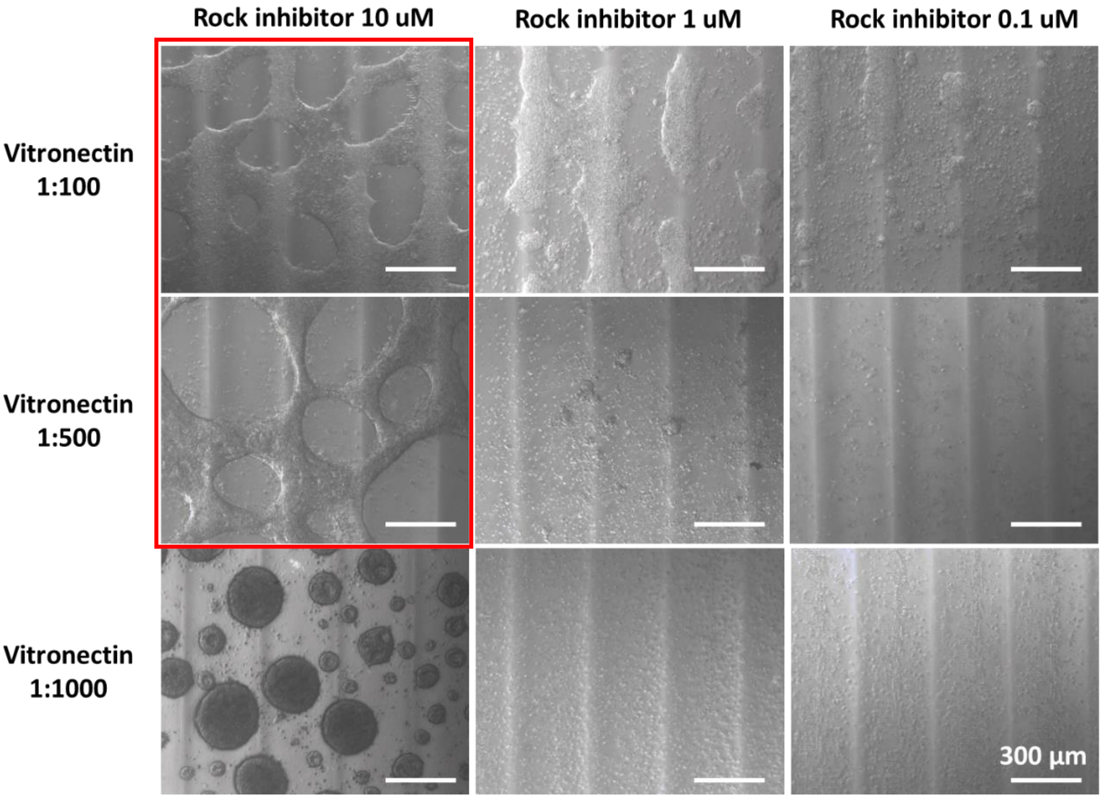

Figure 5.5 Phase contrast images of hiPSCs attach on micropillar substrates with different vitronectin coating and rock inhibitor treatment.

In order to investigate the effect of substrate stiffness on the hiPSCs attachment and proliferation more specifically, the three PDMS pillar arrays were coated with 1:100 or 1:500 diluted vitronectin in PBS. After seeding 3 h, the cells were fixed and stained with DAPI, followed by statistical analyses of the attached cell numbers, as shown in **Fig. 5.6a**. It can be seen that 78.2 ± 3.2% and 86.1 ± 3.4% cells could attach on the flat PDMS with 1:500 and 1:100 diluted vitronectin coating, respective. Compared to that on pillar substrates with stiffness 9 KPa and 3 KPa, more cells attached on the pillar substrate of stiffness 168 KPa (height 2.7 μm) showing 66.6 ± 3.4% and 71.2 ± 5.7% attachment on the 1:500 and 1:100 diluted vitronectin coating sample, respective. This means that hiPSCs are more likely to attach on stiffer substrate. Besides, the vitronectin concentration also played a key role in hiPSCs attachment: The higher the vitronectin concentration, the more the attached cells.

In order to figure out whether the pillars' aspect ratio affects the vitronectin coating, FITC labeled vitronectin was used to coat the pillar substrates with 1:100 and 1:500

diluted solutions. As shown in **Fig. 5.6b**, the amount of vitronectin absorption on pillar substrates was independent on pillar height for the same dilution. Therefore, the stiffness is the main influencing factor to the hiPSCs attachment.

To study the hiPSCs proliferation on the micropillar substrates, MTT assay was carried out after incubation for 1, 2 and 3 days to evaluate the cell viability. **Fig. 5.6c-d** show the results obtained with 1:100 and 1:500 diluted vitronectin coating, respectively. In both cases, the hiPSCs proliferation rate increased with the substrate effective stiffness. On the stiffer pillar substrate (168 KPa), the number of viable cells increased more rapidly on the pillars with 1:100 diluted coating than on that of 1:500 diluted coating, meaning that the integrin mediated adhesion facilitated hiPSC growth. However, on the softer pillar substrate (3 and 9 KPa), the increase of viable cells was comparable on two types of vitronectin coating. It is known that cells adhered to a substrate assemble well-organized networks of fibrous actin terminated at focal adhesions that link the cytoskeleton to the extracellular matrix via integrins. The cell proliferation is tightly related to the contractility of actin fibers and the focal adhesions [28–30]. The stiffer the substrate is, the larger the cell spreading, the more focal adhesion and the larger the contractility. With the same effective stiffness, a higher concentration adhesion molecule coating would increase the focal adhesions. With the same coating, a higher stiffness would increase the contractility. Within the saturation limit, both are in favor to the cell growth and proliferation.

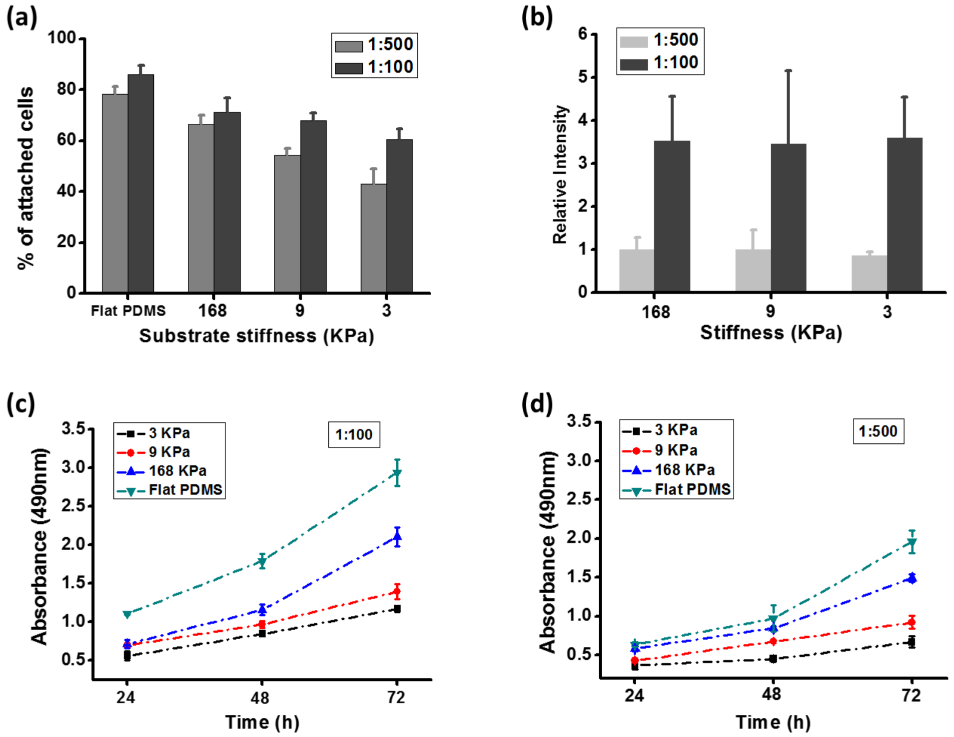

Figure 5.6 (a) The hiPSCs attachment on micropillar substrates. (b) Effect of substrate stiffness on vitronectin absorption. (c, d) MTT assay of cell proliferation on substrates with 1:100 and 1:500 diluted vitronectin coating.

5.3.3 Stencil assistant EBs formation

In order to obtain homogeneous EB on the micropillar arrays, a PDMS stencil mounted with a PDMS ring was placed on the pillar substrate during cells seeding. The schematic diagram is shown in Fig. 5.7a. Briefly, the stencil was placed on the pillar substrate. After coating with 1:500 diluted vitronectin, the cells in single state were seeded on the substrate. Then, the stencil was peeled off from the pillar surface after cells attachment (1 h after seeding), leaving separate cell colonies. Thus, EBs of hiPSCs could be formed on the pillar arrays with different pillar height. Since both pillars and stencil were made of PDMS, the stencil and pillar substrate could be well fitted (Fig. 5.7b and c). The PDMS ring was added for easy handling. Note that the PDMS stencil can be reused for several times.

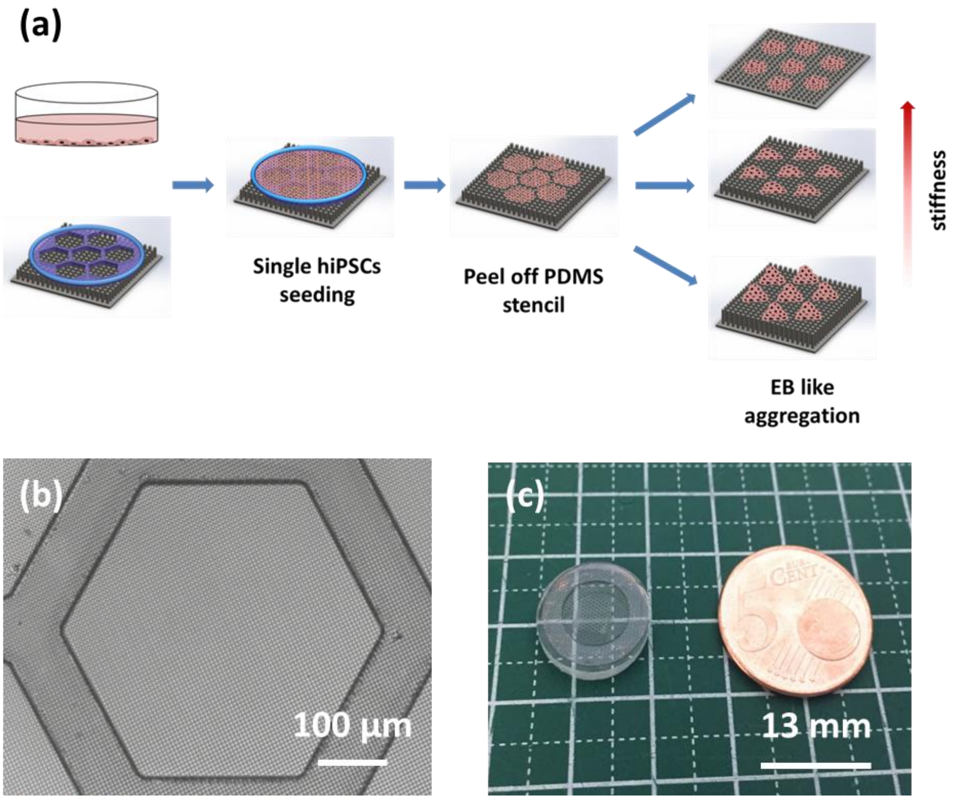

Figure 5.7 (a) A schematic depicting an experimental procedure to examine substrate mechanics-dependent hiPSCs embryoid body (EB) formation. (b, c) Phase contrast image and photograph of micropillar arrays covered with PDMS stencil.

5.3.3.1 The effect of the substrate stiffness

The formation of EBs on the pillar substrates with different stiffness is shown in **Fig. 5.8**. Clearly, the shape of EBs is substrate stiffness dependent. At day-2 after cell seeding, the stencil was removed, resulting in cell colonies in the area of each of the honeycomb compartments, separated by the blank of the stencil covered area. On the flat PDMS subtract, hiPSCs spread and crossed the area of the previously covered area. On the pillars, especially on the substrate of effective stiffness 3 KPa and 9 KPa, the cell aggregates were contracted. After 24 h culture in E8 medium with rock inhibitor (day -1), the cells were gathered in the center of each honeycomb compartment. After changing to fresh E8 medium without rock inhibitor and culture for 24 h (day 0), the hiPSCs were contracted and formed uniform EB like hiPSC colonies on the pillar substrates. While on the flat PDMS, the neighboring hiPSCs colonies might be connected as rigid substrates promote hiPSCs spreading and proliferation.

Clearly, the stencil, the vitronectin coating and the substrate stiffness are all important for the formation of uniform EBs. The stencil initiated the process by creating separated cell clusters which are homogenously distributed on the surface of the honeycomb defined pattern. Vitronectin is an important component of the ECM for hiPSCs attachment through interactions with a variety of integrin, especially αVβ5 integrin. Compared with 1:100 diluted vitronectin coating for normal iPSCs culture, 1:500 diluted vitronectin gave a weaker cell attachment on substrate so that hiPSCs can be more easily attached between each other (**Fig. 5.5**). Finally, a stiffer substrate promotes cell spreading and formation of a cytoskeleton at higher contractile forces so that it resulted in more platen EBs.

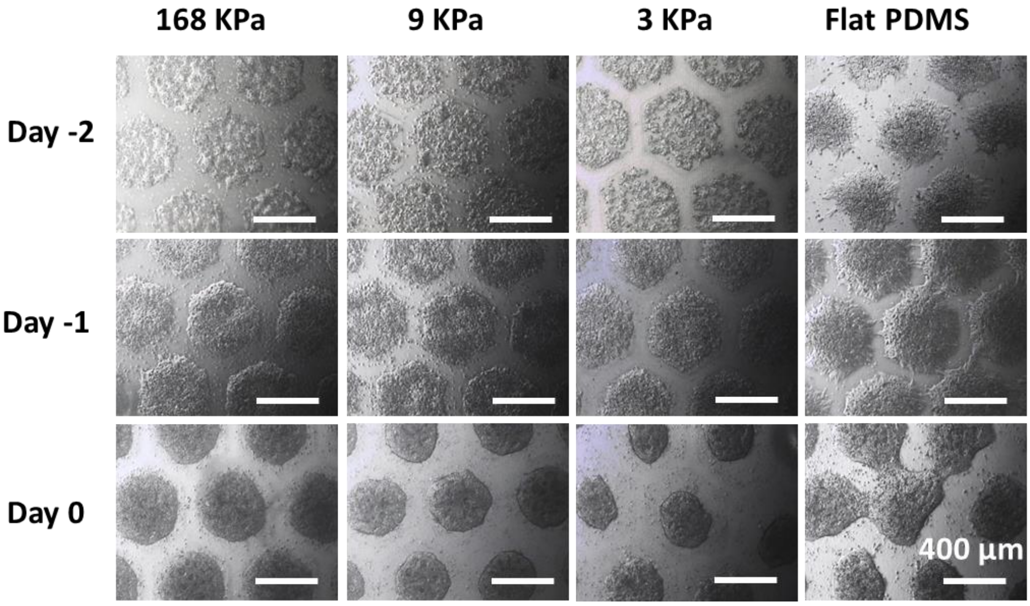

Figure 5.8 Phase contrast images of the formation of hiPSC EBs on micropillar arrays with different stiffness.

5.3.3.2 The effect of cell seeding density

Previous studies reported that the morphology and the homogeneity of the EBs is a deciding factor in the lineage commitment of hiPSCs. Herein, the effect of the cell seeding density on EBs morphology was evaluated (**Fig. 5.9**). Cell densities with 4×10^6, 3×10^6 and 2×10^6 cells/mL were tested on micropillars. As can be seen, with the cell density decreasing, the EBs were smaller on the three types of micropillar substrates, suggesting that the EBs size can be controlled by the cell seeding density. And it proved again that smaller EBs formed on soft substrate with different cell seeding densities. As statistic, when seeding 4×10^6 cells/mL, the average EB area was about 1.1×10^5, 7.7×10^4 and 7.5×10^4 μm^2 on pillar substrates with stiffness 168 KPa, 9 KPa and 3 KPa, respectively. While with cell density 2×10^6 cells/mL, the EB area were much smaller with 3.5×10^4, 3.4×10^4 and 2.4×10^4 μm^2, respectively (**Fig. 5.9b**). The EB circularity was also investigated with the different seeding density. No significant differences were found in the circularity between different cell density on the same stiffness, or in crossed comparisons at a distinct stiffness, with generally the circularity 0.9 on three types of pillar substrates with tested cell densities, except that a slightly lower circularity (0.87) was observed on stiff substrate when the cell density was low (2×10^6 cells/mL) (**Fig. 5.9c**).

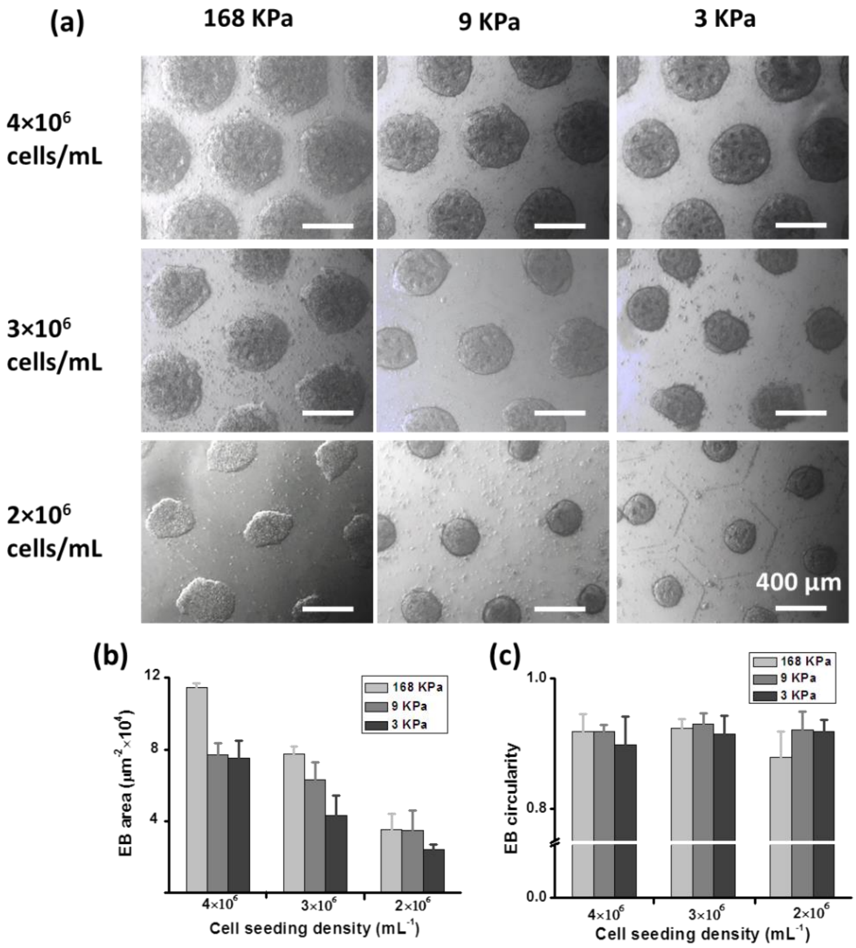

Figure 5.9 Effect of cell seeding density on the morphology of EBs on micropillar substrates. (a) Phase contrast images of EBs on pillars with different cell densities. (b, c) statistic of EBs area and circularity with the cells seeding density 4×10^6, 3×10^6 and 2×10^6 cells/mL.

5.3.3.3 Pluripotency of hemisphere EBs

To evaluate the stemness of the EBs generated on the micropillar substrates, the pluripotent stem cell markers OCT4 and SSEA4 were used to stain the EBs and flat cell layer on flat PDMS as control after cultured 3 days. The immunofluorescence images show clearly that the expression of these markers was maintained (**Fig. 5.10a**). By measuring the fluorescence intensity ratio of OCT4/SSEA4 to DAPI using imageJ software, the OCT4/SSEA4 positive cells on flat PDMS and the micropillar substrates could be compared quantitatively, as shown in **Fig. 5.10b** and **c**, indicating that the expression levels of the positive pluripotent stem cells markers OCT4 and SSEA4 were maintained for the hiPSCs cultured on micropillar arrays compared with control, and the distinctive colony morphology did not affect levels of pluripotency during the examined culture period.

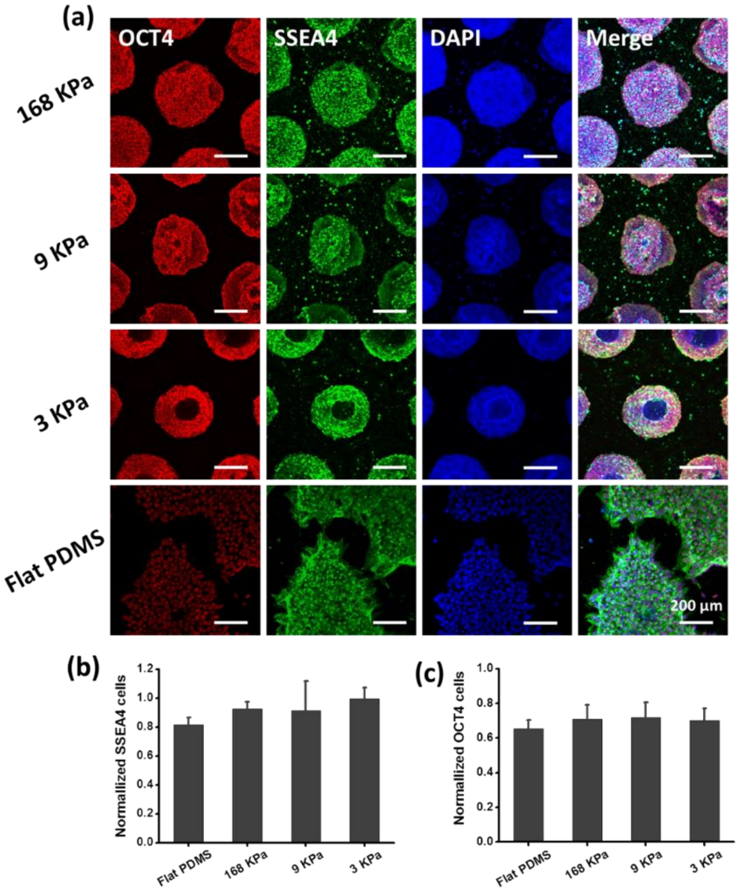

Figure 5.10 (a) Immunostaining images of hiPSCs on micropillar substrates with stiffness 168 KPa, 9 KPa and 3 KPa after culture 3 days (red: OCT4, green: SSEA4, blue: DAPI) (b, c) Bar plot showing the normalized SSEA4 and OCT4 cells on micropillar substrates and flat PDMS.

5.3.3.4 3D view of the EBs

The dependency of EB morphology on scaffold stiffness was confirmed by confocal z stack imaging. The internal structure of 3D cell colonies on micropillar substrate with stiffness 168 KPa and 3 KPa were shown in **Fig. 5.11** and **Fig. 5.12**. The hiPSCs seeded onto the substrates proliferated and formed distinct cell colonies depending on the scaffold stiffness. After a pre-culture period of 3 days with proliferation medium, the colonies on rigid substrate exhibited round and more flat morphology with relatively large diameter (around 350 µm). While cells on softer substrate (3 KPa) diaplayed more 3D morphology and with smaller diameter. Interestingly, a central cavity formed on the softer substrate. To the best our knowledge, this unique phenomenon of 3D colony formation has never been demonstrated on micropillar substrates with specific mechanical properties.

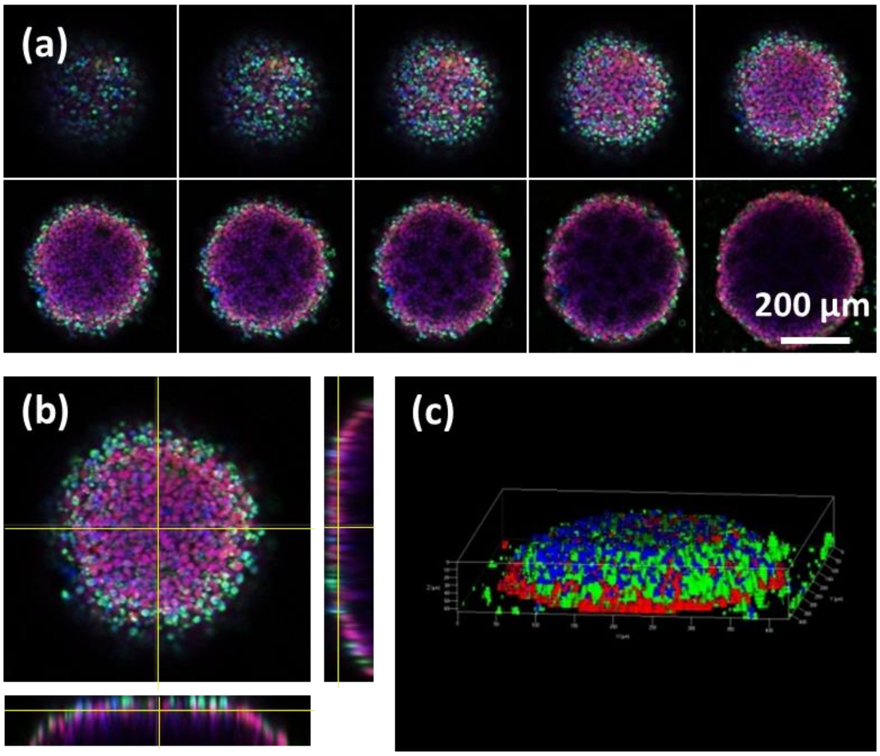

Figure 5.11 Immunofluorescence images of a hiPSCs EB cultured on a 168 kPa pillar substrate by confocal microscopy (red: OCT4, green: SSEA4, blue: DAPI). (a) A series of depth-wise cross-sectional images were acquired at 5 µm distances. (b) A cross-section of the merged images. (c) 3D view of the EB.

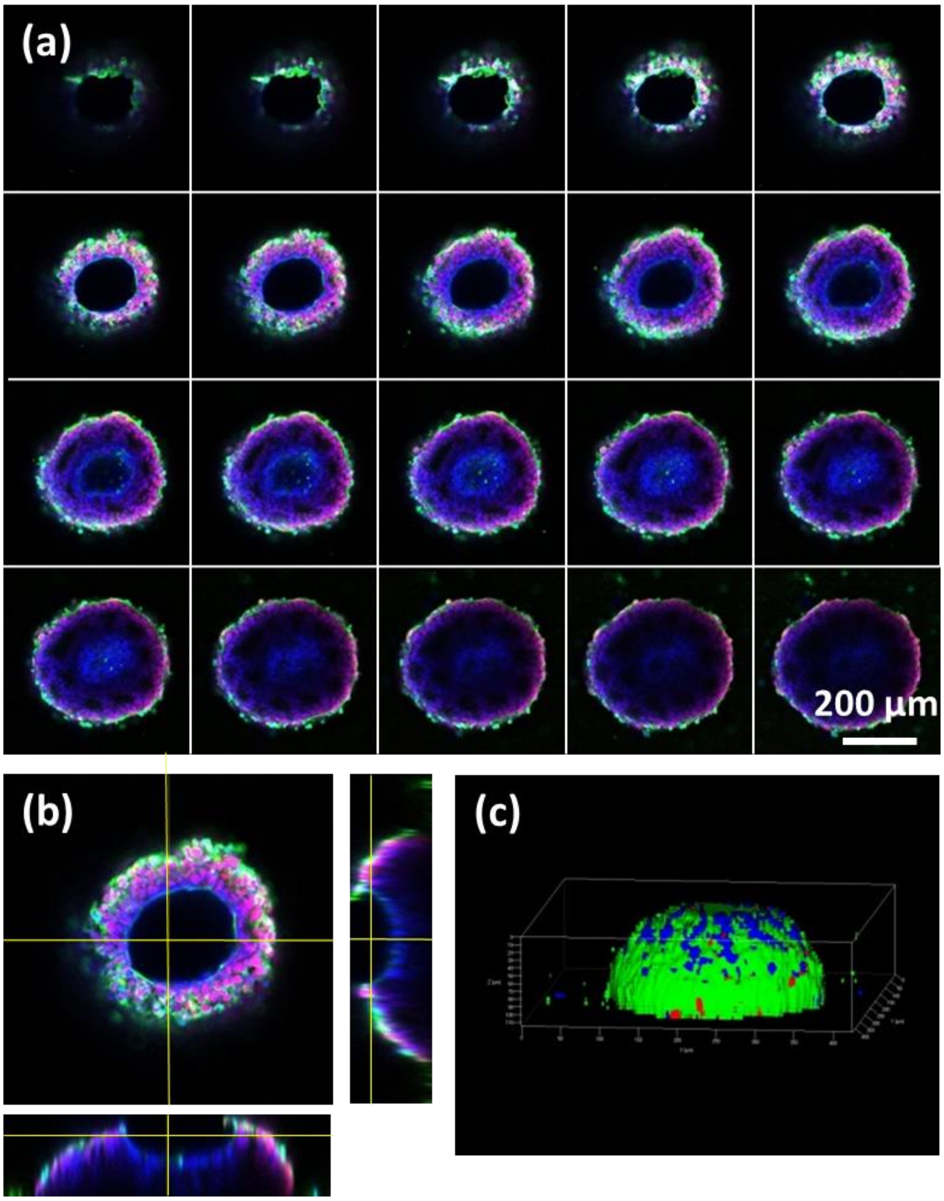

Figure 5.12 Immunofluorescence images of a hiPSCs EB cultured on a 3 kPa pillar substrate by confocal microscopy (red: OCT4, green: SSEA4, blue: DAPI). (a) A series of depth-wise cross-sectional images were acquired at 5 mm distances. (b) A cross-section of the merged images shows a pit in the upper of the EB. (c) 3D view of the EB.

The 3D morphology of EB on pillar substrates with different stiffness was demonstrated in **Fig. 5.13**. As can be seen, the central cavity only formed on softer substrates, i.e., 9 KPa and 3 KPa. Moreover, a bigger cavity generated on substrate with stiffness 3 KPa (**Fig. 5.13c**). From the side view, it is obvious that with the stiffness decreasing, the diameter decreased (350 µm, 300 µm and 260 µm, respectively), but the height of the EBs increased (around 60 µm, 80 µm and 110 µm, respectively).

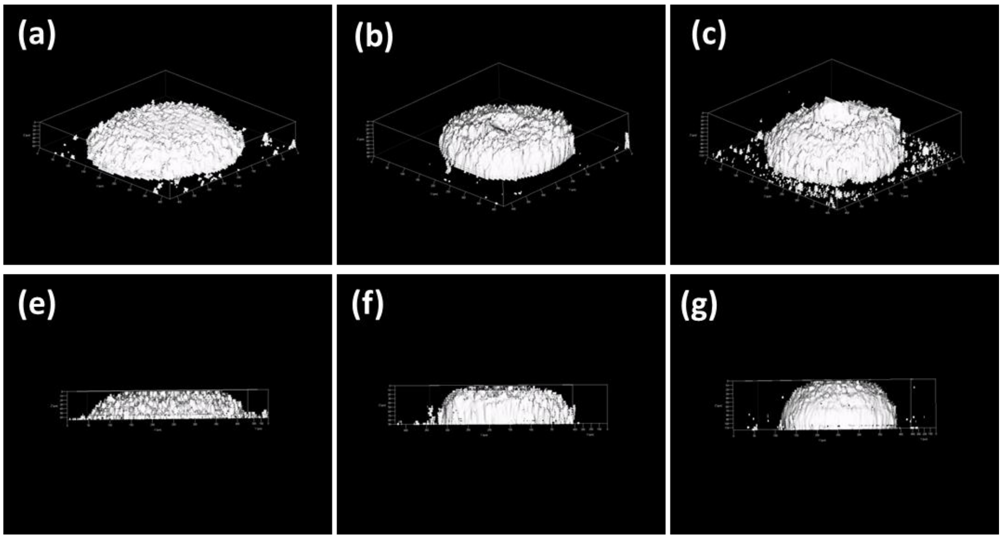

Figure 5.13 Confocal images were reconstructed to render a 3D surface of hiPSCs colony by using ImageJ software (a and e, b and f, c and g: representative colony morphologies on 168 KPa, 9 KPa and 3 KPa substrates, respectively).

To understand the mechanism of the development of 3D colony on pillar substrates, we examined the morphological changes using SEM. With short pillars (2.7 µm, shown as **Fig. 5.14a**), cells can spread largely due to the effective rigid substrate. With higher magnification image (**Fig. 5.14a**), we can see the cells stretched on the top surface of pillars with minimal deform of the elastic micropillars. However, on high pillar arrays (**Fig. 5.14b** and **Fig. 5.14c**), the cells on the edges were contractive, especially on pillar arrays with height 10.3 µm. Due to the cells contraction, the high pillars were deformed. The cavity found in **Fig. 5.14b** and **Fig. 5.14c** confirmed that this novel three-dimensionality was developed by cell-mediated tension on the soft micropillar substrates. Unlike large EBs, which form central cavities due to nutrient limitations, cells on micropillar substrates have the advantage of nutrient diffusion through the space between the pillar. Considering the fact that the maximization of cell–cell interaction by forming EBs typically results in priming of the cells for subsequent differentiation, the control of colony dimensionality using micropillar arrays may provide a more robust and efficient means to control pluripotent stem cell differentiation.

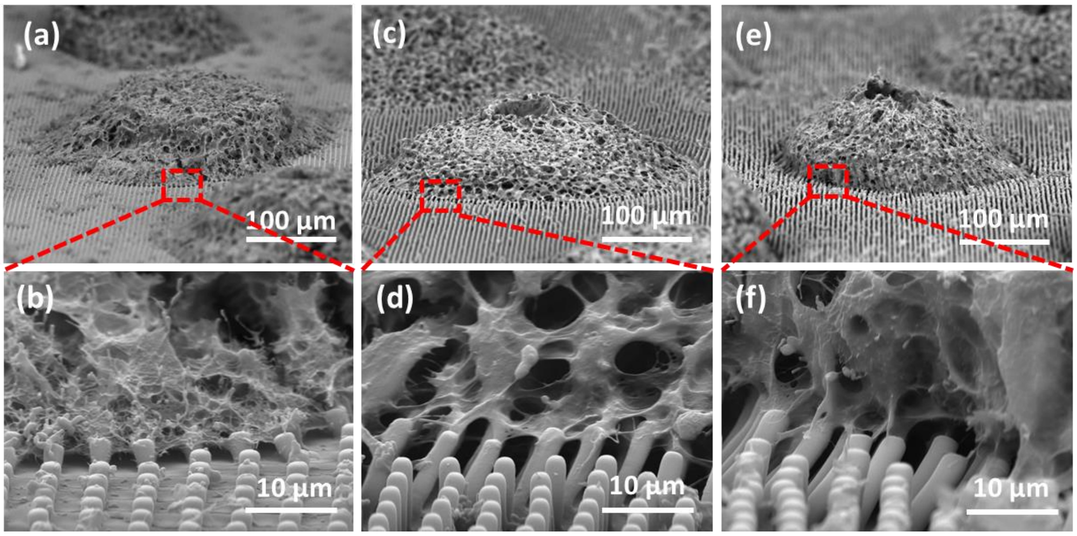

Figure 5.14 SEM images of EB on micropillar substrates with stiffness (a, b) 168 KPa, (c, d) 9 KPa and (e, f) 3 KPa.

5.3.4 Cardiac differentiation on micropillar substrates

5.3.4.1 Differentiation protocol

After formed EBs on micropillar substrates, cadiomyocytes were started to differentiate according to the developed protocol, by modulating Wnt signaling with small molecules. Cardiac differentiation was then initiated by reverting the medium to RPMI 1640 enriched with 2% B27 supplement without insulin and 12 µM CHIR99021. This medium was replaced with RPMI supplemented with B27 minus insulin after 24 h. Two days later, the medium was exchanged for fresh RPMI-B27 minus insulin containing 5 µM of IWP2 for 48 h. On day 5 of differentiation, IWP2 was removed by changing new RPMI/B27 without insulin medium. Then the medium was replaced by RPMI 1640 completed with 2% B27 supplement. As shown in **Fig. 5.15a**, the cells morphology on different substrates during the proliferation process was recorded with microscope. After adding the GSK3 inhibiotr, the cells around the edges of the EBs began to migrate and as the protocol processing. After around 5 days, the separated EBs begun to connect to each other and formed a thick cell sheet (**Fig. 5.15b**). With the same protocol, hiPSCs cultured on flat PDMS were differentiated into cardiomyocytes as a control. At day 7 or day 8, the differentiated cardiac cells begun to contract on the micropillars and the flat PDMS. At day 14, the cardiac contraction became robust and homogeneous over the whole micropillar area. In contrast, the contraction of the cells differentiated on flat PDMS was much less uniform with separate areas beating.

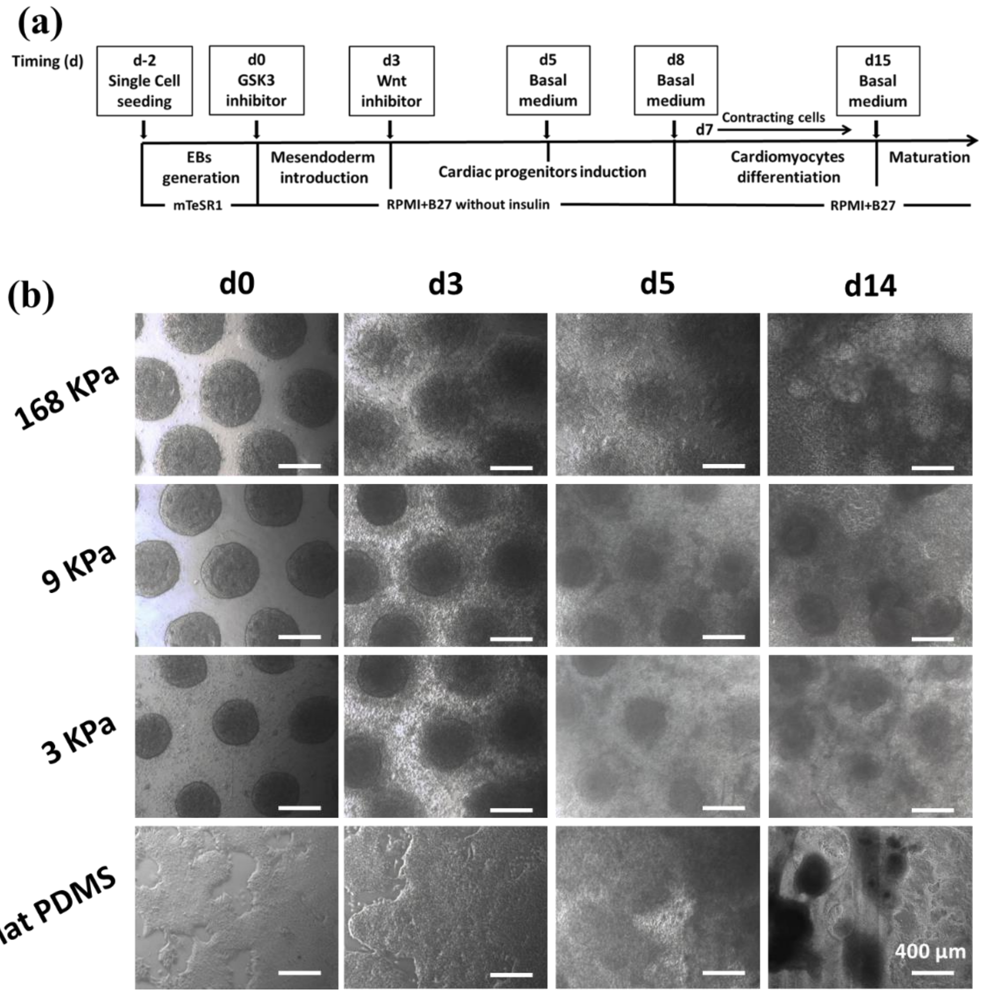

Figure 5.15 (a) Schematic diagram of the protocol for cardiomyocytes differentiation from hiPSCs generated EBs on micropillar substrates. (b) Phase contrast images of hiPSCs morphology during differentiation process.

5.3.4.2 Immunostaining of differentiated cardiomyocytes

Cardiac-specific markers including sarcomeric α-actinin, troponin I, α-MHC and connexin43 were immunostained to assess the phenotype of the obtained cardiomyocytes after differentiation for 15 days (shown as Fig. 5.17 and Fig. 5.18). While sarcomeric α-actinin and troponin I are the two specific proteins, involved in the actin-myosin contraction complex, connexin43 is a well-known gap junction protein responsible for synchronous contraction of the cells. α-MHC, a cardiac muscle-specific protein involved in active force generation. As can be seen, the cells mainly adopted a round morphology without intact formation of troponin I and α-MHC on soft pillar substrate (3 KPa) while cells on 9 KPa or 168 KPa substrates displayed much clearer sarcomeric organization in troponin I and α-MHC, which is typical in mature cardiomyocytes. On flat PDMS, only a few cells had positive expression in troponin I and α-MHC, indicating a relatively low differentiation efficiency on flat PDMS. α-actinin was positive in the cells differentiated on all substrates but more uniform and highly organised sarcomeric α-actinin structures were evident across 9 KPa or 168 KPa substrates in contrast to soft pillar substrate. On control (flat PDMS), the cells also displayed positively in α-actinin but with less less sarcomeric structure. Thus, the differentiated cells on pillar substrate, especially on substrate with stiffness 9 KPa, exhibited more organised myofilament assembly. Our immunostaining results for connexin43 gap junction proteins also demonstrated a similar trend. While on pillar substrate with stiffness 3 KPa, connexin43 was found to be less expressed in the cells compared with stiffer substrates. Therefore, rigid pillar substrates demonstrated improved cell-cell coupling with mature contractile machinery as compared to soft pillar substrate.

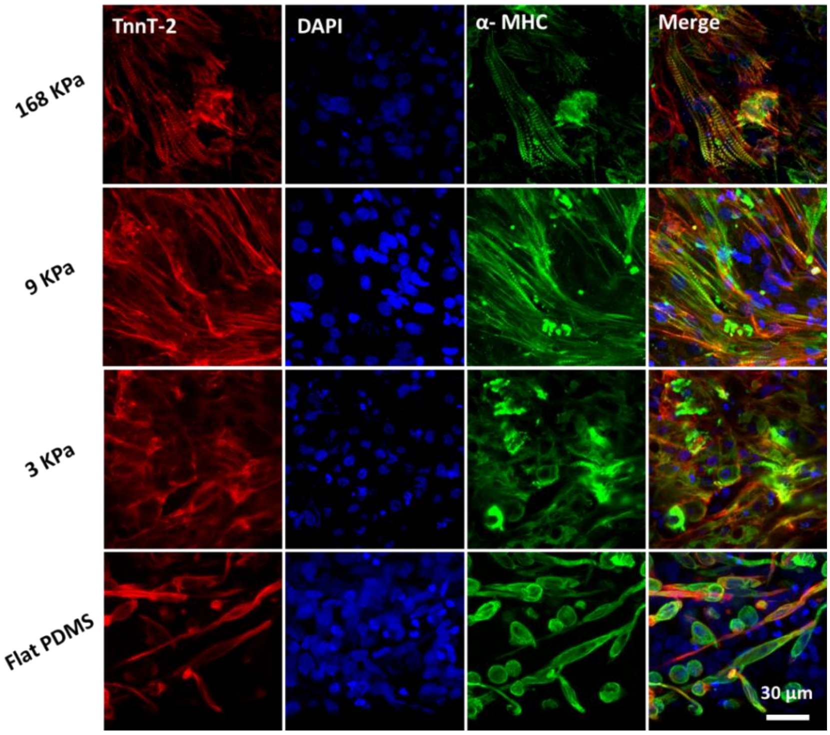

Figure 5.17 Immunofluorescence images of differentiated cells on micropillar substrates with stiffness 168 KPa, 9 KPa and 3 KPa at day 15. Differentiated cells on flat PDMS as a control. TnnT2 (red), α-MHC (green), nuclei (blue).

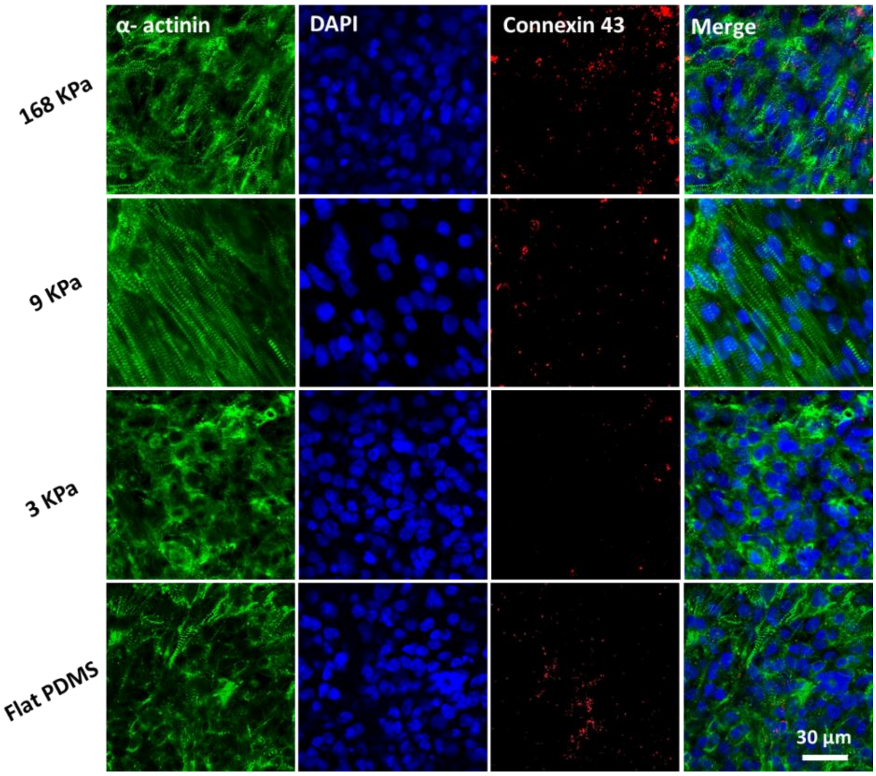

Figure 5.18 Immunofluorescence images of differentiated cells on micropillar substrates with stiffness 168 KPa, 9 KPa and 3 KPa at day 15. Differentiated cells on flat PDMS as a control. α-actinin (green), connexin43 (red), nuclei (blue).

5.3.5 Beating behavior of differentiated cardiomyocytes

To assess tissue-level functionalities, beating behavior of cardiomyocytes differentiated on micropillar substrates was further analyzed by calcium (Ca^{2+}) transient. **Fig. 5.19** shows the calcium images of differentiated cardiac cells cultured on different substrates. In order to evaluate the synchronization of the beating behavior, three different sites within each sample were randomly selected and the time course of averaged fluorescence intensity were plotted in **Fig. 5.19**. It is known that the fluorescence intensity of a calcium image is proportional to the concentration of intracellular Ca^{2+}, which is an important messenger related to the electric and mechanical activities of the cells. As can be observed, calcium signal occurred at different frequencies across the considered spots on flat PDMS, which is may contributed to the cell clusters formation during differentiation and thus beating separately. While cardiomyocytes cultured on micropillar substrate exhibited more synchronous, stable and robust beating behavior, especially on micropillar substrates with lower stiffness (9 KPa and 3 KPa) on which the cells demonstrated synchronized calcium spikes within all 3 selected spots. Notably, the cells on rigid pillar substrate (168 KPa) exhibited a rhythmically and intermittently beating behavior.

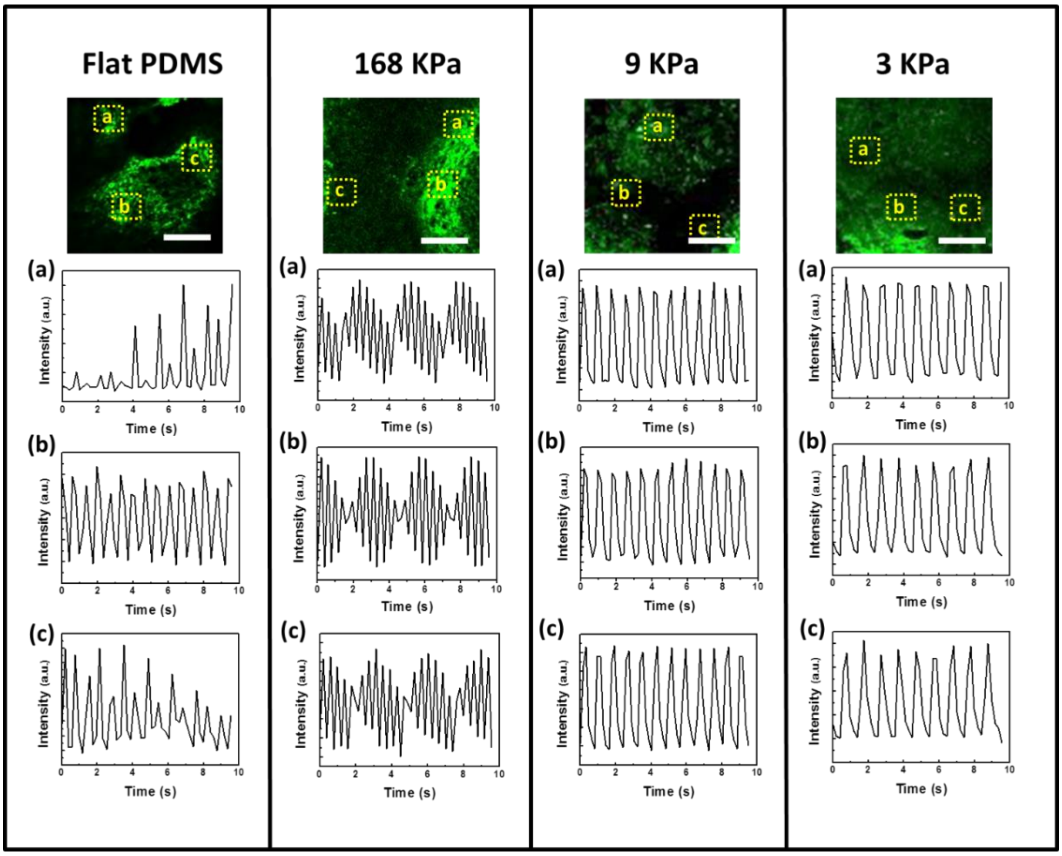

Figure 5.19 Calcium transients of cardiomyocytes at day 21 on flat PDMS, micropillar substrates with stiffness 168 KPa, 9 KPa and 3 KPa. Scale bar: 200 μm. Three independent regions of interest were randomly selected in each sample and the corresponding time course of fluorescence intensity taken from the regions were plotted in each group.

The beating frequency of cardiomyocytes differentiated on substrates with different mechanical properties is shown in **Fig. 5.20**. As can be seen, cardiac cells on flat PDMS displayed higher beating frequency (78 ± 12 /min) compared to that on soft micropillar substrate (9 KPa and 3 KPa). However, the cells on pillar substrates with stiffness 168 KPa exhibited a significantly higher beating frequency (138 ± 6 /min).

Such calcium transient profile further confirmed that the contraction of cardiac sheet on micropillars showed much better synchronism and homogeneity, compared to the control differentiation on flat PDMS. This is because on micropillars, cells formed separated homogeneous EBs first before differentiation, and during differentiation, each EB was exposed to the differentiation factors equally all over the whole substrate. Then the cells migrated and connected to form one thick cell layer, leading to a homogeneous beating cardiac sheet. However, on flat PDMS, cells were a large flat clone before differentiation and cell migration occurred during differentiation leading to a annular apophysis close to the edge, which was the only beating region, while most areas in the center of the annular apophysis circle were clam with almost no contraction. In addition, cardiomyocytes on micropillars displayed rigidity-dependent beating frequency. On micropillar substrate with stiffness 168 KPa, the cells had the fastest beating frequency, which could be explained as follows: as expected, cell strain always exceeded matrix strain, i.e., $\varepsilon_{cell} \geq \varepsilon_{out}$, because the cells are the source of contraction [31]. The strain sustained within the cell is the difference that is ‘felt’ intracellularly during contraction: $\varepsilon_{in}=\varepsilon_{cell}-\varepsilon_{out}$. Note that on stiffest micropillar arrays, which mechanically mimic a post-infarct fibrotic scar, cells overstrained themselves, and stopped beating periodicity. On soft matrices, cell strains transmit almost completely to the matrix and, so, intracellular strain ε_{in} is small. On the stiffest matrices, cells are highly strained but cannot significantly strain the matrix ($\varepsilon_{out}\rightarrow 0$), yielding $\varepsilon_{in}\approx\varepsilon_{cell}$. In addition, the difference of beating frequency between flat PDMS and micropillars with stiffness 168 KPa may result from the minimal exogenous contact and a maximal efficiency of cell–medium exchange.

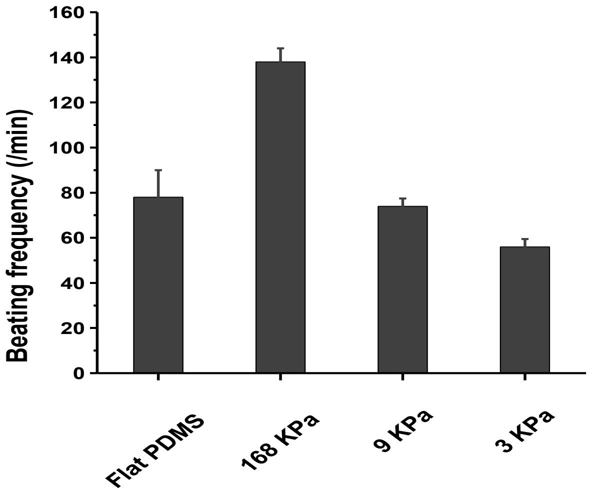

Figure 5.20 Synchronous beating frequency of cardiomyocytes at day 21 cultured on flat PDMS and micropillar substrates with stiffness 168 KPa, 9 KPa and 3 KPa.

5.3.6 Impact of external electrical stimulation

Differentiation cardiomyocytes were utilized to evaluate the capability of the micropillar constructs for accommodation of external electrical stimuli, as shown in **Fig. 5.21**. On stiffest micropillars, the beating frequencies did not change with the electrical stimuli, whereas the frequency of periodic stopping became shorter. On substrate with lower stiffness, the beating frequencies of cells were much faster with the increasing stimuli frequency. In particular, the beating frequency of cells on pillar with intermediate stiffness (9 KPa) almost doubled (from 72 ± 6 to 120 ± 9 /min), indicating that the cardiomyocytes on matrix with heart-like elasticity were highly impressionable to electrical stimuli.

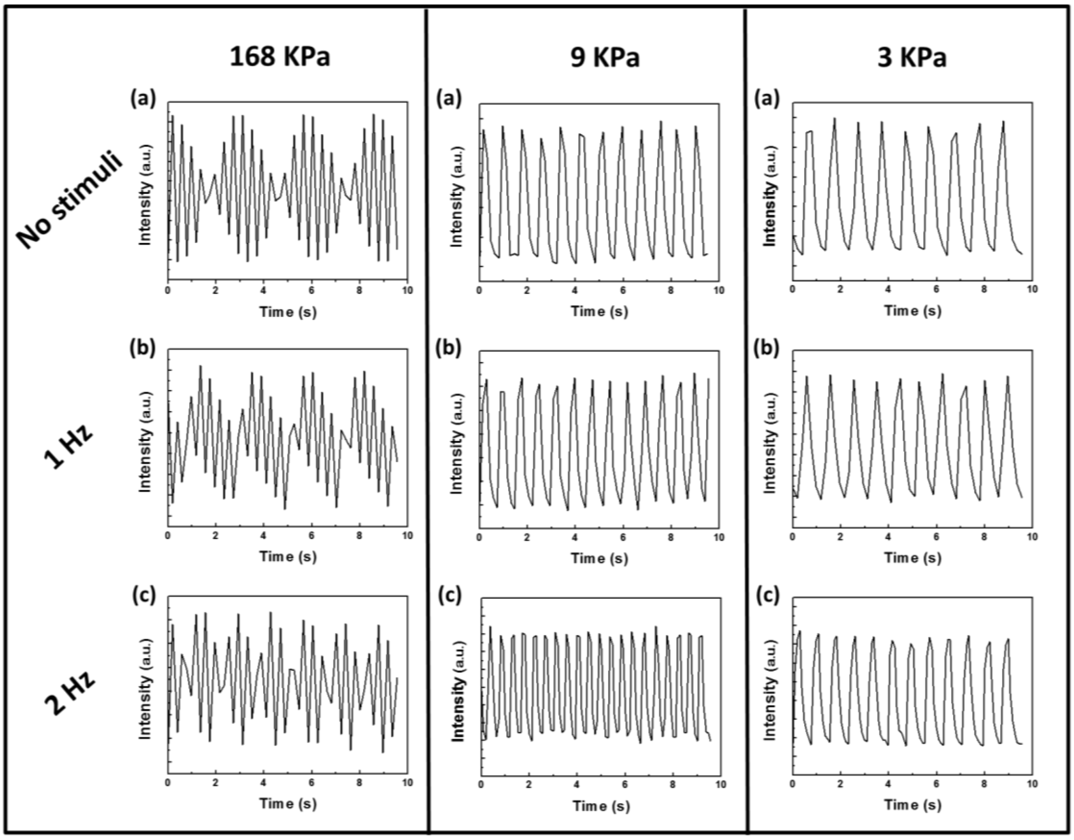

Figure 5.21 Beating frequency signals for all types of micropillar substrates at different applied electrical stimuli frequencies.

5.4 Conclusion

We have demonstrated the use of micropillar substrates with controlled stiffness for cardiomyocytes differentiation from hiPSCs. Firstly, the culture behaviors of hiPSCs on micropillars showed that stiffer substrates favor the hiPSCs attachment and proliferation. Then, uniform EBs were formed on the micropillar arrays with the assist of a patterned PDMS stencil. Interestingly, the immunostaining and SEM results showed that the morphology and dimensionality of the EBs displayed distinguish differences because of the elasticity of the underlying substrates. Afterward, the EB-like colonies were used for cardiac differentiation on the micropillars, showing a clear stiffness dependence of the processes. In addition, the beating behaviors were investigated. The Ca^{2+} transient analysis illustrated that differentiation from uniform EBs could benefit the synchronous beating of cardiac cells and the beating frequencies were highly dependent on matrix. Finally, the results also showed that cardiomyocytes on matrix with heart-like elasticity were highly impressionable to electrical stimuli.

References

[1] K. Takahashi, K. Tanabe, M. Ohnuki, M. Narita, T. Ichisaka, K. Tomoda, S. Yamanaka, Induction of Pluripotent Stem Cells from Adult Human Fibroblasts by Defined Factors, Cell. 131 (2007) 861–872.

[2] J. Yu, M.A. Vodyanik, K. Smuga-Otto, J. Antosiewicz-Bourget, J.L. Frane, S. Tian, J. Nie, G.A. Jonsdottir, V. Ruotti, R. Stewart, I.I. Slukvin, J.A. Thomson, Induced Pluripotent Stem Cell Lines Derived from Human Somatic Cells, Science (80). 318 (2007).

[3] V.K. Singh, M. Kalsan, N. Kumar, A. Saini, R. Chandra, Induced pluripotent stem cells: applications in regenerative medicine, disease modeling, and drug discovery., Front. Cell Dev. Biol. 3 (2015) 2.

[4] M. Rosner, K. Schipany, M. Hengstschläger, The Decision on the “Optimal” Human Pluripotent Stem Cell, Stem Cells Transl. Med. 3 (2014) 553–559.

[5] J. Li, W. Song, G. Pan, J. Zhou, H. Yu, T. Zhao, N. Goshima, S. Yamanaka, K. Lau, D. Baylink, X. Zhang, T. Kunisada, M. Takahashi, J. Takahashi, H. Saji, S. Yamanaka, S. Hartouni, E. Howie, L. Jakkula, D. Joo, K. Killpack, A. Laufer, J. Mazzotta, R. Smith, L. Stevens, C. Stuber, L. Tan, R. Ventura, A. Woo, I. Zakrajsek, Advances in understanding the cell types and approaches used for generating induced pluripotent stem cells, J. Hematol. Oncol. 7 (2014) 50.

[6] P. Joanne, M. Kitsara, S.-E. Boitard, H. Naemetalla, V. Vanneaux, M. Pernot, J. Larghero, P. Forest, Y. Chen, P. Menasché, O. Agbulut, Nanofibrous clinical-grade collagen scaffolds seeded with human cardiomyocytes induces cardiac remodeling in dilated cardiomyopathy, Biomaterials. 80 (2016) 157–168.

[7] S. Asgari, M. Moslem, K. Bagheri-Lankarani, B. Pournasr, M. Miryounesi, H. Baharvand, Differentiation and Transplantation of Human Induced Pluripotent Stem Cell-derived Hepatocyte-like Cells, Stem Cell Rev. Reports. 9 (2013) 493–504.

[8] T. Kondo, M. Funayama, K. Tsukita, A. Hotta, A. Yasuda, S. Nori, S. Kaneko, M. Nakamura, R. Takahashi, H. Okano, S. Yamanaka, H. Inoue, Focal Transplantation of Human iPSC-Derived Glial-Rich Neural Progenitors Improves Lifespan of ALS Mice, Stem Cell Reports. 3 (2014) 242–249.

[9] S. Ahadian, S. Yamada, M. Estili, X. Liang, R. Banan Sadeghian, K. Nakajima, H.

Shiku, T. Matsue, A. Khademhosseini, Carbon nanotubes embedded in embryoid bodies direct cardiac differentiation, Biomed. Microdevices. 19 (2017) 57.

[10] S. Ahadian, S. Yamada, J. Ramón-Azcón, K. Ino, H. Shiku, A. Khademhosseini, T. Matsue, T. Matsue, Y. Sakka, H. Bae, T. Matsue, A. Khademhosseini, Rapid and high-throughput formation of 3D embryoid bodies in hydrogels using the dielectrophoresis technique, Lab Chip. 14 (2014) 3690–3694.

[11] A. Higuchi, Q.-D. Ling, S.S. Kumar, Y. Chang, A.A. Alarfaj, M.A. Munusamy, K. Murugan, S.-T. Hsu, A. Umezawa, Physical cues of cell culture materials lead the direction of differentiation lineages of pluripotent stem cells, J. Mater. Chem. B. 3 (2015) 8032–8058.

[12] Y. Sun, S. Weng, J. Fu, Microengineered synthetic cellular microenvironment for stem cells., Wiley Interdiscip. Rev. Nanomed. Nanobiotechnol. 4 (2012) 414–27.

[13] Y. Shao, J. Sang, J. Fu, On human pluripotent stem cell control: The rise of 3D bioengineering and mechanobiology, Biomaterials. 52 (2015) 26–43.

[14] J.A. Efe, S. Ding, The evolving biology of small molecules: controlling cell fate and identity, Philos. Trans. R. Soc. London B Biol. Sci. 366 (2011).

[15] X.-L. Wang, C.-Y. Wang, X.-J. Yu, Y.-S. Zhao, J. Li, C.-M. Duan, X.-M. Guo, [Scalable production of embryoid bodies with the rotay cell culture system.]., Sheng Li Xue Bao. 57 (2005) 486–92.

[16] M. Winkler, N. Trieu, T. Feng, L. Jin, S. Walker, L. Singh, H.T. Ku, A quantitative assay for insulin-expressing colony-forming progenitors., J. Vis. Exp. (2011) e3148.

[17] D.P. Spelke, D. Ortmann, A. Khademhosseini, L. Ferreira, J.M. Karp, Methods for Embryoid Body Formation: The Microwell Approach, in: Methods Mol. Biol., 2011: pp. 151–162.

[18] J. Dahlmann, G. Kensah, H. Kempf, D. Skvorc, A. Gawol, D.A. Elliott, G. Dräger, R. Zweigerdt, U. Martin, I. Gruh, The use of agarose microwells for scalable embryoid body formation and cardiac differentiation of human and murine pluripotent stem cells, Biomaterials. 34 (2013) 2463–2471.

[19] S. Gerecht, J.A. Burdick, L.S. Ferreira, S.A. Townsend, R. Langer, G. Vunjak-Novakovic, Hyaluronic acid hydrogel for controlled self-renewal and differentiation of human embryonic stem cells., Proc. Natl. Acad. Sci. U. S. A. 104 (2007) 11298–303.

[20] J. Zhang, G.F. Wilson, A.G. Soerens, C.H. Koonce, J. Yu, S.P. Palecek, J.A. Thomson, T.J. Kamp, Functional Cardiomyocytes Derived From Human Induced Pluripotent Stem Cells, Circ. Res. 104 (2009).

[21] H. Kurosawa, Methods for inducing embryoid body formation: in vitro differentiation system of embryonic stem cells, J. Biosci. Bioeng. 103 (2007) 389–398.

[22] Y. Tang, L. Liu, J. Li, L. Yu, L. Wang, J. Shi, Y. Chen, J. Nam, A. Baessler, M. Fischer, R. Passier, L. Tertoolen, I. Gruh, A. Haverich, U. Martin, R. Zweigerdt, Induction and differentiation of human induced pluripotent stem cells into functional cardiomyocytes on a compartmented monolayer of gelatin nanofibers, Nanoscale. 8 (2016) 14530–14540.

[23] Y. Tang, L. Liu, J. Li, L. Yu, F.P.U. Severino, L. Wang, J. Shi, X. Tu, V. Torre, Y. Chen, Effective motor neuron differentiation of hiPSCs on a patch made of crosslinked monolayer gelatin nanofibers, J. Mater. Chem. B. 4 (2016) 3305–3312.

[24] A.J. Engler, S. Sen, H.L. Sweeney, D.E. Discher, Matrix elasticity directs stem cell lineage specification., Cell. 126 (2006) 677–89.

[25] S. Musah, P.J. Wrighton, Y. Zaltsman, X. Zhong, S. Zorn, M.B. Parlato, C. Hsiao, S.P. Palecek, Q. Chang, W.L. Murphy, L.L. Kiessling, Substratum-induced differentiation of human pluripotent stem cells reveals the coactivator YAP is a potent regulator of neuronal specification., Proc. Natl. Acad. Sci. U. S. A. 111 (2014) 13805–10.

[26] Y. Sun, L.G. Villa-Diaz, R.H.W. Lam, W. Chen, P.H. Krebsbach, J. Fu, Mechanics Regulates Fate Decisions of Human Embryonic Stem Cells, PLoS One. 7 (2012).

[27] A.J. Keung, P. Asuri, S. Kumar, D. V Schaffer, Soft microenvironments promote the early neurogenic differentiation but not self-renewal of human pluripotent stem cells., Integr. Biol. (Camb). 4 (2012) 1049–58.

[28] W. Ronan, V.S. Deshpande, R.M. McMeeking, J.P. McGarry, Cellular contractility and substrate elasticity: a numerical investigation of the actin cytoskeleton and cell adhesion, Biomech. Model. Mechanobiol. 13 (2014) 417–435.

[29] E.A. Papakonstanti, C. Stournaras, Cell responses regulated by early reorganization of actin cytoskeleton, FEBS Lett. 582 (2008) 2120–2127.

[30] P.P. Provenzano, P.J. Keely, Mechanical signaling through the cytoskeleton

regulates cell proliferation by coordinated focal adhesion and Rho GTPase signaling., J. Cell Sci. 124 (2011) 1195–205.

[31] A.J. Engler, C. Carag-Krieger, C.P. Johnson, M. Raab, H.-Y. Tang, D.W. Speicher, J.W. Sanger, J.M. Sanger, D.E. Discher, Embryonic cardiomyocytes beat best on a matrix with heart-like elasticity: scar-like rigidity inhibits beating, J. Cell Sci

Conclusion and perspective

This thesis work aimed at exploring micro- and nano-fabrication techniques to manufacture new types of cell culture substrates and scaffolds based on a biomimetic approach. We were particularly interested in three-dimensional cell culture and cell migration as well as expansion and differentiation of human pluripotent stem cells.

We firstly developed a novel method to fabricate dense elastomer pillar arrays with height gradient and uniform top surface. By spin-coating a low-viscosity resist on a pre-patterned stripe array on a chrome mask, sloped tails could be formed aside the stripes. Such a wavy resist layer was then back side UV exposed, creating pillars with height gradients and the same top level after the resist development. Double replicated by elastomer PDMS casting, micropillar arrays of high density, high aspect ratio and high stiffness gradient could be produced. NIH 3T3 cells were then cultured, showing remarkable elongation and directed migration, depending clearly on the stiffness gradient strength. PDMS micropillars can also be organized in more complex patterns, such as ripple-like height gradient patterns, resulting in similar cell culture behaviors. Thus, we conclude that elastomer pillar arrays with pillar height gradient can be used as a new type of culture substrate with high surface stiffness gradient. Besides, this novel fabrication technique could also be used to generate other pattern types such as microwave shapes, rice leaf-like microstructures and convex microlens arrays (MLAs), etc., thereby holding high application potential in different fields including biotechnology, surface engineering and microfluidics.

We then challenged the fabrication of the in-vivo like extracellular matrix (ECM) for advanced cell culture studies. To begin with, we produced monolayer nanofibers on up and down sides of a thin and high porosity membrane, which was inspired by the three-dimensional organization of the in-vivo ECM. Again, UV lithography and soft lithography techniques were used to fabricate the membrane in poly (ethylene glycol) diacrylate (PEGDA) hydrogel. Electrospinning was used to produce monolayer gelatin nanofibers on both sides of the membrane, followed by crosslinking. By controlling the thickness of the membrane, the distance between the two monolayer nanofibers could be adjusted. By controlling the electrospinning time, the porosity of nanofibers could be modulated. NIH 3T3 cells were cultured with such as a device to demonstrate the three-dimensional cell adhesions. As expected, cells could infiltrate, adhere, and proliferate in the free-space between the two nanofibers monolayers. The advantage of this culture method relies on the 3D permeability and easy formation of multilayer tissues, with one or several cell types. This device was designed in form of culture patch, so that it is compatible to both conventional culture and microfluidic integration or organ on-a-chip system. We therefore conclude that narrowly spaced monolayer nanofibers are well suited for advanced applications including disease modeling, tissue engineering and drug development.

Finally, we studied cardiac differentiation from human induced pluripotent stem cells (hiPSCs) on micropillar substrates of different effective stiffness and different stiffness gradients. Our results showed that stiffer substrates and vitronectin surface coating favored the hiPSCs attachment and proliferation. In order to generate homogenous cardiac tissue, we first produced size and uniformity controlled embryoid bodies of hiPSCs. This has been done by placing a PDMS honeycomb frame (stencil) on the surface of PDMS micropillars to create temporal compartments for cell clustering. The effects of cells seeding density and substrate stiffness on the formation of EBs were then studied. Interestingly, our immunostaining and SEM results showed remarkable differences in EBs morphology and dimensionality, depending on the effective stiffness of the underlying substrates. Stiffer substrates promoted cell spreading by forming cytoskeleton with higher contractile forces so that more platen EBs generated. Afterward, the hemispheric EBs colonies were used for cardiac differentiation on the micropillars, showing again a clear stiffness dependence of the processes. In addition, the beating behaviors were investigated. The $Ca2^+$ transient analysis illustrated that differentiation from uniform EBs could benefit the synchronous beating of cardiac cells and the beating frequencies were highly dependent on matrix. Finally, the results also showed that cardiomyocytes on matrix with heart-like elasticity were highly impressionable to electrical stimuli.

We believe that the methods developed in this work could be used for large scale applications, thereby providing a way to go ahead in tissue engineering and regenerative medicine. For micropillar substrates, which can be easily produced and used as stiffness adjustable substrate for cell culture. The advantage of using this type of substrate compared to the other types of substrates such as hydrogel relies on the precise stiffness control and localized adhesion when cells are attached on the top of the pillar area. Moreover, the free space underneath the cells or EBs facilitates the diffusion of nutrients, metabolites, and soluble cell factors. our approach allowed us to regulate the mechanical properties of the polymeric pillar array device. More specifically, the developed novel method enables us to fabricate micropillar arrays with height gradient and thus obtained substrates with stiffness gradient. This technique is a unique tool for studying cellular motion and behavior in relation to various stiffness gradients of the environment. The newly developed platform introduced here can be further used to investigate cell migration for many other biological applications, such as artificial tissue engineering, plastic surgery, and the study of the migration behavior of cancerous cells.

In perspective of the developed tri-layer scaffold, though in this thesis work, we used as a culture scaffold for 3D cell handling, it could be used in various aspects of tissue engineering. For example, it will be a suitable model to establish the co-culture system due to the mimetic structure features with ECM as well as the good permeability which facilitates cells communication. Furthermore, it also can be well integrated into a microfluidic chip for drug screening, tissue formation, organ on chip, etc. because of the robust mechanical property and easy handling. In another hand, this scaffold holds the potential to improve. For instance, the material used in frame fabrication could be replaced with natural or biodegradable polymers like collagen, chitosan or PLGA, which could extend the application to transplantation.

For hiPSCs, mounting evidence indicates that the rigidity of substrates is crucial for the self-renewal and induced differentiation, whereas traditional tissue culture substrates (plastic and glass) have mechanical properties outside the range of many functional tissues. Therefore, the development of alternative strategies to fabricate substrates with adjustable stiffness is of great interest to maximize the differentiation efficiency of hiPSCs. In this thesis work, micropillar substrates were used to demonstrate the effect of substrate elasticity on cardiac differentiation. In principal, the utilize of such substrates could be extended, such as neuron differentiation. In addition, the strategy of stem cell EB formation could also benefit the differentiation efficiency.

Appendix A

A facile photolithographic method of fabricating wavy-like patterns

In this appendix, we present a simple and flexible method for fabricating microwave-like patterns with precisely controlled features using photolithography. With this method, microwave shapes, rice leaf-like microstructures and convex microlens arrays (MLAs) could be fabricated. Afterwards, the hydrophobic property of rice leaf-like micropatterns and the imaging property of MLAs were demonstrated. This unique method could be a potential alternative to fabricate complex substrates to explore numerous applications in biotechnology, surface engineering and microfluidics.

1 Introduction

Developing practical and cost-effective methods to fabricate patterned microstructures is currently of great interest, particularly in the field of surface studies, cell-substrate interaction, and microfluidic [1–3]. The wave-like patterns are highly desirable features due to its widely used in biological applications and wetting properties adjustment [4, 5]. So far, the wave features could be fabricated by a standard technique that depositing a thin layer of metal on thermally- or mechanically-induced pre-strained polydimethylsiloxane (PDMS) substrates [6, 7]. The wavy pattern successfully generated after releasing the strain. However, methods based on the pre-strain of a substrate have inherently limits; particularly the diversity of pattern profiles, only specific profiles can be produced by the pre-strain method. As an alternative, the grayscale lithography method was developed to fabricate wrinkle and other three-dimensional microstructures [8, 9]. This approach has generated wrinkle patterns with controllable wavelength and amplitude, while the photomasks or digital micro-mirror system used in this method were not cost-effective.

Therefore, we present a facile idea realized by a widespread photolithography technology with two step spin coating to produce wavy-like patterns, i.e., microwave, microlens arrays and rice leaf-like pattern. Furthermore, the imaging properties of MLAs and surface hydrophobic property of rice leaf-like structures were investagated.

2 Experiments

Wavy-like patterns were prepared by incorporating geometry-guided spin coating, photolithography and soft lithography, as schematically illustrated in **Fig. 1**. Briefly, a Cr mask was spin coated with first layer SU-8 resist (Microchem, USA), then exposed with another mask consisted of stripes or circles patterns. After development, the sample was spin-coated with the second SU-8 resist layer with a thinner thickness compared to the first resist layer, resulting in a wavy-like distribution of resist. In order to obtain the microwave and concave microlens patterns, the second resist layer was exposed from the positive side, as illustrated in **Fig. 1a**. the convex microlens arrays were obtained by PDMS casting on the resist mold. On the other hand, rice leaf-like patterns could generate by backside expoure of the second resist layer (**Fig. 1b**). This method can also fabricate micropillar arrays with height gradient (**Fig. 1c**), which has been demonstrated in Chapter 3 in this thesis work.

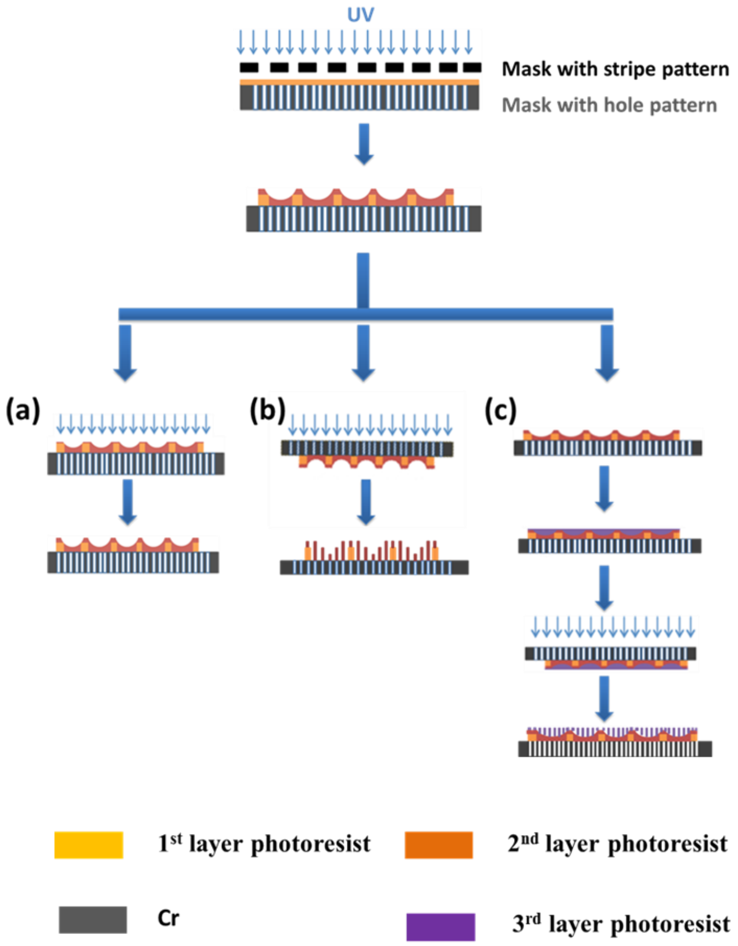

Figure 1 Schematic diagram of the fabrication process of (a) microwave patterns. (b) Rice leaf-like structures and (c) micropillar arrays with height gradient.

3 Results and discussion

3.1 Microwave and MLAs patterns

Fig. 2 shows SEM images of PDMS ripple-like patterns and microlens structures. **Fig. 2 a** and **b** shows images of ripple pattern with period 200μm, circles with designed height 50 μm were firstly introduced, acting as a wall to block second resist layer. After a second spin-coat with designed thickness 7μm, periodic wave pattern was formed. Because of the non-planar surface present during the second spinning step and the second thinner layer resist, the final thickness of the photoresist layer is not anymore correlated to the spin speed, result in concave wave pattern. Base on this principle of this novel process, other concave patterns also can be fabricated, like microlens arrays.

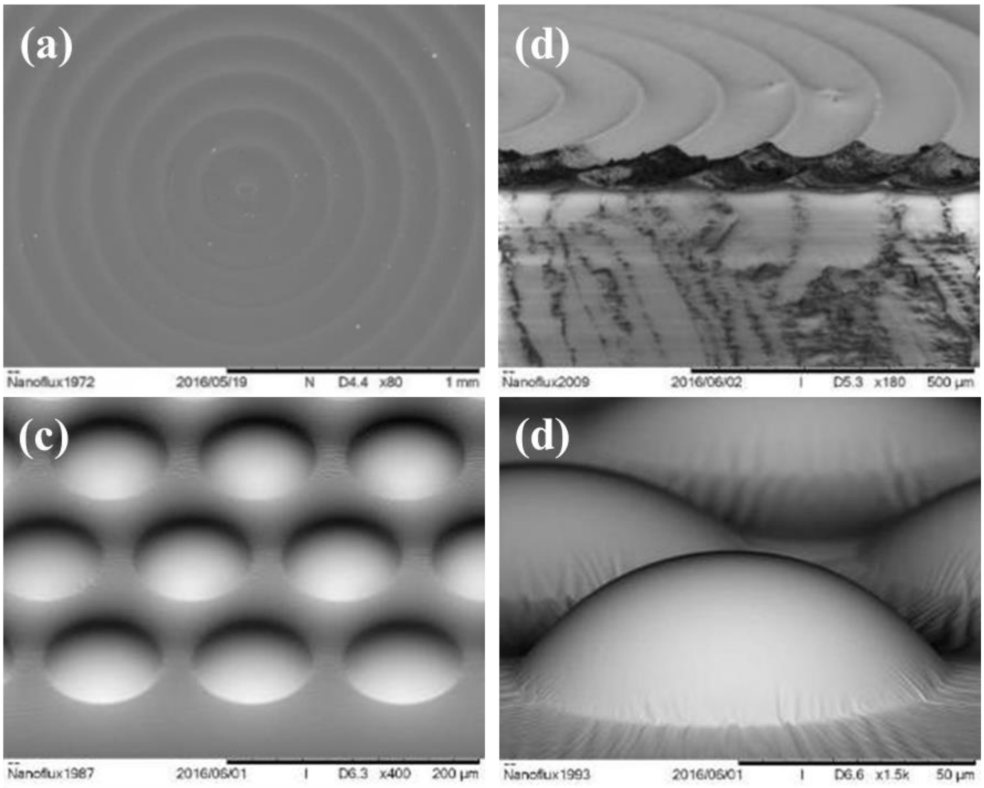

Figure 2 (a, b) Scanning electron microscope (SEM) images of the fabricated ripple pattern from (a) Top and (b) side view. (c, d) SEM images of microlens arrays (MLAs).

Fig. 2 c and **d** shows representative SEM images of the fabricated MLAs. After one-time replication with PDMS, convex microlens array was obtained. As shown in the pictures, the resultant refractive MLAs had good structural and dimensional uniformity.

To demonstrate the optical applications of the curved MLAs for imaging, a projection experiment was performed with an optical digital microscope. The artificial convex MLAs were fixed on a movable sample stage and were illuminated by a tungsten light through a projection mask, which was a black plastic sheet with a transparent letter "ENS" on it (**Fig. 3a**). An array of bright false and reduced images of "ENS" on the false focal plane of the MLAs was clearly captured by an objective lens and a CCD camera which were placed on the other side of the MLAs, as shown in **Fig. 3b**. The clear images of "ENS" were uniform in size and shape, which indicated the uniformity of the structures and the fine imaging property of the MLAs. The diffraction rings were also demonstrated by phase contrast imaging of substrate with ripple patterns (**Fig. 3c** and **d**).

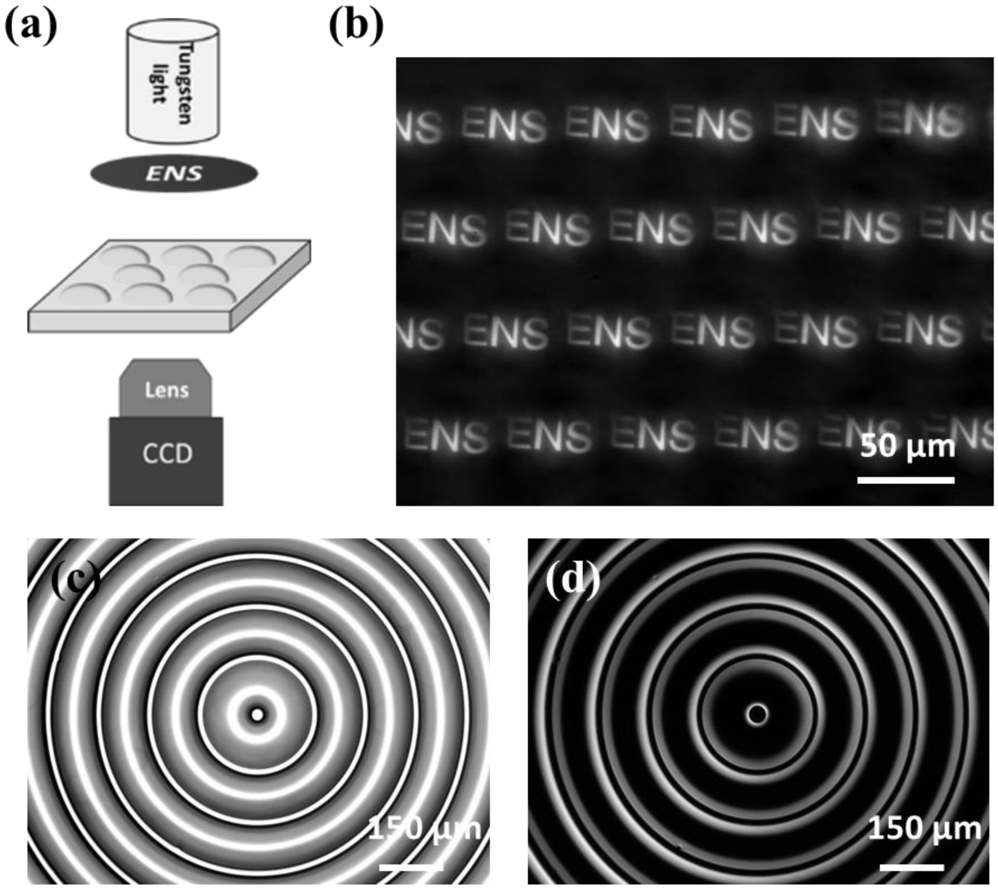

Figure 3 The optical characterization system for the MLAs (a) Schematic diagram of the imaging system. (b) Image arrays made by MLAs. (c, d) Phase contrast images of ripple patterned substrate.

3.2 Rice leaf-like structure and the hydrophobic property

Wettability of solid surfaces has recently been attracting a great deal of attention, as it plays important roles in daily life, in industry, and in agriculture [10, 11]. Bioinspired surfaces with special wettability have aroused much interest owing to their unique morphologies and physicochemical properties. In particular, rice leaves exhibit special anisotropic wetting properties [12, 13]. The leaf surface displayed many parallel ridges formed by vascular bundles and wavy mesophyll layers. Further magnified views displayed a number of papillae 2 μm in diameter and 4 ± 1 μm in height, arranged in a direction parallel to the ridge direction, as shown in **Fig. 4**.

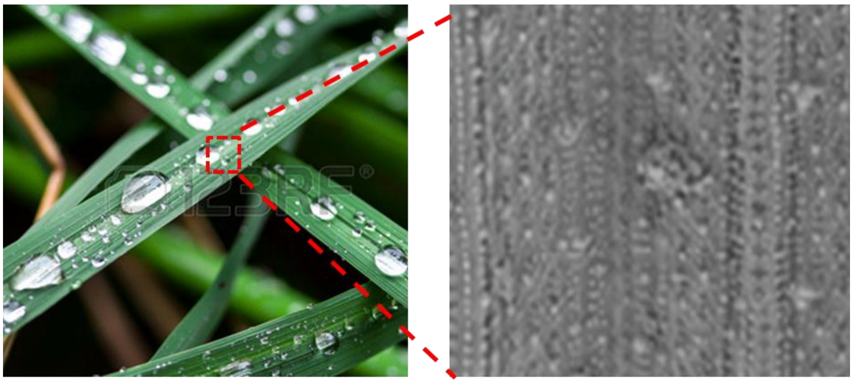

Figure 4 Images of rice leaf and its microstructures [14].

With our fabrication method, we can obtain the rice leaf-like patterns composed of ridges and micropillars with different organizations, as shown in **Fig.5**. As can be observed, the height of micropillars were in periodic gradient, resulting in a waved structure. In addition, the morphology of the waves could be controlled by the thickness of the second resist layer, that is the heights of the micropillars. In this case, the curvatures could be regulated. Afterwards, the hydrophobic properties of these substrates were investigated. Interestingly, different wetting behaviors observed with these substrates. On substrate which had the largest curvature, the water contact angles in parallel and perpendicular displayed remarkable differences, with 131.3 ± 5.3° in parallel and 158.2 ± 2.3° in perpendicular, indicating the special anisotropic wetting properties. Furthermore, the contact angles in perpendicular dcreased with the limited decreasing of curvature (**Fig. 5a** and **b**), while contact angles almost kept constant in parallel. With further decreasing of curvature, contact angles in both directions decresed, which was probablly due to the increasing contacting area in this case. The contact angles in microwave pattern without micropillars further indicated that the effect of rice leaf-like structure on hydrophobic properties.

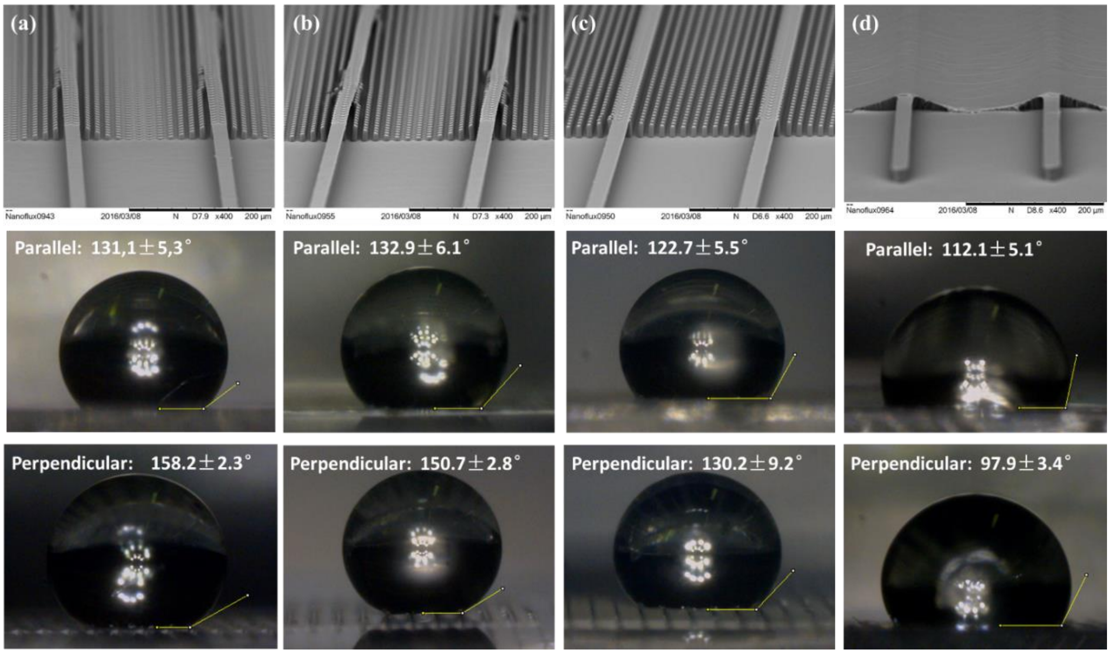

Figure 5 SEM images of rice leaf-like microstructures with the height distances of micropillars (a-c) 20 μm, 15 μm and 10μm, respectively and (d) microwave pattern. And contacting angles of a 5 μL water droplet on the substrates from parallel and perpendicular view.

4 Conclusion

We have introduced a facile method to fabricate wave-like patterns by standard photolithography. Different wave-like patterns were prepared by this novel method. In addition, this effective technology can be extensively applied for microlens arrays and rice leaf-like patterns fabrication. The excellent imaging and hydrophobic properties of the obtained microstructures were further demonstrated. This unique method could be a potential alternative to fabricate complex substrates to explore numerous applications in biotechnology, surface engineering and microfluidics.

Reference

[1] X.J. Feng, L. Jiang, Design and Creation of Superwetting/Antiwetting Surfaces, Adv. Mater. 18 (2006) 3063–3078.

[2] M. Nikkhah, F. Edalat, S. Manoucheri, A. Khademhosseini, Engineering microscale topographies to control the cell–substrate interface, Biomaterials. 33 (2012) 5230–5246.

[3] Y. Zhang, S. Park, K. Liu, J. Tsuan, S. Yang, T.-H. Wang, A surface topography assisted droplet manipulation platform for biomarker detection and pathogen identification., Lab Chip. 11 (2011) 398–406.

[4] J. Hu, C. Hardy, C.-M. Chen, S. Yang, A.S. Voloshin, Y. Liu, Enhanced Cell Adhesion and Alignment on Micro-Wavy Patterned Surfaces, PLoS One. 9 (2014) e104502.

[5] P. Goel, S. Kumar, J. Sarkar, J.P. Singh, Mechanical Strain Induced Tunable Anisotropic Wetting on Buckled PDMS Silver Nanorods Arrays, ACS Appl. Mater. Interfaces. 7 (2015) 8419–8426.

[6] P.-C. Lin, S. Yang, J.Q. Sun, J.C. Shen, W.P. Cai, T.J. McCarthy, T. Watanabe, H.Y. Chen, T. Wu, Mechanically switchable wetting on wrinkled elastomers with dual-scale roughness, Soft Matter. 5 (2009) 1011.

[7] G.M. Whitesides, N. Bowden, S. Brittain, A.G. Evans, J.W. Hutchinson, Spontaneous formation of ordered structures in thin films of metals supported on an elastomeric polymer, Nature. 393 (1998) 146–149.

[8] R. Kirchner, V.A. Guzenko, M. Rohn, E. Sonntag, M. Mühlberger, I. Bergmair, H. Schift, Bio-inspired 3D funnel structures made by grayscale electron-beam patterning and selective topography equilibration, Microelectron. Eng. 141 (2015) 107–111.

[9] R. Du, X. Gao, Q. Feng, Q. Zhao, P. Li, S. Deng, L. Shi, J. Zhang, Microscopic Dimensions Engineering: Stepwise Manipulation of the Surface Wettability on 3D Substrates for Oil/Water Separation, Adv. Mater. 28 (2016) 936–942.

[10] P. Zhang, S. Wang, S. Wang, L. Jiang, Superwetting Surfaces under Different Media: Effects of Surface Topography on Wettability, Small. 11 (2015) 1939–1946.

[11] F. Rupp, R.A. Gittens, L. Scheideler, A. Marmur, B.D. Boyan, Z. Schwartz, J. Geis-Gerstorfer, A review on the wettability of dental implant surfaces I: Theoretical and experimental aspects, Acta Biomater. 10 (2014) 2894–2906.

[12] S.G. Lee, H.S. Lim, D.Y. Lee, D. Kwak, K. Cho, Tunable Anisotropic Wettability of Rice Leaf-Like Wavy Surfaces, Adv. Funct. Mater. 23 (2013) 547–553.

[13] R. He, S. Wang, G. Andrews, W. Shi, Y. Liu, Generation of Customizable Micro-wavy Pattern through Grayscale Direct Image Lithography, Sci. Rep. 6 (2016) 21621.

[14] D. Wu, J.-N. Wang, S.-Z. Wu, Q.-D. Chen, S. Zhao, H. Zhang, H.-B. Sun, L. Jiang, Three-Level Biomimetic Rice-Leaf Surfaces with Controllable Anisotropic Sliding, Adv. Funct. Mater. 21 (2011) 2927–2932.

Appendix B

French Summary

1 Introductions

Au cours des deux dernières décennies, l'ingénierie tissulaire s'est transformée en un domaine multidisciplinaire regroupant la science des matériaux, la biologie et la médecine, dans le but de constituer des substituts biologiques pour remplacer et réparer les tissus endommagés en raison d'une maladie ou d'une blessure traumatique. Les méthodes de reconstitution de novo de tissus ou d'organes fonctionnels se concentrent principalement sur la recherche d'une combinaison optimale des trois principaux composants de l'ingénierie tissulaire, à savoir: i) l'origine des cellules, ii) le substrat (ou scaffold), et iii) les signaux biologiques.

En premier lieu, il est nécessaire d'obtenir un scaffold pour fournir un support transitoire tridimensionnel (3D) pour la migration, l'attachement et la prolifération des cellules, ainsi que pour servir de vecteur pour la distribution de facteurs biochimiques. Les propriétés mécaniques et biologiques de ce scaffold vont également influencer et guider la maturation et l'intégration des cellules, afin de former des tissus. Par conséquent, le principal défi dans l'ingénierie tissulaire est de concevoir et fabriquer un scaffold approprié, qui va répondre aux besoins naissants de ce domaine. De plus, les cellules et leur microenvironnement peuvent également s'influencer l'une l'autre de manière dynamique, et ce pendant le développement normal, l'homéostasie et la réparation des tissus, ainsi que la progression des maladies, via des interactions biochimiques et biophysiques réciproques. Les interactions complexes entre les cellules et leur microenvironnement dans les tissus sont de mieux en mieux comprises, focalisant l'attention portée sur la préparation de scaffolds qui peuvent imiter les composants, la structure et les fonctionnalités de la matrice extracellulaire (ECM), afin de générer des ECM de novo et des néo-tissus. In vivo, les tissus peuvent avoir des rigidités variées et des conditions physiologiques tout aussi différentes. Il est donc important d'avoir des scaffolds ou des substrats avec une rigidité contrôlable et d'enquêter sur les comportements cellulaires mécaniques tels que la migration. En outre, les scaffolds devraient également avoir la capacité de fournir un support transitoire tridimensionnel (3D) pour faciliter le recrutement, l'adhésion, la migration et la prolifération des cellules.

En second lieu, on notera que l'utilisation de cellules souches devient une pratique courante dans des buts de recherche, et pas uniquement pour des applications cliniques. Un intérêt particulier est porté sur l'utilisation de cellules souches pluripotentes induites (iPSC) pouvant être obtenues à partir des cellules stromales du corps, en raison de leur capacité infinie d'auto-renouvellement et la possibilité de les différencier en de nombreux types de cellules adultes. Les iPSCs peuvent donc être utilisés comme des ressources infinies et extrêmement puissantes, au service du développement de nouvelles méthodes et de nouveaux outils d'ingénierie tissulaire, en plus des cellules souches mésenchymateuses et des autres cellules souches adultes déjà utilisées. Cependant, les capacités des iPSC dépendent fortement de l'état de la culture. Les méthodes de culture conventionnelles qui reposent sur l'utilisation quotidienne de substrats durs (les plaques et flasques de culture) ne conviennent pas à la plupart des applications envisagées, même si elles peuvent maintenir la pluripotence et guider la différentiation après un traitement de surface biochimique des substrats. En effet les plaques de culture ne sont pas compatibles avec les cellules au niveau mécanique puisque les valeurs de rigidité des substrats sont généralement beaucoup plus élevées que celles des hiPSC ou des cellules dérivées. À cet égard, il est hautement souhaitable de développer de nouveaux substrats et de nouvelles méthodes de culture pour les applications d'iPSC.

Au fil des deux dernières décennies, de nombreux outils de micro/nano-ingénierie et méthodes de synthèse de biomatériaux fonctionnels ont été développés avec succès, puis appliqués à la recherche biologique et biomédicale. Cela a permis d'établir une riche boîte à outils de divers micro/nano-biomatériaux fonctionnels pour la génération dynamique, la modulation, et la stimulation de divers signaux biochimiques et biophysiques. à un niveau subcellulaire pour des cellules cultivées in vitro. De tels micro/nano-biomatériaux fonctionnels ont particulièrement aidé à découvrir les effets indépendants de signaux biophysiques individuels du microenvironnement cellulaire, comme la forme et la géométrie imposée aux cellules, la rigidité et la topographie de l'ECM, les forces extracellulaires et l'organisation spatiale des protéines d'adhésion, qui agissent sur la régulation des comportements cellulaires tels que la migration, la prolifération, la survie, et la différenciation cellulaire.

Le but de ce travail de thèse est de développer de nouveaux substrats et de nouveaux scaffolds avec l'aide de techniques avancées de micro et de nanofabrication pour réproduire les caractéristiques structurelles et fonctionnelles de la matrice extra-cellulaire (ECM). Nous nous sommes principalement intéressés à :

i) La fabrication de micropilliers en élastomères comme substrats de faible rigidité,

ii) Le contrôle de la rigidité du substrat par modification de la hauteur du pilier,
iii) La génération d'un gradient de rigidité pour les études de migration cellulaire (durotaxis)
iv) La réalisation de scaffolds de nanofibres pour la gestion de cellules en 3D,
v) La création d'un patch de tissu cardiaque à partir d'iPSC.

2 Elongation et migration cellulaire sur des piliers en élastomère dense avec un gradient de rigidité

2.1 Introduction

Dans un environnement naturel, les cellules adhérentes sont entourées par une matrice extracellulaire (ECM), qui transmet des signaux biochimiques et biophysiques complexes. Un exemple de signal biophysique est le module élastique de l'ECM, qui a été démontré comme étant un régulateur important des comportements cellulaires, tels que le développement de l'adhésion focale, la réorganisation du cytosquelette, les caractéristiques de différenciation et l'apoptose. On sait non seulement que la rigidité du microenvironnement cellulaire a une grande variabilité parmi les différents tissus, allant d’un tissu très mou, comme le tissu cérébral (260-490 Pa) à un tissu plus rigide comme celui du rein (2,5 kPa) et, même plus élevé encore pour le tissu osseux (autour de 15 MPa). Cette rigidité peut aussi varier fortement localement, ce qui donne lieu à des gradients complexes de rigidité pouvant atteindre plusieurs ordres de grandeur, tels que ceux observés dans les tissus inter-faciaux. Un tel gradient de rigidité peut jouer un rôle important, par exemple, pour réguler la direction de migration des cellules.

Plus récemment, les progrès dans les méthodes de micro et nanofabrication ont permis aux chercheurs de développer des substrats et des scaffolds plus sophistiqués. Des matrices de micropilliers de hauteur uniforme, fabriquées par des techniques de lithographie, ont été utilisées pour étudier la relation entre les forces de traction, le développement de l'adhésion focale, et la morphologie cellulaire en réponse à la rigidité et à la migration des substrats, fournissant de nouvelles idées sur les mécanismes sous-jacents du mechanosensing (responsivité d’une cellule à des signaux mécaniques). Mais la plupart des publications se concentrent sur l’étude des comportements cellulaires sur des substrats de micropiliers à hauteur uniforme. Des réseaux de piliers possédant un gradient de rigidité ont également été obtenus en changeant de façon continue la taille des piliers, ou en utilisant une matrice micropillée à étages. Ces approches sont toutes les deux limitées, car les grands écarts d'espacement et de diamètre des piliers affectent l'adhérence ainsi que d'autres fonctions cellulaires.

Nous présentons ici une méthode simple mais directe pour fabriquer des réseaux de piliers denses avec un gradient de rigidité en faisant varier en continu la hauteur du pilier. Nous montrions que ces réseaux de piliers sont une méthode fiable pour contrôler et diriger la migration cellulaire (schéma représenté sur la figure 1.2a). Des intensités de gradient variables pourraient également être obtenues en modulant la période ondulatoire. Il est intéressant de noter que différents types de localisation, d'allongement et d'orientation des cellules ont été observés sur ces substrats de piliers.

2.2 Fabrication du substrat

Les réseaux de piliers en PDMS avec un gradient de hauteur ont été préparés par enduction centrifuge guidée en géométrie, puis par photolithographie et lithographie douce, comme le montre le schéma de la figure 1. En bref, des bandes de 15 μm de hauteur ont d'abord été modelées par photolithographie sur un masque de Chrome ayant des dessins spécifiques. Ensuite, une second couche de SU-8 a été déposée par enduction centrifuge sur les piliers et les micropiliers ont été obtenus par exposition UV sur le masque aux dessins spécifiques, de l’autre côté. Cela a fourni un moule, dans lequel les piliers de PDMS ont été produits par réplique du moule.

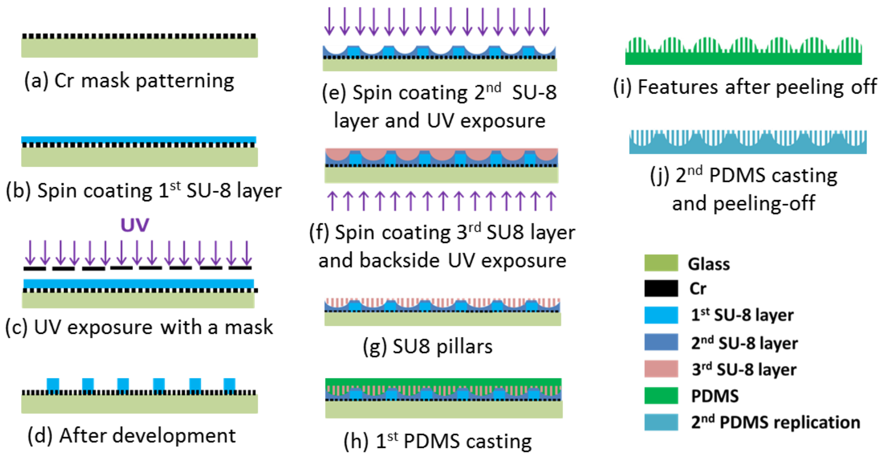

Figure 1 Diagramme schématique du processus de fabrication des tableaux PDMS avec gradient de hauteur.

2.3 Traitement de surface

Avant la culture cellulaire, les échantillons en PDMS ont été stérilisés par lumière UV pendant toute une nuit. Les surfaces supérieures uniformes des piliers ont été fonctionnalisées avec la fibronectine via impression par micro-contact. Par la suite, l'adsorption de protéines sur toutes les surfaces de PDMS non recouvertes de fibronectine a été empêchée en incubant dans du Pluronics F127 à 0,2% dans de l'eau distillée pendant 30 minutes à température ambiante avant de semer les cellules NIH 3T3.

2.4 Caractérisation du substrat

Les figures 2b et 2c montrent des images de microscopie électronique à balayage (MEB) de réseaux de piliers ayant une période spatiale de 160 µm (P160) et 310 µm (P310), respectivement, avec des structures ondulées périodiques visibles. La figure 2d affiche la variation de la hauteur des piliers en fonction de leur position pour des échantillons P160 et P310, allant de 3,79 ± 0,13 (3,52 ± 0,11) µm à 10,13 ± 0,12 (10,25 ± 0,05) µm ; ce qui suggère qu’il n’y a pas de différence significative de la variation de hauteur des piliers selon la période. En utilisant la théorie du faisceau d'Euler-Bernoulli, la constante de raideur des piliers peut être calculée. En conséquence, nous avons obtenu une variation du module effectif de Young des échantillons des piliers en PDMS P160 et P310 (figures 2e et 2f), qui suggère un changement de rigidité de près de 30 fois entre les zones plus molles (2,4 KPa) et les plus dures (60,0 KPa), qui s’expliquent simplement par le changement de hauteur du pilier à la demi-période.

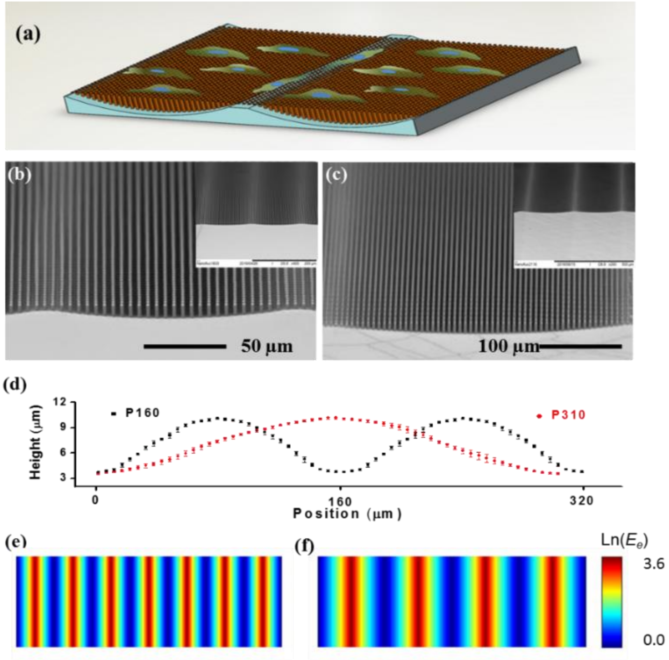

Figure 2 (a) Illustration schématique de la culture cellulaire sur un réseau de micropiliers avec gradient de hauteur. (b, c) Microscopes électroniques à balayage (MEB) des micropiliers de PDMS ayant une période de 160 µm (P160) et 310 µm (P310), respectivement. (d) Variation de la hauteur du pilier en fonction de la position du pilier. (e, f) Calcul effectif des modules Young des échantillons P160 et P310.

2.5 Mobilité et migration cellulaire

Les cellules NIH 3T3 sont couramment utilisées pour étudier l'interaction des fibroblastes avec des substrats de culture. La figure 3a montre des extraits d'un time-lapse des cellules sur les piliers de l'échantillon P160. Après avoir adhérer, les cellules ont commencé à se propager et à ressentir leur environnement. Les cellules qui étaient d'abord attachées sur la zone molle ont tendance à migrer vers la zone plus rigide. Celles déjà situés sur la zone rigides se sont maintenues dans cette même zone. Ensuite, elles se propagées, montrant différents comportements migratoires et différentes morphologies selon les différents domaines des réseaux de piliers (figures 3b et 3c). La distance de déplacement des cellules sur ces deux types de substrats a été tracée dans les figures 3d et 3e. En conséquence, nous avons obtenu une vitesse de déplacement moyenne de 3,23 ± 0,26 µm h^{-1} (1.38 ± 0.19 µm h^{-1}) le long du gradient de rigidité pour l'échantillon P160 (P310), alors qu'aucune différence significative de vitesse de déplacement n'a été observée dans la direction perpendiculaire (figure 3f). Ces résultats suggèrent que non seulement la rigidité mais aussi le gradient de rigidité affectent le comportement des cellules NIH 3T3.

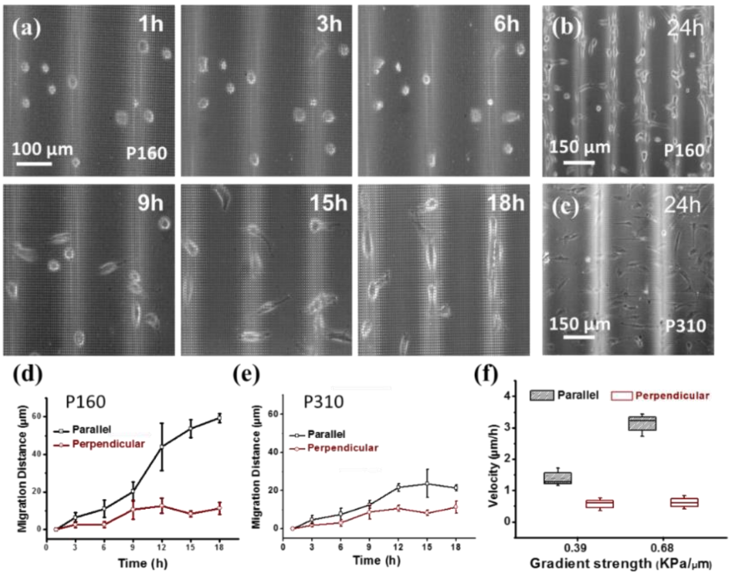

Figure 3 (a) Images temporelles des cellules NIH 3T3 sur l'échantillon P160; (b, c) Images de contraste de phase montrant l'allongement et la localisation des cellules sur les réseaux de piliers en PDMS des échantillons P160 et P310 après 24 heures d'incubation; (d, e) Distances de migration des cellules NIH 3T3 parallèles et perpendiculaires au gradient de rigidité des échantillons P160 et P310. N = 34; (f) Vitesse de migration des cellules sur les réseaux de piliers en PDMS selon les différentes forces de gradient.

2.6 Prolifération cellulaire et morphologie cellulaire

Comme on peut le voir sur la figure 4, les cellules ont été réparties de manière aléatoire sur l'échantillon en PDMS plat sans orientation définie. Sur l'échantillon P160, la plupart des cellules étaient allongées perpendiculairement au gradient de rigidité et se situaient préférentiellement dans la zone rigide le jour 1, même si plus de cellules étaient allongées parallèlement à la direction du gradient de rigidité après 4 jours d'incubation. Sur l'échantillon P310, les cellules se sont allongées parallèlement au gradient de rigidité sans signature claire d'une localisation préférentielle à la fois le jour 1 et le jour 4, ce qui indique que la prolifération n'a pas affecté l'allongement cellulaire. Fait intéressant, les cellules cultivées sur PDMS plat ont de grandes surfaces de propagation et de noyau en raison de la grande rigidité (~ 2 MPa) de ce substrat par rapport aux substrats de piliers de PDMS (figures 5g et5 h). L'anisotropie de forme des cellules sur l'échantillon P310 est significativement plus grande que celle de l'échantillon P160, mais l'anisotropie de forme du noyau sur les deux échantillons est plus grande que celle sur couche plate de PDMS (figures 5i et 5j). Ces résultats indiquent donc que les réseaux de piliers ici présentés ont fourni un scaffold innovant, qui peut induire une anisotropie de forme de cellules et de noyaux.

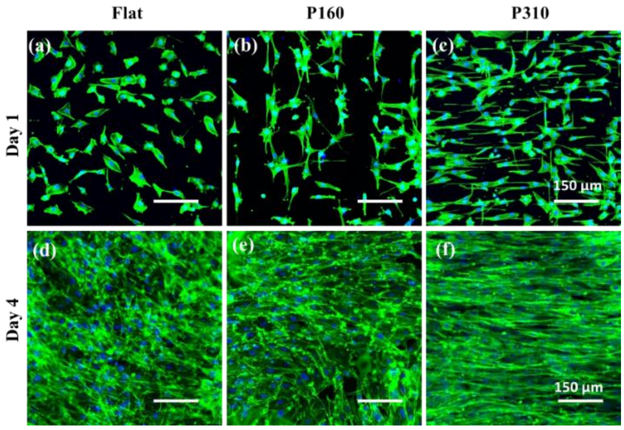

Figure 4 Immunofluorescence des cellules après 1 jour (a-c) et 4 jours (d-f) d’incubation sur des échantillons plats, P160 et P310 en PDMS. Les noyaux cellulaires ont été colorés par DAPI (bleu) et le réseau du cytosquelette par l'actine en vert (Alexa Fluor 488 phalloidine).

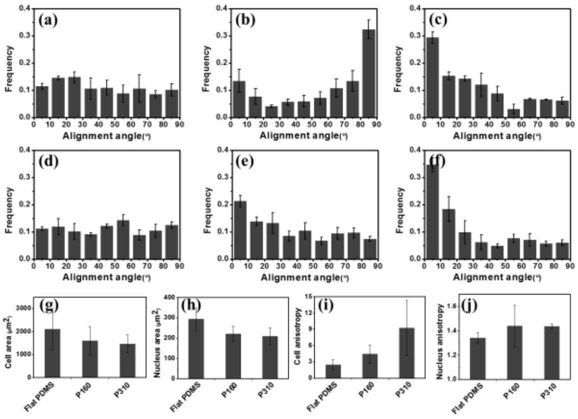

Figure 5 Répartition de l'alignement des cellules NIH 3T3 après 1 jour (a-c) et 4 jours (d-f) d’incubation sur les échantillons plats (a, d), P160 (b, e) et P310 (c, f); (g, h) Surface cellulaire et surface du noyau sur les trois types de substrats après 1 jour d'incubation; (i, j) Le gradient de rigidité du substrat induit une anisotropie de forme du cytosquelette et du noyau (rapport de la longueur à la largeur pour les cellules et leurs noyaux).

D'autres types de structures ondulées peuvent également être fabriquées afin d’obtenir d’autres gradients de rigidité sur différents de substrats de piliers (figure 6). Comme attendu, les cellules se sont principalement localisées dans les zones les plus rigides et, elles se sont également allongées le long de la géométrie définie par la rigidité pendant les trois premiers jours de culture. Avec la prolifération des cellules, l'orientation des cellules a été guidée avec les micropiliers (figure 6f). Ces résultats ont encore prouvé l'effet du gradient de rigidité.

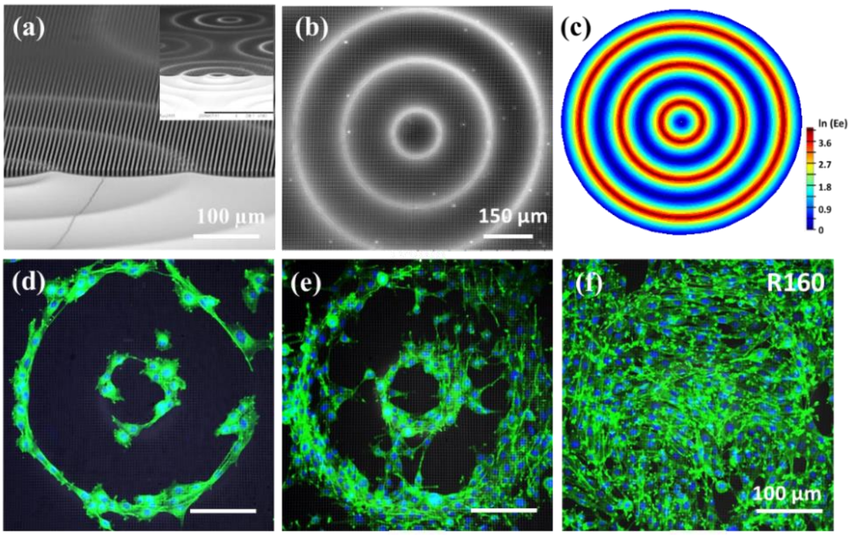

Figure 6 (a, b) Images MEB des réseaux de piliers en PDMS avec un gradient de rigidité ondulé (échantillon R160); (c) Calcul des modules effectifs de Young des matrices de piliers en PDMS avec un gradient de rigidité ondulée; (d-f) Immunofluorescence des cellules NIH 3T3 après 1 jour, 3 jours et 4 jours d'incubation sur l'échantillon R160. Les noyaux cellulaires ont été colorés par DAPI (bleu) et le réseau du cytosquelette par l'actine en vert (Alexa Fluor 488 phalloidine).

3 Monocouche de nanofibres étroitement espacées pour la manipulation cellulaire tridimensionnelle

3.1 Introduction

Cultiver des cellules in vitro tout en conservant des caractéristiques in vivo présente un grand potentiel non seulement pour la fonction cellulaire, mais aussi pour l'ingénierie tissulaire et la médecine régénératrice. La culture classique de cellules présente des conditions non naturelles, telles qu’un espace en 2D et un faible apport de nutriments, ce qui conduit au développement de cellules physiologiquement compromises. Tandis qu'in vivo, les cellules évoluent dans un environnement tridimensionnel entourées d'ECM et d'autres cellules baignées dans un liquide tissulaire. Le manque d'un environnement type ECM, qui est crucial pour générer des signaux physiques et chimiques, sans compter le soutien structurel apporté, est l'obstacle majeur de la croissance cellulaire normale in vitro. Il devient nécessaire de développer un scaffold 3D imitant l'ECM, auquel on peut intégrer des marqueurs pertinents de l'ECM, afin d'obtenir une versatilité cellulaire utile pour différentes applications médicales et non médicales. De plus, afin d'optimiser la culture et l'expansion cellulaire, un tel scaffold doit avoir une porosité élevée et interconnectée, et un ratio surface-volume élevé. Il doit être mécaniquement robuste et, idéalement, incorporer des signaux biophysiques pour guider la migration et l'activité cellulaire.

Notre approche pour aborder ces problèmes est de combiner des méthodes qui permettent de fabriquer de manière reproductible un nouveau type de supports de culture cellulaire tridimensionnels avec des fibres d'hydrogel et de gélatine biocompatibles. Dans cette méthode, une couche mince d'hydrogel avec des trous en nid d'abeille a d'abord été fabriquée par des procédés de photolithographie, cette couche agissant alors comme collecteur et support mécanique pour le dépôt de nanofibres. De plus, avec cette couche d'hydrogel, le scaffold fibreux ainsi fabriqué est facile à manipuler. Les nanofibres de gélatine ont été déposées par électrospinning des deux côtés de la couche de micro-motifs, formant ainsi des couches de nanofibres espacées, adaptées à la manipulation et à la migration des cellules en 3D. Avec une structure fibreuse tridimensionnelle et un biomatériau naturel, ce scaffold pourrait mieux récapituler les fonctions du microenvironnement in vivo. Un tel substrat de culture est mécaniquement robuste et poreux, afin de permettre l'infiltration cellulaire, de limiter la régulation négative des tractions exercées par la matrice cellulaire, et de favoriser la perméabilité 3D et la prolifération des cellules.

3.2 Fabrication d'un scaffold à trois couches

Fabrication du support en PEGDA : Un masque optique de chrome est fabriqué par un faisceau laser focalisé. Puis, une couche de résine (AZ40XT, Microresist) est déposée sur le masque, suivi par un recuit de 10 min à 125°C. Après avoir été irradiée par une lumière UV à travers le masque, la couche de résine est développée, résultant en un moule de résine. Après avoir été exposé au triméthylchlorosilane (TMCS) comme traitement antiadhésif, un mélange des composants A et B de PDMS (GE RTV 615) dans un rapport de 10 : 1 est appliqué au moule. Cette étape est suivie d'un recuit à 80°C pendant 2 h. Puis la couche de PDMS est décollée et posée, côté structuré en contact avec une lame de verre. L'ensemble PDMS-verre est placé dans un dessiccateur pour dégazage pendant 15 min. Puis, la cavité PDMS-verre est remplie par effet de micro-aspiration avec un mélange de PEGDA avec 1% (en volume) d'Irgacure 2959 (photo-amorceur), suivi d'une exposition aux UV à 12mW / cm2 pendant 30 sec. Enfin, la couche de PDMS est retirée, résultant en un réseau de PEGDA solidifié en forme de nid d'abeille. Pour augmenter la résistance mécanique de ce réseau, un anneau de PEGDA est ajouté au-dessus du nid d'abeille. Cet anneau a été préparé selon le protocole décrit ci-dessus et collé sous UV sur le réseau de nid d'abeille en utilisant la solution de PEGDA comme adhésif.

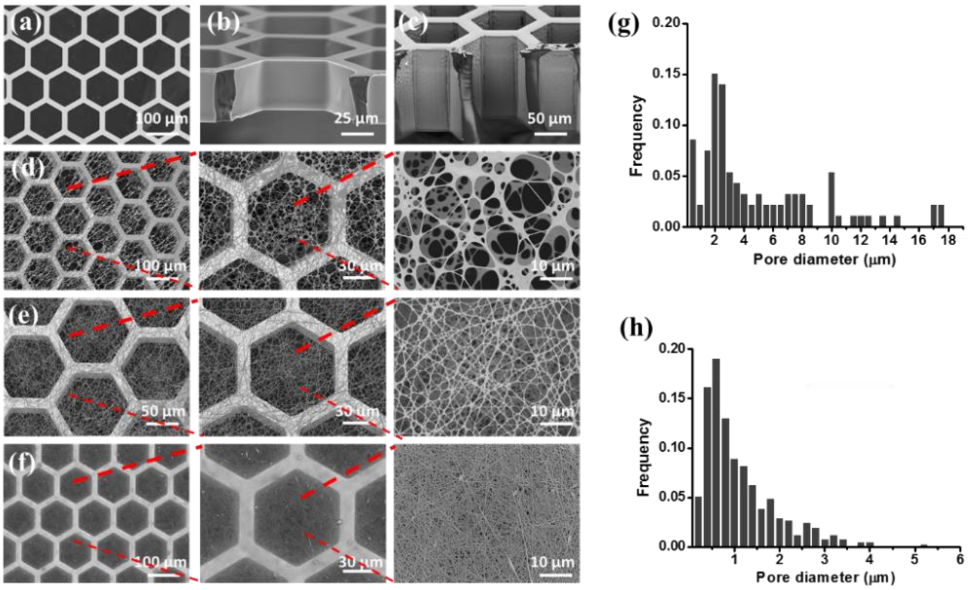

Figure 7 Structure du patch contrôlée par le temps d'électrospinning. (a) Images MEB de nanofibres de gélatine réticulées obtenues par 5min (a-c), 10min (d-f) et 20 min (g-i) d'électrospinning. (J, k) Distribution de la taille des pores des échantillons de 5 et 10min.

Dépôt des nanofibres de gélatine: Les nanofibres de gélatine ont été déposées des deux côtés du cadre PEGDA par électrospinning. Une solution de gélatine de 10% en poids est préparée par dissolution des poudres de gélatine (G2625, Sigma-Aldrich, France) dans une solution mixte d'acide acétique, d'acétate d'éthyle et d'eau distillée selon un rapport volumique de 21:14:10. L’électrospinning est fait en utilisant une pompe à seringue, une source d'alimentation de haut potentiel et une plaquette de silicium comme support de dispositif PEGDA et de collecteur de nanofibres. Les nanofibres de gélatine sont obtenues sur l’échantillon de PEGDA en plaçant la plaquette de silicium à une distance de 10 cm de l’aiguille de la seringue chargée de la solution de gélatine et en appliquant une tension de polarisation de 11KV entre l’aiguille (anode) et la plaquette (cathode), Le flux d’injection de la solution de gélatine est fixé à 0,2 ml / h. Après la récupération, les nanofibres de gélatine sont séchées sous vide pendant une nuit afin d'évaporer le résidu de solvant. Les nanofibres sont ensuite réticulées dans une solution d'éthanol avec 0,2 M d'EDC (1-éthyl-3-(3-diméthylaminopropyl) carbodiimide) et 0,2 M de NHS (N-hydroxysuccinimide, référence) pendant 4 h. Après la réticulation, l’échantillon est rincé trois fois à l'éthanol avant d'être séché pendant une nuit sous vide pour éliminer les produits chimiques restants. La figure 7 montre un patch de culture avec des nanofibres de gélatine de diamètre 100-500 nm et une structure de PEGDA de hauteur et de largeur 50 µm. Nous pouvons contrôler la taille des pores en ajustant le temps d'électrospinning.

3.3 Viabilité cellulaire et morphologie

Après 24 h de culture cellulaire in vitro, un test fluorescent de viabilité des cellules a été effectué et les résultats sont présentés dans la Fig. 8. Comme on peut le voir, presque toutes les cellules étaient vivantes et seules quelques cellules mortes ont été trouvées sur le patch même après 4 jours de culture et de prolifération. Ces résultats ont démontré que les cellules sur scaffold à trois couches présentaient une grande viabilité, due sans doute à la biocompatibilité des matériaux utilisés, à savoir la gélatine et le PEGDA. La figure 8 montre des images d'immunofluorescence de cellules NIH 3T3 cultivées sur un scaffold à trois couches (épaisseur 50 µm) juste après l’adhérence et jusqu’au au jour 3, ainsi que la vue en 3D de la pénétration cellulaire dans le scaffold en fonction du temps. Comme on peut le voir, les cellules se sont attachées sur la couche supérieure de fibres et se sont répandues sur les fibres 3h seulement après l'ensemencement. À partir de l'image en 3D obtenue par Z-stack sur microscope confocal, on peut voir qu'il n'y a pas de cellules dans le côté inférieur en raison de la taille de pore contrôlée (moins de 5 µm). Au cours de la culture, les cellules ont commencé à proliférer. Après un jour, les cellules ont recouvert la surface supérieure, avec peu de cellules infiltrées. À partir du jour 2, il y a des cellules en multi-couches et plus de cellules ont pénétré dans l'espace libre formé entre les réseaux de nanofibres. Enfin, au jour 3, une partie des cellules a atteint la surface inférieure et a formé un patch cellulaire 3D.

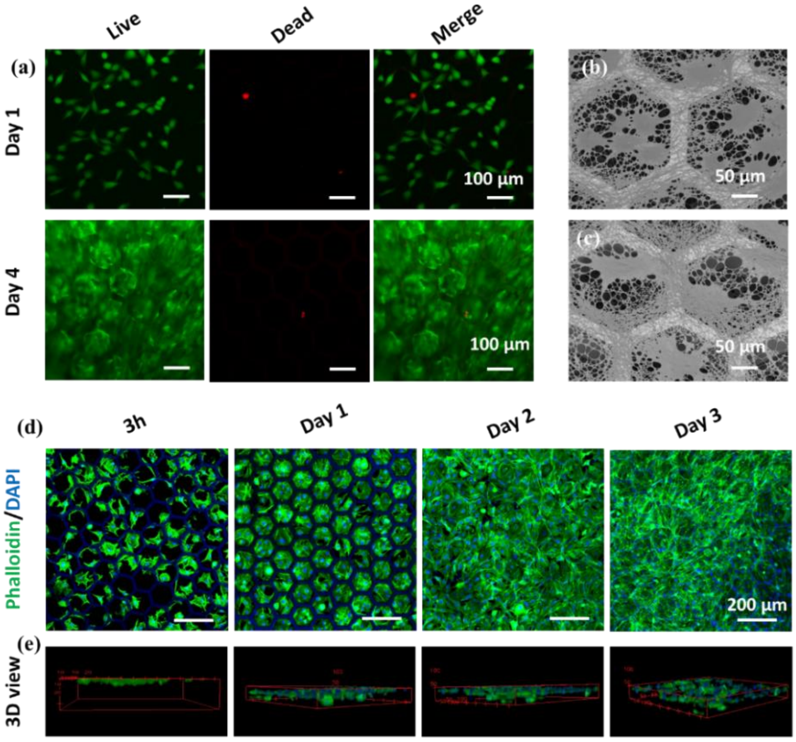

Figure 8 (a) Marquage de cellules vivantes/mortes montrant la viabilité des cellules NIH 3T3 sur un scaffold tri-couche de gélatine-PEGDA après 1 et 4 jours de culture. Images MEB des cellules sur un scaffold tri-couche après ensemencement (b) 1 h et (c) 3 h. (D) Images d'immunofluorescence et vue 3D des cellules NIH 3T3 sur le scaffold tri-couche avec une épaisseur de 50 µm. Les cellules ont été colorées avec de la FITC-phalloidine (vert) pour la F-actine du cytosquelette et du DAPI pour le noyau (bleu).

3.4 Migration cellulaire

Pour étudier le comportement de la migration des cellules sur ce scaffold fibreux 3D, l'infiltration des cellules du haut ou du bas a été étudiée. En outre, deux types de scaffolds avec des couche d'hydrogel d’épaisseurs différentes (50 µm et 100 µm) ont été testés pour étudier la migration en fonction du temps de culture.

Migration vers le haut en bas: les cellules ont été ensemencées sur la couche supérieure de nanofibres pour étudier l'infiltration des cellules de haut en bas. Il est évident que toutes les cellules ont attaché sur les fibres de la couche supérieure et rares sont les cellules qui ont été détectées sur le côté inférieur; indiquant que la distribution de la taille des pores empêche bien les cellules de tomber lors de l'ensemencement. Les cellules se sont progressivement infiltrées dans le scaffold avec le temps, ce qui indique que les cellules ont proliféré et migré dans l'espace creux (figure 9). La figure 10 montre plus clairement l'étirement du cytosquelette et son allongement dans l'espace en nid d'abeilles. Sur le scaffold à trois couches d'épaisseur 100µm, moins de 5% de cellules ont pénétré jusqu'à une profondeur de 25µm après 3 jours de culture. C'est peut-être parce que le filet nanofibreux du côté inférieur pourrait fournir des points d'attache et exercer des forces de traction sur les cellules que sur scaffold avec une épaisseur de 50 µm, on observe une migration cellulaire favorisée. Après 5 jours de culture, environ 4% des cellules ont finalement pénétré vers le bas, formant une couche épaisse de cellules (figures 11a et 11b).

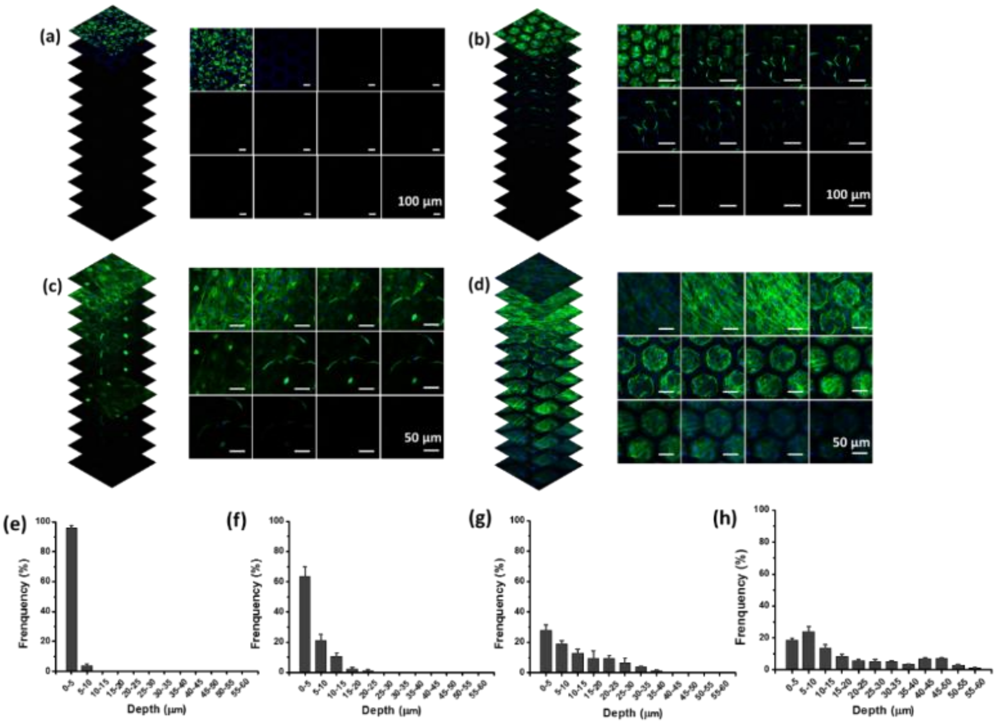

Figure 9 Microscopie confocale en Z-Stack de cellules NIH 3T3 ensemencées sur les scaffolds nanofibreux à trois couches avec une épaisseur de 50 µm après (a) 3 h, (b) 24 h, (c) 2 jours et (d) croissance de 3 jours. Dans chaque groupe, des images d'empilement empilées et non empilées de différents plans montrant de surface en bas avec une épaisseur de plan de 2 µm sont représentées. (E-h) Localisation du noyau en profondeur après la culture (a-d) 3 h, 24 h, 2 jours et 3 jours.

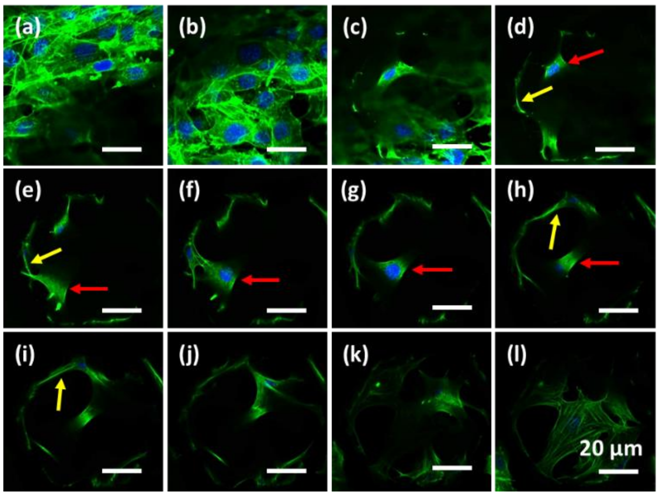

Figure 10 Images en Z-Stack par confocal de l'étirement et de l'allongement du cytosquelette dans l'espace en nid d'abeille après 3 jours de culture 3. (a-l) Section correspondant à différents plans focaux avec une épaisseur de plan de 5 µm entre les surfaces supérieure et inférieure du dispositif. Les flèches en rouge indiquent les cellules dans l'espace creux, tandis que les flèches en jaune indiquent que les cellules migrent le long de la paroi du sommet du nid d'abeille.

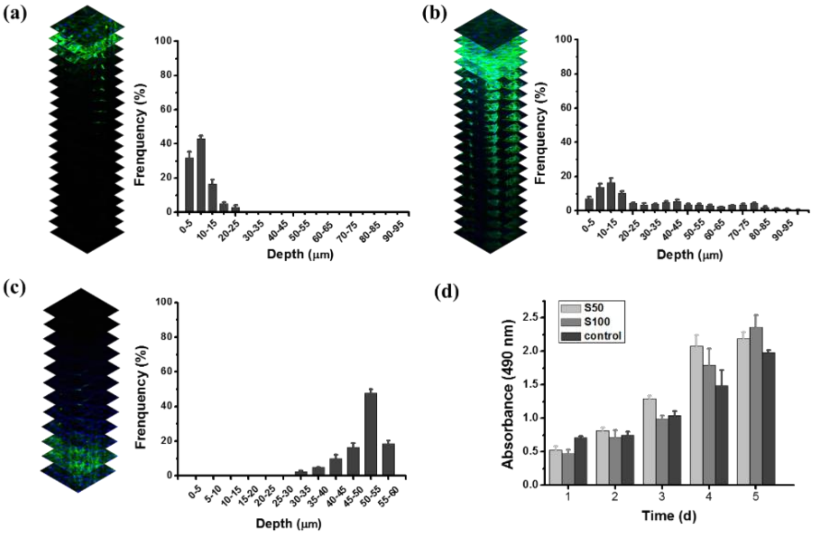

Figure 11 Images en Z-Stack par confocal et distribution des cellules après (a) 3 jours et (b) 5 jours de culture sur un scaffold d'épaisseur 100 µm. (c) Migration de bas en haut sur un scaffold d'épaisseur 50 µm. (d) Dosage MTT de la prolifération cellulaire.

Migration vers le bas vers le haut: Pour étudier la force motrice de la migration cellulaire sur un scaffold tri-couche, nous avons testé la situation des cellules qui ont d'abord été ensemencées sur le côté inférieur (figure 11). Comme on peut le voir, environ 70% des cellules sont restées sur le côté inférieur, avec moins de 5% de cellules migrant jusqu'à une profondeur de 30 µm. Par rapport à la situation des cellules ensemencées sur la surface supérieure dans laquelle les cellules se sont répandues dans l'espace libre et ont formé une couche de cellules sur le fond, il n'y a eu que peu de cellules migrées, indiquant que la gravité naturelle est l'une des causes de la migration, et aussi probablement en raison de la perméabilité améliorée du substrat et de l'effet de la force anisotrope fournie par les fibres de gélatine.

4 Différenciation des cellules souches pluripotentes induites humaines (hiPSC) sur des substrats de micropiliers à propriétés mécaniques contrôlées

4.1 Introduction

La capacité des cellules souches pluripotentes induites humaines (hiPSC) à se renouveler soi-même et la différenciation programmable des hiPSCs vers des lignées multiples en font une stratégie prometteuse pour les thérapies cellulaires. Cependant, les capacités des iPSC dépendent fortement de l'état de la culture. Les méthodes de culture conventionnelles qui reposent sur l'utilisation quotidienne de substrats durs (les plaques et flasques de culture) ne conviennent pas à la plupart des applications envisagées, même si elles peuvent maintenir la pluripotence et guider la différentiation après un traitement de surface biochimique des substrats. En effet les plaques de culture ne sont pas compatibles avec les cellules au niveau mécanique puisque les valeurs de rigidité des substrats sont généralement beaucoup plus élevées que celles des hiPSC ou des cellules dérivées. À cet égard, il est hautement souhaitable de développer de nouveaux substrats et de nouvelles méthodes de culture pour les applications d'iPSC.

En outre, les protocoles de différenciation existants nécessitent une étape de formation de corps embryoïdes (EB). La génération d'une colonie cellulaire tridimensionnelle soumet les cellules à des interactions complexes cellule-cellule, qui vont primer dans la différenciation ultérieure vers diverses lignées. Néanmoins, les méthodologies de génération d'EBs nécessitent des étapes multiples et des processus complexes, qui ont une faible répétabilité. Par conséquent, le développement de stratégies plus fiables pour stimuler la croissance des colonies en 3D est fortement recherchée pour maximiser l'efficacité de la différenciation a posteriori.

Dans cette étude, nous avons fabriqué des réseaux de micropiliers en élastomères denses comme nouveau type de substrat de culture ayant une rigidité contrôlée, dépendant directement de la hauteur du poteau, tout en conservant les propriétés d’adhésion, volumiques et de surface des autres matériaux. Par rapport à d'autres substrats tels que l'hydrogel, les substrats de micropiliers peuvent accéder à la même rigidité effective mais avec moins de contact exogène. En outre, l'espace entre les micropiliers contribue à la diffusion des nutriments, des métabolites et des facteurs cellulaires solubles. Pour obtenir des EBs uniformes sur des substrats de micropiliers, un pochoir de PDMS avec des motifs en nid d'abeille a été intégré lors de l'ensemencement des cellules et enlevé après la fixation des cellules, laissant ainsi un espace vide entre les cellules. Ensuite, la différenciation des cardiomyocytes a été démarrée.

4.2 Caractérisation des réseaux de micropiliers et pochoir de PDMS

Nous avons fabriqué trois types de matrices micropiliers avec le même diamètre (2 µm) et le même écartement (5,5 µm), mais avec des hauteurs différentes (2,7 µm, 7,2 µm et 10,3 µm) (figure 12a). Un pochoir de PDMS a été fabriqué avec un réseau en nid d'abeilles d'une diamètre de 500 µm et une épaisseur de travée de 100 µm, et d'épaisseur finale 50 µm. La rigidité effective déduite des trois types de substrats de pilier a été montrée à la figure 12f (168 KPa, 9 KPa et 3 KPa pour les réseaux de micropiliers avec des hauteurs de 2,7 µm, 7,2 µm et 10,3 µm, respectivement).

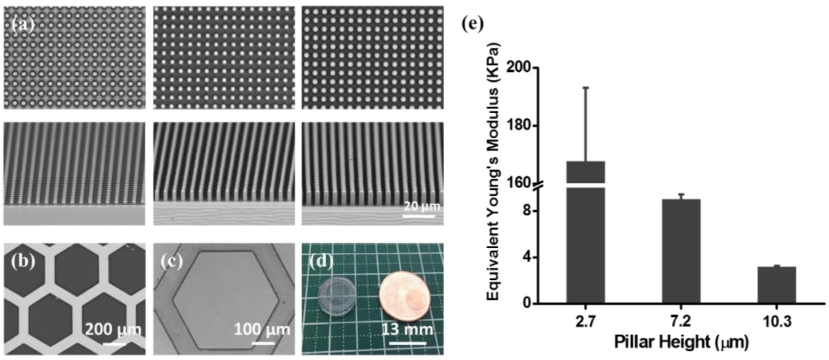

Figure 12 Images MEB de (a) réseaux de micropiliers de hauteurs différentes, (b) Pochoir de PDMS. (C, d) Image de contraste de phase et photographie de réseaux de micropiliers couverts du pochoir PDMS. (E) Module Yong équivalent des substrats de micropiliers.

4.3 Generation d’EB assistée par pochoir de PDMS

Afin d'obtenir un répartition homogène des EB sur le réseau de micropiliers, un pochoir de PDMS monté avec un anneau de PDMS a été posé sur les piliers pendant l'ensemencement des cellules (figure 13). Après avoir enlevé le pochoir et avoir changé le milieu pour un milieu E8 sans ROCK-inhibiteur les cellules sont cultivées 24h, les cellules hiPS se sont contractées et ont formé une forme ronde plus petite par rapport au jour -1 sur des substrats de micropiliers. Sur le substrat de PDMS plat, les motifs étaient connectés l'un à l'autre car les substrats rigides favorisent la propagation et la prolifération des cellules hiPS, Afin de modifier la morphologie des EBs, nous avons testé différentes densités de semis cellulaires (4 × 10^6, 3 × 10^6 et 2 × 10^6 cellules/mL), ce qui suggère que la taille d’un EB peut être contrôlée par la densité d'ensemencement cellulaire (figures 13c et 13d).

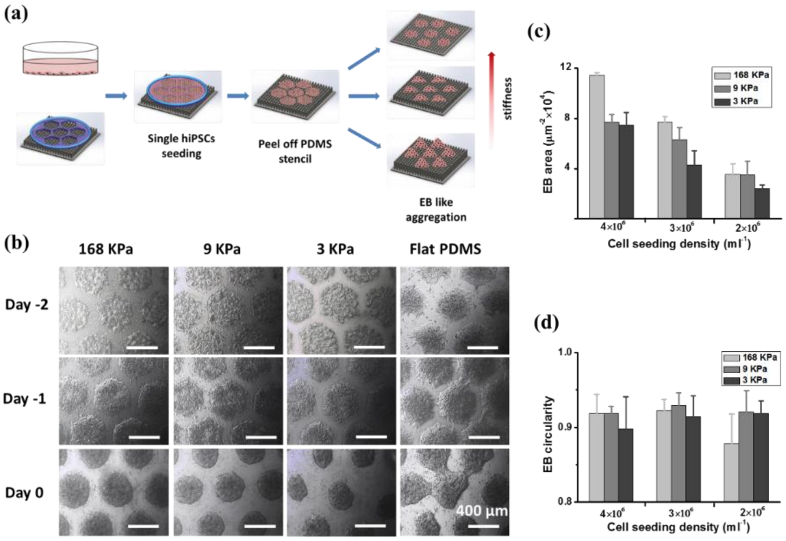

Figure 13 (a) Schéma représentant une procédure expérimentale pour examiner la formation de corps embryoïde (EB) de hiPSC en fonction des propriétés mécaniques des substrats. (b) La formation d’EB d’hiPSC sur des réseaux de micropiliers avec des rigidités différentes. (c, d) Evolution statistique de la surface et de la circularité des EBs avec la densité de semis des cellules 4×10^6, 3×10^6 et 2×10^6 cellules/mL.

4.4 Pluripotence des demi-shères d’EBs

Pour évaluer le caractère « souche » des EBs générés sur les substrats de micropiliers, des marqueurs spécifiques des cellules souches (OCT4 et SSEA4) ont été utilisés pour colorer les EBs et une couche de cellules étalée sur du PDMS plat comme témoin, après 3 jours de culture (figure 14). Ces résultats indiquent que l'expression des marqueurs de cellules souches pluripotentes positives OCT4 et SSEA4 a été maintenue pour les hiPSC cultivées sur des réseaux de micropiliers par rapport au contrôle, et que la morphologie des colonies distinctes n'a pas affecté les niveaux de pluripotence pendant la période de culture examinée (figures 14b et 14c). La dépendance de la morphologie des EBs à la rigidité du scaffold a été confirmée par l'imagerie confocal en Z-Stack (figures 14d et 14e). Après une période de pré-culture de 3 jours avec un milieu de prolifération, les colonies sur substrat rigide présentaient une morphologie EB ronde et plate avec un diamètre relativement important (environ 350 µm), alors que les cellules sur un substrat plus mou (3 KPa) affichent une morphologie plus volumique, et de plus petit diamètre. Fait intéressant, une cavité centrale s'est formée sur les substrats plus mous.

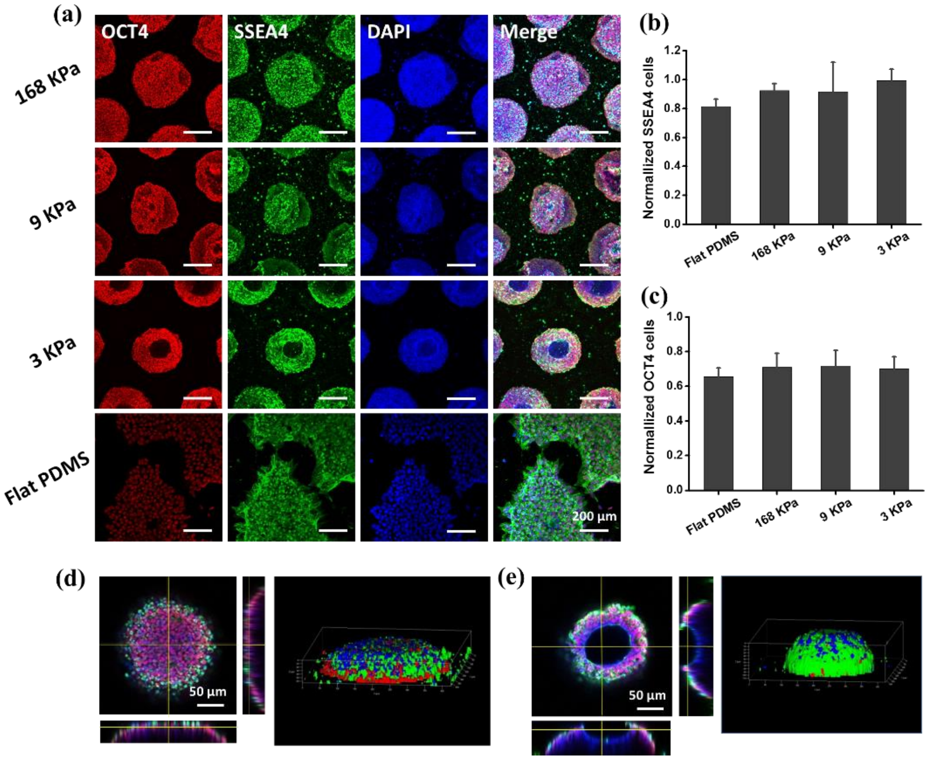

Figure 14 (a) Images d'immunomarquage d'hiPSC sur des substrats de micropiliers avec des rigidités de 168 KPa, 9 KPa et 3 KPa après 3 jours de culture (rouge: OCT4, vert: SSEA4, bleu: DAPI) (b, c) Histogramme montrant les cellules normalisées SSEA4 et OCT4 sur micropiliers et sur PDMS plat. Vue en coupe transversale et vue 3D d'EBs formés sur des substrats de micropiliers avec une rigidité de (d) 168 KPa et (e) 3 KPa.

4.5 Différenciation des cardiomyocytes sur substrat de micropiliers

Après avoir formé des EBs sur des substrats de micropiliers, les cadiomyocytes ont commencé à se différencier selon le protocole choisi, par modulation de la signalisation Wnt avec de petites molécules (figure 5.15). La morphologie des cellules sur différents substrats pendant le processus de prolifération a été enregistrée au microscope. Après avoir ajouté un inhibiteur de GSK3, les cellules au bord des EB ont commencé à migrer. Après environ 5 jours, les EBs ainsi séparés ont commencé à se connecter entre eux et ont formé une couche épaisse de cellules. Au jour 7 ou au jour 8, les cellules cardiaques différenciées ont commencé à se contracter sur les micropiliers et sur le PDMS plat. Au jour 14, la contraction cardiaque est devenue robuste et homogène sur toute la zone de micropiliers. En revanche, la contraction des cellules différenciées sur PDMS plat était beaucoup moins uniforme avec des zones distinctes de battements.

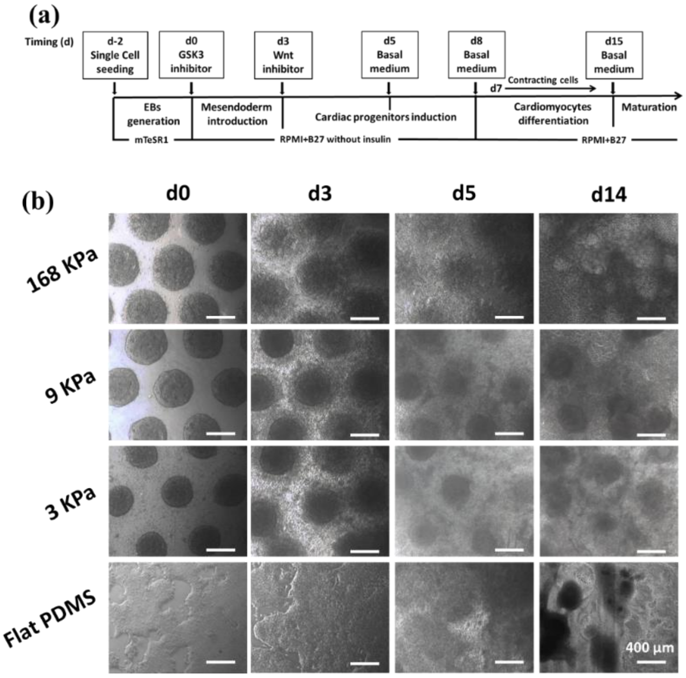

Figure 15 (a) Diagramme schématique du protocole de différenciation des cardiomyocytes à partir d’EBs sur des substrats de micropiliers. (B) Images de contraste de phase de la morphologie des hiPSC au cours de la différenciation.

4.5.1 Immunostaining of differentiated cardiomyocytes

Les marqueurs cardiaques spécifiques, comme l'α-actinine sarcomérique, la troponine I, l'α-MHC et la connexine43 ont été immuno-marqués pour évaluer le phénotype des cardiomyocytes différenciés après 15 jours de différenciation (figure 16). Comme on peut le voir, sur substrat de piliers mous (3 KPa), les cellules ont principalement adopté une morphologie ronde sans formation visible de troponine I et α-MHC, tandis que sur des substrats de 9 KPa ou de 168 KPa les cellules présentaient une organisation sarcomérique beaucoup plus claire en troponine I et α- MHC, ce qui est typique des cardiomyocytes matures. Sur le PDMS, seules quelques cellules ont une expression positive de troponine I et α-MHC, ce qui indique une efficacité de différenciation relativement faible sur le PDMS plat. L'α-actinine était positive dans les cellules différenciées sur tous les substrats, mais des structures d'α-actinine sarcomériques plus uniformes et hautement organisées s'observent pour les substrats de 9 KPa ou 168 KPa contrairement au substrat mou. Sur le contrôle (PDMS plat), les cellules sont également positives pour l'α-actinine, mais avec moins de structures sarcomériques. Ainsi, les cellules différenciées sur le substrat de micropiliers, en particulier sur le substrat de rigidité 9 KPa, ont présenté un assemblage de myofilaments plus organisé. Nos résultats d'immunomarquage pour les protéines des jonction communicantes comme la connexin43 ont également montré une tendance similaire. Sur le substrat de piliers avec une rigidité de 3 KPa, on a constaté que la connexin43 était moins exprimée dans les cellules par rapport aux substrats plus rigides. Par conséquent, les substrats de piliers rigides ont démontré un couplage cellule-cellule amélioré avec une machine contractile plus mature que le substrat de piliers mou.

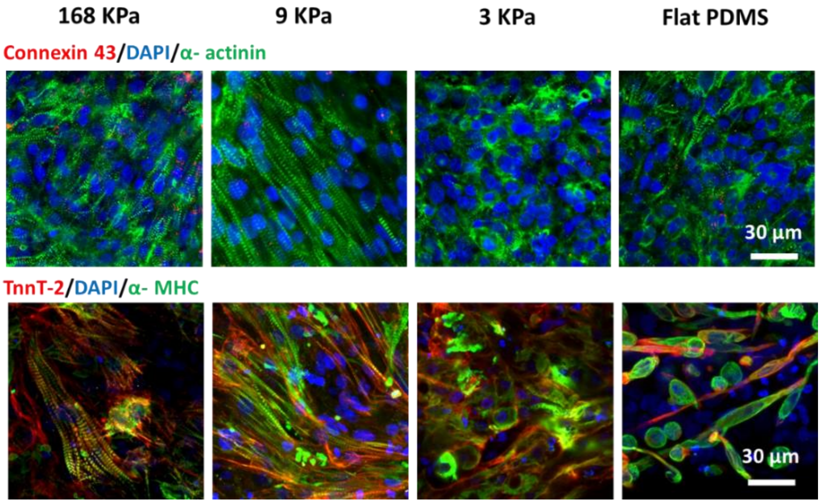

Figure 16 Immunofluorescence des images de cellules différenciées sur des substrats de micropiliers avec une rigidité de 168 KPa, 9 KPa et 3 KPa au 15ème jour.

4.5.2 Comportement des battements des cardiomyocytes différenciés

Pour évaluer les fonctionnalités au niveau des tissus, les battements des cardiomyocytes différenciés sur les substrats micropiliers ont été analysés plus avant par analyse des transitoire de calcium (Ca^{2+}) (figure 17). On sait que l'intensité de fluorescence d'une image de calcium est proportionnelle à la concentration de Ca^{2+} intracellulaire, qui est un messager important lié aux activités électriques et mécaniques des cellules. Comme on peut le constater, un signal de calcium est apparu avec différentes fréquences au niveau des points considérés sur le PDMS plat, ce qui peut contribuer à la formation de groupements cellulaires lors de la différenciation, et donc à des zones qui battent séparément. Les cardiomyocytes cultivés sur un substrat de micropiliers présentaient un comportement de battement synchrone, stable et robuste, en particulier sur les substrats avec une rigidité basse (9 KPa et 3 KPa), sur lesquels les cellules avaient des pointes de calcium synchronisées dans les 3 zones sélectionnées. Notamment, les cellules sur le substrat le plus rigide (168 KPa) ont présenté des battements en rythme et par intermittence. Un tel profil transitoire de calcium indiquait en outre que le comportement battant des cardiomyocytes dépend fortement de la rigidité du substrat et que la différenciation via EBs favorisait un battement synchrone et uniforme.

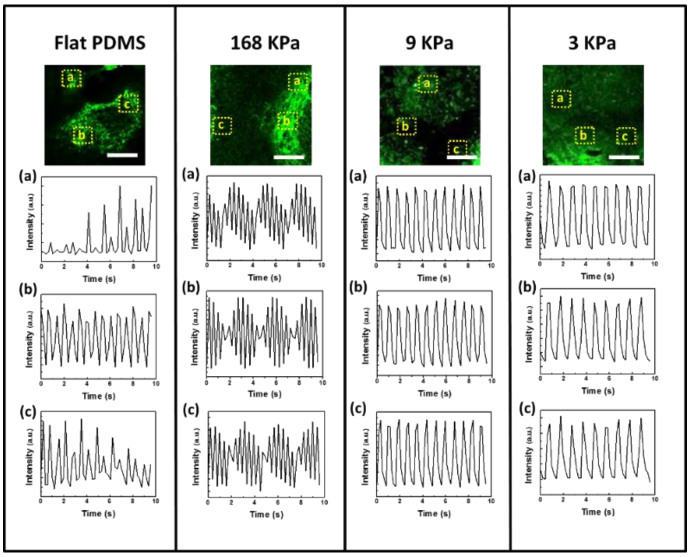

Figure 17 Transitoires de calcium des cardiomyocytes au jour 21 sur PDMS plat, et sur les substrats de micropiliers de raideur 168 KPa, 9 KPa et 3 KPa. Barre d'échelle: 200 µm. Trois régions indépendantes d'intérêt ont été sélectionnées au hasard dans chaque échantillon et l'évolution temporelle de l'intensité de fluorescence de chaque région a été tracé pour chaque groupe.

4.5.3 Impact d’une stimulation électrique externe

Des cardiomyocytes différenciés ont été utilisés pour évaluer la capacité des constructions de micropiliers à recevoir des stimuli électriques externes, comme le montre la figure 18. Sur les micropiliers les plus rigides, les fréquences de battement ne changeaient pas avec les stimuli électriques, alors que la fréquence de l'arrêt périodique devenait plus courte. Sur le substrat avec une rigidité inférieure, les fréquences de battement des cellules étaient beaucoup plus rapides avec lorsque l’on augmentait la fréquence des stimuli. En particulier, la fréquence de battement des cellules sur le substrat de rigidité intermédiaire (9 KPa) a presque doublé (de 72 ± 6 à 120 ± 9 / min), ce qui indique que les cardiomyocytes sur une matrice d’élasticité proche de celle du coeur sont fortement influencées par les stimuli électriques.

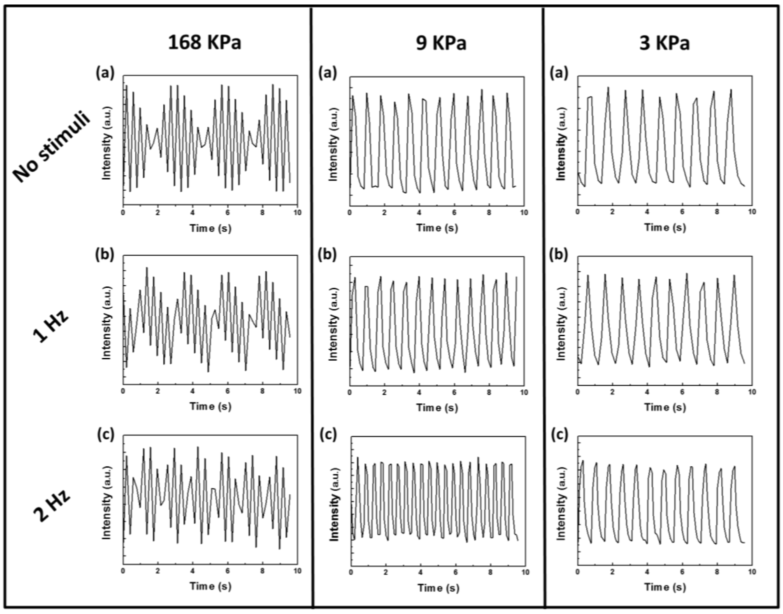

Figure 18 Signaux de battements sur tous les types de substrats de micropiliers pour différentes fréquences de stimuli électriques externes.

Abbreviation list

ECM	extracellular matrix
iPSCs	induced pluripotent stem cells
DNA	deoxyribonucleic acid
RNA	ribonucleic acid
mRNA	messenger RNA
SFKs	Src family kinases
FAK	focal adhesion kinase
2D	two-dimensional
3D	three-dimensional
iPSCs	induced pluripotent stem cells
hiPSCs	human induced pluripotent stem cells
hESCs	human embryonic stem cells
EBs	embryoid bodies
LSC	liquid suspension culture
FBS	Fetal Bovine Serum
KOSR	Knock-Out Serum Replacement
PEGDA	poly (ethylene glycol) diacrylate
SEM	scanning electron microscope
MSCs	mesenchymal stem cells
HA	hydroxyapatite
TCP	tri-calcium phosphate
PGA	polyglycolic acid
PLLA	poly-l-lactic acid
PLGA	poly (lactic-co-glycolic acid)
PEO	polyethylene oxide
PDMS	polydimethylsiloxane
UV	ultraviolet
PAC	photoactive compound
TMCS	trichloromethylesilane

CVD	chemical vapor deposition
PAA	polyacrylamide
DLW	direct laser writing
TX	Triton-X-100
RGD	arginine-glycine-aspartate
EDC	1-ethyl- 3-(3-dimethylaminopropyl) carbodiimide hydrochloride
NHS	N-hydroxysuccinimide
PBS	phosphate-buffered saline
TCPs	tissue culture plates
MTT	3-[4,5-dimethyl-2-thiazolyl]-2,5-diphenyl-2H-tetrazolium bromide
DMSO	dimethyl-sulfoxide
PMGI	polymethylglutarimide
PCL	polycaprolactone
ROCK	rho associated kinase
PFA	paraformaldehyde
BSA	bovine serum albumin
NGS	normal goat serum
MLAs	microlens arrays

Publication list

1. **Wang, B.**, Shi, J., Wei, J. et.al. Fabrication of elastomer pillar arrays with height gradient for cell culture studies. Microelectron.Eng. (2017)
2. **Wang, B.**, Shi, J., Wang, L. et.al. Spaced gelatin nanofiber layers integration with micro-patterned hydrogel for three-dimensional cell handling. In preparation.
3. **Wang, B.**, Wang, L., Wei, J. et.al. Elongation and directed cell migration on dense elastomer pillars with stiffness gradient. In preparation.
4. **Wang, B.**, Wang, L., Tu, X. et.al. Differentiation of human induced pluripotent stem cells (hiPSCs) on micropillar substrates with controlled mechanical property. In preparation.
5. **Wang, B.**, Chen, J. Y., Peng, H. M. et.al. Investigation on Changes in the Miscibility, Morphology, Rheology and Mechanical Behavior of Melt Processed Cellulose Acetate through Adding Polyethylene Glycol as a Plasticizer. J. Macromol. Sci., Part B, Phys. (2016)
6. Tu, X., Wei, J., **Wang, B.** et.al. Patterned parylene C for cell adhesion, spreading and alignment studies. Microelectron.Eng. (2017)
7. Wei, J., Shi, J., **Wang, B.** et.al. Fabrication of adjacent micropillar arrays with different heights for cell studies. Microelectron.Eng. (2016)

Résumé

L'objective de ce travail de thèse est de réaliser des substrats et des dispositifs de culture cellulaire pour des applications à grande échelle. En utilisant à la fois des techniques de lithographie conventionnelles et non conventionnelles, nous avons d'abord fabriqué des matrices denses de piliers élastomère avec un gradient de hauteur pour les études de migration cellulaire et nous avons observé un allongement cellulaire remarquable et une migration cellulaire dirigée, tout dépendant du gradient de rigidité. Les micropiliers élastomères pourraient également être organisés en gradient de hauteur oscillant, montrant des comportements cellulaire similaires. Sur la base d'une approche biomimétique, nous avons produit des nanofibres à deux côtés d'une membrane avec des trous traversants pour l'adhésion et la migration tridimensionnelles de cellules. Nos résultats ont montré qu'un tel substrat peut favoriser l'infiltration et la prolifération des cellules dans un environnement 3D. Enfin, nous avons utilisé des réseaux micropiliers de différentes hauteurs en tant que substrat de rigidité contrôlée pour la différenciation des cardiomyocytes à partir de cellules souches pluripotentes l'homme. À l'aide d'un stencil en élastomère, des embryons uniformes pourraient être obtenus et dérivés vers les cellules de ciblage sur le substrat de différentes rigidité, montrant clairement une dépendance de rigidité des substrats.

Mots Clés

Micropiliers, Nanofibres, Cellules souches, Ingénierie tissulaire

Abstract

The purpose of this work is to develop manufacturable cell culture substrates and devices for large scale applications. By using both conventional and non-conventional lithography techniques, we firstly fabricated dense elastomer pillar arrays with height gradient for cell migration studies and we observed remarkable cell elongation and directed cell migration, all depending on the strength of the stiffness gradient. Elastomer micropillars could also be organized in ripple-like height gradient patterns, showing similar cell behaviors. Based on a biomimetic approach, we produced nanofibers on both side of a membrane with through holes for three-dimensional cell adhesion and migration. Our results showed that such a 3D scaffold can promote the cell infiltration and proliferation. Finally, we used micropillar arrays of different height as stiffness controlled substrate for cardiomyocytes differentiation from human induced pluripotent stem cells (hiPSCs). With the help of an elastomer stencil, uniform embryoids could be obtained and derived to the targeting cells on the substrate of different stiffness, showing a clear stiffness dependence of the substrates.

Keywords

Micropillars, Nanofibers, Stem cells, Tissue engineering